

Algorithms for Fluid-Structure Interaction Problems Arising in Hemodynamics

THÈSE N° 4290 (2009)

PRÉSENTÉE LE 8 JANVIER 2009

À LA FACULTE SCIENCES DE BASE

CHAIRE DE MODÉLISATION ET CALCUL SCIENTIFIQUE

PROGRAMME DOCTORAL EN MATHÉMATIQUES

ÉCOLE POLYTECHNIQUE FÉDÉRALE DE LAUSANNE

POUR L'OBTENTION DU GRADE DE DOCTEUR ÈS SCIENCES

PAR

Annalisa QUAINI

acceptée sur proposition du jury:

Prof. R. Dalang, président du jury
Prof. A. Quarteroni, directeur de thèse
Dr M. Fernandez, rapporteur
Prof. F. Nobile, rapporteur
Prof. J. Rappaz, rapporteur



ÉCOLE POLYTECHNIQUE
FÉDÉRALE DE LAUSANNE

Suisse
2009

A Rossella, Carolina e Gianluigi

Abstract

We discuss in this thesis the numerical approximation of fluid-structure interaction (FSI) problems with a particular concern (albeit not exclusive) on hemodynamics applications.

Firstly, we model the blood as an incompressible fluid and the artery wall as an elastic structure. To solve the coupled problem, we propose new semi-implicit algorithms based on inexact block- LU factorization of the linear system obtained after the space-time discretization and linearization of the FSI problem. As a result, the fluid velocity is computed separately from the coupled pressure-structure velocity system at each iteration, hence reducing the computational cost. This approach leads to two different families of methods which extend to FSI problems schemes that were previously adopted for pure fluid problems.

The algorithms derived from inexact factorization methods are compared with other schemes based on two preconditioners for the FSI system. The first one is the classical Dirichlet-Neumann preconditioner, which has the advantage of modularity (i.e. it allows to reuse existing fluid and structure codes with minimum effort). Unfortunately, its performance is very poor in case of large added-mass effect, as it happens in hemodynamics. Alternatively, we consider a non-modular approach which consists in preconditioning the coupled system with a suitable diagonal scaling combined with an ILUT preconditioner. The system is then solved by a Krylov method. The drawback of this procedure is the loss of modularity. Independently of the preconditioner, the efficiency of semi-implicit algorithms is highlighted. All the methods are tested on two and three-dimensional blood-vessel systems. The algorithm combining the non-modular ILUT preconditioner with Krylov methods proved to be the fastest. However, modular and inexact factorization based methods should not be disregarded because they can considerably benefit from code parallelization, unlike the ILUT-Krylov approach.

Finally, we improve the structure model by representing the vessel wall as a linear poroelastic medium. Our non-modular approach and the partitioned procedures arising from a domain decomposition viewpoint are extended to fluid-poroelastic structure interactions. Their numerical performance are analyzed and compared on simplified blood-vessel systems.

Keywords: Fluid-elastic structure interaction, added-mass effect, semi-implicit coupling, fluid-poroelastic structure interaction, hemodynamics.

Résumé

Dans ce travail, nous nous intéressons à l'approximation numérique de problèmes d'interaction fluide-structure (IFS). L'application principale de cette étude est l'hémodynamique.

Dans une première phase, nous modélisons le sang comme un fluide incompressible et la paroi artérielle comme une structure élastique. Pour résoudre le problème couplé, nous proposons de nouveaux algorithmes semi-implicites basés sur une factorisation LU inexacte par blocs du système linéaire obtenu à partir de la discretisation en espace-temps et de la linéarisation du problème IFS. Par conséquent, la vitesse du fluide est calculée séparément du système pression-vitesse de la structure à chaque itération, ce qui réduit le temps de calcul. Cette approche aboutit à l'extension des schémas traditionnellement utilisés pour des problèmes de fluide purs aux problèmes IFS.

Les algorithmes basés sur la factorisation inexacte sont comparés avec d'autres schémas basés sur deux préconditionneurs pour le système IFS. Le premier est le préconditionneur Dirichlet-Neumann qui a l'avantage d'être modulaire (i.e. il permet de réutiliser des codes existants pour les problèmes de fluides et pour les problèmes de structures à moindre effort). Malheureusement, ce dernier s'avère peu performant dans une situation d'effet de masse ajoutée critique, comme cela se produit en hémodynamique. De façon alternative, nous considérons une approche non-modulaire qui consiste à préconditionner le système couplé avec un reproportionnement diagonal combiné avec un préconditionneur ILUT. Le système est ainsi résolu par une méthode de Krylov. L'inconvénient de cette procédure est la perte de modularité. L'efficacité des algorithmes semi-implicites, qui est indépendante du préconditionneur choisi, est mise en évidence. Toutes les méthodes sont testées sur des vaisseaux sanguins bi et tridimensionnels. L'algorithme combinant le préconditionneur ILUT non-modulaire avec les méthodes de Krylov s'avère le plus rapide. Cependant, les méthodes modulaires et celles basées sur la factorisation inexacte ne doivent pas être négligées car elles peuvent être améliorées considérablement par une parallélisation du code, contrairement à l'approche ILUT-Krylov.

Dans un second temps, nous améliorons le modèle de la structure en représentant la paroi artérielle comme un milieu linéaire poroélastique. Notre approche non-modulaire et les algorithmes partitionnés issus de la décomposition de domaines sont étendus aux interactions fluide-structure poroélastique. Leur efficacité est analysée et comparée sur des

systèmes simplifiés de vaisseaux sanguins.

Mots-clés: Interaction fluide-structure élastique, effet de masse ajouté, couplage semi-implicite, interaction fluide-structure poroélastique, hémodynamique.

Acknowledgements

I have been thinking for a couple of days about how to express my gratitude to Prof. Alfio Quarteroni in an original way, without repeating what his many PhD students have already told him. I surrender, I cannot help being repetitive. In fact, he does provide great opportunities to students by letting them work in his active research groups and he does combine an extremely broad knowledge of mathematics with a charismatic personality. I want to thank him for giving me the honor of working with him.

I consider it a real stroke of luck to have met Dr. Santiago Badia. Although he was not officially involved in this work, he has always helped me by answering my questions and clarifying my doubts. This work greatly benefited from his talent as a young researcher.

I am grateful to Prof. Fausto Saleri and Prof. Ramon Codina, who let me work on their codes: MLIFE and ZEPHYR, respectively.

I thank the president and the members of the jury, who carefully read the manuscript.

I would like to thank all the post-docs, PhD and master students that have worked at CMCS in the past three years. It has been a pleasure to spend time with you. Special thanks go to Gonçalo (and his alter egos: Gonzalo Peña and Frangerella) for all the fun we had together, Davide for having helped me with three-dimensional geometries and backward ice skating, and Marco for being an expert of the Stokes-Darcy coupling.

Many thanks to all the people I met in Lausanne for all the nice dinners, movie nights, and trips during these years. Among them, I would like to mention Chantal and Guillaume, and in particular Matteo, an actor of the theater of the absurd and my personal factotum (Bukowski style!).

I wish to thank all the friends I had before coming to Lausanne and have kept contact with me despite the distance, with a special mention for Giulio and Ligeia, who share with me the condition of emigrant.

My gratitude goes to Rajaa, my dance teacher. A twist of fate brought me to mathematics departments but I have always wanted to be a dancer. She helps me keep my dream alive. Finally, I offer my deepest thanks to my family: to my beloved grandparents, to Gigi and Carrie, for being the wonderful parents they are, and Rossella, the best sister and travel mate one could ask for.

Contents

Introduction	1
1 The incompressible Navier-Stokes equations in moving domains	7
1.1 Problem description	7
1.1.1 The incompressible Navier-Stokes equations in the Eulerian form . .	7
1.1.2 The ALE formulation of the Navier-Stokes equations	8
1.2 Some function spaces	10
1.3 Weak formulation	12
1.4 The fully discrete problem	14
1.4.1 About time discretization	14
1.4.2 About space discretization	15
1.4.3 The problem discretized in time and space	17
1.4.4 The linear fluid system	18
1.5 Inexact factorization methods	19
1.5.1 Pressure correction methods	21
1.5.2 Yosida methods	24
2 The interaction between a fluid and an elastic structure	27
2.1 Problem setting	27
2.1.1 The elastodynamics equation	27
2.1.2 The coupling conditions and the coupled FSI problem	29
2.2 Weak formulation	31
2.2.1 The solid structure subproblem	32
2.2.2 The coupled FSI problem	32
2.3 Analysis of coupled models	33
2.4 Space and time discretization	35
2.4.1 The discretization of the structure subproblem	35
2.4.2 The fully discrete FSI problem	36
2.5 State of the art	38

3	Splitting methods based on algebraic factorization	43
3.1	Introduction	43
3.2	The linear fluid-structure system	44
3.2.1	Features of the monolithic system	47
3.2.2	Block- <i>LU</i> factorization of the coupled system	48
3.3	Semi-implicit procedures for the FSI problem based on inexact factorization methods	50
3.3.1	Pressure-interface correction (PIC) methods	51
3.3.2	Fluid-structure Yosida (FSY) methods	54
3.3.3	Predictor-corrector methods	55
3.4	Comparison between inexact factorization-based methods and the projection scheme	57
3.4.1	Variations on the semi-implicit projection scheme	59
3.5	Analysis of the perturbation error	60
3.5.1	Perturbation terms for PIC schemes	60
3.5.2	Perturbation terms for FSY schemes	61
3.6	The pressure-structure system	63
3.6.1	The pressure-structure system matrix	63
3.6.2	Losing modularity	67
3.6.3	Keeping modularity	68
4	Application of the methods based on inexact factorization to blood flow in large arteries	71
4.1	Introduction	71
4.2	Blood Flow in Large Arteries	72
4.2.1	A generalized string model	73
4.2.2	A simplified 2D problem	74
4.3	Numerical Experiments	75
4.3.1	Semi-Implicit procedures	77
4.3.2	PIC and FSY accuracy	77
4.3.3	Splitting error for the FSY algorithm	79
4.3.4	Convergence of predictor-corrector methods	81
4.3.5	The added-mass effect and the pressure-interface system	82
4.3.6	Qualitative results	83
4.4	Conclusions	85
5	Comparison between modular and non-modular approaches	89
5.1	Introduction	89
5.2	The domain decomposition approach	90

5.3	The Dirichlet-Neumann preconditioner	92
5.3.1	Richardson algorithm for the preconditioned interface system	93
5.3.2	GMRES algorithm for the preconditioned interface system	93
5.3.3	The reduction factor for the residual norm of the DN-GMRES method for a model problem	95
5.4	ILU preconditioners	99
5.5	Numerical results for the straight cylindrical pipe	100
5.5.1	Comparison between the DN-Richardson and DN-GMRES methods	101
5.5.2	The DN-GMRES method: implicit and semi-implicit versions	104
5.5.3	The ILUT-GMRES and ILUT-BiCGStab methods	106
5.5.4	Comparison between the ILUT-solver and PIC-solver	106
5.6	Numerical results for the carotid bifurcation	108
5.6.1	Comparison between the ILUT-solver, PIC-solver, and DN-GMRES methods	109
5.6.2	The ILUT-GMRES and the PIC-BiCGStab methods for hemody- namics problems	111
5.6.3	The ILUT-solver: implicit and semi-implicit versions	113
5.7	Conclusions	114
6	The interaction between a fluid and a poroelastic structure	117
6.1	Introduction	117
6.2	Problem setting	119
6.2.1	The Biot system	119
6.2.2	The coupling conditions and the Biot/Navier-Stokes system	121
6.3	Weak formulation	123
6.4	Space and time discretization of the poroelastic problem	126
6.4.1	Stabilization of the Darcy problem	127
6.4.2	Stabilization of the generalized Darcy problem	132
6.4.3	The stabilized Biot system	135
6.4.4	A limit case	138
6.4.5	Numerical results	142
6.5	The fully discrete problem	147
6.6	The linear fluid-structure system	149
6.7	The monolithic approach	153
6.8	The domain decomposition approach	154
6.8.1	Block Gauss-Seidel interpretation	156
6.8.2	A simplified fluid-structure model	157
6.8.3	The Dirichlet-Neumann algorithm	161

6.8.4	The Robin-Robin and the Robin-Neumann algorithms	164
6.9	Numerical results	166
6.9.1	Comparison between the ILUT-GMRES and the DN methods . . .	167
6.9.2	Comparison between the DN and the RN algorithms	168
6.9.3	The RR algorithm	171
6.9.4	Qualitative results	172
6.10	Conclusions	173
	Conclusions	177
	Curriculum Vitæ	193

Introduction

Computer modeling is expected to play an important role in understanding the relationship between the hemodynamics factors (such as the wall shear stress) and the cardiovascular diseases (e.g. atherosclerosis). The main reason is that resolving phenomena in a living human body is currently beyond the capabilities of in vivo measurement techniques. The blood flow behavior with rigid artery walls differs completely from what happens when the compliance of the arterial walls is taken into account. Thus, the interaction between the blood and the artery wall is a crucial aspect of blood flow simulation. In this thesis, we deal with the mathematical modeling of the blood-vessel wall interaction and provide algorithms for the numerical solution of the coupled problem.

Our mathematical domain is a region split into two parts: a deformable structure Ω_t^s surrounding a moving volume Ω_t^f filled by fluid under motion. Both domains depend on time and their common boundary Σ_t is the fluid-structure interface, see Fig. 1. In each subregion we consider different mathematical models (one for the fluid and the other for the structure), which are coupled through suitable conditions at the interface. The complication of the fluid-structure interaction (FSI) problem appearing in hemodynamics is due to the so-called *added-mass effect* [26]. A simple explanation is as follows: since the structure is thin and light-weighted, the fluid acts on it as an extra-mass, causing “large” structure displacement.

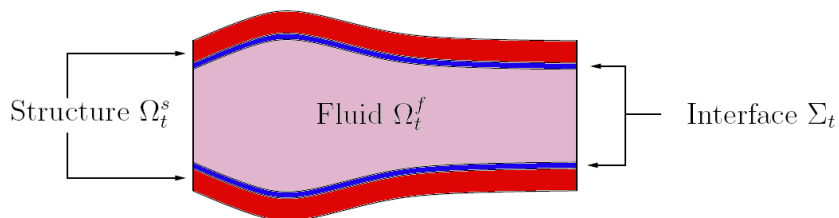


Figure 1: Mathematical domain configuration.

Blood is composed of blood cells suspended in a liquid called blood plasma. We do not consider the microscopic composition of the blood and model it as a homogeneous

and incompressible fluid. Moreover, in large arteries blood can be assumed to behave as a Newtonian fluid. Hence, blood motion in Ω_t^f is described through the incompressible Navier-Stokes equations. In order to deal with the large displacement of the fluid domain, we adopt an Arbitrary Lagrangian Eulerian (ALE) framework.

Neither the complex microscopic structure of the vessel wall is taken into account. The first structure model we consider is a purely elastic one, which accounts for the compliance. So, the structure motion in Ω_t^s is described by the elastodynamics equation for an elastic medium. In this case, the structure subproblem is coupled to the fluid one by two transmission conditions at the interface, ensuring the continuity of fluid and structure velocities and the continuity of stresses.

From the numerical viewpoint, the difficulty of FSI problems is twofold: they couple at each time level the two physically independent subproblems and they are nonlinear. We focus on the coupling aspect and treat the nonlinearities explicitly, i.e. no nonlinear iterations are performed. This leads to *semi-implicit* schemes [55].

After linearization, discretization in time (implicit Euler scheme for the fluid and either implicit Euler scheme or mid-point rule for the structure) and in space (Galerkin finite element method), the FSI problem can be written in a compact matrix form as:

$$A\mathbf{X}^{n+1} = \mathbf{b}^{n+1}, \tag{1}$$

where A is the FSI system matrix, \mathbf{X}^{n+1} is the vector of the nodal values for the fluid velocity, pressure, and the structure velocity, and \mathbf{b}^{n+1} is the right-hand-side, accounting also for the previous approximate solutions. Different strategies to solve the FSI system are taken into consideration. Although we are focused on hemodynamics applications, all the algorithms we propose can, in principle, be applied to any FSI problem involving an incompressible fluid and a thin elastic structure.

The first approach we adopt to solve the FSI system consists in computing the exact block- LU factorization of the fluid-structure system matrix A :

$$A = LU.$$

The key aspect of this factorization is the choice of the blocks to be *decoupled*. We consider a first block related to inner fluid velocity unknowns and a second one composed by the set of pressure and structure velocity. Unluckily, the Schur complements appearing in the exact factors L and U involve the inverse of the fluid matrix. For this reason, we must resort to inexact factorization techniques (see, e.g., [117]) which are feasible from a numerical point of view. We indicate the inexact factors with \tilde{L} and \tilde{U} . Thanks to the blocks choice in decoupling, the two step algorithm based on inexact factorization (L -step and U -step) can be easily rearranged in a three-step procedure, which computes the intermediate fluid velocity, solves the coupled pressure-structure system, and corrects the

fluid velocity. In this way, the fluid velocity computation is decoupled from the strongly coupled fluid-structure system, which only involves pressure and structure unknowns, with the double advantage of reducing computational costs and ensuring stability. Our aim is to take advantage of the good accuracy properties shown by inexact factorization techniques when solving the incompressible Navier-Stokes equations. In this respect, we adapt the algebraic pressure-correction methods and the Yosida method to the coupled fluid-structure problem. So, depending on the approximation of the exact factors, we derived two families of methods:

- *pressure-interface correction (PIC) methods*, FSI counterparts of the pressure correction methods (see, .e.g, [70]) for pure fluid problems;
- *fluid-structure Yosida (FSY) methods*, which adapt the Yosida method [116] to FSI problems.

The PIC scheme approximates system matrix A with $A_{PIC} = \tilde{L}\tilde{U}$ and its solution \mathbf{X}_{PIC}^{n+1} is such that:

$$A_{PIC}\mathbf{X}_{PIC}^{n+1} = \mathbf{b}^{n+1}.$$

The solution of the FSY method, denoted by \mathbf{X}_{FSY}^{n+1} , satisfies

$$A_{FSY}\mathbf{X}_{FSY}^{n+1} = \mathbf{b}^{n+1},$$

where $A_{FSY} = \tilde{L}U$. Due to the coupling between fluid pressure and structure velocity, this approach is non-modular. Modularity is the property of a solver to consist of separated modules and it is typical of *partitioned* procedures, which solve the fluid and the structure subproblems with two different codes. A modular FSI algorithm only requires interface data transfer between the two codes, without any modification of the sources. Thus, it allows to reuse existing (and already optimized) fluid and structure codes.

The Dirichlet-Neumann (DN) algorithm is a classical partitioned procedure stemming from a domain decomposition viewpoint (see, e.g., [45]). By means of Schur complements, the FSI problem can be reformulated as an interface problem for the wall displacement on Σ_t . The classical DN scheme consists in preconditioned Richardson iterations over that interface problem. For this reason, we call this method DN-Richardson; this algorithm is equivalent to iterate over the fluid subproblem (supplemented with a Dirichlet interface condition) and the structure one (endowed with a Neumann interface condition). Hence, the DN preconditioner is modular. Unluckily, as the added-mass effect becomes important, the DN-Richardson scheme, even if improved by an acceleration strategy, is slow or may even fail to converge (see, e.g., [104, 137]). To gain more efficiency, instead of performing Richardson iterations, we apply the GMRES algorithm to the preconditioned interface

problem (see, e.g., [96]). Since GMRES iterations are superior to Richardson ones, the DN-GMRES algorithm behaves well also in presence of a strong added-mass effect.

Another way to solve the FSI problem is to compute the solution of the FSI system without decoupling the fluid and the structure subproblems. This results in the so-called *monolithic methods*. These methods lack of modularity. Existing fluid and structure codes can still be reused, but the coupling of the codes is more involved than bare interface communication. However, monolithic algorithms are appealing thanks to the fact that transmissions conditions are exactly satisfied by construction. Moreover, the FSI system becomes better conditioned as the added-mass effect gets critical. Examples of monolithic methods can be found in [125, 72], and references therein. Our monolithic strategy solves monolithic system (1) with a Krylov method (e.g. GMRES or BiCGStab) preconditioned in two steps. Since fluid and structure entries are not of the same order, we first apply a suitable diagonal scaling of the FSI system. In a second step, the scaled system is preconditioned by an incomplete LU factorization (the ILUT preconditioner).

Despite its inefficiency in case of large added-mass effect, the DN-Richardson method has been widely used because of the simplicity in implementation. A few works [72, 56, 96] proposed to adopt the DN-GMRES algorithm, although never in its semi-implicit version. The monolithic approach combining ILUT preconditioners to Krylov methods and the inexact factorization based schemes are introduced for the first time. We test the numerical properties of the new methods on model problems representing a blood-vessel system. Moreover, we study and compare the behavior of all the algorithms as the added-mass effect varies, for both simplified $2d$ and realistic $3d$ problems.

Modeling the arterial wall as a poroelastic medium can be a step forward in the numerical simulation of the blood-vessel interaction. This more realistic structure model would allow us to deal with complex clinical problems, such as the development and the treatment of atherosclerosis. The dynamics of the structure are described by the Biot equations, which are coupled to the Navier-Stokes system via appropriate interface conditions. While the Navier-Stokes/elastodynamics and the Navier-Stokes/Darcy (see, e.g., [130, 63, 86, 47]) couplings have been broadly analyzed, up to our knowledge only a limited number of works [84, 25] tackles fluid-poroelastic structure interaction (FPSI) problems. Thus, the necessary mathematical theory to couple the two subproblems has to be developed.

After linearization and full discretization, the Navier-Stokes/Biot system can also be written in compact matrix form (1). The difference is that, in this case, A is the linear FPSI system matrix and \mathbf{X}^{n+1} is the vector of the nodal values for fluid velocity and pressure, structure velocity and pressure, and filtration velocity. Hence, the size of the problem increases.

We extend to these more complicated interactions some of the strategies we proposed for fluid-elastic structure interaction problems. In particular, we apply both our monolithic

approach and partitioned procedures to solve the FPSI linear system. Among all the partitioned procedures derived from a domain decomposition viewpoint, we focus our attention on the Dirichlet-Neumann, Robin-Neumann, and Robin-Robin algorithms. The respective preconditioners are applied to Richardson iterations. All the algorithms are considered in their semi-implicit version.

Up to now, only monolithic schemes (implicit version) have been adopted to solve the fully coupled system [84, 25]. This thesis constitutes the first attempt to apply partitioned procedures to FPSI problems. The numerical performance of the two approaches are analyzed and compared for simplified blood-vessel systems.

Thesis Outline

The present work is structured in six chapters:

Chapter 1 is dedicated to the incompressible Navier-Stokes equations in moving domains.

The ALE framework is introduced. The weak formulation and the space and time discretization are discussed. Moreover, we briefly describe inexact factorization based methods to solve the system yielded by linearization and full discretization.

Chapter 2 addresses the coupling of the incompressible Navier-Stokes equations in the ALE formulation with the elastodynamics equations for an elastic structure. Attention is paid to the coupling conditions and how to impose them in the weak form. Then, the FSI problem is discretized and linearized. A synthetic overview of the existing strategies to solve FSI problems ends the chapter.

Chapter 3 presents the semi-implicit algorithms based on inexact block-*LU* factorization of the linear system obtained after the space-time discretization and linearization of the FSI problem. We investigate explicit-implicit decomposition through algebraic splitting techniques originally designed for the FSI problem. Two different families of methods, PIC and FSU, are introduced and compared with the projection scheme in [55]. For both methods the perturbation error is analyzed. Furthermore, we consider the inexact factorization of the fluid-structure system as a preconditioner (predictor-corrector methods).

Chapter 4 shows the numerical behavior of the coupling schemes illustrated in Chapter 3 for a simplified problem. The test problem we consider is the $2d$ benchmark which models the interaction between an incompressible fluid and a thin elastic tube. Through numerical experiments, we study accuracy, splitting errors, and sensitivity to the added-mass effect for PIC, FSU, and predictor-corrector methods.

Chapter 5 aims at comparing the performances of the splitting techniques based on an inexact block-LU factorization of the linear FSI system with those of other two approaches. These two approaches involve different preconditioners for the coupled system matrix: the classical Dirichlet-Neumann preconditioner (for both Richardson and GMRES iterations) and an ILUT preconditioner combined with a diagonal scaling. All the methods are tested on three-dimensional blood-vessel systems and some conclusions on the optimal range of applicability of the methods are drawn.

Chapter 6 deals with fluid-poroelastic structure interaction problems. The differential and variational formulations of the coupled problem are stated and special care is addressed to the coupling conditions. A stabilized formulation for the Biot system is derived in order to write a stable discrete approximation of the Navier-Stokes/Biot problem. The associated system is solved by both our monolithic approach and partitioned procedures. Numerical results are carried out on $2d$ problems.

Chapter 1

The incompressible Navier-Stokes equations in moving domains

1.1 Problem description

Consider a fluid filling a bounded, polyhedral, and moving domain $\Omega_t \subset \mathbb{R}^d$ ($d=2, 3$, being the space dimension), where time t spans the interval of analysis $[0, T]$. We will assume the fluid to be homogeneous, incompressible, and Newtonian. Let \mathbf{n} be the unit outward normal of Ω_t on the boundary.

1.1.1 The incompressible Navier-Stokes equations in the Eulerian form

The problem is governed by the incompressible Navier-Stokes equations

$$\partial_t \mathbf{u} + \mathbf{u} \cdot \nabla \mathbf{u} - \frac{1}{\rho} \nabla \cdot \boldsymbol{\sigma} = \mathbf{f} \quad \text{in } \Omega_t \times (0, T), \quad (1.1a)$$

$$\nabla \cdot \mathbf{u} = 0 \quad \text{in } \Omega_t \times (0, T), \quad (1.1b)$$

where $\mathbf{u} = \mathbf{u}(\mathbf{x}, t)$ (with $\mathbf{x} \in \Omega_t$ and $t \in [0, T]$) is the fluid velocity, ρ the fluid density, $\boldsymbol{\sigma}$ the Cauchy stress tensor and \mathbf{f} the body force. The assumptions of homogeneity and incompressibility of the fluid imply that the density field ρ is constant in space and time. For Newtonian fluids, $\boldsymbol{\sigma}$ has the following expression

$$\boldsymbol{\sigma}(\mathbf{u}, p) = -p\mathbf{I} + 2\mu\boldsymbol{\epsilon}(\mathbf{u}), \quad (1.2)$$

where $p = p(\mathbf{x}, t)$ is the pressure, μ is the dynamic viscosity, and

$$\boldsymbol{\epsilon}(\mathbf{u}) = \frac{1}{2}(\nabla \mathbf{u} + (\nabla \mathbf{u})^T)$$

is the strain rate tensor, with ∇ denoting the spatial gradient operator. The kinematic viscosity is denoted with $\nu = \mu/\rho$.

Being the fluid incompressible, if thermal effects are neglected, the mass and momentum conservation equations ((1.1b) and (1.1a), respectively) suffice to characterize its motion.

In order to be well posed, problem (1.1) must be supplemented with initial conditions for the velocity

$$\mathbf{u}(\mathbf{x}, 0) = \mathbf{u}_0 \quad \text{in } \Omega_0,$$

and suitable boundary conditions. We assume the boundary $\partial\Omega_t$ to be a locally Lipschitz $(d - 1)$ -dimensional manifold. Moreover, we assume that $\partial\Omega_t$ can be divided into two non-overlapping subsets $\partial\Omega_D$ and $\partial\Omega_N$, such that $\partial\Omega_D \cap \partial\Omega_N = \emptyset$, $\partial\Omega_D \cup \partial\Omega_N = \partial\Omega_t$ and:

$$\mathbf{u} = \mathbf{u}_D \quad \text{on } \partial\Omega_D, \quad (1.3a)$$

$$\boldsymbol{\sigma} \cdot \mathbf{n} = \mathbf{g}_N \quad \text{on } \partial\Omega_N, \quad (1.3b)$$

for two given vector functions \mathbf{u}_D and \mathbf{g}_N . Typically, in the case of fluid flows in moving domains \mathbf{u}_D coincides with the velocity of the moving boundary on $\partial\Omega_D$. This is always the case for fluid-structure interaction problems, where $\partial\Omega_D$ corresponds to the interface between fluid and structure.

In many situations involving moving domains the Eulerian description of the fluid motion (1.1) becomes troublesome. In the next subsection, we explain the reasons and adopt the ALE framework as an alternative.

1.1.2 The ALE formulation of the Navier-Stokes equations

The ALE (Arbitrary Lagrangian-Eulerian) description of the fluid motion parametrizes the motion of the actual computational fluid volume Ω_t by a smooth map:

$$\mathcal{A} : \Omega_0 \times [0, T] \longrightarrow \Omega_t, \quad (\mathbf{x}_0, t) \longrightarrow \mathbf{x} = \mathcal{A}(\mathbf{x}_0, t), \quad (1.4)$$

called ALE map. The initial configuration Ω_0 at $t = 0$ is considered as the reference one (Fig. 1.1).

The ALE map $\mathcal{A}_t = \mathcal{A}(\cdot, t)$ gives the deformation of the domain at any time $t \geq 0$. We denote by $J_{\mathcal{A}} = \det(\nabla_{\mathbf{x}_0} \mathcal{A})$ the Jacobian of the deformation gradient. For any function $f : \Omega_t \times [0, T] \longrightarrow \mathbb{R}$, we indicate with $\hat{f} = f \circ \mathcal{A}_t$ the corresponding function in the ALE frame:

$$\hat{f} : \Omega_0 \times [0, T] \longrightarrow \mathbb{R}, \quad \hat{f}(\mathbf{x}_0, t) = f(\mathcal{A}_t(\mathbf{x}_0), t).$$

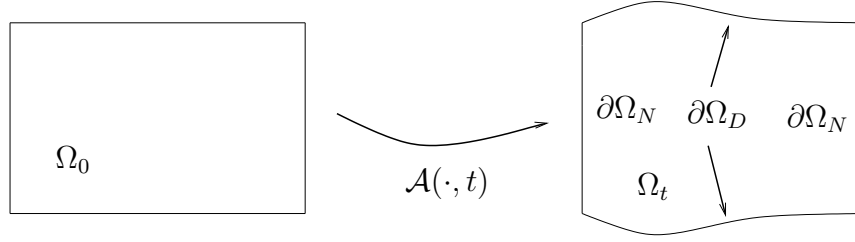


Figure 1.1: Parametrization of the domain with a possible partition of $\partial\Omega_t$ into $\partial\Omega_D$ and $\partial\Omega_N$.

The time derivatives in the ALE frame are defined as follows:

$$\partial_t f|_{\mathbf{x}_0} : \Omega_t \times [0, T] \longrightarrow \mathbb{R}, \quad \partial_t f|_{\mathbf{x}_0}(\mathbf{x}, t) = \partial_t \hat{f} \circ \mathcal{A}_t^{-1}(\mathbf{x}).$$

The domain velocity \mathbf{w} is calculated using the following expression:

$$\mathbf{w}(\mathbf{x}, t) = \partial_t \mathbf{x}|_{\mathbf{x}_0} = \partial_t \mathcal{A}_t \circ \mathcal{A}_t^{-1}(\mathbf{x}).$$

Notice that in general $\mathbf{w}(\mathbf{x}, t) \neq \mathbf{u}(\mathbf{x}, t)$. However, two particular cases can be distinguished:

- $\mathbf{w} = \mathbf{0}$: the domain is fixed, i.e. we recover the Eulerian description of the motion;
- $\mathbf{w} = \mathbf{u}$: we track the fluid domain, therefore the Lagrangian framework is recovered.

In order to write the fluid problem in its ALE form, let us apply the chain rule to the velocity time derivative:

$$\partial_t \mathbf{u}|_{\mathbf{x}_0} = \partial_t \mathbf{u} + \mathbf{w} \cdot \nabla \mathbf{u}, \quad (1.5)$$

where $\partial_t \mathbf{u}$ is the partial time derivative in the spatial frame (Eulerian derivative). The ALE time derivative is a key ingredient for the simulation of fluid problems in moving domains. For those problems, the discretization of the Eulerian derivatives cannot be computed, because a point that belongs to the fluid domain at a time step value does not necessarily belong to it at the previous one (and viceversa). Thus, it becomes natural to work with variables that follow the domain evolution.

By combining (1.5) with (1.1a), we get the incompressible Navier-Stokes equations in ALE non-conservative form:

$$\partial_t \mathbf{u}|_{\mathbf{x}_0} + (\mathbf{u} - \mathbf{w}) \cdot \nabla \mathbf{u} - \frac{1}{\rho} \nabla \cdot \boldsymbol{\sigma} = \mathbf{f} \quad \text{in } \Omega_t \times (0, T), \quad (1.6a)$$

$$\nabla \cdot \mathbf{u} = 0 \quad \text{in } \Omega_t \times (0, T). \quad (1.6b)$$

To obtain the conservative formulation, we consider the following identity [61]

$$\partial_t J_{\mathcal{A}}(\mathbf{x}_0, t) = J_{\mathcal{A}}(\mathbf{x}_0, t) \nabla \cdot \mathbf{w}(\mathcal{A}_t(\mathbf{x}_0), t),$$

from which we have

$$\partial_t \mathbf{u}|_{\mathbf{x}_0} = \frac{1}{J_{\mathcal{A}}} \left(\partial_t (J_{\mathcal{A}} \mathbf{u})|_{\mathbf{x}_0} - J_{\mathcal{A}} \mathbf{u} \nabla \cdot \mathbf{w} \right).$$

Plugging this expression in (1.6a) and exploiting the identity

$$\nabla \cdot (\mathbf{a} \otimes \mathbf{b}) = \mathbf{a} \nabla \cdot \mathbf{b} + \mathbf{b} \cdot \nabla \mathbf{a},$$

we get the ALE conservative form

$$\begin{aligned} \frac{1}{J_{\mathcal{A}}} \partial_t (J_{\mathcal{A}} \mathbf{u})|_{\mathbf{x}_0} + \nabla \cdot \left(\mathbf{u} \otimes (\mathbf{u} - \mathbf{w}) - \frac{1}{\rho} \boldsymbol{\sigma} \right) &= \mathbf{f} && \text{in } \Omega_t \times (0, T), \\ \nabla \cdot \mathbf{u} &= 0 && \text{in } \Omega_t \times (0, T). \end{aligned}$$

So far, we have assumed the ALE map (and related quantities, such as the ALE velocity) to be known. In general, this is not the case, since only the boundary displacement is known.

Let us denote with $\hat{\boldsymbol{\eta}}(\mathbf{x}_0, t)$ the boundary displacement at the reference configuration and suppose it is a given function. The ALE mapping can be defined through an appropriate extension operator of that value:

$$\mathcal{A}_t(\mathbf{x}_0) = \mathbf{x}_0 + \text{Ext}(\hat{\boldsymbol{\eta}}(\mathbf{x}_0, t)). \quad (1.7)$$

Different choices for the operator Ext have been proposed in literature. A classical one is to consider a harmonic extension in the reference domain. Owing to (1.7), we can easily calculate the fluid domain velocity in the ALE frame:

$$\hat{\mathbf{w}}(\mathbf{x}_0, t) = \text{Ext}(\partial_t \hat{\boldsymbol{\eta}}(\mathbf{x}_0, t)).$$

Moreover, supposing that $\partial\Omega_D$ corresponds to the moving part of $\partial\Omega_t$, the boundary velocity in (1.3a) is $\mathbf{u}_D = \partial_t \hat{\boldsymbol{\eta}}(\mathbf{x}_0, t) \circ \mathcal{A}_t^{-1} = \partial_t \boldsymbol{\eta}(\mathcal{A}_t(\mathbf{x}_0), t)$.

1.2 Some function spaces

Let us introduce some notation that will be used in the following. We refer to any standard functional analysis text (e.g. [107]) for a comprehensive exposition of all the concepts that are only mentioned here.

Let $\Omega \subset \mathbb{R}^d$, $d = 2, 3$, be a bounded domain. We indicate with \mathcal{C}_0^∞ the set of infinitely differentiable real functions with compact support in Ω . Let $L^p(\Omega)$, $1 \leq p < \infty$, denote

the space of real functions, defined on Ω , whose p -th power is absolutely integrable with respect to the Lebesgue measure. $L^p(\Omega)$ is a Banach space with the associated norm

$$\|u\|_{L^p(\Omega)} = \left(\int_{\Omega} |u|^p d\Omega \right)^{1/p}.$$

For $1 < p < \infty$, $L^p(\Omega)$ is a reflexive space and its dual space is $L^q(\Omega)$, with q such that $1/p + 1/q = 1$. For $1 < s < r < \infty$, $L^r(\Omega) \subset L^s(\Omega)$.

In the case $p = 2$, $L^2(\Omega)$ is a Hilbert space endowed with the scalar product

$$(u, v)_{\Omega} = \int_{\Omega} u v \, d\Omega$$

and its induced norm

$$\|u\|_{L^2(\Omega)} = (u, u)_{\Omega}^{1/2}.$$

Moreover, $L^2(\Omega)$ is identified with its dual space.

The space $L^{\infty}(\Omega)$ consists of essentially bounded functions in Ω . It is a Banach space equipped with the norm

$$\|u\|_{L^{\infty}(\Omega)} = \operatorname{ess\,sup}_{\Omega} |u|.$$

The space $L^{\infty}(\Omega) \subset L^p(\Omega)$, for all $p \in [1, \infty)$, and its dual space is $L^1(\Omega)$.

The Sobolev space $W^{m,p}(\Omega)$ is the space of functions in $L^p(\Omega)$ whose weak derivatives of order less than or equal to m belong to $L^p(\Omega)$, being m an integer and $1 \leq p \leq \infty$. When $p = 2$, the space $W^{m,2}(\Omega) = H^m(\Omega)$ is a Hilbert space endowed with a scalar product and its associated norm $\|\cdot\|_{H^m(\Omega)}$, also denoted $\|\cdot\|_m$. For instance, when $m = 1$, the scalar product is

$$((u, v))_{\Omega} = (u, v)_{\Omega} + \sum_{i=1}^d (\partial_i u, \partial_i v)_{\Omega}$$

and the norm is

$$\|u\|_{H^1(\Omega)} = ((u, u))_{\Omega}^{1/2}.$$

The space $H_0^1(\Omega)$ consists of the functions of $H^1(\Omega)$ with zero trace on the boundary. Since Ω is a bounded domain, the Poincaré inequality holds:

$$\exists C_{\Omega} > 0 \quad : \quad \|u\|_{L^2(\Omega)} \leq C_{\Omega} \|\nabla u\|_{L^2(\Omega)}, \quad \forall u \in H_0^1(\Omega). \quad (1.8)$$

Hence, the norm $\|u\|_{L^2(\Omega)}$ is equivalent to $\|u\|_{H^1(\Omega)}$ on $H_0^1(\Omega)$. Furthermore, we denote by $H^{-k}(\Omega)$ the dual space of $H_0^k(\Omega)$.

The bilinear form $\langle \cdot, \cdot \rangle_{\Omega}$ from $H^{-1}(\Omega) \times H_0^1(\Omega)$ is called duality pair in $H^1(\Omega)$.

We will often consider d -dimensional vector functions with components in one of those spaces. For instance, if each component of \mathbf{u} belongs to $H^m(\Omega)$, we will indicate it as $\mathbf{u} \in (H^m(\Omega))^d$.

Let us introduce a convenient space for the treatment of the incompressibility constraint:

$$(H(\operatorname{div}, \Omega))^d = \{\mathbf{u} \in (L^2(\Omega))^d \mid \nabla \cdot \mathbf{u} \in L^2(\Omega)\},$$

which is a Hilbert space with the norm $\|\mathbf{u}\|_{\operatorname{div}} = \|\mathbf{u}\|_{L^2(\Omega)} + \|\nabla \cdot \mathbf{u}\|_{L^2(\Omega)}$. Finally, we define a space of weakly divergence-free functions:

$$(J_0)^d = \{\mathbf{u} \in (L^2(\Omega))^d \mid \nabla \cdot \mathbf{u} = 0, \mathbf{u} \cdot \mathbf{n}|_{\partial\Omega_D} = 0\}.$$

Since $(J_0)^d$ is a closed subspace of $(L^2(\Omega))^d$, we can write $(L^2(\Omega))^d = (J_0)^d \oplus (J_0^\perp)^d$, where

$$(J_0^\perp)^d = \{\mathbf{u} \in (L^2(\Omega))^d \mid \mathbf{u} = \nabla p, p \in H^1(\Omega)\}.$$

Finally, we define P_{J_0} as the orthogonal $L^2(\Omega)$ -projector onto $(J_0)^d$. The importance of this operator is explained in Section (1.5.1).

1.3 Weak formulation

We aim at writing the variational formulation of the problem (1.6) supplied with boundary conditions (1.3). Without affecting the generality of the discussion, we assume $\mathbf{u}_D = \partial_t \boldsymbol{\eta}(\mathbf{x}, t)$ in (1.3a) and $\mathbf{g}_N = \mathbf{0}$ (with $\partial\Omega_N \neq \emptyset$) in (1.3b) for the sake of simplicity.

We define the following spaces, for any given $t \in [0, T)$:

$$V(t) = \{\mathbf{v} : \Omega_t \rightarrow \mathbb{R}^d, \mathbf{v} = \hat{\mathbf{v}} \circ (\mathcal{A}_t)^{-1}, \hat{\mathbf{v}} \in (H^1(\Omega_0))^d\}, \quad (1.9a)$$

$$V_0(t) = \{\mathbf{v} \in V(t), \mathbf{v}|_{\partial\Omega_D} = \mathbf{0}\}, \quad (1.9b)$$

$$Q(t) = \{q : \Omega_t \rightarrow \mathbb{R}, q = \hat{q} \circ (\mathcal{A}_t)^{-1}, \hat{q} \in L^2(\Omega_0)\}. \quad (1.9c)$$

We introduce two bilinear forms associated to two terms of the Navier-Stokes equations in their weak form. The first one is related to the viscous term:

$$a(\mathbf{u}, \mathbf{v}_0)_{\Omega_t} = 2\mu(\boldsymbol{\epsilon}(\mathbf{u}), \boldsymbol{\epsilon}(\mathbf{v}_0))_{\Omega_t}, \quad \forall \mathbf{u} \in V_0(t), \forall \mathbf{v}_0 \in V_0(t).$$

This form is continuous and coercive with respect to the norm $\|\cdot\|_{H^1(\Omega_t)}$. The second form comes from the pressure gradient term and the incompressibility constraint:

$$b(\mathbf{v}_0, p)_{\Omega_t} = -(p, \nabla \cdot \mathbf{v}_0)_{\Omega_t}, \quad \forall p \in Q(t), \forall \mathbf{v}_0 \in V_0(t),$$

and it is continuous with respect to the norms $\|p\|_{L^2(\Omega_t)}$ and $\|\mathbf{v}\|_{H^1(\Omega_t)}$.

In its standard form, the trilinear form associated to the convective term (with convective velocity \mathbf{a}) is:

$$c(\mathbf{a}, \mathbf{u}, \mathbf{v}_0)_{\Omega_t} = \rho(\mathbf{a} \cdot \nabla \mathbf{u}, \mathbf{v}_0)_{\Omega_t} \quad \forall \mathbf{a}, \mathbf{u} \in V(t), \forall \mathbf{v}_0 \in V_0(t),$$

which is also continuous and well defined on those spaces.

The variational formulation of the problem under consideration reads: given $t \in (0, T)$, find $(\mathbf{u}, p) \in V(t) \times Q(t)$ such that

$$\rho (\partial_t \mathbf{u}|_{\mathbf{x}_0}, \mathbf{v}_0)_{\Omega_t} + \mathcal{N}(\mathbf{u} - \mathbf{w}; \mathbf{u}, p, \mathbf{v}_0, q)_{\Omega_t} = \langle \mathbf{f}, \mathbf{v}_0 \rangle_{\Omega_t}, \quad (1.10a)$$

$$\mathbf{u} = \partial_t \boldsymbol{\eta}(\mathbf{x}, t) \quad \text{on } \partial\Omega_D, \quad (1.10b)$$

for all $(\mathbf{v}_0, q) \in V_0(t) \times Q(t)$, where the form $\mathcal{N}(\cdot; \cdot, \cdot, \cdot, \cdot)$ is defined as follows

$$\mathcal{N}(\mathbf{u} - \mathbf{w}; \mathbf{u}, p, \mathbf{v}_0, q)_{\Omega_t} = a(\mathbf{u}, \mathbf{v}_0)_{\Omega_t} + c(\mathbf{u} - \mathbf{w}, \mathbf{u}, \mathbf{v}_0)_{\Omega_t} + b(\mathbf{v}_0, p)_{\Omega_t} - b(\mathbf{u}, q)_{\Omega_t}. \quad (1.11)$$

In order for problem (1.10) to be well posed, the following condition must be satisfied: there exists a constant $\beta > 0$ such that

$$\inf_{q \in Q(t)} \sup_{\mathbf{v} \in V(t)} \frac{|b(\mathbf{v}, q)_{\Omega_t}|}{\|\mathbf{v}\|_{H^1(\Omega_t)} \|q\|_{L^2(\Omega_t)}} \geq \beta. \quad (1.12)$$

This condition, referred to as *inf-sup condition* in this work, is also called LBB condition, honoring the works of Ladyzhenskaya [85], Babûska [2], and Brezzi [17].

Problem (1.10) represents the non-conservative formulation. We can introduce also the conservative one: given $t \in (0, T)$, find $(\mathbf{u}, p) \in V(t) \times Q(t)$ such that

$$\rho \partial_t (\mathbf{u}, \mathbf{v}_0)_{\Omega_t} + \mathcal{N}_c(\mathbf{u} - \mathbf{w}; \mathbf{u}, p, \mathbf{v}_0, q)_{\Omega_t} = \langle \mathbf{f}, \mathbf{v}_0 \rangle_{\Omega_t}, \quad (1.13a)$$

$$\mathbf{u} = \partial_t \boldsymbol{\eta}(\mathbf{x}, t) \quad \text{on } \partial\Omega_D, \quad (1.13b)$$

for all $(\mathbf{v}_0, q) \in V_0(t) \times Q(t)$, where the form \mathcal{N}_c is equal to \mathcal{N} (1.11) upon replacement of the trilinear form c with

$$c_c(\mathbf{a}, \mathbf{u}, \mathbf{v}_0)_{\Omega_t} = \rho (\nabla \cdot (\mathbf{u} \otimes \mathbf{a}), \mathbf{v}_0)_{\Omega_t} \quad \forall \mathbf{a}, \mathbf{u} \in V(t), \quad \forall \mathbf{v}_0 \in V_0(t).$$

For $2d$ problems, the existence and uniqueness theory for the weak form of the evolutionary Navier-Stokes equations in fixed domains is fairly complete. The solution is as regular as allowed by the data and we have continuous dependence from the data in the corresponding function spaces (see [142]). In the case of three-dimensional problems, the $2d$ result cannot be extended because of lack of information about the regularity of the weak solution. Only partial results have been proved [142]. As for strong solutions, existence and uniqueness have been proved over some interval depending on the data. It is known [87] that, provided the data are regular enough, there is locally in time a unique solution. But uniqueness is proved (on some interval $(0, T_*)$, with $T_* < T$) for a class of strong solutions for which existence is generally not proved. For $3d$ problems, the existence is known only for weak solutions, as stated in [74], but for those solutions uniqueness is not proved.

In the case of moving domains, in literature there exist several theoretical results concerning problem (1.1). Existence of a weak solution for the non-homogeneous Dirichlet problem is proved in [62, 78]. The proof of the existence of a weak solution can also be found in [131, 132], together with regularity results.

1.4 The fully discrete problem

1.4.1 About time discretization

With regard to time discretization, among all the possible schemes we choose Backward Discretization Formulas of order k (BDF k), with $k \leq 2$.

Given $\delta t \in (0, T]$, we set $t^n = n\delta t$, with $n = 1, \dots, N$, and $N = T/\delta t$. We need to introduce the backward discretization operators, here applied to a generic function f :

$$\begin{aligned} D_t^k f^{n+1} &= \frac{1}{\gamma^k \delta t} \left(f^{n+1} - \sum_{i=0}^{k-1} \alpha_i^k f^{n-i} \right) && \text{BDF}k \text{ operator,} \\ D_t^1 f^{n+1} &= \delta_t f^{n+1} = \frac{1}{\delta t} \left(f^{n+1} - f^n \right) && \text{BDF1 (or Backward Euler) operator,} \\ D_t^2 f^{n+1} &= \frac{1}{\delta t} \frac{3}{2} \left(f^{n+1} - \frac{4}{3} f^n + \frac{1}{3} f^{n-1} \right) && \text{BDF2 operator.} \end{aligned}$$

The first (BDF1) and second (BDF2) order scheme are A -stable. A -stability is based on the Dahlquist test equation:

$$\frac{dy}{dt} = \lambda y.$$

This property implies that $|y(t)| \leq |y(0)|$ for $t \geq 0$ if $\lambda \in \mathbb{C}^-$, being

$$\mathbb{C}^- = \{z \in \mathbb{C} \mid \text{Re}(z) \leq 0\},$$

where $\text{Re}(z)$ stands for the real part of the complex number z . For the BDF k schemes, given the test equation:

$$D_t^k y^{n+1} = \lambda y^{n+1},$$

the A -stability implies that $|y^{n+1}| \leq |y^n|$. Higher order BDF schemes do not satisfy this property anymore and this limitation is known as the *second Dahlquist barrier*.

The BDF k scheme applied to problem (1.6) reads: Given \mathbf{u}^n , for $n \geq 0$ find $(\mathbf{u}^{n+1}, p^{n+1})$ such that

$$D_t^k \mathbf{u}^{n+1}|_{x_0} + (\tilde{\mathbf{u}}^{n+1} - \mathbf{w}^{n+1}) \cdot \nabla \mathbf{u}^{n+1} - \frac{1}{\rho} \nabla \cdot \boldsymbol{\sigma}(\mathbf{u}^{n+1}, p^{n+1}) = \mathbf{f}^{n+1} \quad \text{in } \Omega_{t^{n+1}}, \quad (1.14a)$$

$$\nabla \cdot \mathbf{u}^{n+1} = 0 \quad \text{in } \Omega_{t^{n+1}}. \quad (1.14b)$$

System (1.14) is fully implicit and non-linear when $\tilde{\mathbf{u}}^{n+1} = \mathbf{u}^{n+1}$. Otherwise, it can be linearized by choosing for $\tilde{\mathbf{u}}^{n+1}$ an approximation of \mathbf{u}^{n+1} . Different extrapolations can be considered:

$$\begin{aligned}\tilde{\mathbf{u}}^{n+1} &= \mathbf{u}^n && \text{1st order approximation,} \\ \tilde{\mathbf{u}}^{n+1} &= 2\mathbf{u}^n - \mathbf{u}^{n-1} && \text{2nd order approximation.}\end{aligned}$$

Usually, the BDF scheme of order k is combined with a k -th approximation of the convective velocity in order to have a k -th order discretization.

1.4.2 About space discretization

A finite element approximation of problem (1.10) (or equivalently (1.13)) involves at the same time the discretization of the fluid equations and domain definition problem (1.7).

Let us consider a family of *quasi-uniform* finite element partitions $\mathcal{T}_h(t)$ (see e.g. [119]) defined, for every $t > 0$, by the partition at the reference fluid configuration $\hat{\mathcal{T}}_h$ and the discrete ALE mapping \mathcal{A}_t , i.e., abusing notation, $\mathcal{T}_h(t) = \mathcal{A}_t(\hat{\mathcal{T}}_h)$. As usual, h represents the maximum size of the elements of \mathcal{T}_h . The discrete ALE mapping should be such that $\hat{\mathcal{T}}_h$ maintains in time its suitability with respect to the chosen finite element space. For instance, if we use linear finite elements to approximate a fluid variable we must ensure that the mesh images maintain straight edges in the domain movement.

Let $\hat{V}_h \subset (H^1(\Omega_0))^d$, $\hat{V}_{0,h} \subset (H_0^1(\Omega_0))^d$, and $\hat{Q}_h \subset L^2(\Omega_0)$ be the finite element spaces approximating V , V_0 , and Q at the reference configuration, respectively. With an abuse of notation, we can define the finite element spaces for a given time step t^n using the domain map (1.4), e.g. $V_h(t^n) = \mathcal{A}_{t^n}(\hat{V}_h)$. From now on, we omit the time label t^n from the finite element spaces names.

The standard Galerkin approximation of the incompressible Navier-Stokes equations may fail for two different reasons. First, pressure stability can only be obtained for suitable velocity-pressure finite element spaces (Q_h, V_h) . On the other hand, the method exhibits instabilities when the convective term is dominant.

We deal first with pressure stability. Whenever the fluid problem is defined in a fixed domain, e.g. the reference one, the pair (\hat{Q}_h, \hat{V}_h) is required to satisfy the discrete counterpart of (1.12) (see [21]):

$$\inf_{\hat{q}_h \in \hat{Q}_h} \sup_{\hat{\mathbf{v}}_h \in \hat{V}_h} \frac{\left| \int_{\Omega_0} \nabla \cdot \hat{\mathbf{v}}_h \hat{q}_h \, d\Omega \right|}{\|\hat{\mathbf{v}}_h\|_{H^1(\Omega_0)} \|\hat{q}_h\|_{L^2(\Omega_0)}} \geq \beta_d, \quad (1.15)$$

where the constant $\beta_d > 0$ is uniform with respect to h .

We restrict our attention to continuous approximations of the pressure. Among the choices that satisfy (1.15), we mention the so-called (*P*₁*isoP*₂) - *P*₁ finite elements. The

pressure is piecewise linear, while the velocity has the same number of degrees of freedom as in the \mathbb{P}_2 case but it is piecewise linear over a suitable decomposition of each triangle of $\hat{\mathcal{T}}_h$. For these finite elements a linear convergence with respect to h can be proved for a Stokes problem:

$$\|\hat{\mathbf{u}} - \hat{\mathbf{u}}_h\|_{H^1(\Omega_0)} + \|\hat{p} - \hat{p}_h\|_{L^2(\Omega_0)} \leq Ch \left(\|\hat{\mathbf{u}}\|_{H^2(\Omega_0)} + \|\hat{p}\|_{H^1(\Omega_0)} \right), \quad (1.16)$$

provided the solution is regular enough. Another possible choice is the $\mathbb{P}_1^b - \mathbb{P}_1$ elements. The approximation for the pressure is again piecewise linear, while the velocity is approximated by piecewise linear functions enriched by bubble functions. These are element-based polynomials vanishing on the element boundary. Also for these finite elements error estimate (1.16) holds.

Now, let us consider the fluid problem in moving domains. Whenever the domain definition problem is solved using \mathbb{P}_1 finite elements, each triangle with straight edges in $\hat{\mathcal{T}}_h$ is transformed in a triangle with straight edges in \mathcal{T}_h . Thus, it can be easily verified that, if \hat{V}_h and \hat{Q}_h are either $(\mathbb{P}_1 \text{iso}\mathbb{P}_2) - \mathbb{P}_1$ or $\mathbb{P}_1^b - \mathbb{P}_1$ finite element spaces on $\hat{\mathcal{T}}_h$, then V_h and Q_h are finite element spaces of the same kind on \mathcal{T}_h . Moreover, $\partial\Omega_t$ is linearly interpolated and this is enough to recover the error estimate (1.16).

Unfortunately, the simplest combinations of velocity-pressure pairs (e.g. equal order nodal interpolation) do not satisfy condition (1.15) and are unstable.

An alternative to using inf-sup stable pairs is to resort to stabilization techniques: they modify the discrete problem so that it is stable for equal order velocity-pressure interpolations (like the $\mathbb{P}_1 - \mathbb{P}_1$ pair, for example). Among all the possible stabilization methods, we consider the orthogonal subgrid scales (OSS) one, proposed in [37]. It allows to have pressure stability and it stabilizes the convective term for high Reynolds numbers. In this way, it is possible to overcome the two pitfalls of the standard Galerkin approximation at the same time. We refer to [3] for the numerical analysis of the OSS technique in the ALE framework. The stabilized version of the fluid problem is obtained by using the form

$$\mathcal{N}_s(\mathbf{a}_h; \mathbf{u}_h, p_h, \mathbf{v}_h, q_h)_\Omega = \mathcal{N}(\mathbf{a}_h; \mathbf{u}_h, p_h, \mathbf{v}_h, q_h)_\Omega + \mathcal{S}(\mathbf{a}_h; \mathbf{u}_h, p_h, \mathbf{v}_h, q_h)_\Omega,$$

where the perturbation term introduced by OSS (in its quasi-static form) reads

$$\begin{aligned} \mathcal{S}(\mathbf{a}_h; \mathbf{u}_h, p_h, \mathbf{v}_h, q_h)_\Omega &= (\tau_1 \Pi^\perp(\mathbf{a}_h \cdot \nabla \mathbf{u}_h + \nabla p_h), \mathbf{a}_h \cdot \nabla \mathbf{v}_h + \nabla q_h)_\Omega \\ &\quad + (\tau_2 \Pi^\perp(\nabla \cdot \mathbf{u}_h), \nabla \cdot \mathbf{v}_h)_\Omega. \end{aligned} \quad (1.17)$$

Here, $\Pi^\perp(\cdot)$ is the L^2 orthogonal projection onto the finite element space, i.e.:

$$\Pi^\perp(\cdot) = \mathcal{I}(\cdot) - \Pi(\cdot),$$

where $\Pi(\cdot)$ is the L^2 projection onto the finite element space and $\mathcal{I}(\cdot)$ the identity operator. We use the following expressions for the stabilization coefficients

$$\tau_1 = \left[c_1 \frac{\mu}{\rho h^2} + c_2 \frac{|\mathbf{a}_h|}{h} \right]^{-1}, \quad \tau_2 = \frac{h^2}{c_1 \tau_1},$$

where c_1 and c_2 are appropriate constants, justified in [37] through a Fourier analysis. We refer to [37] for a thorough description of this stabilization technique.

The OSS method has been widely analyzed by Codina, Blasco, and Badia. In [39] the pressure stabilization introduced by this technique was fully analyzed for the stationary Navier-Stokes equations. Its extension to the transient case was developed in [16]. Therein, some error estimates for the fully discrete solution are provided. They show that the velocity is first order accurate in time step and attains optimal order accuracy in the mesh size for the given spatial interpolation, both in the spaces $L^2(\Omega)$ and $H_0^1(\Omega)$. As for the pressure, it is shown to be order $1/2$ accurate in time step and optimal in the mesh size.

When we consider inf-sup stable elements, the OSS technique is employed for the stabilization of the convective term only. We denote by c_h the trilinear forms that stands for the convective term and stabilization terms. Consequently, \mathcal{N}_h stands for the form that replaces c with c_h in (1.11).

1.4.3 The problem discretized in time and space

We restrict our attention to the non-conservative problem (1.10) to be solved in a domain whose boundary displacement in the reference configuration at the time t^{n+1} is denoted with $\hat{\boldsymbol{\eta}}_h^{n+1}$. We recall that the problem requires to solve first a domain definition problem, and then the fluid problem (1.10) in the domain just computed.

Let us indicate with $\text{Ext}_h(\cdot)$ a discretized version of the extension operator $\text{Ext}(\cdot)$ in (1.7). At each time level t^{n+1} , the problem discretized in space with stabilized finite elements and in time with BDF k reads:

1. Domain definition problem: Find the domain displacement

$$\mathcal{A}_{t^{n+1}}(\mathbf{x}_0) = \mathbf{x}_0 + \text{Ext}_h(\tilde{\boldsymbol{\eta}}_h^{n+1}), \quad \mathbf{w}_h^{n+1} = \delta_t \mathcal{A}_{t^{n+1}} \circ \mathcal{A}_{t^{n+1}}^{-1}, \quad \Omega_{t^{n+1}} = \mathcal{A}_{t^{n+1}}(\Omega_0). \quad (1.18)$$

2. Fluid problem: Find $(\mathbf{u}_h^{n+1}, p_h^{n+1}) \in V_h \times Q_h$ such that

$$\begin{aligned} & \rho (D_t^k \mathbf{u}_h^{n+1}|_{\mathbf{x}_0}, \mathbf{v}_h)_{\Omega_{t^{n+1}}} \\ & + \mathcal{N}_s (\tilde{\mathbf{u}}_h^{n+1} - \mathbf{w}_h^{n+1}; \mathbf{u}_h^{n+1}, p_h^{n+1}, \mathbf{v}_h, q_h)_{\Omega_{t^{n+1}}} = \langle \mathbf{f}^{n+1}, \mathbf{v}_h \rangle_{\Omega_{t^{n+1}}}, \end{aligned} \quad (1.19a)$$

$$\mathbf{u}_h^{n+1} = \delta_t \hat{\boldsymbol{\eta}}_h^{n+1} \circ \mathcal{A}_{t^{n+1}}^{-1} \quad \text{on } \partial\Omega_D, \quad (1.19b)$$

for all $(\mathbf{v}_h, q_h) \in V_{0,h} \times Q_h$. The choices for $\tilde{\mathbf{u}}^{n+1}$ are the same as for problem (1.14). We ask $\tilde{\mathbf{u}}^{n+1}$ and \mathbf{w}_h^{n+1} to satisfy the same boundary conditions on $\partial\Omega_D$. So, the value of $\tilde{\boldsymbol{\eta}}_h^{n+1}$ depends on $\tilde{\mathbf{u}}^{n+1}$:

$$\begin{aligned} \tilde{\mathbf{u}}_h^{n+1} &= \mathbf{u}_h^{n+1}, \quad \tilde{\boldsymbol{\eta}}_h^{n+1} = \hat{\boldsymbol{\eta}}_h^{n+1} && \text{nonlinear,} \\ \tilde{\mathbf{u}}_h^{n+1} &= \mathbf{u}_h^n, \quad \tilde{\boldsymbol{\eta}}_h^{n+1} = \hat{\boldsymbol{\eta}}_h^n && \text{linearized, 1st order approximation,} \\ \tilde{\mathbf{u}}_h^{n+1} &= 2\mathbf{u}_h^n - \mathbf{u}_h^{n-1}, \quad \tilde{\boldsymbol{\eta}}_h^{n+1} = 2\hat{\boldsymbol{\eta}}_h^n - \hat{\boldsymbol{\eta}}_h^{n-1} && \text{linearized, 2nd order approximation.} \end{aligned}$$

When using inf-sup stable finite elements, the only difference is that the form \mathcal{N}_s has to be replaced by \mathcal{N}_h in (1.19a).

1.4.4 The linear fluid system

We aim at writing the system yielded by the linearized and fully discretized fluid problem.

We start by introducing the Lagrange basis $\{\phi_i\}_{\mathcal{N}_v} \oplus \{\phi_j^D\}_{\mathcal{N}_D}$ and $\{\pi_i\}_{\mathcal{N}_p}$ associated to V_h and Q_h , respectively. \mathcal{N}_D denotes the set of velocity nodes on $\partial\Omega_D$ and \mathcal{N}_v the rest of velocity nodes. The set of pressure nodes is denoted by \mathcal{N}_p . The finite element approximation of the unknowns is as follows:

$$\mathbf{u}_h^{n+1}(\mathbf{x}, t^{n+1}) = \sum_{i \in \mathcal{N}_v} \phi_i(\mathbf{x}, t^{n+1})(\mathbf{U}^{n+1}(t^{n+1}))_i + \sum_{j \in \mathcal{N}_D} \phi_j^D(\mathbf{x}, t^{n+1})(\mathbf{U}_D^{n+1}(t^{n+1}))_j, \quad (1.20a)$$

$$p_h^{n+1}(\mathbf{x}) = \sum_{k \in \mathcal{N}_p} \pi_k(\mathbf{x}, t^{n+1})(\mathbf{P}^{n+1}(t^{n+1}))_k, \quad (1.20b)$$

where \mathbf{U}_D^{n+1} , \mathbf{U}^{n+1} and \mathbf{P}^{n+1} are the arrays of nodal values for the velocity of the nodes on $\partial\Omega_D$, the velocity of the rest of the fluid nodes, and the pressure. The nodal values \mathbf{U}_D^{n+1} are known from the boundary datum (1.3a), while the other nodal values \mathbf{U}^{n+1} and \mathbf{P}^{n+1} are the unknowns of the problem. Obviously, the finite element shape functions vary (in time) in the following way: $\phi_i(\mathbf{x}, t^n) = \mathcal{A}_{t^n}(\hat{\phi}_i(\mathbf{x}_0))$, where $\hat{\phi}_i(\mathbf{x}_0)$ are the Lagrangian shape finite element functions on the reference grid $\hat{\mathcal{T}}_h$.

In order to write the fully discretized problem for a given time value t^{n+1} , we need to define a set of matrices. Subindexes i and j will denote the nodes. Let N_e denote the number of elements of \mathcal{T}_h and let K_e^k , with $k = 1, \dots, N_e$, indicate the generic element. Then:

$$K_{ij} = \frac{1}{\rho} a(\phi_i, \phi_j)_{\Omega_{t^{n+1}}} + \frac{1}{\rho} c_h(\tilde{\mathbf{u}}_h^{n+1} - \mathbf{w}_h^{n+1}, \phi_i, \phi_j)_{\Omega_{t^{n+1}}}, \quad i \in \mathcal{N}_v, \quad j \in \mathcal{N}_v, \quad (1.21a)$$

$$M_{ij} = (\phi_i, \phi_j)_{\Omega_{t^{n+1}}}, \quad i \in \mathcal{N}_v, \quad j \in \mathcal{N}_v, \quad (1.21b)$$

$$C_{ij} = \frac{\alpha}{\delta t} M_{ij} + K_{ij}, \quad i \in \mathcal{N}_v, \quad j \in \mathcal{N}_v, \quad (1.21c)$$

$$G_{ij} = b(\phi_i, \pi_j)_{\Omega_{t^{n+1}}}, \quad D = G^T, \quad i \in \mathcal{N}_v, \quad j \in \mathcal{N}_p, \quad (1.21d)$$

$$L_{ij}^\tau = - \sum_{k=1}^{N_e} (\tau_1^k \nabla \pi_i, \nabla \pi_j)_{K_e^k}, \quad i \in \mathcal{N}_p, \quad j \in \mathcal{N}_p. \quad (1.21e)$$

The coefficient α in the definition of matrix C depends on the order of the BDF scheme employed

$$\begin{aligned} \text{BDF1} &: \quad \alpha = 1, \\ \text{BDF2} &: \quad \alpha = 3/2. \end{aligned}$$

Matrix (1.21e) is weighted Laplacian matrix that comes from the term $(\tau_1 \nabla p_h^{n+1}, \nabla q_h)_{\Omega_{t^{n+1}}}$ in (1.17). Furthermore, let us denote with G^τ and D^τ the gradient and divergence matrices which include the corresponding stabilization terms (see (1.17)).

At a given time value t^{n+1} , equations (1.19) can be written in matrix form as:

$$A \mathbf{X}^{n+1} = \mathbf{b}^{n+1}, \quad (1.22)$$

with

$$A = \begin{bmatrix} C & G^\tau \\ D^\tau & L^\tau \end{bmatrix}, \quad \mathbf{X}^{n+1} = \begin{bmatrix} \mathbf{U}^{n+1} \\ \mathbf{P}^{n+1} \end{bmatrix}, \quad \mathbf{b}^{n+1} = \begin{bmatrix} \mathbf{b}_v^{n+1} \\ \mathbf{b}_p^{n+1} \end{bmatrix}.$$

For the standard (non-stabilized) Galerkin approach, A has the form

$$A = \begin{bmatrix} C & G \\ D & 0 \end{bmatrix}. \quad (1.23)$$

The force term \mathbf{b}_v^{n+1} accounts for body forces and time integration terms related to the BDF scheme chosen. The term \mathbf{b}_p^{n+1} is equal to zero when we deal with inf-sup stable elements, while in case of stabilized elements it accounts for terms coming from the stabilization.

When considering the Stokes problem, matrix (1.23) is indefinite, i.e. its eigenvalues are real with variable sign. Moreover, if C is non-singular and (positive or negative) definite, it is invertible if and only if $\text{Ker}(G) = 0$. This is the case when the inf-sup condition (1.15) holds. By using stabilized formulations, the zero pressure block of the indefinite system in (1.23) is replaced by a semi-negative definite matrix.

1.5 Inexact factorization methods

The solution of system (1.22) by direct or iterative methods might be unfeasible when dealing with realistic 3d problems. One of the most known techniques for the efficient

solution of the incompressible Navier-Stokes equations in fixed domains consists in using fractional-step procedures. The idea is to decouple the computation of the fluid velocity from that of the pressure, in order to pass from the solution of a large system to that of smaller ones. There are two types of fractional-step methods: differential or algebraic ones. In the former the splitting is based either on physical considerations (see, e.g., [68]), or on the Helmholtz decomposition principle. These are also called projection methods.

On the other hand, algebraic fractional-step methods are based on an algebraic decomposition of the matrix arising from the full discretization of the Navier-Stokes equations. Such a decomposition can be performed either by a sum of simpler matrices (see, e.g., [153, 91]) or a product of block-triangular matrix. We focus on the latter.

In this section, we consider inf-sup stable elements and the associated matrix (1.23) even though all the schemes suggested can be easily extended to the case of pressure stabilized methods. Let us start by writing an exact block- LU factorization of A

$$A = \begin{bmatrix} C & 0 \\ D & S \end{bmatrix} \begin{bmatrix} I & C^{-1}G \\ 0 & I \end{bmatrix} = LU. \quad (1.24)$$

The matrix S is the so-called pressure Schur complement. Its formal definition is:

$$S = -DC^{-1}G. \quad (1.25)$$

This factorization induces a splitting for the computation of velocity and pressure variables. In fact, solving system (1.22) through (1.24) consists in finding the solutions of the following subsystems:

1. L - step: find $\tilde{\mathbf{U}}^{n+1}, \tilde{\mathbf{P}}^{n+1}$:

$$\begin{aligned} C\tilde{\mathbf{U}}^{n+1} &= \mathbf{b}_v^{n+1}, \\ S\tilde{\mathbf{P}}^{n+1} &= -D\tilde{\mathbf{U}}^{n+1}; \end{aligned}$$

2. U - step: find $\mathbf{U}^{n+1}, \mathbf{P}^{n+1}$:

$$\begin{aligned} \mathbf{P}^{n+1} &= \tilde{\mathbf{P}}^{n+1}, \\ C\mathbf{U}^{n+1} &= C\tilde{\mathbf{U}}^{n+1} - G\mathbf{P}^{n+1}. \end{aligned}$$

However, the definition of S (1.25) involves the inverse of matrix C . The computational complexity of the exact LU factorization can be reduced provided C^{-1} is approximated by a matrix cheaper to compute. This yields inexact factorizations which are still based on variable splitting but are much more computationally convenient than the exact splitting.

In the next subsections, we consider different approximations of (1.24). These approximations are acceptable if they introduce an error not larger than the truncation error due to

the time discretization itself. Yet, the perturbation they involve can be reduced if the inexact factorization is carried out over the incremental system (instead of the non-incremental (1.22)):

$$A(\mathbf{X}^{n+1} - \mathbf{X}^*) = \mathbf{b}^{n+1} - A\mathbf{X}^*, \quad (1.26)$$

where \mathbf{X}^* is the vector made of \mathbf{U}^* and \mathbf{P}^* , which are predictions of \mathbf{U}^{n+1} and \mathbf{P}^{n+1} . For instance, a first order prediction would be $\mathbf{X}^* = \mathbf{X}^n$.

1.5.1 Pressure correction methods

In this subsection, we consider an inexact factorization which leads to pressure correction (PC) schemes. At the differential level, these methods were developed independently by Chorin (see [30, 31, 32, 33]) and Temam (see [138, 139, 140, 141]). They are based on the orthogonal Helmholtz decomposition $(L^2(\Omega))^d = (J_0)^d \oplus (J_0^\perp)^d$, according to which a vector field can be decomposed into the sum of a solenoidal field and a gradient of a scalar function. This derives from a more general theorem by De Rham [43].

In the pressure correction method by Chorin and Temam, also called *projection method*, an intermediate velocity $\tilde{\mathbf{u}}^{n+1}$ obtained from the momentum equation without the pressure term is decomposed into a solenoidal field (the end-of-step velocity \mathbf{u}^{n+1}) and the gradient of a scalar field (the pressure p^{n+1}). The end-of-step velocity is the projection of $\tilde{\mathbf{u}}^{n+1}$ onto the space $(J_0)^d$, that is

$$\mathbf{u}^{n+1} = P_{J_0}(\tilde{\mathbf{u}}^{n+1}).$$

This explains the name “projection methods”.

To derive algebraic pressure correction methods, the exact L and U factors in (1.24) are replaced by inexact ones in which C^{-1} is substituted by a truncation of its Neumann expansion. In fact, we can write

$$C^{-1} = \left(\frac{\alpha}{\delta t}M + K\right)^{-1} = \frac{\delta t}{\alpha} \left(I + \frac{\delta t}{\alpha}M^{-1}K\right)^{-1} M^{-1} = \frac{\delta t}{\alpha} \left(\sum_{i=0}^{\infty} \left(-\frac{\delta t}{\alpha}M^{-1}K\right)^i\right) M^{-1},$$

and truncate the sum up to a desired order. In particular, we consider the zero-th order term:

$$C^{-1} = \frac{\delta t}{\alpha}M^{-1} + \mathcal{O}(\delta t^2) \simeq \frac{\delta t}{\alpha}M^{-1}. \quad (1.27)$$

The Neumann expansion of C^{-1} makes sense if $\delta t < \alpha/\rho(M^{-1}K)$, where $\rho(\cdot)$ denotes the spectral radius. This condition justifies only approximation (1.27) and is by no means a stability condition on δt .

After approximating C^{-1} by $(\delta t/\alpha)M^{-1}$, the Schur complement (1.25) becomes:

$$S \simeq T = -\frac{\delta t}{\alpha}DM^{-1}G. \quad (1.28)$$

Consequently, the lower block-triangular matrix L is approximated by:

$$L_{PC} = \begin{bmatrix} C & 0 \\ D & T \end{bmatrix}.$$

Using the same approximation (1.27) for the upper block-triangular matrix U , the following inexact U factor is obtained:

$$U_{PC} = \begin{bmatrix} I & \frac{\delta t}{\alpha}M^{-1}G \\ 0 & I \end{bmatrix}.$$

The system matrix for the PC scheme is obtained by replacing matrices L and U with L_{PC} and U_{PC} :

$$A_{PC} = L_{PC}U_{PC} = \begin{bmatrix} C & \frac{\delta t}{\alpha}CM^{-1}G \\ D & 0 \end{bmatrix}. \quad (1.29)$$

Let us apply this inexact factorization to the incremental version of the system (1.26). The non-incremental version is recovered by choosing $\mathbf{X}^* = \mathbf{0}$. We rearrange the resulting system into three steps:

1. Computation of the intermediate velocity:

$$C\tilde{\mathbf{U}}^{n+1} = \mathbf{b}_v^{n+1} - G\mathbf{P}^*; \quad (1.30a)$$

2. Computation of the pressure:

$$T(\mathbf{P}^{n+1} - \mathbf{P}^*) = -D\tilde{\mathbf{U}}^{n+1}; \quad (1.30b)$$

3. Computation of the end-of-step velocity:

$$\frac{\alpha}{\delta t}M\mathbf{U}^{n+1} = \frac{\alpha}{\delta t}M\tilde{\mathbf{U}}^{n+1} - G(\mathbf{P}^{n+1} - \mathbf{P}^*). \quad (1.30c)$$

With PC schemes, we pass from an indefinite system coupling velocity components and pressure to a set of smaller systems. At each time step we have to solve a linear system whose matrix is C . The system to solve at step 2 has T as system matrix. Being the inf-sup condition satisfied, matrix G is a full-rank matrix and T is symmetric, negative definite. The third step is very cheap since its system matrix is M (see remark 1.1).

Scheme (1.30) can be interpreted as the algebraic counterpart of the Chorin-Temam method [110]. This is based on a formal analogy between matrix $DM^{-1}G$ in (1.28) and the discretization of the Laplace operator $-\Delta = -\nabla \cdot (\nabla)$. With respect to the differential Chorin-Temam scheme, method (1.30) is eased by the fact that no additional boundary condition has to be provided for the computation of the end-of-step velocity (nor for that of the pressure, therefore).

Remark 1.1. *The computational efficiency of the approximation (1.27) is evident if we replace the original mass matrix with a suitable diagonal matrix obtained by quadrature formulas for the space integrals (the so-called mass lumping, see [119]). In any case, we understand that M^{-1} is “easy” to compute.*

Remark 1.2. *It is known that projection methods impose an artificial boundary condition over the pressure on Dirichlet boundaries. There has been much discussion about whether the pressure p^{n+1} is a good approximation for the exact pressure $p(t^{n+1})$ (see [143]). Rannacher [121] and Gresho [69] conjectured that the non-physical boundary condition lives in a narrow boundary layer of width $\mathcal{O}(\sqrt{\nu\delta t})$.*

Inexact factorization methods do not impose explicitly any artificial pressure boundary condition. However, it can be shown [70] that they enforce weakly an artificial pressure boundary condition. Whether inexact factorization methods provide better accuracy than their differential counterpart is a controversial issue. We refer to [117, 70, 67] for some insights on the subject.

The PC schemes (1.30) yield an approximate solution affected by the splitting error. Notice that the prediction of the velocity \mathbf{U}^* does not appear in (1.30). Therefore, only \mathbf{P}^* can affect the order of accuracy in time of the method. In order to understand how the perturbation terms due to the inexact factors L_{PC} and U_{PC} depend on \mathbf{P}^* , we set

$$A_{PC} = A + E_{PC}$$

where E_{PC} is the perturbation matrix:

$$E_{PC} = \begin{bmatrix} 0 & \frac{\delta t}{\alpha} KM^{-1}G \\ 0 & 0 \end{bmatrix}. \quad (1.31)$$

The PC scheme guarantees the mass conservation, since only the momentum conservation equation is perturbed. Hence, it can be written as a monolithic system with a perturbed momentum equation:

$$C\tilde{\mathbf{U}}^{n+1} = \mathbf{b}_v^{n+1} - G\mathbf{P}^* + \mathbf{e}_{PC}$$

with

$$\mathbf{e}_{PC} = -\frac{\delta t}{\alpha} K M^{-1} G (\mathbf{P}^{n+1} - \mathbf{P}^*). \quad (1.32)$$

Should \mathbf{P}^* be a q -th order approximation of \mathbf{P}^{n+1} , the pressure term is of order $\mathcal{O}(\delta t^{q+1})$. Therefore, in order to get a first order PC scheme, it is sufficient to take $\mathbf{P}^* = \mathbf{0}$. Anyway, it is advised to use a first order pressure approximation $\mathbf{P}^* = \mathbf{P}^n$ for reducing drastically the numerical dissipation. This does not yield any significant increasing of CPU cost. In this case, the splitting error related to the pressure is second order in time. So, when we discretize in time by the BDF1 scheme, the PC method with $\mathbf{P}^* = \mathbf{P}^n$ introduces a splitting error that is smaller than the discretization one. While when we choose the BDF2 scheme, it introduces an error of the same order.

If we want to use a PC method with a BDF scheme of order $p \geq 2$ and we want to preserve the accuracy given by the BDF scheme chosen, we need to introduce more accurate inexact LU factorizations, which produce smaller splitting errors.

1.5.2 Yosida methods

The revisitation of the Chorin-Temam method as an approximate block- LU factorization of the fluid system matrix [110] gave rise to the investigation of new families of algebraic fractional-step methods, some of which do not have a differential counterpart (see, e.g., [73]). One of these is the Yosida method, introduced in [148, 117] for incompressible fluid problems in fixed domains.

The inexact factorization of matrix A (1.23) is again based on the approximation (1.27), but it is applied only to the pressure Schur complement in the lower block-triangular matrix. In the U factor, the inverse of matrix C is not approximated. Thus, the inexact factorization leads to matrix:

$$A_Y = L_{PC}U.$$

Also the incremental version of the Yosida scheme can be rewritten as a three-step method: the first two steps coincide with (1.30a) and (1.30b), while the third one becomes:

- computation of the end-of-step velocity:

$$C\mathbf{U}^{n+1} = C\tilde{\mathbf{U}}^{n+1} - G(\mathbf{P}^{n+1} - \mathbf{P}^*). \quad (1.33)$$

The latter step differs from (1.30c) and it is more involved due to the presence of C as system matrix.

A theoretical analysis of Yosida schemes for the numerical approximation of the Navier-Stokes equations has been carried out in [116]. Therein, strong stability results and optimal

error estimates are proved. The matrix:

$$Y = \delta t^{-1}C^{-1} - \frac{1}{\alpha}M^{-1} = \mathcal{O}(\delta t) \quad (1.34)$$

discussed in [116] plays an important role in understanding how the inexact factors perturb the system. We set:

$$A_Y = A + E_Y,$$

where the perturbation matrix is:

$$E_Y = \begin{bmatrix} 0 & 0 \\ 0 & \delta t DYG \end{bmatrix}. \quad (1.35)$$

Note that this time the strategy is “momentum preserving”, since the momentum equation is unperturbed. Unlike PC schemes, mass conservation is no more guaranteed and quasi-compressibility arises. To identify the order of the perturbation errors we can write the perturbed mass conservation equation:

$$DU^{n+1} = \mathbf{e}_Y,$$

with

$$\mathbf{e}_Y = -\delta t DYG (\mathbf{P}^{n+1} - \mathbf{P}^*).$$

Thus, if \mathbf{P}^* is a q -th order approximation of \mathbf{P}^{n+1} , the pressure term is of order $\mathcal{O}(\delta t^{q+2})$. So, in its non-incremental version the Yosida method introduces a splitting error which is second order in time. By choosing either the BDF1 or the BDF2 scheme to discretize in time, the global error (discretization error + splitting error) in time has the same order of magnitude of the discretization one. This result is confirmed by the numerical experiments carried out in [67].

Improved versions of the Yosida method called *Yosida3* [65, 129] and *Yosida4* [67] introduce higher order splitting errors.

Chapter 2

The interaction between a fluid and an elastic structure

2.1 Problem setting

Consider an heterogeneous mechanical system which covers a bounded, polyhedral, and moving domain $\Omega_t \subset \mathbb{R}^d$ ($d=2, 3$, being the space dimension), where time t spans the interval of analysis $[0, T]$. This domain is divided into a domain Ω_t^s occupied by a solid structure and its complement Ω_t^f occupied by the fluid. Both domains depend on time. The fluid-structure interface Σ_t is the common boundary between Ω_t^f and Ω_t^s , i.e. $\Sigma_t = \partial\Omega_t^f \cap \partial\Omega_t^s$. Furthermore, \mathbf{n}_f is the outward normal of Ω_t^f on Σ_t and \mathbf{n}_s is its counterpart for the structure domain.

The fluid-structure interaction (FSI) problem we consider in this chapter involves an incompressible and Newtonian fluid (see Chapter 1) and an elastic structure.

2.1.1 The elastodynamics equation

We assume the solid structure to be governed by the elastodynamics equations

$$\mathrm{D}_t \mathbf{u}_s - \frac{1}{\rho_s} \nabla \cdot \boldsymbol{\sigma}^s = \mathbf{f}_s \quad \text{in } \Omega_t^s \times (0, T), \quad (2.1)$$

where \mathbf{u}_s is the structure velocity and \mathbf{f}_s the body force. We denote by D_t the classical material derivative.

We adopt a purely Lagrangian approach for the structure. Thus, the motion of the solid medium is described in terms of its displacement $\hat{\boldsymbol{\eta}}$ (with $\hat{\mathbf{u}}_s = \partial_t \hat{\boldsymbol{\eta}}$) evaluated at the reference configuration through a smooth injective mapping:

$$\mathcal{L} : \Omega_0^s \times [0, T] \longrightarrow \Omega_t^s, \quad (\mathbf{x}_0, t) \longrightarrow \mathbf{x} = \mathcal{L}(\mathbf{x}_0, t), \quad (2.2)$$

with

$$\mathcal{L}_t(\mathbf{x}_0) = \mathbf{x}_0 + \hat{\boldsymbol{\eta}}(\mathbf{x}_0, t).$$

The map $\mathcal{L}_t = \mathcal{L}(\cdot, t)$ tracks the solid domain in time. We use the “hat” overscript to indicate that the function is defined on the structure reference configuration. Let $\hat{\mathbf{F}}_s(\mathbf{x}_0, t) = \nabla_{\mathbf{x}_0} \mathcal{L}_t(\mathbf{x}_0)$ be the corresponding deformation gradient and $\hat{J}_s(\mathbf{x}_0, t)$ its determinant. We introduce the first Piola-Kirchhoff tensor $\hat{\boldsymbol{\Lambda}}_s$, i.e. the Piola transform of the Cauchy stress tensor $\boldsymbol{\sigma}^s$

$$\hat{\boldsymbol{\Lambda}}_s = \hat{J}_s \boldsymbol{\sigma}^s (\hat{\mathbf{F}}_s)^{-T}.$$

$\hat{\boldsymbol{\Lambda}}_s$ is a Lagrangian second order tensor field. The following proposition [34] states the main properties of the Piola transform.

Proposition 2.1. *Let $\hat{\mathbf{T}}(\mathbf{x}_0, t) = \mathbf{T}(\mathcal{L}(\mathbf{x}_0, t), t)$, $\mathbf{x}_0 \in \hat{\Omega}$ and $t > 0$, be an Eulerian second order tensor field and $\hat{\boldsymbol{\Lambda}}_{\mathbf{T}}(\mathbf{x}_0, t) = \hat{J} \mathbf{T}(\hat{\mathbf{F}})^{-T}$ its Piola transform. Then*

$$\nabla_{\mathbf{x}_0} \cdot \hat{\boldsymbol{\Lambda}}_{\mathbf{T}}(\mathbf{x}_0, t) = \hat{J} \nabla \cdot \mathbf{T}(\mathcal{L}(\mathbf{x}_0, t), t), \quad \text{in } \hat{\Omega}.$$

As a result, for all $\hat{D} \subset \hat{\Omega}$ part of $\hat{\Omega}$ we have

$$\begin{aligned} \int_{\partial D} \mathbf{T} \mathbf{n} \, dD &= \int_{\partial \hat{D}} \hat{\boldsymbol{\Lambda}}_{\mathbf{T}} \hat{\mathbf{n}} \, d\hat{D}, \\ \int_{\partial D} \mathbf{n} \, dD &= \int_{\partial \hat{D}} \hat{J}(\hat{\mathbf{F}})^{-T} \hat{\mathbf{n}} \, d\hat{D}, \\ dD &= \hat{J} |(\hat{\mathbf{F}})^{-T} \hat{\mathbf{n}}| \, d\hat{D}, \\ \mathbf{n} &= \frac{(\hat{\mathbf{F}})^{-T} \hat{\mathbf{n}}}{|(\hat{\mathbf{F}})^{-T} \hat{\mathbf{n}}|}. \end{aligned}$$

Here, \mathbf{n} and $\hat{\mathbf{n}}$ stand for the outward unit normal vectors to ∂D and $\partial \hat{D}$, respectively.

Unlike $\boldsymbol{\sigma}^s$, the first Piola-Kirchhoff tensor $\hat{\boldsymbol{\Lambda}}_s$ is non-symmetric. Since constitutive laws usually involve symmetric stress tensor, we introduce the second Piola-Kirchhoff tensor:

$$\hat{\boldsymbol{\Pi}} = \hat{J}_s (\hat{\mathbf{F}}_s)^{-1} \boldsymbol{\sigma}^s (\hat{\mathbf{F}}_s)^{-T}. \quad (2.3)$$

In general, a hyperelastic material is characterized by the following relation between $\hat{\boldsymbol{\Pi}}$ and $\hat{\boldsymbol{\eta}}$:

$$\hat{\boldsymbol{\Pi}} = \frac{\partial \hat{W}(\hat{\mathbf{E}})}{\partial \hat{\mathbf{E}}},$$

where \hat{W} is a given density of elastic energy and $\hat{\mathbf{E}}$ the Green-Lagrange strain tensor [34], defined by:

$$\hat{\mathbf{E}} = \frac{1}{2} \left((\hat{\mathbf{F}}_s)^T \hat{\mathbf{F}}_s - \mathbf{I} \right).$$

We are now able to write the elastodynamics equation in the reference domain:

$$\partial_{tt}\hat{\boldsymbol{\eta}} - \frac{1}{\hat{J}_s\hat{\rho}_s}\nabla_{\mathbf{x}_0} \cdot (\hat{\mathbf{F}}_s\hat{\boldsymbol{\Pi}}(\hat{\boldsymbol{\eta}})) = \hat{\mathbf{f}}_s \quad \text{in } \Omega_0^s \times (0, T). \quad (2.4)$$

This equation must be supplemented with a constitutive law that relates the structural displacement $\hat{\boldsymbol{\eta}}$ and the stress tensor $\hat{\boldsymbol{\Pi}}$. As a simple example, we can consider the Saint-Venant Kirchhoff three-dimensional elastic model, where the solid stress is defined as:

$$\hat{\boldsymbol{\Pi}}(\hat{\boldsymbol{\eta}}) = 2\mu_\ell\hat{\mathbf{E}}(\hat{\boldsymbol{\eta}}) + \lambda_\ell\text{tr}(\hat{\mathbf{E}}(\hat{\boldsymbol{\eta}}))\mathbf{I}. \quad (2.5)$$

For the simulations in Chapter 5, we make the hypothesis of small deformations: $\hat{\mathbf{E}}(\hat{\boldsymbol{\eta}}) \simeq \hat{\boldsymbol{\epsilon}}(\hat{\boldsymbol{\eta}}) = (\nabla\hat{\boldsymbol{\eta}} + (\nabla\hat{\boldsymbol{\eta}})^T)/2$. Thus, we deal with a linear structure model. In (2.5), μ_ℓ and λ_ℓ are the Lamé constants, representing the shear and dilation moduli of elasticity. The first constant accounts for distortion and the second for compression of the medium [34]. Of course, other structural models can be selected according to the specific problem under consideration.

Again, we assume that $\partial\Omega_0^s \setminus \Sigma_0$ can be divided into two subsets, $\partial\Omega_D^s$ and $\partial\Omega_N^s$, such that $\partial\Omega_D^s \cap \partial\Omega_N^s = \emptyset$, $\partial\Omega_D^s \cup \partial\Omega_N^s = \partial\Omega_0^s \setminus \Sigma_0$ and we impose the boundary conditions:

$$\begin{aligned} \hat{\boldsymbol{\eta}} &= \hat{\boldsymbol{\eta}}_D && \text{on } \partial\Omega_D^s, \\ \hat{\mathbf{F}}_s\hat{\boldsymbol{\Pi}} \cdot \hat{\mathbf{n}}_s &= \hat{J}_s|(\hat{\mathbf{F}}_s)^{-T}\hat{\mathbf{n}}_s|\hat{\mathbf{g}}_N^s && \text{on } \partial\Omega_N^s, \end{aligned}$$

for two given vector functions $\hat{\boldsymbol{\eta}}_D$ and $\hat{\mathbf{g}}_N^s$.

2.1.2 The coupling conditions and the coupled FSI problem

The fluid and structure subproblems are coupled on the interface by two transmission conditions. Due to the fact that we are dealing with viscous fluids, the continuity of velocities (normal and tangential)

$$\mathbf{u} = \partial_t\boldsymbol{\eta} \quad \text{on } \Sigma_t \times (0, T) \quad (2.6)$$

must be satisfied. On the other hand, the continuity of stresses

$$\boldsymbol{\sigma}^s \cdot \mathbf{n}_s + \boldsymbol{\sigma}^f \cdot \mathbf{n}_f = 0 \quad \text{on } \Sigma_t \times (0, T) \quad (2.7)$$

must hold, due to the action-reaction principle. Condition (2.6) is a kinematic coupling condition, while (2.7) is a dynamic one.

Moreover, the map $\mathcal{L}_t = \mathcal{L}(\cdot, t)$, representing the deformation of the structure, and $\mathcal{A}_t = \mathcal{A}(\cdot, t)$, describing the evolution of the fluid domain (see Section 1.1.2)

$$\mathcal{A} : \Omega_0^f \times [0, T] \longrightarrow \Omega_t^f, (\mathbf{x}_0, t) \longrightarrow \mathbf{x} = \mathcal{A}_t(\mathbf{x}_0), \quad (2.8)$$

must agree on Σ_t :

$$\mathcal{L}_t = \mathcal{A}_t \quad \text{on } \Sigma_t, \quad (2.9)$$

in order to define an homeomorphism over Ω_t (Fig. 2.1).

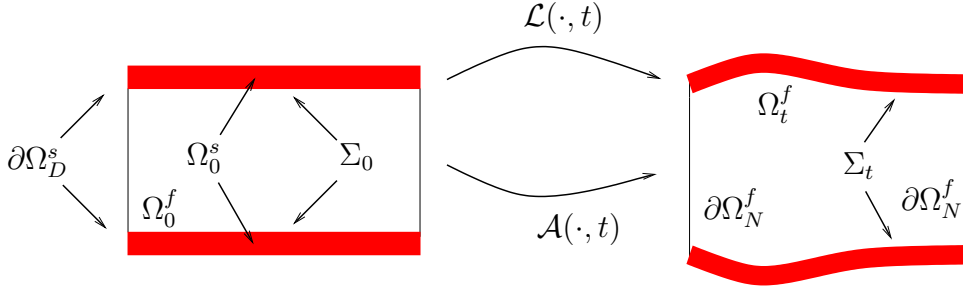


Figure 2.1: Parametrization of the domain with a possible partition of the physical boundary between Dirichlet and Neumann boundary.

Apart from the constraint of satisfying (2.9), the fluid domain mapping \mathcal{A}_t can otherwise be chosen arbitrarily. E.g., it can be defined as an appropriate extension operator of its value on the interface:

$$\mathcal{A}_t(\mathbf{x}_0) = \mathbf{x}_0 + \text{Ext}(\hat{\boldsymbol{\eta}}(\mathbf{x}_0, t)|_{\Sigma_0}). \quad (2.10)$$

Then, the fluid domain velocity in the ALE frame can be obtained from:

$$\hat{\mathbf{w}}(\mathbf{x}_0, t) = \text{Ext}(\partial_t \hat{\boldsymbol{\eta}}(\mathbf{x}_0, t)|_{\Sigma_0}). \quad (2.11)$$

The fluid-structure problem we will consider couples the incompressible -Stokes equations in its ALE non-conservative form (1.6) to the elastodynamics equations (2.1). We state this coupled problem only considering the boundary conditions on Σ_t . Those on the physical boundary are understood and do not affect the interaction. Thus, the strong form of the fluid-structure problem in the actual domain reads as follows:

1. Geometry problem: Find the fluid domain displacement:

$$\mathcal{A}_t(\mathbf{x}_0) = \mathbf{x}_0 + \text{Ext}(\hat{\boldsymbol{\eta}}|_{\Sigma_0}), \quad \mathbf{w} = \partial_t \mathcal{A}_t \circ \mathcal{A}_t^{-1}, \quad \Omega_t^f = \mathcal{A}_t(\Omega_0^f). \quad (2.12)$$

2. Fluid-structure problem: Find velocity \mathbf{u} , pressure p and displacement $\boldsymbol{\eta}$ such that

$$\partial_t \mathbf{u}|_{x_0} + (\mathbf{u} - \mathbf{w}) \cdot \nabla \mathbf{u} - \frac{1}{\rho_f} \nabla \cdot \boldsymbol{\sigma}^f = \mathbf{f}_f \quad \text{in } \Omega_t^f \times (0, T), \quad (2.13a)$$

$$\nabla \cdot \mathbf{u} = 0 \quad \text{in } \Omega_t^f \times (0, T), \quad (2.13b)$$

$$\mathbb{D}_t \mathbf{u}_s - \frac{1}{\rho_s} \nabla \cdot \boldsymbol{\sigma}^s = \mathbf{f}_s \quad \text{in } \Omega_t^s \times (0, T), \quad (2.13c)$$

$$\mathbf{u} = \partial_t \boldsymbol{\eta} \quad \text{on } \Sigma_t \times (0, T), \quad (2.13d)$$

$$\boldsymbol{\sigma}^s \cdot \mathbf{n}_s + \boldsymbol{\sigma}^f \cdot \mathbf{n}_f = 0 \quad \text{on } \Sigma_t \times (0, T), \quad (2.13e)$$

with $\mathbf{u}_s = \partial_t \boldsymbol{\eta}$.

The following result [61] shows that the above interface conditions ensure a correct energy balance within the coupled system:

Proposition 2.2. *Assume that the coupled fluid-structure system is isolated, i.e.*

- $\mathbf{u} = \mathbf{0}$ on $\partial\Omega_t^f \setminus \Sigma_t$;
- $\boldsymbol{\sigma}^s \cdot \mathbf{n}_s = \mathbf{0}$ on $\partial\Omega_t^s \setminus \Sigma_t$.

Then, should a solution to the coupled problem (2.12)-(2.13) exist, it would satisfy the following energy balance:

$$\frac{d}{dt} [E_K + E_P] + P_V = 0,$$

where

$$\begin{aligned} E_K &= \int_{\Omega_t^f} \frac{\rho_f}{2} |\mathbf{u}|^2 \, d\Omega_t^f + \int_{\Omega_t^s} \frac{\rho_s}{2} |\mathbf{u}_s|^2 \, d\Omega_t^s && \text{kinetic energy,} \\ E_P &= \int_{\Omega_t^s} W(\mathbf{E}) \, d\Omega_t^s && \text{elastic potential energy,} \\ P_V &= \int_{\Omega_t^f} 2\mu |\boldsymbol{\epsilon}(\mathbf{u})|^2 \, d\Omega_t^f && \text{dissipated viscous power.} \end{aligned}$$

The idea of the proof [61] consists in multiplying the fluid equation (2.13a) by \mathbf{u} and the solid equation (2.13c) by \mathbf{u}_s . Then, we integrate by parts, use the assumption of isolation and the interface conditions. Finally, we sum the resulting expressions so that all the interface integral contributions cancel thanks to the coupling conditions.

2.2 Weak formulation

In Section 1.3, we tackled the variational formulation of the Navier-Stokes equations in a moving domain. To adapt it to the fluid subproblem of the FSI problem we introduce the

spaces $V^f(t)$, $V_0^f(t)$, and $Q(t)$. Their definitions correspond to (1.9) upon setting $\Omega_t = \Omega_t^f$. Furthermore, the Dirichlet boundary $\partial\Omega_D$ coincides with the fluid-structure interface Σ_t .

In the next subsection, we consider some aspects of the variational formulation of the solid subproblem, in order to write the weak form of the coupled problem in the following one.

2.2.1 The solid structure subproblem

For any given $t \in [0, T)$, we define the following spaces

$$\begin{aligned}\hat{V}^s &= \{ \hat{\mathbf{v}} : \Omega_0^s \rightarrow \mathbb{R}^d, \hat{\mathbf{v}} \in (H^1(\Omega_0^s))^d \}, \\ V^s(t) &= \left\{ \mathbf{v} : \Omega_t^s \rightarrow \mathbb{R}^d, \mathbf{v} = \hat{\mathbf{v}} \circ (\mathcal{L}_t)^{-1}, \hat{\mathbf{v}} \in \hat{V}^s \right\}.\end{aligned}$$

Let the interface Σ_t coincide with the Neumann boundary $\partial\Omega_N^s$, on which coupling condition (2.13e) is imposed.

To write the variational formulation for the solid subproblem, we multiply the elastodynamics equation in the reference domain (2.4) by $\hat{\mathbf{v}}^s \in \hat{V}^s$. After integration by parts and taking into account condition (2.13e), we get

$$\hat{J}_s \hat{\rho}_s (\partial_{tt} \hat{\boldsymbol{\eta}}, \hat{\mathbf{v}}^s)_{\Omega_0^s} + \left\langle \hat{\mathbf{F}}_s \hat{\boldsymbol{\Pi}} (\hat{\boldsymbol{\eta}}_h^{n+1}), \nabla_{\mathbf{x}_0} \hat{\mathbf{v}}^s \right\rangle_{\Omega_0^s} = \left\langle \hat{\mathbf{f}}_s, \hat{\mathbf{v}}^s \right\rangle_{\Omega_0^s} - \langle \hat{J}_s \boldsymbol{\sigma}^f (\hat{\mathbf{F}}_s)^{-T} \cdot \hat{\mathbf{n}}_f, \hat{\mathbf{v}}^s \rangle_{\Sigma_0},$$

which, thanks to Proposition 2.1, can be rewritten as

$$\hat{J}_s \hat{\rho}_s (\partial_{tt} \hat{\boldsymbol{\eta}}, \hat{\mathbf{v}}^s)_{\Omega_0^s} + \left\langle \hat{\mathbf{F}}_s \hat{\boldsymbol{\Pi}} (\hat{\boldsymbol{\eta}}_h^{n+1}), \nabla_{\mathbf{x}_0} \hat{\mathbf{v}}^s \right\rangle_{\Omega_0^s} = \left\langle \hat{\mathbf{f}}_s, \hat{\mathbf{v}}^s \right\rangle_{\Omega_0^s} - \langle \boldsymbol{\sigma}^f \cdot \mathbf{n}_f, \mathbf{v}^s \rangle_{\Sigma_t}. \quad (2.14)$$

In (2.14), we have set $\mathbf{v}_s = \hat{\mathbf{v}}_s \circ (\mathcal{L}_t)^{-1}$.

2.2.2 The coupled FSI problem

By putting together the variational formulations of the fluid (1.10) and structure (2.14) subproblems, we have the weak form of the fluid-structure problem. That is, given $t \in (0, T)$, find $(\mathbf{u}, p, \hat{\boldsymbol{\eta}}) \in V^f(t) \times Q(t) \times \hat{V}^s$ such that

$$\rho_f \left(\partial_t \mathbf{u}|_{\mathbf{x}_0}, \mathbf{v}_0^f \right)_{\Omega_t^f} + \mathcal{N}(\mathbf{u} - \mathbf{w}; \mathbf{u}, p, \mathbf{v}_0^f, q)_{\Omega_t^f} = \left\langle \mathbf{f}_f, \mathbf{v}_0^f \right\rangle_{\Omega_t^f}, \quad (2.15a)$$

$$\hat{J}_s \hat{\rho}_s (\partial_{tt} \hat{\boldsymbol{\eta}}, \hat{\mathbf{v}}^s)_{\Omega_0^s} + \left\langle \hat{\mathbf{F}}_s \hat{\boldsymbol{\Pi}} (\hat{\boldsymbol{\eta}}_h^{n+1}), \nabla_{\mathbf{x}_0} \hat{\mathbf{v}}^s \right\rangle_{\Omega_0^s} = \left\langle \hat{\mathbf{f}}_s, \hat{\mathbf{v}}^s \right\rangle_{\Omega_0^s} - \langle \boldsymbol{\sigma}^f \cdot \mathbf{n}_f, \mathbf{v}^s \rangle_{\Sigma_t}, \quad (2.15b)$$

$$\mathbf{u} = \partial_t \hat{\boldsymbol{\eta}} \circ (\mathcal{A}_t)^{-1} \quad \text{on } \Sigma_t, \quad (2.15c)$$

for all $(\mathbf{v}_0^f, q, \hat{\mathbf{v}}^s) \in V_0^f(t) \times Q(t) \times \hat{V}^s$.

The continuity of velocities has been enforced in a strong way by (2.15c).

The last term at the right-hand-side in (2.15b) is not appropriate from the discretization point of view, since it contains a description of the interface fluid load in terms of a surface integral. In fact, the direct space discretization of (2.15b) by finite elements might lead to unstable numerical schemes because the discrete fluid and solid interface load might not cancel. Furthermore, that approach would destroy the optimal accuracy of the method. To overcome those difficulties, the continuity of stresses on the interface is imposed in a weak way. Notice that the fluid interface load can be seen as the variational residual of the weak form of the momentum conservation equation when tested with test functions $\mathbf{v}^f \in V^f(t)$ that do not vanish on Σ_t :

$$\begin{aligned} \langle \boldsymbol{\sigma}^f \cdot \mathbf{n}_f, \mathbf{v}^f \rangle_{\Sigma_t} &= \rho_f (\partial_t \mathbf{u}|_{\mathbf{x}_0}, \mathbf{v}^f)_{\Omega_t^f} + \mathcal{N}(\mathbf{u} - \mathbf{w}; \mathbf{u}, p, \mathbf{v}^f, q)_{\Omega_t^f} - \langle \mathbf{f}_f, \mathbf{v}^f \rangle_{\Omega_t^f} \\ &= - \langle \mathcal{R}(\mathbf{u}, p), \mathbf{v}^f \rangle_{\Omega_t^f}. \end{aligned}$$

Therefore, for the last term in equation (2.15b), we have the following equality:

$$\langle \boldsymbol{\sigma}^f \cdot \mathbf{n}_f, \mathbf{v}^s \rangle_{\Sigma_t} = - \langle \mathcal{R}(\mathbf{u}, p), \mathcal{E}_t(\mathbf{v}^s|_{\Sigma_t}) \rangle_{\Omega_t^f}$$

for all $\mathbf{v}^s \in V^s(t)$, \mathcal{E}_t being an arbitrary extension operator from the trace finite element space associated to $V^s(t)$ to $V^f(t)$.

The advantages of the weak transmission of the fluid loads at the interface are that it still makes sense after space discretization and leads to stable numerical results. Moreover, it is crucial when carrying out stability and convergence analysis. Other advantages of this way to impose the continuity of stresses are reported in Section 3.2.1.

2.3 Analysis of coupled models

In this section, we aim at summarizing some results on the well-posedness of problems coupling fluid and structure models as in (2.13).

The first model we consider can be found in [89]. It couples equations (1.1) to (2.1) and could represent the fluid-structure interaction in case the interface movement is negligible. It is a simplified model since both the interface and the fluid domain are assumed to be fixed. This assumption simplifies the analysis, which is, nevertheless, not immediate. Also the constitutive law for the structure is simplified: $\boldsymbol{\sigma}^s = \mu_l \nabla \boldsymbol{\eta}$. The assumption of fixed interface and fluid domain imposes a correction to coupling condition (2.13e), which becomes:

$$\boldsymbol{\sigma}^s \cdot \mathbf{n}_s + \boldsymbol{\sigma}^f \cdot \mathbf{n}_f - \frac{1}{2} \left(\sum_{i=1}^d u_i \cos(n_{f,i}) \right) \mathbf{u} = 0, \quad (2.16)$$

where the subscript i refers to the i -th component. The nonlinear contribution needs to be added to the normal stress equilibrium for the fact that the interface movement does

not enter in the model. The mathematical analysis of this problem results in the following theorem:

Theorem 2.1. *There exists a solution $(\mathbf{u}, p, \boldsymbol{\eta})$ to the transmission problem (1.1)-(2.1) with coupling conditions(2.13d)-(2.16) that is unique in two dimensions.*

The proof [89] makes use of the so-called Faedo-Galerkin method.

In [27], the authors deal with a more general situation where the fluid domain is time dependent. The fluid is assumed to fill a three-dimensional cavity and to interact with a thin elastic structure lying on one of its sides. The deformation of the elastic part of the boundary is modeled by a classical linear plate theory for transverse displacements and in-plane displacements are neglected. The existence of a weak solution for this problem is proved over time interval $[0, T^*]$, with $T^* \in (0, \infty]$. The proof relies on the Faedo-Galerkin method combined with a fixed point procedure to linearize the nonlinearities. However, well-posedness can be proved thanks to the a-priori estimates and compactness properties that hold because of the simple shape of the geometry due to the use of a plate bending model.

In [11], the FSI problem under consideration couples a $2d$ fluid in the ALE form (2.13a)-(2.13b) with a $1d$ membrane. The structure is supposed to be governed by the following generalized string model (see also Section 4.2.1):

$$\frac{\partial^2 \eta}{\partial t^2} - \beta \frac{\partial^2 \eta}{\partial x^2} - \gamma \frac{\partial^3 \eta}{\partial x^2 \partial t} + \alpha \frac{\partial^4 \eta}{\partial x^4} + \sigma \eta = f_{\Gamma}(x, t),$$

with $\gamma > 0$ and $\alpha, \beta, \sigma \geq 0$. The existence of a solution $(\mathbf{u}, p, \boldsymbol{\eta})$ on time interval $[0, T]$ is proved. The regular feature of the structure is a fundamental ingredient of the proof. Indeed, the presence of a viscoelastic contribution leads to increased stability that gives enough compactness to the solutions. A result of well-posedness in the case of standard elasticity, i.e. with no viscoelastic contribution, still has to be provided.

The last result we mention deals with the full FSI problem where the fluid, modeled as viscous and incompressible, is enclosed by a moving thin nonlinear elastic shell [28]. The $3d$ fluid interacts with a structure represented by a $2d$ quasilinear elastic model of Koiter shell type. The movement of the structure is assumed to be inertia-free. Nonetheless, the main difficulty of the coupling is present, since the shape of the fluid domain is nonstationary and unknown. Under the hypothesis that the shell traction is composed only of bending contribution and with suitable assumptions on forcing terms and initial data, existence of a solution is proved for the full interaction problem in Lagrangian form. Moreover, the uniqueness of this solution is proved under appropriate compatibility conditions.

2.4 Space and time discretization

Let $\mathcal{T}_h(t)$ be a family of finite element partitions for the fluid subdomain with the characteristics specified in Section 1.4.2. Let \mathcal{I}_H be an independent partition of Ω_0^s into finite elements whose maximum diameter is denoted by H . For the sake of clarity, from now on we consider the case of matching grids on Σ_t . Thus, the partition of Ω_0^s is no more independent and will be indicated by \mathcal{I}_h .

Let $\hat{V}_h^f \subset (H^1(\Omega_0^f))^d$, $\hat{V}_{0,h}^f \subset (H_0^1(\Omega_0^f))^d$, $\hat{Q}_h^f \subset L^2(\Omega_0^f)$ and $\hat{V}_h^s \subset (H^1(\Omega_0^s))^d$ be the finite element spaces approximating V^f , V_0^f , Q and \hat{V}^s at the reference configuration, respectively. We can define the finite element spaces for a given time step t^n using the domain maps (2.2)-(2.8), e.g. $V_h^f(t^n) = \mathcal{A}_{t^n}(\hat{V}_h^f)$.

2.4.1 The discretization of the structure subproblem

For the time discretization of the structure subproblem, we consider two schemes: BDF1 (of first order, see Section 1.4.1) and *mid-point rule* (of second order, see [137]). In the following, we denote by $\hat{\boldsymbol{\eta}}^{n+1}$ an approximation of $\hat{\boldsymbol{\eta}}(t^{n+1})$.

We introduce the first order approximation of the second derivative in time:

$$\delta_{tt}f^{n+1} = \frac{1}{\delta t^2} \left(f^{n+1} - 2f^n + f^{n-1} \right).$$

The BDF1 scheme applied to problem (2.4) reads: Given $\hat{\boldsymbol{\eta}}^n$ and $\hat{\boldsymbol{\eta}}^{n-1}$, for $n \geq 1$ find $\hat{\boldsymbol{\eta}}^{n+1}$ such that

$$\hat{J}_s \hat{\rho}_s \delta_{tt} \hat{\boldsymbol{\eta}}^{n+1} - \nabla_{\mathbf{x}_0} \cdot (\hat{\mathbf{F}}_s \hat{\boldsymbol{\Pi}}(\hat{\boldsymbol{\eta}}^{n+1})) = \hat{\mathbf{f}}_s^{n+1} \quad \text{in } \Omega_0^s \times (0, T). \quad (2.17)$$

The so-called mid-point scheme can be seen as a particular case of the Newmark discretization (see, e.g., [123]). In order to apply it to the structure equation, we need to introduce another variable $\dot{\hat{\boldsymbol{\eta}}}^{n+1}$, an approximation of the structure velocity $\dot{\hat{\boldsymbol{\eta}}}(t^{n+1})$. Equation (2.4) discretized in time by the mid-point rule reads: Given $\hat{\boldsymbol{\eta}}^n$ and $\dot{\hat{\boldsymbol{\eta}}}^n$, for $n \geq 0$ find $\hat{\boldsymbol{\eta}}^{n+1}$ such that

$$\hat{J}_s \hat{\rho}_s \frac{\dot{\hat{\boldsymbol{\eta}}}^{n+1} - \dot{\hat{\boldsymbol{\eta}}}^n}{\delta t} - \nabla_{\mathbf{x}_0} \cdot \left(\hat{\mathbf{F}}_s \hat{\boldsymbol{\Pi}} \left(\frac{\hat{\boldsymbol{\eta}}^{n+1} + \hat{\boldsymbol{\eta}}^n}{2} \right) \right) = \hat{\mathbf{f}}_s^{n+1/2} \quad \text{in } \Omega_0^s \times (0, T), \quad (2.18a)$$

$$\frac{\dot{\hat{\boldsymbol{\eta}}}^{n+1} + \dot{\hat{\boldsymbol{\eta}}}^n}{2} = \frac{\hat{\boldsymbol{\eta}}^{n+1} - \hat{\boldsymbol{\eta}}^n}{\delta t} \quad \text{in } \Omega_0^s \times (0, T). \quad (2.18b)$$

Both equations (2.17) and (2.18) are implicit. Moreover, they are either linear or nonlinear depending on the chosen constitutive law.

For the space discretization, we make use of the same finite element spaces for fluid velocity and structure displacement (or velocity). This is extremely simple when using

stabilization techniques because the velocity-pressure pair can circumvent the discrete inf-sup condition (1.15). In that case, the same finite element interpolation spaces can be used for fluid velocity, pressure and structure unknowns. Instead, when we adopt the (\mathbb{P}_1 iso \mathbb{P}_2) - \mathbb{P}_1 finite elements for the fluid, we approximate the structure displacement with the \mathbb{P}_1 finite elements on a grid that matches at the interface the one used to compute the fluid velocity. The reason for these choices in space discretization is that they ease the imposition of the transmission conditions (see Section 3.2.1).

2.4.2 The fully discrete FSI problem

With regard to time discretization, we consider first a BDF k scheme (see Section 1.4.1) for the fluid equations and the BDF1 scheme for the structure problem. For the space discretization of the fluid subproblem, we adopt a stabilized finite element formulation. Then, the fully discretized fluid-structure problem reads:

1. Geometry problem: Find the fluid domain displacement

$$\begin{aligned} \mathcal{A}_{t^{n+1}}(\mathbf{x}_0) &= \mathbf{x}_0 + \text{Ext}_h(\hat{\boldsymbol{\eta}}_h^{n+1}|_{\Sigma_0}), \\ \mathbf{w}_h^{n+1} &= \delta_t \mathcal{A}_{t^{n+1}} \circ \mathcal{A}_{t^{n+1}}^{-1}, \quad \Omega_{t^{n+1}}^f = \mathcal{A}_{t^{n+1}}(\Omega_0^f). \end{aligned} \quad (2.19)$$

2. Fluid-structure problem: Find $(\mathbf{u}_h^{n+1}, p_h^{n+1}, \hat{\boldsymbol{\eta}}_h^{n+1}) \in V_h^f \times Q_h \times \hat{V}_h^s$ such that

$$\begin{aligned} &\rho_f \left(D_t^k \mathbf{u}_h^{n+1} |_{\mathbf{x}_0}, \mathbf{v}_h^f \right)_{\Omega_{t^{n+1}}^f} \\ &+ \mathcal{N}_s \left(\mathbf{u}_h^{n+1} - \mathbf{w}_h^{n+1}; \mathbf{u}_h^{n+1}, p_h^{n+1}, \mathbf{v}_h^f, q_h \right)_{\Omega_{t^{n+1}}^f} = \left\langle \mathbf{f}_f^{n+1}, \mathbf{v}_h^f \right\rangle_{\Omega_{t^{n+1}}^f}, \end{aligned} \quad (2.20a)$$

$$\begin{aligned} &\hat{J}_s \hat{\rho}_s \left(\delta_{tt} \hat{\boldsymbol{\eta}}_h^{n+1}, \hat{\mathbf{v}}_h^s \right)_{\Omega_0^s} + \left\langle \hat{\mathbf{F}}_s \hat{\boldsymbol{\Pi}} \left(\hat{\boldsymbol{\eta}}_h^{n+1} \right), \nabla_{\mathbf{x}_0} \hat{\mathbf{v}}_h^s \right\rangle_{\Omega_0^s} \\ &= \left\langle \hat{\mathbf{f}}_s^{n+1}, \hat{\mathbf{v}}_h^s \right\rangle_{\Omega_0^s} - \left\langle \mathcal{R} \left(\mathbf{u}_h^{n+1}, p_h^{n+1} \right), \mathcal{E}_h(\mathbf{v}_h^s |_{\Sigma_t}) \right\rangle_{\Omega_{t^{n+1}}^f}, \end{aligned} \quad (2.20b)$$

$$\mathbf{u}_h^{n+1} = \delta_t \hat{\boldsymbol{\eta}}_h^{n+1} \circ \mathcal{A}_{t^{n+1}}^{-1} \quad \text{on } \Sigma_t, \quad (2.20c)$$

for all $(\mathbf{v}_h^f, q_h, \hat{\mathbf{v}}_h^s) \in V_{0,h}^f \times Q_h \times \hat{V}_h^s$.

An improvement to the previous coupled system can be obtained by considering the less dissipative mid-point rule for the structure time discretization. In this case, equation

(2.20b) in Step 2 has to be replaced by

$$\begin{aligned} & \hat{J}_s \hat{\rho}_s \left(\frac{\dot{\hat{\boldsymbol{\eta}}}_h^{n+1} - \dot{\hat{\boldsymbol{\eta}}}_h^n}{\delta t}, \hat{\mathbf{v}}_h^s \right)_{\Omega_0^s} + \left\langle \hat{\mathbf{F}}_s \hat{\Pi} \left(\frac{\hat{\boldsymbol{\eta}}_h^{n+1} + \hat{\boldsymbol{\eta}}_h^n}{2} \right), \nabla_{\mathbf{x}_0} \hat{\mathbf{v}}_h^s \right\rangle_{\Omega_0^s} \\ &= \left\langle \hat{\mathbf{f}}_s^{n+1}, \hat{\mathbf{v}}_h^s \right\rangle_{\Omega_0^s} - \left\langle \mathcal{R}(\mathbf{u}_h^{n+1}, p_h^{n+1}), \mathcal{E}_h(\mathbf{v}_h^s |_{\Sigma_t}) \right\rangle_{\Omega_{t^{n+1}}^f}, \end{aligned} \quad (2.21a)$$

$$\left(\frac{\dot{\hat{\boldsymbol{\eta}}}_h^{n+1} + \dot{\hat{\boldsymbol{\eta}}}_h^n}{2}, \hat{\mathbf{v}}_h^s \right)_{\Omega_0^s} = \left(\frac{\hat{\boldsymbol{\eta}}_h^{n+1} - \hat{\boldsymbol{\eta}}_h^n}{\delta t}, \hat{\mathbf{v}}_h^s \right)_{\Omega_0^s}. \quad (2.21b)$$

The fluid domain $\Omega_{t^{n+1}}^f$ defined by $\mathcal{A}_{t^{n+1}}$ does depend on $\hat{\boldsymbol{\eta}}_h^{n+1}$ and the fluid problem depends on $\Omega_{t^{n+1}}^f$ in a nonlinear way. So, not only the fluid (and in some cases the structure) equations are nonlinear, but also the structure displacement modifies the fluid domain generating geometrical nonlinearities.

We can linearize the FSI problem in several possible ways, among which fixed point, Newton, or quasi-Newton algorithms. Let us detail the first one, which is perhaps the simplest approach.

We consider a *fixed point algorithm* to linearize both nonlinearities, the geometrical one and the one due to the convective term in (2.20a). The linearization of the fluid-structure problem (2.19)-(2.20) (or (2.19)-(2.20a)-(2.21)-(2.20c)) by the fixed point algorithm consists of: given the predictions $\tilde{\boldsymbol{\eta}}_h^{n+1}$ and $\tilde{\mathbf{u}}_h^{n+1}$

- Step 1: Compute the fluid domain displacement as in (2.19) but replacing the first equation with

$$\mathcal{A}_{t^{n+1}}(\mathbf{x}_0) = \mathbf{x}_0 + \text{Ext}_h(\tilde{\boldsymbol{\eta}}_h^{n+1} |_{\Sigma_0}). \quad (2.22)$$

- Step 2: Solve the fluid-structure problem as in (2.20) (or (2.20a)-(2.21)-(2.20c)) replacing the momentum equation (2.20a) by its linearized version:

$$\begin{aligned} & \rho_f \left(D_t^k \mathbf{u}_h^{n+1} |_{\mathbf{x}_0}, \mathbf{v}_h^f \right)_{\Omega_{t^{n+1}}^f} \\ &+ \mathcal{N}_s \left(\tilde{\mathbf{u}}_h^{n+1} - \mathbf{w}_h^{n+1}; \mathbf{u}_h^{n+1}, p_h^{n+1}, \mathbf{v}_h^f, q_h \right)_{\Omega_{t^{n+1}}^f} = \left\langle \mathbf{f}_f^{n+1}, \mathbf{v}_h^f \right\rangle_{\Omega_{t^{n+1}}^f}. \end{aligned} \quad (2.23)$$

- Step 3: Check the stopping criterion. If it is not satisfied, update $\tilde{\boldsymbol{\eta}}_h^{n+1} = \hat{\boldsymbol{\eta}}_h^{n+1}$, $\tilde{\mathbf{u}}_h^{n+1} = \mathbf{u}_h^{n+1}$ and go to Step 1.

We have ended up with a *fully discretized and linearized fluid-structure problem* that can be solved by a linear solver. We remind that we suppose the structure equations to be linear.

When using inf-sup stable finite elements, the only difference is that the form \mathcal{N}_s has to be replaced by \mathcal{N}_h in (2.20a) and (2.23), just as for the pure fluid problem in Section 1.4.3.

The fixed point method suffers from slow convergence and in some cases it may even fail to converge. In the past years, many alternative strategies have been developed to overcome this weakness, as we report in the next section.

2.5 State of the art

Many engineering problems involve the interaction of a fluid with a structure. For this reason, much attention has been paid to the numerical approximation of FSI problems over the last years. We aim at reviewing the great variety of approaches which have been proposed. However, this review is inevitably incomplete and synthetic.

From the numerical viewpoint, the difficulty of FSI problems is twofold: they couple at each time level the two physically independent subproblems (fluid and structure) and they are nonlinear. We focus first on the coupling aspect.

The stability of the numerical simulations relies on the accuracy of the coupled problem solved at each time step. A key role is played by the transmission relations (2.13d)-(2.13e). A solution algorithm which enforces simultaneously the discrete counterpart of both transmission conditions (kinematic and dynamic) is said to be *strongly* or *implicitly coupled*. Hence, strongly coupled methods are generally stable in the energy norm. When the coupling conditions are not exactly satisfied at each time step, a scheme is called *weakly* or *explicitly coupled*. For instance, in the linearized algorithm (2.22)-(2.23)-(2.20b)-(2.20c) the fluid and structure problems are strongly coupled: the fluid solution depends on $\hat{\boldsymbol{\eta}}_h^{n+1}$ through (2.20c), whereas to solve the structure problem in (2.20b) \mathbf{u}_h^{n+1} and p_h^{n+1} are needed. A method that deals with the fluid-structure coupling in an explicit way replaces (2.20c) by the condition $\mathbf{u}_h^{n+1} = \delta_t \tilde{\boldsymbol{\eta}}_h^{n+1}$.

A primary role in coupled fluid-structure systems is played by the so-called *added-mass effect* [26]. In fact, it can be shown that the fluid acts over the structure as an extra mass (usually called added-mass) at the interface. The importance of the extra inertia term appearing in the structure equation increases with the quotient ρ_f/ρ_s . Therefore, when the structure density is much bigger than the fluid one, the added-mass effect is almost negligible. However, some problems involve a fluid and a structure whose densities are of the same order of magnitude. We focus on those cases, in which the added-mass effect becomes important.

Fluid-structure interaction problems are usually solved via *partitioned procedures*, stemming from a domain decomposition viewpoint [120]. These algorithms consist in the evaluation of independent fluid and structure problems, coupled via transmission conditions

in an iterative fashion. A partitioned scheme can be either weakly or strongly coupled. In order for a partitioned scheme to be strongly coupled, subiterations need to be performed at each time step to enforce the transmission conditions with high accuracy. Nevertheless, partitioned procedures are often used to implement weakly coupled schemes, that is only one coupling iteration is performed per time step.

The Dirichlet-Neumann (DN) algorithm is one of the most popular partitioned procedures in FSI. A Dirichlet boundary condition (continuity of velocities) is imposed at the interface for the fluid subproblem, whereas the structure subproblem is supplemented with Neumann boundary conditions (continuity of stresses). The DN algorithm iterates over these two problems until convergence. These are Richardson (also called fixed point) iterations on the interface displacement and they are denoted as coupling iterations.

Fluid-structure algorithms were initially developed for aeroelastic applications, where typically $\rho_s \gg \rho_f$. In this case, the classical DN algorithm (that we will denote by DN-Richardson) converges in a few iterations. Thus, it is common practice in computational aeroelasticity to use an explicit treatment of the coupling (see, e.g., [111, 54]). Explicit coupling, unless stabilized (see [24], in which the continuity of velocities is enforced in a weak way by applying Nitsche's method), does not work for problems with critical added-mass effect [26]. In fact, the convergence properties of the DN-Richardson algorithm depend heavily on the added-mass effect. When the density of the structure is comparable to the fluid one, the method fails to converge (see, e.g., [104, 137]). In order to enforce convergence, relaxation is needed [97]. The relaxation parameter diminishes as the added-mass effect increases and it might become so small that convergence is reached extremely slowly [26].

Many interesting applications are located in the large added-mass effect range, like most of FSI problems involving light and thin-walled structures (e.g., sail-wind systems or airbags). In particular, we are interested in the simulation of the deformation of the arterial walls, whose density is almost identical to the blood one, in the circulatory system.

Despite its inefficiency in case of a large added-mass effect, the DN-Richardson algorithm has still been used. The reason relies on its *modularity*. A FSI algorithm that only requires interface data transfer between the two codes, without any modification of the sources, is called modular. A modular FSI algorithm allows to reuse existing (and already optimized) fluid and structure codes.

Since the nineties, many works have been focused on the development of FSI algorithms capable of improving the convergence velocity of modular algorithms. Some of them suggested the use of dynamic evaluations of the relaxation parameters based on line-search techniques, like steepest descent or Aitken acceleration (see, e.g., [97]). In this minimization approach, robust Krylov methods have replaced Richardson iterations in [72, 56, 96]. Other works proposed to diminish the computational cost by reducing the coupled fluid-structure

problem to a pressure-structure problem, using the continuous projection method [55]. In [100], the partitioned procedure is based on an optimization approach to identify the stress at the interface. Another approach consists in modifying the boundary conditions at the interface. The Neumann-Dirichlet method has even worse convergence properties than the DN one. The Neumann-Neumann algorithm slightly reduces the number of iterations, but every iteration is more expensive, making its efficiency similar to the one of the DN (see [45]). An improved partitioned procedure has been designed: it sets Robin boundary conditions on the interface [6]. Recently [71], a strategy based on splitting the structure in its hydrodynamic and elastic part has been proposed. The hydrodynamic part is treated together with the fluid problem, which is supplemented with the kinematic interface condition. In this way, the fluid problem deals with the inertia of both fluid and the structure, overcoming the difficulties related to the added-mass effect.

Opposite to partitioned procedure are the *monolithic methods*. A method is said to be *monolithic* or *direct* when the fluid and the structure subproblems are solved by means of a unique solver. A monolithic method is strongly coupled by construction, however this approach requires the development of a specific software. Examples of monolithic methods can be found in [125, 72], and references therein. In [58] a simplified monolithic FSI algorithm embedding the structure into the fluid problem has been proposed. There, the $(d - 1)$ -dimensional structure is modeled as a membrane. The same idea of writing the FSI problem only in terms of fluid unknowns is presented in [105], where an algebraic law for approximating the structure problem is employed. In any case, the use of non-modular preconditioners for the FSI system has received much less attention. The first reason is the fact that they are not needed in applications with a negligible added-mass effect because partitioned procedures are very efficient. The second reason is the loss of modularity. Existing fluid and structure codes can still be reused, but the coupling of the codes is more involved than bare interface communication. In fact, fluid and structure matrices must be stored in a unique FSI matrix, which has to be accessed to compute the preconditioner.

All the approaches listed above aim at reducing the computational cost by abating coupling iterations. Another way to serve the same purpose is to reduce the nonlinear iterations by adopting more efficient linearization techniques. There exist two ways for an algorithm to treat the nonlinearities given by the convective term and the fluid domain: explicitly and implicitly. In the first case, only one fixed point iteration is performed per time step. In the other case, nonlinear iterations are performed till convergence of the fixed point, Newton or quasi-Newton algorithm. The use of a full Newton algorithm is suggested in [56]. Even though the Newton method reduces the number of nonlinear iterations, every iteration is more expensive because shape derivative evaluations are needed, making the implementation complicated. Quasi-Newton algorithms have been suggested in [144, 66, 93, 72, 146].

The FSI algorithms treating nonlinearity explicitly are called semi-implicit. In general, the treatment of the fluid domain in an explicit way does not affect the unconditional stability of the coupled FSI problem, even when the added-mass effect is critical. This is not the case for the fluid-structure coupling: explicit or weak coupling is unstable when the added-mass effect is important [26], as already pointed out. In particular, if the problem is discretized with a first order method (in time) and the condition

$$\tilde{\mathbf{u}}_h^{n+1} = \mathbf{w}_h^{n+1}, \quad \text{on } \Sigma_t,$$

is satisfied (e.g. by taking $\tilde{\mathbf{u}}_h^{n+1} = \mathbf{u}_h^n$ and $\tilde{\boldsymbol{\eta}}_h^{n+1} = \hat{\boldsymbol{\eta}}_h^n$ in (2.22)-(2.23)-(2.20b)-(2.20c)), the semi-implicit method keeps the stability properties of the implicit procedure (see [104]). Semi-implicit methods treat explicitly nonlinearity (reducing CPU cost) and implicitly the fluid-structure coupling (keeping stability).

The first semi-implicit algorithm was presented in [55]. Therein, the coupled system of equations is solved through the Chorin-Temam projection scheme. The resulting algorithm couples the pressure stress to the structure in an implicit way, while the remaining terms of the fluid equations (dissipation, convection, and geometrical non-linearities) are explicitly treated. In the next chapter, we propose some semi-implicit procedures which perform the implicit-explicit splitting using algebraic fractional-step methods instead of a differential one.

Other semi-implicit schemes were proposed in [105, 6, 136].

CHAPTER 2. THE INTERACTION BETWEEN A FLUID AND AN ELASTIC
STRUCTURE

Chapter 3

Splitting methods based on algebraic factorization

3.1 Introduction

In Section 2.5, we gave an overview of the methods proposed so far to solve FSI problems affected by a critical added-mass effect. A relevant improvement was introduced by semi-implicit schemes [55]: although not strongly coupled, they exhibit very good stability properties, i.e. remain stable for a reasonable range of physical and discretization parameters. In [55], the Chorin-Temam method is applied to the fluid subproblem, i.e. an intermediate velocity is calculated using a prediction of the structure displacement and in a second step the end-of-step velocity, pressure, and structure displacement are computed. It is the implicit coupling of the pressure to the structure that allows to have stability for a wide range of parameters. On the other side, the explicit treatment of the fluid velocity enables computational time savings.

In this chapter, we present new semi-implicit algorithms based on inexact block- LU factorization of the linear system obtained after the space-time discretization and linearization of the FSI problem (see Section 2.4.2). As a result, the fluid velocity is computed separately from the coupled pressure-structure velocity system at each iteration, reducing the computational cost. We investigate explicit-implicit decomposition through algebraic splitting techniques originally designed for the FSI problem. This approach leads to two different families of methods which extend to FSI algebraic pressure correction methods (Section 1.5.1) and Yosida methods (Section 1.5.2), two schemes that were previously adopted for pure fluid problems.

Furthermore, we have considered the inexact factorization of the fluid-structure system as a preconditioner.

3.2 The linear fluid-structure system

In Section 2.4.2, we tackled the space-time discretization (2.19)-(2.20) (or (2.19)-(2.20a)-(2.21)-(2.20c)) of the fluid-structure problem. Being the problem nonlinear, we proposed to adopt a fixed point algorithm to linearize at the same time both the geometrical non-linearity and that due to the convective term. In this section, we aim at writing the linear fluid-structure system that has to be solved at every iteration of the fixed point method.

Like it has been done in Section 1.4.4 for fluid problems in rigid domains, we start by introducing the Lagrange basis associated to the finite element spaces. We denote by $\{\phi_i\}_{\mathcal{N}_f} \oplus \{\phi_j^\sigma\}_{\mathcal{N}_\sigma}$, $\{\pi_i\}_{\mathcal{N}_p}$, and $\{\psi_i\}_{\mathcal{N}_s} \oplus \{\psi_j^\sigma\}_{\mathcal{N}_\sigma}$ the basis for V_h^f , Q_h , and \hat{V}_h^s , respectively. As in Section 1.4.4, \mathcal{N}_p indicates the set of pressure nodes, while the set of fluid inner nodes is now referred to by \mathcal{N}_f . \mathcal{N}_σ and \mathcal{N}_s denote the set of velocity nodes on Σ_t and the set of inner structure nodes, respectively. The time evolution of the finite element shape functions depends on the maps (2.2)-(2.8). Being $\hat{\phi}_i(\mathbf{x}_0)$ and $\hat{\psi}_i(\mathbf{x}_0)$ the Lagrangian shape function on the reference grid, on the current mesh we have $\phi_i(\mathbf{x}, t^n) = \mathcal{A}_{t^n}(\hat{\phi}_i(\mathbf{x}_0))$ and $\psi_i(\mathbf{x}, t^n) = \mathcal{L}_{t^n}(\hat{\psi}_i(\mathbf{x}_0))$.

Since we restricted our attention to the case of geometrical conforming grids, the nodes \mathcal{N}_σ belong to the grids of both subdomains. Moreover, $\mathcal{E}_h(\psi_i^\sigma) = \phi_i^\sigma$, for $i \in \mathcal{N}_\sigma$.

The finite element approximation of the pressure is (1.20b), while for the fluid velocity we write

$$\mathbf{u}_h^{n+1}(\mathbf{x}, t^{n+1}) = \sum_{i \in \mathcal{N}_f} \phi_i(\mathbf{x}, t^{n+1})(\mathbf{U}_f^{n+1}(t^{n+1}))_i + \sum_{j \in \mathcal{N}_\sigma} \phi_j^\sigma(\mathbf{x}, t^{n+1})(\mathbf{U}_\sigma^{n+1}(t^{n+1}))_j,$$

where \mathbf{U}_f^{n+1} and \mathbf{U}_σ^{n+1} are the arrays of nodal values for the velocity of the inner nodes and interface nodes. The difference with respect to (1.20a) is that the ‘‘boundary’’ nodal values \mathbf{U}_σ^{n+1} (\mathbf{U}_D^{n+1} in (1.20a)) are now unknown.

We also set:

$$\hat{\boldsymbol{\eta}}_h^{n+1}(\mathbf{x}_0) = \sum_{i \in \mathcal{N}_s} \hat{\psi}_i(\mathbf{x}_0)(\mathbf{D}_s^{n+1}(t^{n+1}))_i + \sum_{j \in \mathcal{N}_\sigma} \hat{\psi}_j^\sigma(\mathbf{x}_0)(\mathbf{D}_\sigma^{n+1}(t^{n+1}))_j, \quad (3.1a)$$

$$\dot{\hat{\boldsymbol{\eta}}}_h^{n+1}(\mathbf{x}_0) = \sum_{i \in \mathcal{N}_s} \dot{\hat{\psi}}_i(\mathbf{x}_0)(\dot{\mathbf{D}}_s^{n+1}(t^{n+1}))_i + \sum_{j \in \mathcal{N}_\sigma} \dot{\hat{\psi}}_j^\sigma(\mathbf{x}_0)(\dot{\mathbf{D}}_\sigma^{n+1}(t^{n+1}))_j, \quad (3.1b)$$

where \mathbf{D}_σ^{n+1} and \mathbf{D}_s^{n+1} are the arrays of nodal values for $\hat{\boldsymbol{\eta}}_h^{n+1}$ on the interface and inside the structure, respectively. In the same way, $\dot{\mathbf{D}}_\sigma^{n+1}$ and $\dot{\mathbf{D}}_s^{n+1}$ are related to $\dot{\hat{\boldsymbol{\eta}}}_h^{n+1}$. We remind that (3.1b) is needed only in case the structure equations are discretized in time by the the mid-point scheme.

From (2.20c) we know that:

$$\mathbf{U}_\sigma^{n+1} = \delta_t \mathbf{D}_\sigma^{n+1}. \quad (3.2)$$

Thanks to (3.2) and by introducing $\mathbf{U}_s^{n+1} = \delta_t \mathbf{D}_s^{n+1}$, we can easily rewrite the structure equations in terms of velocity.

In order to write the fully discretized coupled problem for a given time value t^{n+1} , we need matrices (1.21). To define submatrices of the matrices in (1.21), let us introduce the subindexes β and γ associated to the position of fluid nodes: the “value” σ is used for nodes on Σ_t , f otherwise. For example, $C_{\beta\gamma}^{ij} = C_{ij}$ (where C_{ij} is defined by (1.21c)), with $i \in \mathcal{N}_\beta$, $j \in \mathcal{N}_\gamma$, and $G_{\beta\gamma}^{ij} = G_{ij}$ (G_{ij} defined in (1.21d)), with $i \in \mathcal{N}_\beta$, $j \in \mathcal{N}_\gamma$.

Let us denote with N the matrix associated to the structure written in terms of \mathbf{U}_σ^{n+1} and \mathbf{U}_s^{n+1} . For instance, if the structure is modeled by the Saint-Venant Kirchhoff constitutive law and the BDF1 scheme is adopted for the time discretization (see (2.20b)), the definition of matrix N (and submatrices) is the following:

$$N_{\beta\gamma} = \frac{1}{\rho_f} \left(\frac{\rho_s}{\delta t} M_{\beta\gamma}^s + \delta t F_{\beta\gamma} \right), \quad (3.3a)$$

with

$$F_{\beta\gamma}^{ij} = \mu_\ell \left(\nabla \hat{\boldsymbol{\psi}}_i, \nabla \hat{\boldsymbol{\psi}}_j \right)_{\Omega_0^s} + \lambda_\ell \left(\nabla \cdot \hat{\boldsymbol{\psi}}_i, \nabla \cdot \hat{\boldsymbol{\psi}}_j \right)_{\Omega_0^s}, \quad i \in \mathcal{N}_\beta, \quad j \in \mathcal{N}_\gamma, \quad (3.3b)$$

$$M_{\beta\gamma}^{s,ij} = \left(\hat{\boldsymbol{\psi}}_i, \hat{\boldsymbol{\psi}}_j \right)_{\Omega_0^s}, \quad i \in \mathcal{N}_\beta, \quad j \in \mathcal{N}_\gamma. \quad (3.3c)$$

Again, superindexes i and j denote the nodes. For structure matrices (3.3), subindexes β and γ can take the “value” σ for nodes on Σ_t , s otherwise.

At a given time value t^{n+1} , equations (2.23)-(2.20b)-(2.20c) (or (2.23)-(2.21a)-(2.20c)) can be written in matrix form as:

$$A \mathbf{X}^{n+1} = \mathbf{b}^{n+1}, \quad (3.4)$$

where

$$A = \begin{bmatrix} C_{ff} & G_f^\tau & C_{f\sigma} & 0 \\ D_f^\tau & L^\tau & D_\sigma^\tau & 0 \\ C_{\sigma f} & G_\sigma^\tau & C_{\sigma\sigma} + N_{\sigma\sigma} & N_{\sigma s} \\ 0 & 0 & N_{s\sigma} & N_{ss} \end{bmatrix}, \quad \mathbf{X}^{n+1} = \begin{bmatrix} \mathbf{U}_f^{n+1} \\ \mathbf{P}^{n+1} \\ \mathbf{U}_\sigma^{n+1} \\ \mathbf{U}_s^{n+1} \end{bmatrix}, \quad \mathbf{b}^{n+1} = \begin{bmatrix} \mathbf{b}_f^{n+1} \\ \mathbf{b}_p^{n+1} \\ \mathbf{b}_\sigma^{n+1} \\ \mathbf{b}_s^{n+1} \end{bmatrix}. \quad (3.5)$$

The right-hand-side terms \mathbf{b}_f^{n+1} , \mathbf{b}_p^{n+1} , \mathbf{b}_σ^{n+1} , and \mathbf{b}_s^{n+1} account for body forces, time integration and stabilization terms, and the structure terms related to the fact that the structure equation is stated in terms of velocities.

Using the subscript S to indicate both the inner structure and interface nodes, the matrix and the vectors in (3.5) can be rewritten in a more compact form:

$$A = \begin{bmatrix} C_{ff} & G_f^\tau & C_{fS} \\ D_f^\tau & L^\tau & D_S^\tau \\ C_{Sf} & G_S^\tau & N_{SS} + C_{SS} \end{bmatrix}, \quad \mathbf{X}^{n+1} = \begin{bmatrix} \mathbf{U}_f^{n+1} \\ \mathbf{P}^{n+1} \\ \mathbf{U}_S^{n+1} \end{bmatrix}, \quad \mathbf{b}^{n+1} = \begin{bmatrix} \mathbf{b}_f^{n+1} \\ \mathbf{b}_p^{n+1} \\ \mathbf{b}_S^{n+1} \end{bmatrix}. \quad (3.6)$$

Remark 3.1. *The algebraic splitting algorithms we introduce in this chapter are based on the block structure of matrix A in (3.5) (or (3.6), equivalently). Other time discretization schemes for the fluid and structure subproblems can be used without altering that structure. Therefore, the procedures proposed in the next section can be easily extended to other time integration methods.*

Remark 3.2. *For $(d-1)$ -dimensional structures (d being the dimension of the fluid problem), system (3.5) becomes:*

$$A = \begin{bmatrix} C_{ff} & G_f^\tau & C_{f\sigma} \\ D_f^\tau & L^\tau & D_\sigma^\tau \\ C_{\sigma f} & G_\sigma^\tau & C_{\sigma\sigma} + N \end{bmatrix}, \mathbf{X}^{n+1} = \begin{bmatrix} \mathbf{U}_f^{n+1} \\ \mathbf{P}^{n+1} \\ \mathbf{U}_\sigma^{n+1} \end{bmatrix}, \mathbf{b}^{n+1} = \begin{bmatrix} \mathbf{b}_f^{n+1} \\ \mathbf{b}_p^{n+1} \\ \mathbf{b}_\sigma^{n+1} \end{bmatrix}. \quad (3.7)$$

Matrix A in (3.7) has the same block structure as the matrix in (3.6). Thus, also the extension of our methodology to the case of $(d-1)$ -dimensional structures is straightforward.

Remark 3.3. *It is also possible to linearize the fluid and structure problems by Newton methods. Again, the block structure of matrix A is left unchanged and our procedures can be applied.*

We do not consider the application of Newton methods to the FSI problem.

Remark 3.4. *The orthogonal projection in the stabilization term (1.17) complicates the assembling of the fluid block. Therefore, for practical purposes, only the term*

$$\left(\tau_1 (\tilde{\mathbf{u}}_h^{n+1} \cdot \nabla \mathbf{u}_h^{n+1} + \nabla p_h^{n+1}), \tilde{\mathbf{u}}_h^{n+1} \cdot \nabla \mathbf{v}_h^f + \nabla q_h \right)_{\Omega_{t^{n+1}}^f} + \left(\tau_2 (\nabla \cdot \mathbf{u}_h^{n+1}), \nabla \cdot \mathbf{v}_h^f \right)_{\Omega_{t^{n+1}}^f}$$

is assembled in the matrix, whereas the missing term is treated explicitly and sent to the right-hand side

$$\left(\tau_1 \Pi (\tilde{\mathbf{u}}_h^n \cdot \nabla \mathbf{u}_h^n + \nabla p_h^n), \tilde{\mathbf{u}}_h^{n+1} \cdot \nabla \mathbf{v}_h^f + \nabla q_h \right)_{\Omega_{t^{n+1}}^f} + \left(\tau_2 \Pi (\nabla \cdot \mathbf{u}_h^n), \nabla \cdot \mathbf{v}_h^f \right)_{\Omega_{t^{n+1}}^f}.$$

Alternatively, we could use the algebraic subgrid scales (ASGS) technique (see [75]), which introduces the stabilization term

$$\begin{aligned} & \left(\tau_1 (\rho_f \delta_t \mathbf{u}_h^{n+1} |_{\mathbf{x}_0} + \tilde{\mathbf{u}}_h^{n+1} \cdot \nabla \mathbf{u}_h^{n+1} + \nabla p_h^{n+1}), \tilde{\mathbf{u}}_h^{n+1} \cdot \nabla \mathbf{v}_h^f + \nabla q_h \right)_{\Omega_{t^{n+1}}^f} \\ & + \left(\tau_2 (\nabla \cdot \mathbf{u}_h^{n+1}), \nabla \cdot \mathbf{v}_h^f \right)_{\Omega_{t^{n+1}}^f}. \end{aligned}$$

In case we use inf-sup stable finite elements, the FSI system matrix is

$$A = \begin{bmatrix} C_{ff} & G_f & C_{f\sigma} & 0 \\ D_f & 0 & D_\sigma & 0 \\ C_{\sigma f} & G_\sigma & C_{\sigma\sigma} + N_{\sigma\sigma} & N_{\sigma s} \\ 0 & 0 & N_{s\sigma} & N_{ss} \end{bmatrix}, \quad (3.8)$$

or equivalently

$$A = \begin{bmatrix} C_{ff} & G_f & C_{fs} \\ D_f & 0 & D_s \\ C_{sf} & G_s & N_{ss} + C_{ss} \end{bmatrix}. \quad (3.9)$$

Furthermore, vector \mathbf{b}_p^{n+1} at the right-hand-side is equal to zero.

Remark 3.5. *In case of considering non-matching grids and a mortar method (see, e.g., [12]) on the interface, the monolithic system has to be modified. Two different interface arrays must be considered: the interface fluid velocity $\mathbf{U}_{\sigma,f}^{n+1}$ and the interface structure velocity $\mathbf{U}_{\sigma,s}^{n+1}$. For instance, considering the structure interface as the master, and the fluid interface as the slave, we can define the rectangular matrix R that projects the structure interface velocity into the fluid interface space. The continuity of velocities is imposed as*

$$\mathbf{U}_{\sigma,f}^{n+1} = R\mathbf{U}_{\sigma,s}^{n+1}.$$

Matrix R involves an inverse mass matrix (better if lumped) on the fluid interface. Then, we must multiply the blocks $C_{\sigma f}$, G_σ and $C_{\sigma\sigma}$ in (3.8) (or $C_{\sigma f}$, G_σ^τ and $C_{\sigma\sigma}$ in (3.5)) by R on the right and solve the problem with $\mathbf{U}_{\sigma,s}^{n+1}$ as interface unknown.

3.2.1 Features of the monolithic system

Let us address the basic aspects of monolithic system (3.4).

Firstly, we deal with matching grids on the fluid-structure interface. Then, we make use of the same finite element spaces for fluid velocity and structure displacement (or velocity). For example, for the numerical experiments in Sections 5.5 and 5.6, we use stabilized $\mathbb{P}_1/\mathbb{P}_1$ finite elements for the fluid and \mathbb{P}_1 finite elements for the structure. Moreover, we reformulate the structure equations in terms of velocities. This is attained by a simple modification of the right-hand side and does not affect at all the generality of the formulation.

By virtue of all these choices, the velocity unknowns are defined over the whole domain (fluid and structure) and interpolated with the same finite element space, and the problem is discretized using one finite element partition.

In this frame, the transmission conditions are easily imposed. The continuity of velocities on the interface is implicitly enforced by the finite element space interpolation used over the whole domain. The continuity of stresses is imposed weakly. The weak transmission of stresses simply arises from the fact that shape functions on the interface nodes have support on both fluid and structure subdomains. In this way, the final system has the form reported in (3.5) or (3.8).

Remark 3.6. *When using continuous finite element spaces (as we do all along this thesis), the continuity of velocities at the interface is assured, because there is only one value on the interface nodes. However, we could also think about discontinuous Galerkin methods. In that case, the continuity of velocities between element edges or faces (in particular, those that define the interface) is enforced weakly. Another approach, in the spirit of [24], is to consider continuous finite element formulations everywhere except on the interface, where a discontinuous Galerkin approach is used. It has been shown in [24] that a weak enforcement of transmission conditions improves the properties of partitioned procedures.*

Another option for the dynamic coupling condition would be to impose it in a strong form. Once the fluid problem is solved, the stresses are integrated on the boundary elements by evaluating the fluid stress on the Gauss points, and passed to the structure solver. In this case, supposing to use the stabilized formulation, the monolithic matrix reads as

$$A = \begin{bmatrix} C_{ff} & G_f^\tau & C_{f\sigma} & 0 \\ D_f^\tau & L_p^\tau & D_\sigma^\tau & 0 \\ J_{\sigma f} & J_p & N_{\sigma\sigma} & N_{\sigma s} \\ 0 & 0 & N_{s\sigma} & N_{ss} \end{bmatrix},$$

where $J_{\sigma f}$ comes from the term

$$\langle \nu \mathbf{n}_f \cdot (\nabla \mathbf{u}_h^{n+1} + (\nabla \mathbf{u}_h^{n+1})^T), \mathbf{v}_h^s \rangle_{\Sigma_t}$$

and J_p from

$$\langle -p_h^{n+1} \mathbf{I} \cdot \mathbf{n}_f, \mathbf{v}_h^s \rangle_{\Sigma_t}.$$

This approach destroys the symmetry of the system (in case of using the Stokes problem), affects the unconditional stability of (3.5) and spoils the order of accuracy of the method (see [23]). For these reasons, we consider the weak transmission of stresses.

3.2.2 Block- LU factorization of the coupled system

The solution of the fluid-structure system (3.4) by a monolithic method, like a preconditioned Krylov method, can be very expensive. The associated matrix A is indefinite and for real applications its size is prohibitive. Therefore, we need to employ more efficient methods.

In this section and in the following ones, we consider inf-sup stable elements and the associated matrix (3.9). The extension to the case of pressure stabilized methods requires only minor adaptations.

Following the procedure presented in Section 1.5, we solve system (3.4) using an exact block- LU factorization of the fluid-structure system matrix A , for a suitable choice of the

blocks to be *decoupled*. If the first block is that related to \mathbf{U}_f^{n+1} and the second one is associated to the fluid pressure and structure variables $[\mathbf{P}^{n+1}, \mathbf{U}_S^{n+1}]$, the L and U factors read:

$$A = \begin{bmatrix} C_{ff} & 0 & 0 \\ D_f & S_{pp} & S_{pS} \\ C_{Sf} & S_{Sp} & S_{SS} \end{bmatrix} \begin{bmatrix} I & C_{ff}^{-1}G_f & C_{ff}^{-1}C_{fS} \\ 0 & I & 0 \\ 0 & 0 & I \end{bmatrix} = LU. \quad (3.10)$$

The S -matrices represent the Schur complements. Their formal definition is:

$$S_{pp} = -D_f C_{ff}^{-1} G_f, \quad (3.11a)$$

$$S_{pS} = D_S - D_f C_{ff}^{-1} C_{fS}, \quad (3.11b)$$

$$S_{Sp} = G_S - C_{Sf} C_{ff}^{-1} G_f, \quad (3.11c)$$

$$S_{SS} = N_{SS} + C_{SS} - C_{Sf} C_{ff}^{-1} C_{fS}. \quad (3.11d)$$

Solving system (3.4) through the block- LU factorization (3.10) involves the solution of the following subsystems:

1. L - step: find $\tilde{\mathbf{U}}_f^{n+1}$, $\tilde{\mathbf{P}}^{n+1}$, $\tilde{\mathbf{U}}_S^{n+1}$:

$$C_{ff} \tilde{\mathbf{U}}_f^{n+1} = \mathbf{b}_f^{n+1}, \quad (3.12a)$$

$$\begin{bmatrix} S_{pp} & S_{pS} \\ S_{Sp} & S_{SS} \end{bmatrix} \begin{bmatrix} \tilde{\mathbf{P}}^{n+1} \\ \tilde{\mathbf{U}}_S^{n+1} \end{bmatrix} = \begin{bmatrix} -D_f \tilde{\mathbf{U}}_f^{n+1} \\ \mathbf{b}_S^{n+1} - C_{Sf} \tilde{\mathbf{U}}_f^{n+1} \end{bmatrix}; \quad (3.12b)$$

2. U - step: find \mathbf{U}_f^{n+1} , \mathbf{P}^{n+1} , \mathbf{U}_S^{n+1} :

$$\begin{bmatrix} \mathbf{P}^{n+1} \\ \mathbf{U}_S^{n+1} \end{bmatrix} = \begin{bmatrix} \tilde{\mathbf{P}}^{n+1} \\ \tilde{\mathbf{U}}_S^{n+1} \end{bmatrix}, \quad (3.13a)$$

$$C_{ff} \mathbf{U}_f^{n+1} = C_{ff} \tilde{\mathbf{U}}_f^{n+1} - G_f \mathbf{P}^{n+1} - C_{fS} \mathbf{U}_S^{n+1}. \quad (3.13b)$$

Scheme (3.12)-(3.13) decouples the computation of the fluid velocity (an intermediate one in (3.12a) and the end-of-step one in (3.13b)) from a coupled pressure-structure velocity system (3.12b).

The computational complexity of the exact LU factorization lies in system (3.12b). Its system matrix is made up of Schur complements whose definitions involve the inverse fluid matrix C_{ff}^{-1} . Since the goal is finding a computationally cheap variable splitting, resorting to inexact factorization is mandatory. Like in the case of pure fluid problems (see Section 1.5), we need to approximate C_{ff}^{-1} with a matrix easy to compute. In the next sections, different approximations will be considered and the inexact factorization is applied to the

incremental system (1.26), rather than to (3.4). Here, \mathbf{X}^* is the vector made of \mathbf{U}_f^* , \mathbf{P}^* , and \mathbf{U}_S^* which are predictions of \mathbf{U}_f^{n+1} , \mathbf{P}^{n+1} , and \mathbf{U}_S^{n+1} .

One could think of decoupling all the variables, instead of leaving the pressure coupled to the structure as in (3.12)-(3.13). Then, the L and U steps would become:

1. L - step: find $\tilde{\mathbf{U}}_f^{n+1}$, $\tilde{\mathbf{P}}^{n+1}$, $\tilde{\mathbf{U}}_S^{n+1}$:

$$C_{ff}\tilde{\mathbf{U}}_f^{n+1} = \mathbf{b}_f^{n+1}, \quad (3.14a)$$

$$S_{pp}\tilde{\mathbf{P}}^{n+1} = -D_f\tilde{\mathbf{U}}_f^{n+1}, \quad (3.14b)$$

$$(S_{SS} - S_{Sp}S_{pp}^{-1}S_{pS})\tilde{\mathbf{U}}_S^{n+1} = \mathbf{b}_S^{n+1} - C_{Sf}\tilde{\mathbf{U}}_f^{n+1}; \quad (3.14c)$$

2. U - step: find \mathbf{U}_f^{n+1} , \mathbf{P}^{n+1} , \mathbf{U}_S^{n+1} :

$$\begin{aligned} \mathbf{U}_S^{n+1} &= \tilde{\mathbf{U}}_S^{n+1}, \\ S_{pp}\mathbf{P}^{n+1} &= S_{pp}\tilde{\mathbf{P}}^{n+1} - S_{pS}\mathbf{U}_S^{n+1}, \\ C_{ff}\mathbf{U}_f^{n+1} &= C_{ff}\tilde{\mathbf{U}}_f^{n+1} - G_f\mathbf{P}^{n+1} - C_{fS}\mathbf{U}_S^{n+1}. \end{aligned}$$

This scheme is further complicated by the presence of the inverse of the pressure Schur complement S_{pp} in (3.14c). To reduce the computational cost, we should find an appropriate approximation of S_{pp}^{-1} , which is not immediate. For this reason, we focus on (3.12)-(3.13).

3.3 Semi-implicit procedures for the FSI problem based on inexact factorization methods

In Section 2.5, we outlined the difference between *explicit*, *implicit*, and *semi-implicit* coupling algorithms for FSI problems.

Our goal is to derive semi-implicit algorithms from splitting techniques originally designed for the FSI problem at the fully discrete level instead of the differential one designed in [55]. The extension of algebraic splitting procedures to fluid-structure problems is not straightforward, especially when the added-mass effect is critical. We propose to adapt two methods to the coupled fluid-structure problem (3.4): the algebraic version of the Chorin-Temam method and the Yosida scheme. This will lead to two families of methods:

- *pressure-interface correction (PIC) methods*;
- *fluid-structure Yosida (FSY) methods*.

Differences and analogies between these procedures and the projection scheme in [55] will be analyzed in Section 3.4.

The third family of algorithms introduced in this section will exploit the inexact factors of the PIC and FSY schemes as preconditioners, leading to predictor-corrector methods.

FSY methods were introduced in [113] and developed in [9], where PIC schemes were presented together with predictor-corrector methods. In those works, inf-sup stable finite element pairs were used for fluid velocity and pressure and only $(d - 1)$ -dimensional structures were considered. All the methods were tested on a $2d$ benchmark involving a one-dimensional structure (see Chapter 4). The extension to stabilized finite element methods with equal order velocity-pressure interpolation and the generalization to the case of d -dimensional structures is reported in [8] (see Chapter 5).

3.3.1 Pressure-interface correction (PIC) methods

In this section, we consider an inexact factorization which is the FSI counterpart of pressure correction methods (see Section 1.5.1). We will call these methods pressure-interface correction (PIC) schemes since both the pressure and the interface (and structure) velocity are treated explicitly (or ignored) in the first step and corrected in the second one.

As done for pure fluid problems, the exact L and U factors (3.10) are replaced by inexact ones in which C_{ff}^{-1} is substituted by the zero-th order term of its Neumann expansion:

$$C_{ff}^{-1} = \left(\frac{1}{\delta t} M_{ff} + K_{ff} \right)^{-1} = \delta t M_{ff}^{-1} + \mathcal{O}(\delta t^2) \simeq \delta t M_{ff}^{-1}. \quad (3.15)$$

Approximation (3.15) is a particular case of (1.27): it corresponds to the use of the BDF1 scheme for the time discretization of the fluid equations. For the sake of clarity and without affecting the generality of the results, we only consider this case in the subsequent exposition.

Remark 3.7. *When using the OSS technique, none of the stabilization terms is multiplied by δt^{-1} ; the time derivative terms in the residual disappear with the orthogonal projection. We can include all the stabilization terms in K_{ff} and use the previous expansion with a lumped mass matrix. However, for some other techniques, like algebraic subgrid scales or Galerkin/least-squares, there are stabilization terms that are multiplied by δt^{-1} . Matrix M_{ff} is not a standard mass matrix anymore and cannot be lumped, making its inversion more involved.*

After approximating C_{ff}^{-1} by $\delta t M_{ff}^{-1}$, the Schur complements matrices (3.11) become:

$$S_{pp} \simeq T_{pp} = -\delta t D_f M_{ff}^{-1} G_f, \quad (3.16a)$$

$$S_{pS} \simeq T_{pS} = D_S - \delta t D_f M_{ff}^{-1} C_{fS}, \quad (3.16b)$$

$$S_{Sp} \simeq T_{Sp} = G_S - \delta t C_{Sf} M_{ff}^{-1} G_f, \quad (3.16c)$$

$$S_{SS} \simeq T_{SS} = N_{SS} + C_{SS} - \delta t C_{Sf} M_{ff}^{-1} C_{fS}. \quad (3.16d)$$

Consequently, the lower block-triangular matrix L is approximated by:

$$L_{PIC} := \begin{bmatrix} C_{ff} & 0 & 0 \\ D_f & T_{pp} & T_{pS} \\ C_{Sf} & T_{Sp} & T_{SS} \end{bmatrix}.$$

Using the same approximation (3.15) for the upper block-triangular matrix U in (3.10), the following inexact U factor is obtained:

$$U_{PIC} := \begin{bmatrix} I & \delta t M_{ff}^{-1} G_f & \delta t M_{ff}^{-1} C_{fS} \\ 0 & I & 0 \\ 0 & 0 & I \end{bmatrix}.$$

The system matrix for the PIC scheme is obtained by replacing matrices L and U with L_{PIC} and U_{PIC} :

$$A_{PIC} = L_{PIC} U_{PIC} = \begin{bmatrix} C_{ff} & \delta t C_{ff} M_{ff}^{-1} G_f & \delta t C_{ff} M_{ff}^{-1} C_{fS} \\ D_f & 0 & D_S \\ C_{Sf} & G_S & N_{SS} + C_{SS} \end{bmatrix}. \quad (3.17)$$

Let us apply this inexact factorization to the incremental version of the FSI system (the non-incremental version is nothing but a special case corresponding to the trivial choice $\mathbf{X}^* = \mathbf{0}$). We rearrange the resulting system into three sequential steps:

1. Computation of the intermediate velocity:

$$C_{ff} \tilde{\mathbf{U}}_f^{n+1} = \mathbf{b}_f^{n+1} - G_f \mathbf{P}^* - C_{fS} \mathbf{U}_S^*; \quad (3.18a)$$

2. Solution of the coupled pressure-structure system:

$$\begin{bmatrix} T_{pp} & T_{pS} \\ T_{Sp} & T_{SS} \end{bmatrix} \begin{bmatrix} \mathbf{P}^{n+1} - \mathbf{P}^* \\ \mathbf{U}_S^{n+1} - \mathbf{U}_S^* \end{bmatrix} = \begin{bmatrix} -D_f \tilde{\mathbf{U}}_f^{n+1} \\ \mathbf{b}_S^{n+1} - C_{Sf} \tilde{\mathbf{U}}_f^{n+1} \end{bmatrix} - \begin{bmatrix} 0 & D_S \\ G_S & N_{SS} + C_{SS} \end{bmatrix} \begin{bmatrix} \mathbf{P}^* \\ \mathbf{U}_S^* \end{bmatrix}; \quad (3.18b)$$

3. Computation of the end-of-step velocity:

$$\frac{1}{\delta t} M_{ff} \mathbf{U}_f^{n+1} = \frac{1}{\delta t} M_{ff} \tilde{\mathbf{U}}_f^{n+1} - G_f(\mathbf{P}^{n+1} - \mathbf{P}^*) - C_{fS}(\mathbf{U}_S^{n+1} - \mathbf{U}_S^*). \quad (3.18c)$$

Scheme (3.18) couples the pressure stress to the structure in an implicit way, while the remaining terms of the fluid equations are explicitly treated, as the algorithm in [55].

Like in PC methods, the prediction of the fluid velocity \mathbf{U}_f^* does not enter in the PIC scheme (3.18), therefore it cannot affect the order of accuracy in time of the method. The perturbation terms due to the inexact factors L_{PIC} and U_{PIC} (see Section 3.5.1) depend only on \mathbf{P}^* and \mathbf{U}_S^* . Different approximations for \mathbf{P}^* and \mathbf{U}_S^* can be considered:

$$\begin{aligned} \mathbf{P}^* = \mathbf{0}, \quad \mathbf{U}_S^* = \mathbf{0}, & \quad \text{0-th order approximation} \\ \mathbf{P}^* = \mathbf{P}^n, \quad \mathbf{U}_S^* = \mathbf{U}_S^n, & \quad \text{1st order approximation} \\ \mathbf{P}^* = 2\mathbf{P}^n - \mathbf{P}^{n-1}, \quad \mathbf{U}_S^* = 2\mathbf{U}_S^n - \mathbf{U}_S^{n-1} & \quad \text{2nd order approximation.} \end{aligned}$$

With PIC schemes, we pass from an indefinite system coupling velocity components, pressure and structure unknowns, to a set of smaller systems. For instance, neglecting convective terms, the PIC schemes involve the solution of:

1. A definite system (3.18a) for the fluid velocity. In case we use the Laplace form of the viscous term, every velocity component is decoupled from one another.
2. A non-singular system (3.18b) coupling the fluid and the structure through the coupling of pressure and structure velocity. Therefore, with PIC schemes, the dimension of the *fluid-structure system* affected by the added-mass effect has been clearly reduced. In the following we denote by T the system matrix of the pressure-structure problem. Further comments on matrix T and how to solve system (3.18b) are made in Section 3.6.
3. A cheap system (3.18c) with a diagonal system matrix if we apply mass lumping (see Remark 1.1).

In conclusion, this method not only reduces the dimension of the fluid-structure system but changes its nature too, becoming much more convenient from a computational point of view.

The explicit treatment of the expensive ALE-advection-viscous term is based on the approximation of the domain shape at time t^{n+1} with the domain Ω^n calculated at the previous time step (2.22). Semi-implicit PIC methods perform the three steps (3.18) only once per time step. A standard strongly coupled approach (replacing (2.22) with (2.19)) would require to iterate the whole procedure, increasing the overall computational cost.

Thanks to the implicit coupling of the pressure (3.18b) we can avoid these iterations without severely affecting the stability. However, one could adopt implicit PIC methods to solve the FSI problem.

Remark 3.8. *In Remark 1.2 we comment on the artificial pressure boundary condition that pressure correction methods introduce. With the PIC scheme, a more consistent boundary condition is imposed over the interface, due to the presence of the interface velocity terms (see Section 3.4).*

Remark 3.9. *In the case of $(d - 1)$ -dimensional structures, the inexact block-LU factorization is carried out on matrix A in (3.7). The first block is still associated to \mathbf{U}_f^{n+1} , while the second one is related to the variables $[\mathbf{P}^{n+1}, \mathbf{U}_\sigma^{n+1}]$. The resulting PIC scheme is obtained by replacing in (3.18) subindex S with σ .*

3.3.2 Fluid-structure Yosida (FSY) methods

In this subsection, we extend the Yosida method (Section 1.5.2) to the FSI problem (3.4).

The inexact factorization of matrix A (3.9) is again based on the approximation (3.15) but it is only used on the lower block-triangular matrix, i.e. for the evaluation of the Schur complements. In the U factor, matrix C_{ff}^{-1} is not approximated. Thus, the inexact factorization we use in this case is simply

$$A_{FSY} = L_{PIC}U. \quad (3.19)$$

The incremental version of the FSY scheme can be accomplished in three steps: the first two steps coincide with (3.18a) and (3.18b), whereas the third one becomes

3. Computation of the end-of-step velocity:

$$C_{ff}\mathbf{U}_f^{n+1} = C_{ff}\tilde{\mathbf{U}}_f^{n+1} - G_f(\mathbf{P}^{n+1} - \mathbf{P}^*) - C_{fS}(\mathbf{U}_S^{n+1} - \mathbf{U}_S^*). \quad (3.20)$$

The latter step differs from (3.18c) and is actually more expensive due to the presence of matrix C_{ff} .

When solving the FSI problem through the Yosida algorithm, at each time step we have to solve three linear systems, two of which (step 1 and 3) share the same matrix C_{ff} and can be solved by preconditioned Krylov methods (such as Bi-CGStab or GMRES) with incomplete LU preconditioner [127]. The linear system in step 2, common to the PIC scheme, is a little more critical (see Section 3.6) .

3.3.3 Predictor-corrector methods

The non-incremental version of pressure correction methods has led to new iterative algorithms for the solution of the monolithic fluid system (see [42]).

In this section, we consider using A_{PIC} and A_{FSY} as preconditioners for Richardson iterations. We deal with Richardson iterations for the sake of simplicity, but more efficient Krylov iterations could be considered. Using, e.g., A_{PIC} as preconditioner, we have to solve: given $\mathbf{X}^{n+1,k}$, find $\mathbf{X}^{n+1,k+1}$ such that

$$A_{PIC}\delta\mathbf{X}^{n+1,k+1} = \mathbf{b}^{n+1} - A\mathbf{X}^{n+1,k}, \quad k \geq 0,$$

until convergence. The operator $\delta\mathbf{X}^{n+1,k+1} = \mathbf{X}^{n+1,k+1} - \mathbf{X}^{n+1,k}$ denotes the backward increment at iteration $k+1$. We can also write this scheme in the fashion of (3.18). In this case, iteration $k+1$ of the predictor-corrector scheme consists in solving three different steps:

1. Computation of the intermediate velocity:

$$C_{ff}\tilde{\mathbf{U}}_f^{n+1,k+1} = \mathbf{b}_f^{n+1} - G_f\mathbf{P}^{n+1,k} - C_{fS}\mathbf{U}_S^{n+1,k}; \quad (3.21a)$$

2. Solution of the pressure-structure system:

$$\begin{aligned} & \begin{bmatrix} T_{pp} & T_{pS} \\ T_{Sp} & T_{SS} \end{bmatrix} \begin{bmatrix} \delta\mathbf{P}^{n+1,k+1} \\ \delta\mathbf{U}_S^{n+1,k+1} \end{bmatrix} = \\ & \begin{bmatrix} -D_f\tilde{\mathbf{U}}_f^{n+1,k+1} \\ \mathbf{b}_\sigma^{n+1} - C_{Sf}\tilde{\mathbf{U}}_f^{n+1,k+1} \end{bmatrix} - \begin{bmatrix} 0 & D_S \\ G_S & N_{SS} + C_{SS} \end{bmatrix} \begin{bmatrix} \mathbf{P}^{n+1,k} \\ \mathbf{U}_S^{n+1,k} \end{bmatrix}; \end{aligned} \quad (3.21b)$$

3. Computation of the end-of-step velocity:

$$\frac{1}{\delta t}M_{ff}\mathbf{U}_f^{n+1,k+1} = \frac{1}{\delta t}M_{ff}\tilde{\mathbf{U}}_f^{n+1,k+1} - G_f\delta\mathbf{P}^{n+1,k+1} - C_{fS}\delta\mathbf{U}_S^{n+1,k+1}. \quad (3.21c)$$

Similarly, taking as preconditioner A_{FSY} we get a different version of the predictor-corrector method, which shares step 1 and 2 with (3.21) but replaces (3.21c) with:

$$C_{ff}\mathbf{U}_f^{n+1,k+1} = C_{ff}\tilde{\mathbf{U}}_f^{n+1,k+1} - G_f\delta\mathbf{P}^{n+1,k+1} - C_{fS}\delta\mathbf{U}_S^{n+1,k+1}. \quad (3.22)$$

In a compact form, the predictor-corrector method based on the FSY algorithm reads: given $\mathbf{X}^{n+1,k}$, solve:

$$A_{FSY}\delta\mathbf{X}^{n+1,k+1} = \mathbf{b}^{n+1} - A\mathbf{X}^{n+1,k}$$

until convergence.

We can now see that the end-of-step velocity does not play any role in the iterative process, because $\mathbf{U}_f^{n+1,k}$ does not appear in the iteration $k + 1$. Therefore, (3.21c) (or (3.22) for FSU) can be disregarded without perturbing the convergence of the algorithm. The resulting predictor-corrector method reduces to (3.21a) and (3.21b) upon replacing $\tilde{\mathbf{U}}_f^{n+1,k+1}$ with $\mathbf{U}_f^{n+1,k+1}$. This is a preconditioned Richardson iteration with preconditioner L_{PIC} , that is:

$$L_{PIC}\delta\mathbf{X}^{n+1,k+1} = \mathbf{b}^{n+1} - A\mathbf{X}^{n+1,k}.$$

We remind that $L_{PIC} = L_{FSU}$.

The convergence of the predictor-corrector method is *added-mass independent*. Fluid and structure are not fully decoupled and we treat the added-mass effect implicitly. This is essential for the good convergence properties of the predictor-corrector iterative procedure when dealing with hemodynamics problems (see Section 4.3).

Predictor-corrector methods are particularly well suited when considering domain and/or convective terms in an implicit way. In this case, the FSI system has to be evaluated as many times as implicit iterations. Therefore, we can consider *one-loop algorithms*, i.e. dealing with implicit treatment and predictor-corrector iterations with only one external loop. One-loop algorithms were designed in [4] for aeroelastic applications. Therein, the predictor-corrector method dealt with the added-mass effect, because fluid and structure problems were fully decoupled (main difference with respect to the one suggested here).

Remark 3.10. *The preconditioners suggested in this section are based on approximation (3.15) for the Schur complements. Improved preconditioners, approximating also the effect of the convective and diffusive terms, have been successfully used for the numerical approximation of the Navier-Stokes equations (see [147, 51, 90]).*

Remark 3.11. *From the FSI system we can write the pressure-structure system:*

$$\begin{bmatrix} S_{pp} & S_{pS} \\ S_{Sp} & S_{SS} \end{bmatrix} \begin{bmatrix} \mathbf{P}^{n+1} \\ \mathbf{U}_S^{n+1} \end{bmatrix} = \begin{bmatrix} -D_f C_{ff}^{-1} \mathbf{b}_f^{n+1} \\ \mathbf{b}_S^{n+1} - C_{Sf} C_{ff}^{-1} \mathbf{b}_f^{n+1} \end{bmatrix}, \quad (3.23)$$

that is obtained upon formal elimination of the flow velocity \mathbf{U}_f^{n+1} . Our predictor-corrector method can be interpreted as a preconditioned Richardson iterative solver on (3.23) with preconditioner

$$\begin{bmatrix} T_{pp} & T_{pS} \\ T_{Sp} & T_{SS} \end{bmatrix}. \quad (3.24)$$

Needless to say, this pressure-structure Schur complement (3.24) can also serve as preconditioner for Krylov iterative solvers, such as GMRES.

Note that a single Richardson iteration for system (3.23) with preconditioner (3.24) differs from a Dirichlet-Neumann iteration applied directly on the original FSI system (3.4).

3.4 Comparison between inexact factorization-based methods and the projection scheme

In this section, we compare the projection-based coupling scheme in [55] with the semi-implicit procedures introduced in Section 3.3.

In [55], the Chorin-Temam method applied to the fluid problem leads to an algorithm that obtains the intermediate velocity using a prediction of the structure displacement, then, at a second step, it solves the end-of-step velocity and pressure coupled to the structure model. Furthermore, the load exerted by the fluid on the structure is computed in a peculiar residual way: the diffusive and convective terms of this fluid residual are evaluated using the intermediate velocity, whereas the time derivative using the end-of-step velocity. Since the fluid problem has been split at the continuous level (in space), only the normal component of the velocity can be imposed.

This approach could also be considered at the fully discrete level using a pressure correction method for the fluid problem obtained as an inexact factorization of the fluid matrix (see [115]). The main advantage of this approach is the fact that boundary conditions are accounted for intrinsically, allowing, e.g., to hold the continuity of velocities over the boundary. The discrete counterpart of the method suggested in [55] reads as:

- Step 1: intermediate velocity:

$$C_{ff}\tilde{\mathbf{U}}_f^{n+1} = \mathbf{b}_f^{n+1} - C_{fS}\tilde{\mathbf{U}}_S^{n+1}. \quad (3.25a)$$

- Step 2: end-of-step velocity & pressure-structure:

$$\begin{bmatrix} \frac{1}{\delta t}M_{ff} & G_f & \frac{1}{\delta t}M_{fS} \\ D_f & 0 & D_S \\ \frac{1}{\delta t}M_{Sf} & G_S & \frac{1}{\delta t}M_{SS} + N_{SS} \end{bmatrix} \begin{bmatrix} \mathbf{U}_f^{n+1} \\ \mathbf{P}^{n+1} \\ \mathbf{U}_S^{n+1} \end{bmatrix} = \begin{bmatrix} \frac{1}{\delta t}M_{ff}\tilde{\mathbf{U}}_f^{n+1} + \frac{1}{\delta t}M_{fS}\tilde{\mathbf{U}}_S^{n+1} \\ \mathbf{0} \\ \mathbf{b}_S^{n+1} - K_{Sf}\tilde{\mathbf{U}}_f^{n+1} - K_{SS}\tilde{\mathbf{U}}_S^{n+1} \end{bmatrix}, \quad (3.25b)$$

where $\tilde{\mathbf{U}}_S^{n+1}$ is computed by means of a second order extrapolation for the interface displacement, calculated at a step 0. In the second step, the diffusive and convective terms are treated explicitly, even for the interface velocity, and fluid velocity, pressure and structure unknowns are coupled.

The scheme (3.25) cannot be derived from an inexact factorization of the FSI system matrix in (3.9). In order to compare the discrete counterpart of the projection method in [55] with PIC and FSU schemes, we need to reformulate the second step and rearrange

(3.25) in a three step scheme. Through the Schur complements of the system matrix in (3.25b), it is possible to decouple the computation of \mathbf{U}_f^{n+1} from step 2. Then, after the first step (3.25a), the algorithm becomes:

- Step 2: solution of the coupled pressure-structure system:

$$\begin{bmatrix} T_{pp} & \hat{T}_{pS} \\ \hat{T}_{Sp} & \hat{T}_{SS} \end{bmatrix} \begin{bmatrix} \mathbf{P}^{n+1} \\ \mathbf{U}_S^{n+1} \end{bmatrix} = \begin{bmatrix} -D_f \tilde{\mathbf{U}}_f^{n+1} - D_f M_{ff}^{-1} M_{fS} \tilde{\mathbf{U}}_S^{n+1} \\ \mathbf{b}_S^{n+1} - K_{Sf} \tilde{\mathbf{U}}_f^{n+1} - K_{SS} \tilde{\mathbf{U}}_S^{n+1} \end{bmatrix}; \quad (3.26a)$$

- Step 3: computation of the end-of-step velocity:

$$\frac{1}{\delta t} M_{ff} \mathbf{U}_f^{n+1} = \frac{1}{\delta t} M_{ff} \tilde{\mathbf{U}}_f^{n+1} - G_f \mathbf{P}^{n+1} - \frac{1}{\delta t} M_{fS} (\mathbf{U}_S^{n+1} - \tilde{\mathbf{U}}_S^{n+1}). \quad (3.26b)$$

Matrices \hat{T}_{pS} , \hat{T}_{Sp} and \hat{T}_{SS} are further approximations of the approximated Schur complements (3.16), obtained by replacing $C_{\beta\gamma}$ with $\frac{1}{\delta t} M_{\beta\gamma}$ (see Section 3.2):

$$\begin{aligned} \hat{T}_{pS} &= D_S - D_f M_{ff}^{-1} M_{fS}, \\ \hat{T}_{Sp} &= G_S - M_{Sf} M_{ff}^{-1} G_f, \\ \hat{T}_{SS} &= \frac{1}{\delta t} M_{SS} + N_{SS} - \frac{1}{\delta t} M_{Sf} M_{ff}^{-1} M_{fS}. \end{aligned}$$

Let \mathcal{N}_S be the number of nodes of \mathcal{I}_h , the triangulation of the structure subdomain. Matrices $M_{SS}, K_{SS} \in \mathbb{R}^{\mathcal{N}_S \times \mathcal{N}_S}$ are defined as follows:

$$M_{SS} = \begin{bmatrix} M_{\sigma\sigma} & 0 \\ 0 & 0 \end{bmatrix}, \quad K_{SS} = \begin{bmatrix} K_{\sigma\sigma} & 0 \\ 0 & 0 \end{bmatrix}. \quad (3.27)$$

The algebraic counterpart of the semi-implicit projection algorithm in [55] shares step 1 with the other two methods (with zero-th order approximation for the pressure and a different first order approximation for the interface velocity) and like them at the second step it couples only the pressure term to the structure. Nonetheless, \mathbf{P}^{n+1} and \mathbf{U}_S^{n+1} are computed through a different, simplified, system. Also step 3 is simplified with respect to (3.18c): matrix C_{fS} is replaced by $\frac{1}{\delta t} M_{fS}$.

In particular, we remark the differences between the PIC method and algorithm (3.25a)-(3.26a)-(3.26b). The PIC scheme extends the inexact factorization of the algebraic Chorin-Temam method to the FSI system, while algorithm (3.25a)-(3.26a)-(3.26b) derives from the discretization of the differential Chorin-Temam method applied to the fluid only. For the latter, the coupling with the structure is given by the boundary condition at the second step of the Chorin-Temam scheme, whose differential form is:

$$\frac{1}{\delta t} (\mathbf{u}^{n+1} - \tilde{\mathbf{u}}^{n+1}) + \nabla p^{n+1} = 0, \quad \text{in } \Omega_{t^{n+1}}^f, \quad (3.28a)$$

$$\nabla \cdot \mathbf{u}^{n+1} = 0, \quad \text{in } \Omega_{t^{n+1}}^f, \quad (3.28b)$$

where these velocities over the interface hold:

$$\begin{aligned}\tilde{\mathbf{u}}^{n+1} &= \tilde{\mathbf{u}}_\sigma^{n+1}, \\ \mathbf{u}^{n+1} \cdot \mathbf{n}_f &= \mathbf{u}_\sigma^{n+1} \cdot \mathbf{n}_f.\end{aligned}$$

We indicate with \mathbf{u}_σ^{n+1} and $\tilde{\mathbf{u}}_\sigma^{n+1}$ the interface velocity and its prediction calculated at a step 0 of the scheme, respectively. By multiplying (3.28a) evaluated on Σ_t^{n+1} by \mathbf{n}_f , we obtain the boundary condition imposed over the pressure on the Dirichlet boundaries:

$$\frac{\partial p^{n+1}}{\partial \mathbf{n}_f} = -\frac{1}{\delta t} (\mathbf{u}_\sigma^{n+1} - \tilde{\mathbf{u}}_\sigma^{n+1}) \cdot \mathbf{n}_f. \quad (3.30)$$

The same boundary condition is imposed in a weak form by the PIC scheme.

As already said (Section 1.5.1), the matrix $D_f M_{ff}^{-1} G_f = -\frac{1}{\delta t} T_{pp}$ is sometimes referred to as *discrete Laplacian*, because of the analogies with the discretization of the Laplace operator. Another way to discretize the scheme proposed in [55] would be to replace $D_f M_{ff}^{-1} G_f$ at step 2 (3.26a) with the classical discretization of the Laplace operator.

3.4.1 Variations on the semi-implicit projection scheme

Let us consider some slight modifications of algorithm (3.25). First of all, we can handle the pressure term using the incremental version of the Chorin-Temam method for the fluid problem (first order approximation) in order to make the scheme less dissipative and improve its accuracy. Then, we can manipulate (3.25b) in order to decouple the computation of the end-of-step velocity from the pressure and structure unknowns. After rewriting it as:

$$\begin{aligned}-\delta t D_f M_{ff}^{-1} G_f (\mathbf{P}^{n+1} - \mathbf{P}^n) + (D_S - D_f M_{ff}^{-1} M_{fS}) \mathbf{U}_S^{n+1} &= \\ &= -D_f \tilde{\mathbf{U}}_f^{n+1} - D_f M_{ff}^{-1} M_{fS} \tilde{\mathbf{U}}_S^{n+1}, \\ \frac{1}{\delta t} M_{Sf} \mathbf{U}_f^{n+1} + G_S \mathbf{P}^{n+1} + \left(\frac{1}{\delta t} M_{SS} + N_{SS} \right) \mathbf{U}_S^{n+1} &= \mathbf{b}_S^{n+1} - K_{Sf} \tilde{\mathbf{U}}_f^{n+1} - K_{SS} \tilde{\mathbf{U}}_S^{n+1},\end{aligned}$$

we suggest to evaluate the stress of the fluid on the structure with the intermediate velocity. The resulting algorithm reads as follows:

1. Intermediate velocity:

$$C_{ff} \tilde{\mathbf{U}}_f^{n+1} = \mathbf{b}_f^{n+1} - G_f \mathbf{P}^n - C_{fS} \tilde{\mathbf{U}}_S^{n+1}; \quad (3.31a)$$

2. Pressure-structure problem:

$$\begin{aligned}-\delta t D_f M_{ff}^{-1} G_f (\mathbf{P}^{n+1} - \mathbf{P}^n) + (D_S - D_f M_{ff}^{-1} M_{fS}) \mathbf{U}_S^{n+1} &= \\ &= -D_f \tilde{\mathbf{U}}_f^{n+1} - D_f M_{ff}^{-1} M_{fS} \tilde{\mathbf{U}}_S^{n+1},\end{aligned} \quad (3.31b)$$

$$G_S \mathbf{P}^{n+1} + N_{SS} \mathbf{U}_S^{n+1} = \mathbf{b}_S^{n+1} - C_{Sf} \tilde{\mathbf{U}}_f^{n+1} - C_{SS} \tilde{\mathbf{U}}_S^{n+1}; \quad (3.31c)$$

3. End-of-step velocity:

$$\frac{1}{\delta t} M_{ff} \mathbf{U}_f^{n+1} = \frac{1}{\delta t} M_{ff} \tilde{\mathbf{U}}_f^{n+1} - G_f (\mathbf{P}^{n+1} - \mathbf{P}^n) - \frac{1}{\delta t} M_{fS} (\mathbf{U}_S^{n+1} - \tilde{\mathbf{U}}_S^{n+1}). \quad (3.31d)$$

The definition of C_{SS} is $C_{SS} = \frac{1}{\delta t} M_{SS} + K_{SS}$, where M_{SS} and K_{SS} are defined in (3.27).

The advantage of this new scheme with respect to (3.25a)-(3.26a)-(3.26b) is that the second equation of step 2 involves no Schur complement and is therefore easier (and cheaper) to solve. Again, matrix $D_f M_{ff}^{-1} G_f$ in (3.31b) might be replaced by the classical discretization of the Laplace operator, further simplifying step 2.

Method (3.31) couples implicitly only the pressure term, while the rest of the fluid load is treated explicitly. Then it is expected to be well suited for problems where the effect of the viscous stress exerted by the fluid on the structure is less important than the one of the pressure.

These modifications could also be considered at the continuous level. Instead of (3.31b), we would get the pressure from the classical pressure Poisson equation with boundary condition (3.30).

These variations on the semi-implicit scheme in [55] are proposed because of their simplicity and good properties but no numerical results on them are shown.

3.5 Analysis of the perturbation error

At every time step, the use of inexact factorization of the system matrix A by either PIC or FSU schemes perturbs the original FSI system. The solution of a semi-implicit *monolithic* algorithm, which solves the incremental FSI system (1.26) by, e.g., a global preconditioned GMRES, differs from the solutions of the PIC and FSU methods. This section is devoted to the identification of the perturbation terms introduced by the two schemes in order to infer the (formal) order of accuracy of the method in time. The results are confirmed by the numerical experiments in Section 4.3.2.

3.5.1 Perturbation terms for PIC schemes

Setting:

$$A_{PIC} = A + E_{PIC}$$

and subtracting A (3.9) from A_{PIC} (3.17), we can calculate the perturbation matrix E_{PIC} :

$$E_{PIC} = \delta t \begin{bmatrix} 0 & K_{ff} M_{ff}^{-1} G_f & K_{ff} M_{ff}^{-1} C_{fS} \\ 0 & 0 & 0 \\ 0 & 0 & 0 \end{bmatrix}.$$

The PIC scheme perturbs only the momentum conservation equation for the fluid, exactly like pressure correction methods do for fluid problems in rigid domains (see (1.31)). No approximation is introduced in the mass conservation equation and in the structure equation. Mass conservation is an excellent feature when considering problems with free surfaces or structures over fluid boundaries.

The incremental PIC scheme can be written as a monolithic system with a perturbed momentum equation:

$$C_{ff}\tilde{\mathbf{U}}_f^{n+1} + G_f\mathbf{P}^* + C_{fS}\mathbf{U}_S^* = \mathbf{b}_f^{n+1} + \mathbf{e}_{PIC}$$

with

$$\begin{aligned} \mathbf{e}_{PIC} &= -\delta t K_{ff} M_{ff}^{-1} G_f (\mathbf{P}^{n+1} - \mathbf{P}^*) - \delta t K_{ff} M_{ff}^{-1} C_{fS} (\mathbf{U}_S^{n+1} - \mathbf{U}_S^*) \\ &= -\delta t K_{ff} M_{ff}^{-1} G_f (\mathbf{P}^{n+1} - \mathbf{P}^*) - K_{ff} M_{ff}^{-1} M_{fS} (\mathbf{U}_S^{n+1} - \mathbf{U}_S^*) \\ &\quad + \delta t K_{ff} M_{ff}^{-1} K_{fS} (\mathbf{U}_S^{n+1} - \mathbf{U}_S^*). \end{aligned}$$

We have identified three different perturbation terms, one related to the pressure and two related to the structure velocity. Should \mathbf{P}^* be a q_p -th order approximation of \mathbf{P}^{n+1} , the pressure term is of order $\mathcal{O}(\delta t^{q_p+1})$. This perturbation term associated to the pressure is the same that affects the momentum conservation equation of pure fluid problems solved by pressure correction methods (see (1.32)). With regard to interface velocity terms, the one related to K_{fS} is of order $\mathcal{O}(\delta t^{q_S+1})$, being q_S the order of approximation of \mathbf{U}_S^* . However, we lose one order of accuracy in the term related to M_{fS} . Therefore, in order to get a first order PIC scheme, it is enough to take $\mathbf{P}^* = \mathbf{0}$ and $\mathbf{U}_S^* = \mathbf{U}_S^n$.

Numerical experiments for the fluid problem alone show that a zero-th order approximation for the pressure leads to splitting procedures that, even though first order in time, are plagued by severe numerical dissipation (see [38]). Hence, it is advised to use a first order pressure approximation $\mathbf{P}^* = \mathbf{P}^n$ for reducing drastically the numerical dissipation without increasing the CPU cost. In this case, the splitting error related to the pressure is second order in time.

Concluding, in (3.18) we choose $\mathbf{U}_S^* = \mathbf{U}_S^n$ in order to get the desired accuracy and $\mathbf{P}^* = \mathbf{P}^n$ in order to reduce the numerical dissipation. The numerical results that are shown in Section 4.3 are obtained with this incremental PIC scheme.

3.5.2 Perturbation terms for FSU schemes

In Section 1.5.2, we discussed the perturbation due to the application of the Yosida scheme for the numerical approximation of the Navier-Stokes equations. There, we introduced matrix Y (1.34). So far, we have considered the BDF1 scheme for the time discretization

of the fluid subproblem. Thus, for the FSI problem we redefine that matrix in the following way:

$$Y = \delta t^{-1} C_{ff}^{-1} - M_{ff}^{-1} = \mathcal{O}(\delta t),$$

Setting:

$$A_{FSY} = A + E_{FSY},$$

performing the matrix-product in (3.19) and subtracting A (3.9) from it, we obtain the following expression for the perturbation matrix:

$$E_{FSY} = \delta t \begin{bmatrix} 0 & 0 & 0 \\ 0 & D_f Y G_f & D_f Y C_{fS} \\ 0 & C_{Sf} Y G_S & C_{Sf} Y C_{fS} \end{bmatrix}.$$

Note that this time the perturbation affects both the mass conservation and structure equations, while PIC schemes only perturb the momentum conservation equation for the fluid. Like the Yosida scheme for pure fluid problems (see (1.35)), the FSY methods are “momentum preserving”. To identify the order of the perturbation errors we can write the FSY problem as a perturbed monolithic system. The perturbed mass conservation equation is:

$$D_f \mathbf{U}_f^{n+1} + D_S \mathbf{U}_S^{n+1} = \mathbf{e}_{FSY}^1$$

with

$$\begin{aligned} \mathbf{e}_{FSY}^1 &= -\delta t D_f Y G_f (\mathbf{P}^{n+1} - \mathbf{P}^*) - \delta t D_f Y C_{fS} (\mathbf{U}_S^{n+1} - \mathbf{U}_S^*) \\ &= -\delta t D_f Y G_f (\mathbf{P}^{n+1} - \mathbf{P}^*) - D_f Y M_{fS} (\mathbf{U}_S^{n+1} - \mathbf{U}_S^*) \\ &\quad - \delta t D_f Y K_{fS} (\mathbf{U}_S^{n+1} - \mathbf{U}_S^*). \end{aligned}$$

Whereas the pressure term is of order $\mathcal{O}(\delta t^{q_p+2})$, the structure term related to M_{fS} is $\mathcal{O}(\delta t^{q_s+1})$. Proceeding similarly for the structure equation, we get:

$$C_{Sf} \mathbf{U}_f^{n+1} + G_S \mathbf{P}^{n+1} + (N_{SS} + C_{SS}) \mathbf{U}_S^{n+1} = \mathbf{b}_S^{n+1} + \mathbf{e}_{FSY}^2$$

with

$$\mathbf{e}_{FSY}^2 = -\delta t C_{Sf} Y G_S (\mathbf{P}^{n+1} - \mathbf{P}^*) - \delta t C_{Sf} Y C_{fS} (\mathbf{U}_S^{n+1} - \mathbf{U}_S^*).$$

Expanding C_{Sf} and C_{fS} we can see that the order of accuracy of the pressure terms are $\mathcal{O}(\delta t^{q_p+1})$ and for the structure terms $\mathcal{O}(\delta t^{q_s})$.

According to the previous considerations, a first order FSY scheme should involve a zero-th order pressure approximation and a first order interface velocity approximation. In our numerical experiments (Section 4.3) for the first order FSY scheme we use $\mathbf{P}^* = \mathbf{P}^n$ and $\mathbf{U}_S^* = \mathbf{U}_S^n$, as for the first order PIC scheme. Again, the error related to the pressure in this case is second order in time but the one of the interface velocity is only first order.

3.6 The pressure-structure system

At every time step (or predictor-corrector iteration), all the methods presented in Section 3.3 evaluate the velocity field (at inner nodes) decoupled from the coupled structure and pressure fields, both for intermediate and end-of-step velocity. As already pointed out, the numerical complexity of those schemes lies in step 2, where the pressure is coupled to the structure velocity.

The system in step 2 has the form

$$\begin{bmatrix} T_{pp} & T_{pS} \\ T_{Sp} & T_{SS} \end{bmatrix} \begin{bmatrix} \mathbf{P}^{n+1} - \mathbf{P}^* \\ \mathbf{U}_S^{n+1} - \mathbf{U}_S^* \end{bmatrix} = \begin{bmatrix} \mathbf{b}_{2p}^{n+1} \\ \mathbf{b}_{2S}^{n+1} \end{bmatrix}, \quad (3.32)$$

where the force term depends on the method adopted and involves the intermediate velocity $\tilde{\mathbf{U}}_f^{n+1}$. Let us make some comments about the system matrix and how to solve system (3.32). The added-mass effect can only appear in (3.32), which is much smaller than the original FSI system (3.9). The coupling problem involves the solution of T , which is made of the approximated Schur complements.

In the next subsection, we prove a sufficient condition on the non-singularity of matrix T for a slightly simplified problem. In Sections 3.6.2 and 3.6.3, we present two different approaches for the solution of system (3.32), even though other methods, e.g. multigrid, could be considered.

3.6.1 The pressure-structure system matrix

We remark at first that (3.32) can be equivalently reformulated as:

$$T_{pp}(\mathbf{P}^{n+1} - \mathbf{P}^*) = \mathbf{b}_{2p}^{n+1} - T_{pS}(\mathbf{U}_S^{n+1} - \mathbf{U}_S^*), \quad (3.33a)$$

$$(T_{SS} - T_{Sp}T_{pp}^{-1}T_{pS})(\mathbf{U}_S^{n+1} - \mathbf{U}_S^*) = \mathbf{b}_{2S}^{n+1} - T_{Sp}T_{pp}^{-1}\mathbf{b}_{2p}^{n+1}, \quad (3.33b)$$

where, for instance, for the PIC and FSU schemes we have

$$\begin{aligned} \mathbf{b}_{2p}^{n+1} &= -D_f \tilde{\mathbf{U}}_f^{n+1} - D_S \mathbf{U}_S^*, \\ \mathbf{b}_{2S}^{n+1} &= \mathbf{b}_S^{n+1} - C_{Sf} \tilde{\mathbf{U}}_f^{n+1} - G_S \mathbf{P}^* - (N_{SS} + C_{SS}) \mathbf{U}_S^*. \end{aligned}$$

In order to simplify the proof of the non-singularity of system (3.32), we consider a low Reynolds regime and assume that the interface undergoes infinitesimal displacements. Then, the fluid can be described by the Stokes equations in a fixed domain, corresponding to the reference one Ω_0^f . The fluid domain being fixed, no ALE terms appear in the equations. Despite those assumptions, the main features of the coupled FSI problem are preserved. Being the domain fixed and since no confusion can arise, in the proof we omit the ‘‘hats’’ over the variables. In this way, we lighten the burden of notation.

We will provide in the next Proposition a sufficient condition that guarantees that matrix $T_{SS} - T_{Sp}T_{pp}^{-1}T_{pS}$ is positive definite. This will prove the existence and uniqueness of \mathbf{U}_S^{n+1} . Then, from (3.33a) we derive that \mathbf{P}^{n+1} exists and is unique too, since T_{pp} is symmetric, negative definite if the inf-sup condition is satisfied.

Proposition 3.1. *Suppose we are using quasi-uniform conforming meshes whose elements have maximum diameter h . We assume that, for a suitable positive constant C (to be introduced later),*

$$h^{1-\alpha} < \frac{1}{C} \frac{\rho_s}{\rho_f}, \quad \text{with } \alpha = \begin{cases} 0, & \text{if } \overline{\Omega_0^s} = \Sigma_0, \\ 1, & \text{if } \overline{\Omega_0^s} \neq \Sigma_0. \end{cases} \quad (3.34)$$

A sufficient condition for matrix $T_{SS} - T_{Sp}T_{pp}^{-1}T_{pS}$ to be positive definite is that the time step δt obey the following restriction:

$$\delta t \leq \delta t_{cr} = \frac{h^2}{C_I^2 \gamma_K} \left(-1 + \sqrt{\frac{h^{\alpha-1} \rho_s}{C} \frac{\rho_s}{\rho_f}} \right), \quad (3.35)$$

where γ_K is the continuity constant of the operator associated to $K_{\sigma f}$ (see Section 3.2) and C_I is the constant in the inverse inequality (see (3.36) below). Then, equation (3.33b) has a unique solution \mathbf{U}_S^{n+1} , system (3.32) is non-singular and the semi-implicit algorithms (3.18) and (3.18a)-(3.18b)-(3.20) are well defined.

Proof. Since, for all

$$\mathbf{D}_S = \begin{bmatrix} \mathbf{D}_\sigma \\ \mathbf{D}_s \end{bmatrix} \in \mathbb{R}^{\mathcal{N}_S}, \quad \text{with } \mathbf{D}_S \neq \mathbf{0},$$

we have that $-\mathbf{D}_S^T T_{Sp} T_{pp}^{-1} T_{pS} \mathbf{D}_S \geq 0, \forall t > 0$, being $T_{Sp} = (T_{pS})^T$, it suffices to prove that (3.34) and (3.35) are sufficient conditions for matrix T_{SS} to be positive definite. Arrays \mathbf{D}_σ and \mathbf{D}_s correspond to \mathbf{D}_σ^{n+1} and \mathbf{D}_s^{n+1} in (3.1a). The time step superscript is omitted for simplicity.

We consider:

$$\begin{aligned} \mathbf{D}_S^T T_{SS} \mathbf{D}_S &= \mathbf{D}_S^T (N_{SS} + C_{SS} - \delta t C_{Sf} M_{ff}^{-1} C_{fS}) \mathbf{D}_S \\ &= \begin{bmatrix} \mathbf{D}_\sigma^T & \mathbf{D}_s^T \end{bmatrix} \left(\begin{bmatrix} C_{\sigma\sigma} + N_{\sigma\sigma} & N_{\sigma s} \\ N_{s\sigma} & N_{ss} \end{bmatrix} - \delta t \begin{bmatrix} C_{\sigma f} \\ 0 \end{bmatrix} M_{ff}^{-1} \begin{bmatrix} C_{f\sigma} & 0 \end{bmatrix} \right) \begin{bmatrix} \mathbf{D}_\sigma \\ \mathbf{D}_s \end{bmatrix} \\ &= \mathbf{D}_\sigma^T (C_{\sigma\sigma} + N_{\sigma\sigma} - \delta t C_{\sigma f} M_{ff}^{-1} C_{f\sigma}) \mathbf{D}_\sigma + \mathbf{D}_s^T N_{s\sigma} \mathbf{D}_\sigma + \mathbf{D}_\sigma^T N_{\sigma s} \mathbf{D}_s + \mathbf{D}_s^T N_{ss} \mathbf{D}_s. \end{aligned}$$

Let us focus on the first term and define $T_{\sigma\sigma} = C_{\sigma\sigma} + N_{\sigma\sigma} - \delta t C_{\sigma f} M_{ff}^{-1} C_{f\sigma}$. We have

$$\mathbf{D}_\sigma^T T_{\sigma\sigma} \mathbf{D}_\sigma = \mathbf{D}_\sigma^T \left(\frac{1}{\delta t} M_{\sigma\sigma} + \frac{1}{\delta t} \frac{\rho_s}{\rho_f} M_{\sigma\sigma}^s + A_{\sigma\sigma} - \delta t C_{\sigma f} M_{ff}^{-1} C_{f\sigma} \right) \mathbf{D}_\sigma,$$

where matrix $A_{\sigma\sigma}$ is defined as follows:

$$A_{\sigma\sigma} = K_{\sigma\sigma} + \frac{\delta t}{\rho_f} F_{\sigma\sigma}.$$

Multiplying both sides by δt , we find:

$$\delta t \mathbf{D}_\sigma^T T_{\sigma\sigma} \mathbf{D}_\sigma = \frac{\rho^s}{\rho_f} \|\boldsymbol{\eta}_{\sigma,h}\|_{L^2(\Sigma_0)}^2 + \|\mathcal{E}_h \boldsymbol{\eta}_{\sigma,h}\|_{L^2(\Omega_0^f)}^2 + \delta t \mathbf{D}_\sigma^T A_{\sigma\sigma} \mathbf{D}_\sigma - \delta t^2 \mathbf{D}_\sigma^T C_{\sigma f} M_{ff}^{-1} C_{f\sigma} \mathbf{D}_\sigma,$$

where $\boldsymbol{\eta}_{\sigma,h}$ is the finite element approximation of the interface displacement. For geometric conforming meshes $\mathcal{E}_h \boldsymbol{\psi}_i^\sigma = \boldsymbol{\phi}_i^\sigma$, for $i \in \mathcal{N}_\sigma$. Then, $\mathcal{E}_h \boldsymbol{\eta}_{\sigma,h} = \sum_{i \in \mathcal{N}_\sigma} \eta_i \boldsymbol{\phi}_i^\sigma$ and matrix $M_{\sigma\sigma}$ is symmetric and associated to a scalar product:

$$\mathbf{D}_\sigma^T M_{\sigma\sigma} \mathbf{D}_\sigma = \|\mathcal{E}_h \boldsymbol{\eta}_{\sigma,h}\|_{L^2(\Omega_0^f)}^2.$$

For matrix $A_{\sigma\sigma}$ we have:

$$\mathbf{D}_\sigma^T A_{\sigma\sigma} \mathbf{D}_\sigma = \mathbf{D}_\sigma^T K_{\sigma\sigma} \mathbf{D}_\sigma + \frac{\delta t}{\rho_f} \mathbf{D}_\sigma^T F_{\sigma\sigma} \mathbf{D}_\sigma \geq \alpha_K \|\mathcal{E}_h \boldsymbol{\eta}_{\sigma,h}\|_{H^1(\Omega_0^f)}^2 + \alpha_F \frac{\delta t}{\rho_f} \|\boldsymbol{\eta}_{\sigma,h}\|_{H^1(\Sigma_0)}^2,$$

where α_K and α_F are the coercivity constants of the operators associated respectively to $K_{\sigma\sigma}$ and $F_{\sigma\sigma}$.

Set the array

$$\mathbf{U} = M_{ff}^{-1} C_{f\sigma} \mathbf{D}_\sigma,$$

whose length is equal to the number of inner fluid nodes. Then:

$$\begin{aligned} \mathbf{D}_\sigma^T C_{\sigma f} \mathbf{U} &= \mathbf{D}_\sigma^T \left(\frac{1}{\delta t} M_{\sigma f} + K_{\sigma f} \right) \mathbf{U} = \frac{1}{\delta t} \mathbf{D}_\sigma^T M_{\sigma f} \mathbf{U} + \mathbf{D}_\sigma^T K_{\sigma f} \mathbf{U} \\ &\leq \frac{1}{\delta t} \|\mathcal{E}_h \boldsymbol{\eta}_{\sigma,h}\|_{L^2(\Omega_0^f)} \|\mathbf{u}_h\|_{L^2(\Omega_0^f)} + \gamma_K \|\mathcal{E}_h \boldsymbol{\eta}_{\sigma,h}\|_{H^1(\Omega_0^f)} \|\mathbf{u}_h\|_{H^1(\Omega_0^f)} \\ &\leq \left(\frac{1}{\delta t} + \frac{C_I^2 \gamma_K}{h^2} \right) \|\mathcal{E}_h \boldsymbol{\eta}_{\sigma,h}\|_{L^2(\Omega_0^f)} \|\mathbf{u}_h\|_{L^2(\Omega_0^f)}, \end{aligned}$$

where γ_K is the continuity constant of the operator associated to $K_{\sigma f}$, and C_I is the constant showing up in the following inverse inequality:

$$\|\mathbf{v}_h\|_{H^1(\Omega_0^f)} \leq C_I h^{-1} \|\mathbf{v}_h\|_{L^2(\Omega_0^f)}, \quad \forall \mathbf{v}_h \in V_h^f, \quad (3.36)$$

that holds under the assumption that the triangulation in Ω_0^f is quasi-uniform. By \mathbf{u}_h we denote the finite element approximation associated to \mathbf{U} .

Since $C_{f\sigma} \mathbf{D}_\sigma = M_{ff} \mathbf{U}$, it follows that

$$\mathbf{D}_\sigma^T C_{\sigma f} = \mathbf{U}^T M_{ff}$$

and so:

$$\left(\frac{h^2 + C_I^2 \gamma_K \delta t}{h^2 \delta t}\right) \|\mathcal{E}_h \boldsymbol{\eta}_{\sigma,h}\|_{L^2(\Omega_0^f)} \|\mathbf{u}_h\|_{L^2(\Omega_0^f)} \geq \mathbf{D}_\sigma^T C_{\sigma f} \mathbf{U} = \mathbf{U}^T M_{ff} \mathbf{U} = \|\mathbf{u}_h\|_{L^2(\Omega_0^f)}^2.$$

Therefore, we get

$$\|\mathbf{u}_h\|_{L^2(\Omega_0^f)} \leq \left(\frac{h^2 + C_I^2 \gamma_K \delta t}{h^2 \delta t}\right) \|\mathcal{E}_h \boldsymbol{\eta}_{\sigma,h}\|_{L^2(\Omega_0^f)}.$$

Lemma 1 in [55] states that, for $H = h$,

$$\|\mathcal{E}_h \boldsymbol{\eta}_{\sigma,h}\|_{L^2(\Omega_0^f)}^2 \leq C h^{1-\alpha} \|\boldsymbol{\eta}_{\sigma,h}\|_{L^2(\Sigma_0)}^2, \quad \forall \boldsymbol{\eta}_{\sigma,h} \in V_h^\sigma, \quad (3.37)$$

where α is defined in (3.34), $C > 0$ is a mesh-independent constant, and V_h^σ is the finite element space approximating $(H^1(\Sigma_0))^d$. Then, we have:

$$\begin{aligned} \delta t \mathbf{D}_\sigma^T T_{\sigma\sigma} \mathbf{D}_\sigma &\geq \frac{\rho_s}{\rho_f} \|\boldsymbol{\eta}_{\sigma,h}\|_{L^2(\Sigma_0)}^2 + \|\mathcal{E}_h \boldsymbol{\eta}_{\sigma,h}\|_{L^2(\Omega_0^f)}^2 \\ &+ \delta t \left(\alpha_K \|\mathcal{E}_h \boldsymbol{\eta}_{\sigma,h}\|_{H^1(\Omega_0^f)}^2 + \alpha_F \frac{\delta t}{\rho_f} \|\boldsymbol{\eta}_{\sigma,h}\|_{H^1(\Sigma_0)}^2 \right) - \delta t \mathbf{D}_\sigma^T (M_{\sigma f} + \delta t K_{\sigma f}) \mathbf{U} \\ &\geq \frac{\rho_s}{\rho_f} \|\boldsymbol{\eta}_{\sigma,h}\|_{L^2(\Sigma_0)}^2 + \|\mathcal{E}_h \boldsymbol{\eta}_{\sigma,h}\|_{L^2(\Omega_0^f)}^2 + \delta t \left(\alpha_K \|\mathcal{E}_h \boldsymbol{\eta}_{\sigma,h}\|_{H^1(\Omega_0^f)}^2 \right. \\ &+ \left. \alpha_F \frac{\delta t}{\rho_f} \|\boldsymbol{\eta}_{\sigma,h}\|_{H^1(\Sigma_0)}^2 \right) - \delta t \left(1 + \delta t \frac{C_I^2 \gamma_K}{h^2} \right) \|\mathcal{E}_h \boldsymbol{\eta}_{\sigma,h}\|_{L^2(\Omega_0^f)} \|\mathbf{u}_h\|_{L^2(\Omega_0^f)} \\ &\geq \frac{\rho_s}{\rho_f} \|\boldsymbol{\eta}_{\sigma,h}\|_{L^2(\Sigma_0)}^2 + \|\mathcal{E}_h \boldsymbol{\eta}_{\sigma,h}\|_{L^2(\Omega_0^f)}^2 + \delta t \left(\alpha_K \|\mathcal{E}_h \boldsymbol{\eta}_{\sigma,h}\|_{H^1(\Omega_0^f)}^2 \right. \\ &+ \left. \alpha_F \frac{\delta t}{\rho_f} \|\boldsymbol{\eta}_{\sigma,h}\|_{H^1(\Sigma_0)}^2 \right) - \left(\frac{h^2 + C_I^2 \gamma_K \delta t}{h^2} \right)^2 C h^{1-\alpha} \|\boldsymbol{\eta}_{\sigma,h}\|_{L^2(\Sigma_0)}^2 \\ &\geq \left[\frac{\rho_s}{\rho_f} - \frac{C}{h^{3+\alpha}} (h^2 + C_I^2 \gamma_K \delta t)^2 \right] \|\boldsymbol{\eta}_{\sigma,h}\|_{L^2(\Sigma_0)}^2 + \|\mathcal{E}_h \boldsymbol{\eta}_{\sigma,h}\|_{L^2(\Omega_0^f)}^2 \\ &+ \delta t \left(\alpha_K \|\mathcal{E}_h \boldsymbol{\eta}_{\sigma,h}\|_{H^1(\Omega_0^f)}^2 + \alpha_F \frac{\delta t}{\rho_f} \|\boldsymbol{\eta}_{\sigma,h}\|_{H^1(\Sigma_0)}^2 \right). \end{aligned}$$

Hence, we have:

$$\begin{aligned} \delta t \mathbf{D}_S^T T_{SS} \mathbf{D}_S &\geq \left[\frac{\rho_s}{\rho_f} - \frac{C}{h^{3+\alpha}} (h^2 + C_I^2 \gamma_K \delta t)^2 \right] \|\boldsymbol{\eta}_{\sigma,h}\|_{L^2(\Sigma_0)}^2 + \|\mathcal{E}_h \boldsymbol{\eta}_{\sigma,h}\|_{L^2(\Omega_0^f)}^2 \\ &+ \delta t \left(\alpha_K \|\mathcal{E}_h \boldsymbol{\eta}_{\sigma,h}\|_{H^1(\Omega_0^f)}^2 + \alpha_F \frac{\delta t}{\rho_f} \|\boldsymbol{\eta}_{\sigma,h}\|_{H^1(\Sigma_0)}^2 \right) \\ &+ 2 \mathbf{D}_\sigma^T N_{\sigma s} \mathbf{D}_s + \alpha_N \|\boldsymbol{\eta}_{s,h}\|_{L^2(\Omega_0^s)}, \end{aligned}$$

α_N being the coercivity constant of the operator associated to N_{ss} . With $\boldsymbol{\eta}_{s,h}$ we indicate the finite element approximation of the displacement in $\Omega_0^s \setminus \Sigma_0$. To simplify the calculations, since the last four terms are positive, we impose the first one to be positive too, that is:

$$\frac{\rho_s}{\rho_f} - \frac{C}{h^{3+\alpha}} (h^2 + C_I^2 \gamma_K \delta t)^2 > 0. \quad (3.38)$$

This is a more restrictive condition. We calculate the critical time steps:

$$\delta t_{cr}^{1,2} = \frac{h^2}{C_I^2 \gamma_K} \left(-1 \pm \sqrt{\frac{h^{\alpha-1} \rho_s}{C \rho_f}} \right).$$

One of the two critical time steps must be positive, so we get a restriction on the densities ratio:

$$\frac{\rho_s}{\rho_f} > \frac{C}{h^{\alpha-1}},$$

which can however be regarded as a restriction on the mesh-size h if $\alpha \neq 1$, see (3.34).

From (3.38) it follows that, under condition (3.34), matrix T_{SS} is positive definite for

$$\delta t \leq \delta t_{cr} = \frac{h^2}{C_I^2 \gamma_K} \left(-1 + \sqrt{\frac{h^{\alpha-1} \rho_s}{C \rho_f}} \right).$$

This proves our Proposition. □

Remark 3.12. *In order to simplify the proof of the non-singularity of system (3.32), we derived two conditions on mesh-size and time step ((3.34) and (3.35), respectively) which are more restrictive than what would be necessary.*

Numerical evidence suggests that matrix $T_{SS} - T_{Sp}T_{pp}T_{pS}$ is positive definite for all the physical and discrete parameters we tested, also when the convective term is taken into account to model the fluid motion.

Remark 3.13. *In view of our previous results, for $\delta t \leq \delta t_{cr}$, matrix T is indefinite, however its eigenvalues are real with variable sign. System (3.32) has therefore a unique solution.*

3.6.2 Losing modularity

Modularity is the property of a solver to consist of separated modules and it is typical of *partitioned* procedures, which solve the fluid and the structure with two different codes.

A first and natural approach to solve system (3.32) would consist in adopting a matrix-free method (GMRES or BiCGStab, for example), which prevents us from assembling T . Despite the fact that the matrix is not assembled, this approach is non-modular because the system solver needs to access the fluid and structure matrices in the respective codes. Matrix T is ill-conditioned, with condition number $\kappa(T) = C_T h^{-2}$. An iterative solver applied to the non-preconditioned system (3.32) will exhibit slow convergence. Then, a preconditioner is mandatory.

The choice of a good preconditioner for T is not trivial. The computation of the ILU preconditioner would require the evaluation of the elements of T . Hence, it is too expensive

for real applications and does not make much sense, since we want to avoid to assemble T . In the simulation of the carotid bifurcation (Sec. 5.6), we employed two preconditioners: the point-diagonal and the block-diagonal one. The former proves to be cheaper in terms of CPU time (see Fig. 5.14(b)).

However, for simplified problems (like the one presented in Chapter 4), the assembling of matrix T might not be too expensive. It is only feasible when the mass matrix is diagonal, otherwise the assembling of the Schur complements is not affordable. In case of using non-matching grids and a L^2 -projection, the inverse mass matrix that will appear should be diagonal too. Once matrix T is assembled, we are able to use a classical preconditioner (such as $ILU(q)$) together with an iterative solver.

3.6.3 Keeping modularity

When solving system (3.32) by a Krylov iterative solver such as GMRES the key point is how to choose a good preconditioner in order to keep modularity. In [56], a preconditioned GMRES is used for solving every tangent system of the Newton method.

Problem (3.32) can be reformulated as an interface equation. First of all, we rewrite it expanding \mathbf{U}_S^{n+1} in the interface and inner structure components

$$\begin{bmatrix} T_{pp} & T_{p\sigma} & 0 \\ T_{\sigma p} & T_{\sigma\sigma} & N_{\sigma s} \\ 0 & N_{s\sigma} & N_{ss} \end{bmatrix} \begin{bmatrix} \mathbf{P}^{n+1} \\ \mathbf{U}_\sigma^{n+1} \\ \mathbf{U}_s^{n+1} \end{bmatrix} = \begin{bmatrix} \mathbf{b}_{2p}^{n+1} \\ \mathbf{b}_{2\sigma}^{n+1} \\ \mathbf{b}_s^{n+1} \end{bmatrix}.$$

Then, by means of Schur complements, we write the interface problem

$$(T_{\sigma\sigma} - T_{\sigma p} T_{pp}^{-1} T_{p\sigma} - N_{\sigma s} N_{ss}^{-1} N_{s\sigma}) \mathbf{U}_\sigma^{n+1} = \mathbf{b}_{2\sigma}^{n+1} - T_{\sigma p} T_{pp}^{-1} \mathbf{b}_{2p}^{n+1} - N_{\sigma s} N_{ss}^{-1} \mathbf{b}_s^{n+1}. \quad (3.39)$$

Also in this case, the system matrix is ill-conditioned, with a condition number of order h^{-1} . Thus, an optimal preconditioner must be used in (3.39). In order to keep modularity, this preconditioner can only involve structure (or fluid) terms. A classical choice is to take

$$\tilde{N}_\sigma = N_{\sigma\sigma} - N_{\sigma s} N_{ss}^{-1} N_{s\sigma}$$

as preconditioner for the system matrix in (3.39). This is the so-called *Dirichlet-Neumann* preconditioner, and gives rise to the Dirichlet-Neumann iterative method. It can be proved that this preconditioner is optimal with respect to h (see [120]). The preconditioned Richardson system is:

$$\begin{aligned} \left(I + \tilde{N}_\sigma^{-1} C_{\sigma\sigma} - \delta t \tilde{N}_\sigma^{-1} C_{\sigma f} M_{ff}^{-1} C_{f\sigma} - \tilde{N}_\sigma^{-1} T_{\sigma p} T_{pp}^{-1} T_{p\sigma} \right) \mathbf{U}_\sigma^{n+1} = \\ \tilde{N}_\sigma^{-1} \mathbf{b}_{2\sigma}^{n+1} - \tilde{N}_\sigma^{-1} T_{\sigma p} T_{pp}^{-1} \mathbf{b}_{2p}^{n+1} - \tilde{N}_\sigma^{-1} N_{\sigma s} N_{ss}^{-1} \mathbf{b}_s^{n+1}, \end{aligned} \quad (3.40)$$

and its convergence rate is therefore independent of h .

However, even though the spectral properties of the preconditioned matrix $\tilde{N}_\sigma^{-1}T_{\sigma p}T_{pp}^{-1}T_{p\sigma}$ are mesh size independent, its spectral radius involves a relationship between structure and fluid physical parameters, becoming ill-conditioned when the added-mass effect is critical. When the *weight* of this matrix is small, the convergence properties of iterative procedures are good, while the convergence is slow or (for Richardson iterations) impossible in presence of a strong added-mass effect.

Using a matrix-free iterative solver, we must evaluate a matrix-vector product at every iteration. Given a test vector \mathbf{Z} , we have to compute:

$$\tilde{N}_\sigma^{-1} (T_{\sigma\sigma} - T_{\sigma p}T_{pp}^{-1}T_{p\sigma} - N_{\sigma s}N_{ss}^{-1}N_{s\sigma}) \mathbf{Z},$$

that is the solution \mathbf{W} of

$$\tilde{N}_\sigma \mathbf{W} = (T_{\sigma\sigma} - T_{\sigma p}T_{pp}^{-1}T_{p\sigma} - N_{\sigma s}N_{ss}^{-1}N_{s\sigma}) \mathbf{Z}.$$

We can rewrite this system as

$$T_{pp} \mathbf{R} = T_{p\sigma} \mathbf{Z}, \quad (3.41a)$$

$$\tilde{N}_\sigma \mathbf{W} = \tilde{N}_\sigma \mathbf{Z} + (C_{\sigma\sigma} - \delta t C_{\sigma f} M_{ff}^{-1} C_{f\sigma}) \mathbf{Z} - T_{\sigma p} \mathbf{R}. \quad (3.41b)$$

From (3.41), it is easily grasped why this preconditioner has been called Dirichlet-Neumann. At the first step, where we evaluate the auxiliary array \mathbf{R} (with the dimension of the pressure array), we are solving the pressure Schur complement associated to a Dirichlet fluid problem. The second step consists of a Neumann structure problem with the updated value of the pressure. Then, we are keeping modularity, and appropriate solvers can be used separately for the solution of every field (pressure and structure).

Let us make some further comments about how to solve the fluid (3.41a) and structure (3.41b) subproblems. For the fluid one:

$$T_{pp} \mathbf{R} = -\delta t D_f M_{ff}^{-1} G_f \mathbf{R} = T_{p\sigma} \mathbf{Z}, \quad (3.42)$$

we can use a matrix-free iterative solver and avoid the assembling of the matrices involving the inverse mass matrix. Anyway, it is much more appealing in terms of CPU cost to build T_{pp} with a non-diagonal matrix and solve (3.42) using an appropriate solver.

A matrix-free solver can also be used for the structure subproblem to avoid the assembling of the structure Schur complement \tilde{N}_σ . By introducing another auxiliary array \mathbf{V} , we switch from the interface equation (3.41b) to a structure problem

$$\begin{aligned} N_{ss} \mathbf{V} + N_{s\sigma} (\mathbf{W} - \mathbf{Z}) &= \mathbf{0}, \\ N_{\sigma s} \mathbf{V} + N_{\sigma\sigma} (\mathbf{W} - \mathbf{Z}) &= (C_{\sigma\sigma} - \delta t C_{\sigma f} M_{ff}^{-1} C_{f\sigma}) \mathbf{Z} - T_{\sigma p} \mathbf{R}. \end{aligned}$$

Further details on the Dirichlet-Neumann preconditioner can be found in Section 5.3. Numerical experiments to compare the approaches reported in Sections 3.6.2 and 3.6.3 are carried out in Section 5.5 and 5.6.

Chapter 4

Application of the methods based on inexact factorization to blood flow in large arteries

4.1 Introduction

In this chapter we analyze the numerical behavior of the coupling schemes illustrated in Chapter 3. To this purpose, we consider a problem which models the interaction between an incompressible fluid and a thin elastic tube. This is the typical situation arising in the simulation of blood flow in large arteries. In fact, we aim at reproducing, in an idealized framework, the interaction between the blood and the arterial wall. However, all the methods presented in Section 3.3 can be adopted for other fluid-structure applications.

The test problem we consider is the $2d$ benchmark proposed in [60]. The simplified blood flow problem couples the $2d$ incompressible Navier-Stokes equations for the fluid with the so called *generalized string model* ($1d$, see Section 4.2.1) for the structure. An overpressure is applied at the inlet of the fluid for a short duration of time to simulate the heart beat. Although the fluid is modeled as incompressible, there is a finite velocity propagation of the overpressure due to the fluid-structure coupling, as shown in Section 4.3.6.

We let the physical parameters take the values in the physiological range. Thus, the FSI problem under consideration is characterized by a large added mass effect. Since all the procedures we introduced in Section 3.3 are semi-implicit, we first check the convergence in time of a semi-implicit method to the corresponding implicit one (Section 4.3.1). We study the accuracy of PIC and FSU algorithms in Section 4.3.2. In Section 4.3.3, we compute the splitting error for the FSU method. Then, we let the structure density vary in order to understand how the predictor-corrector methods (Section 4.3.4) and the pressure-structure

system (Section 4.3.5) are affected by the added-mass effect. Finally, all the tests performed on the semi-implicit methods we introduced allow us to draw some preliminary conclusions in Section 4.4.

4.2 Blood Flow in Large Arteries

We consider a portion of a blood flow vessel that occupies at time t a region denoted by Ω_t . The interior of the vessel is called *lumen*, through which blood flows. Thus, this part of Ω_t corresponds to Ω_t^f . The lumen is surrounded by three layers of tissue called *intima*, *media*, and *adventitia*, which form the artery wall (Ω_t^s). In Figure 4.1, we report the anatomy of an artery and the corresponding simplified representation for the mathematical modelling of the blood flow. The mathematical domain is delimited by the sections \mathcal{S}_{in} and \mathcal{S}_{out} , which connect the vessel to the rest of the system. More precisely, through \mathcal{S}_{in} , the upstream section, and \mathcal{S}_{out} , the downstream one, the fluid enters and leaves Ω_t , respectively. In hemodynamics, those sections are also called *proximal* and *distal*, to indicate that one is nearer and the other further with respect to the heart.

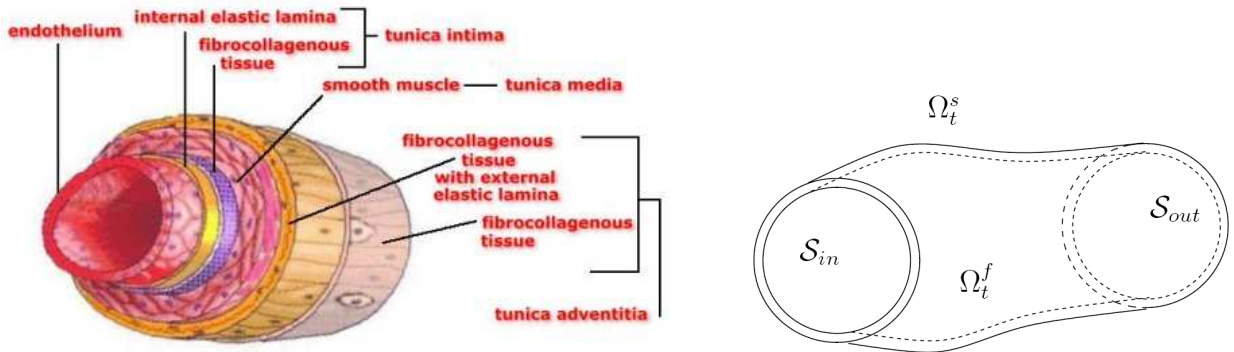


Figure 4.1: Anatomy of an artery and its simplified representation for the mathematical modelling of the blood-vessel system.

Blood is composed of blood cells suspended in a liquid called blood plasma. Plasma, which constitutes 55% of blood fluid, is mostly water (90% by volume), and contains dissolved proteins, glucose, mineral ions, hormones, carbon dioxide, platelets and blood cells themselves. The blood cells present in blood are mainly red blood cells and white blood cells. We do not consider the microscopic composition of blood and model it as a homogeneous and incompressible fluid. Moreover, in large arteries (i.e., those whose diameter is roughly larger than 0.2 cm) blood can be assumed to behave as a Newtonian fluid [94, 152], while in small vessel and capillaries its rheology is more complex. Thus,

we describe the blood motion through the Navier-Stokes equations. Since the deformation of the arterial wall are quite large, the fluid equations are treated in ALE framework (2.13a)-(2.13b).

Neither the complex microscopic structure of the vessel wall is taken into account. The arterial wall is merely represented as an elastic medium. In this chapter, we limit our attention to a very simple model derived for a cylindrical configuration. The next subsection is devoted to the description of the model.

In modelling the arterial wall as purely elastic we are neglecting an important characteristics: the porosity. We will consider this aspect of the vessel structure in Chapter 6, where we adopt a poroelastic model instead of an elastic one.

4.2.1 A generalized string model

Let

$$\Sigma_0 = \{(r, \theta, x) : r = R_0, 0 \leq x \leq L, 0 \leq \theta \leq 2\pi\}$$

be a cylindrical reference surface of radius R_0 . We neglect the longitudinal and angular displacement, while the radial displacement $\eta = \eta(t, \theta, x)$ satisfies

$$\rho_s h_s \frac{\partial^2 \eta}{\partial t^2} - k G h_s \frac{\partial^2 \eta}{\partial x^2} + \frac{E h_s}{1 - \nu^2} \frac{\eta}{R_0^2} - \gamma \frac{\partial^3 \eta}{\partial x^2 \partial t} = f_\Sigma(t, \theta, x). \quad (4.1)$$

Here, x indicates the axial direction (see Fig. 4.2), h_s is the wall thickness, k is the so called Timoshenko shear correction factor, G , E and ν are respectively the shear modulus, the Young modulus and the Poisson ratio, while γ is a viscoelastic parameter. Finally $f_\Sigma(t, \theta, x)$ is an external forcing term. The term $k G h_s \frac{\partial^2 \eta}{\partial x^2}$ accounts for shear deformations, while $\gamma \frac{\partial^3 \eta}{\partial x^2 \partial t}$ introduces the viscoelastic behavior. Another way to understand a term in the form $k G h_s \frac{\partial^2 \eta}{\partial x^2}$ is that it accounts for longitudinal pre-stress (i.e. at the equilibrium position) in the arterial wall. Indeed, in physiological conditions, arteries experience a longitudinal pre-stress and parameter $k G h_s$ represents the longitudinal tension at rest.

Model (4.1), called *generalized string*, has been widely used in many works devoted to blood flows (see, for instance, [118, 114]). Basically, it derives from the equations of linear elasticity for a cylindrical tube of small thickness, under the hypotheses of plane stress and membrane deformations (i.e. negligible elastic bending terms). Equation (4.1) must be supplemented with boundary conditions. The conditions $\eta = 0$ at $x = 0$ and $x = L$ (L being the length of the portion of vessel under consideration), corresponding to clamped wall ends, are not realistic in the blood flow context. Since the structural model is of

propagative type, first order absorbing boundary conditions are a better choice:

$$\begin{aligned}\frac{\partial \eta}{\partial t} - \sqrt{\frac{kG}{\rho_s}} \frac{\partial \eta}{\partial x} &= 0 \text{ at } x = 0, \\ \frac{\partial \eta}{\partial t} + \sqrt{\frac{kG}{\rho_s}} \frac{\partial \eta}{\partial x} &= 0 \text{ at } x = L.\end{aligned}$$

Other simpler structure models can be derived from (4.1) by neglecting some terms. By neglecting the viscoelastic term and the term with the second derivative in x , we obtain the so called *independent ring* model:

$$\rho_s h_s \frac{\partial^2 \eta}{\partial t^2} + \frac{E h_s}{1 - \nu^2} \frac{\eta}{R_0^2} = p - p_{ext},$$

where p is the fluid pressure. This model has been adopted in [109, 81], for instance. If we further neglect the inertia term, we obtain the simple algebraic relation

$$\frac{E h_s}{1 - \nu^2} \frac{\eta}{R_0^2} = p - p_{ext},$$

which is widely used to derive simplified monodimensional models for the circulatory system (see, e.g., [124, 150]).

4.2.2 A simplified 2D problem

We want to simulate the propagation of a pressure pulse coming from the heart in a straight artery of length L . To this purpose, we adopt a $2d$ model obtained by intersecting a portion of blood flow vessel Ω_t^f (Fig. 4.1, on the right) with a plane, see Fig. 4.2. The $2d$ problem arises from the combination of the $2d$ Navier-Stokes equations for the fluid with the generalized string model (4.1) to describe the motion of the upper and lower boundaries.

The initial domain is a rectangle of height $H = 1$ cm and length $L = 6$ cm, whose upper and lower edges are deformable in the vertical direction. The fluid and structure physical parameters used in the simulation have been listed in Table 4.1. These parameters have been chosen in the physiological range for a human body. Note that the values of ρ_s and ρ_f are very close.

On the inflow section \mathcal{S}_{in} we impose the following Neumann boundary condition:

$$\boldsymbol{\sigma}_{in}^f \cdot \mathbf{n} = -\frac{P_{in}}{2} \left[1 - \cos \left(\frac{\pi t}{2.5 \cdot 10^{-3}} \right) \right] \mathbf{n}, \quad (4.2)$$

while on the outflow section \mathcal{S}_{out} a homogeneous Neumann condition has been imposed. The amplitude P_{in} of the pressure pulse has been taken equal to $2 \cdot 10^4$ dynes/cm² and the

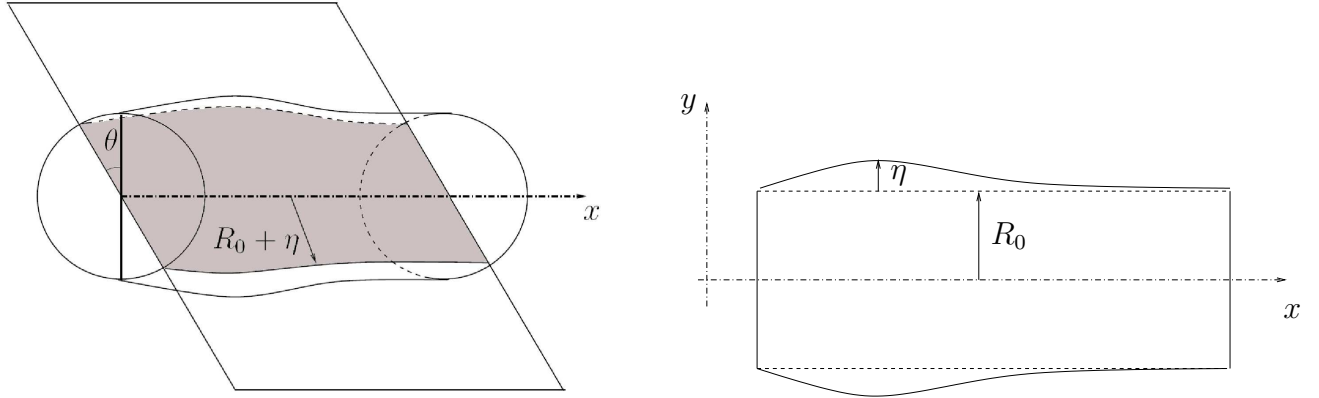


Figure 4.2: By intersecting the cylinder with a plane we obtain the 2d geometry with a 1d wall.

Fluid density: $\rho_f = 1.0 \text{ g/cm}^3$	Fluid viscosity: $\mu = 0.035 \text{ poise}$
Structure density: $\rho_s = 1.1 \text{ g/cm}^3$	Wall thickness: $h_s = 0.1 \text{ cm}$
Young modulus: $E = 7.5 \cdot 10^5 \text{ dynes/cm}^2$	Viscoelastic parameter: $\gamma = 10^{-1} \text{ dyne} \cdot \text{s}$
Shear modulus: $G = 2.5 \cdot 10^5 \text{ dynes/cm}^2$	Poisson coefficient: $\nu = 0.5$

Table 4.1: Fluid and structure physical properties for the numerical test

time duration of the pulse is 5 ms. Fig. 4.3 shows the input profile $\sigma_{in}^f \cdot \mathbf{n}$. The value of P_{in} is about 1/8 of the real amplitude in a cardiac beat. Also the duration of the pulse is much smaller than the one of a cardiac beat, whose systolic phase lasts about 0.3 s. We solve the problem over the time interval $[0, 0.012]$ s. The variation from the real values is justified by the fact that they amplify the propagative phenomena due to the fluid-structure coupling.

Remark 4.1. *Although not completely realistic for blood flow problems, this 2d benchmark maintains the peculiar aspects of the coupled fluid-structure problem. Therefore, it will be adopted to test the semi-implicit algorithms presented in Section 3.3.*

More realistic applications are shown in Chapter 5.

4.3 Numerical Experiments

We choose a conforming space discretization between fluid and structure: $(\mathbb{P}_1 \text{iso}\mathbb{P}_2) - \mathbb{P}_1$ finite elements for the fluid and \mathbb{P}_1 finite elements for the structure. We have solved the problem with the algorithms described in Section 3.3 on the elliptic mesh of 31×21 \mathbb{P}_1 fluid nodes (2501 $\mathbb{P}_1 \text{iso}\mathbb{P}_2$ nodes) shown in Figure 4.4. With regard to time discretization, we choose the backward Euler scheme for the fluid equations and the mid-point rule for

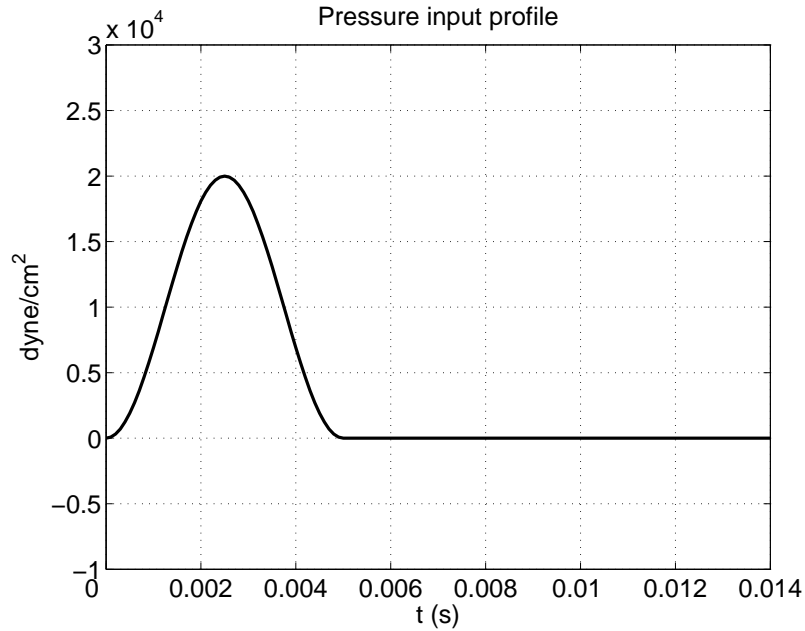


Figure 4.3: Input profile of the inflow Neumann boundary condition on the normal stress.

the structure problem.

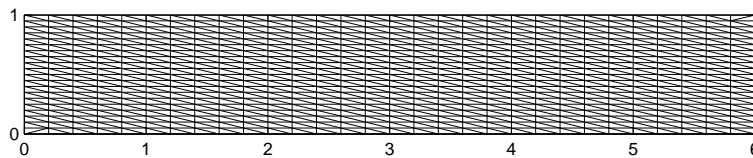


Figure 4.4: Elliptic mesh used for the simulations.

Fig. 4.5 shows the fluid pressure contour lines together with the structural deformation at time $t = 4, 8,$ and 12 ms. The solid displacement, definitely non-negligible, has not been magnified. We see that initial pressure pulse propagates in the artery at a finite speed, even though the fluid model consists of incompressible Navier-Stokes equations. The reason of this fact lies in the compliance of the vessel wall.

In Section 4.3.6, we calculated the diameter of the artery, the average pressure, and the flux at each time step. We will see that a propagative pulse is associated to all these three quantities.

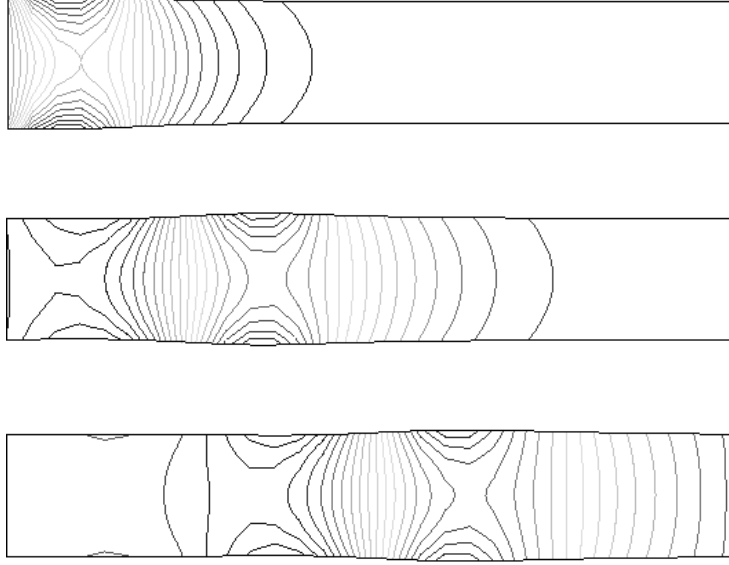


Figure 4.5: Propagation of the initial pressure pulse, moving from the inflow to the outflow section. Solutions every 4 *ms*.

4.3.1 Semi-Implicit procedures

In Figure 4.6, we check the good behavior of a first order semi-implicit algorithm by evaluating its order of convergence in time. In order to do that, we solve the monolithic implicit scheme for $\delta t = 10^{-6}$. The corresponding solution will be considered as *exact*.

We compare the solution of the first order semi-implicit monolithic method, computed on the mesh of Figure 4.4 for a sequence of decreasing time steps ($\delta t = 4 \cdot 10^{-4}, 2 \cdot 10^{-4}, 10^{-4}, 5 \cdot 10^{-5}, 4 \cdot 10^{-5}$) with the exact solution. The semi-implicit monolithic scheme solves system (3.4) by a global preconditioned GMRES once per time step. In Figure 4.6, we report the L^2 -error on the fluid velocity, pressure, and structure displacement at time $t = 10$ ms. In all cases, the method exhibits a first order of accuracy in time. Besides that, the semi-implicit method has remained stable. This means that avoiding to subiterate over the domain shape allows important time savings without compromising accuracy and stability.

4.3.2 PIC and FSU accuracy

The next step is to evaluate the convergence of the inexact factorization techniques designed in Chapter 3.

We solve the test problem with the first order FSU and PIC schemes (with first order predictions for pressure and interface velocity in the incremental FSI system) for the same

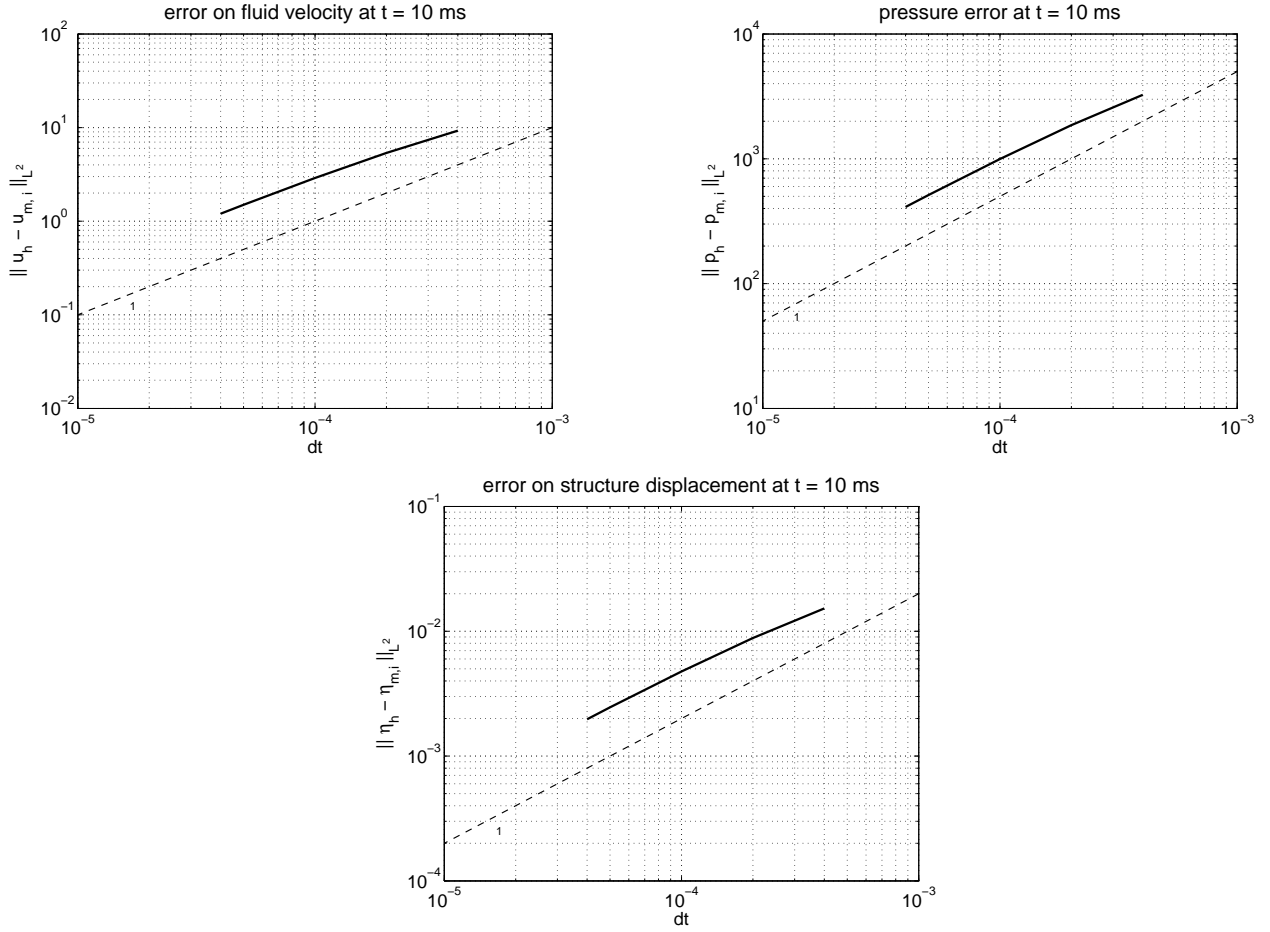


Figure 4.6: Convergence of the semi-implicit monolithic method to the implicit monolithic one. The dashed line in each graph indicates slope 1.

sequence of time steps ($\delta t = 4 \cdot 10^{-4}, 2 \cdot 10^{-4}, 10^{-4}, 5 \cdot 10^{-5}, 4 \cdot 10^{-5}$), always on the mesh of Figure 4.4. The FSI nonlinearity is treated in an explicit way using semi-implicit schemes.

We compute the solution of the semi-implicit monolithic algorithm on the same mesh but with time step $\delta t = 10^{-6}$: we will address to this solution as the *exact solution*. We compare the solutions computed by the FSY and PIC methods at the different time steps with this exact solution. Figure 4.7 shows the error on the fluid velocity, pressure, and the structure displacement at time $t = 10$ ms, all evaluated in the L^2 -norm. As it was expected, we recover a linear convergence for both methods.

For the first order FSY scheme, we repeat the same procedure on the refined grid $61 \times 26 \mathbb{P}_1$ fluid nodes. Fig. 4.8 shows again the error on the fluid velocity, pressure, and the structure displacement at time $t = 10$ ms in the L^2 -norm, for the two meshes. We

4.3. NUMERICAL EXPERIMENTS

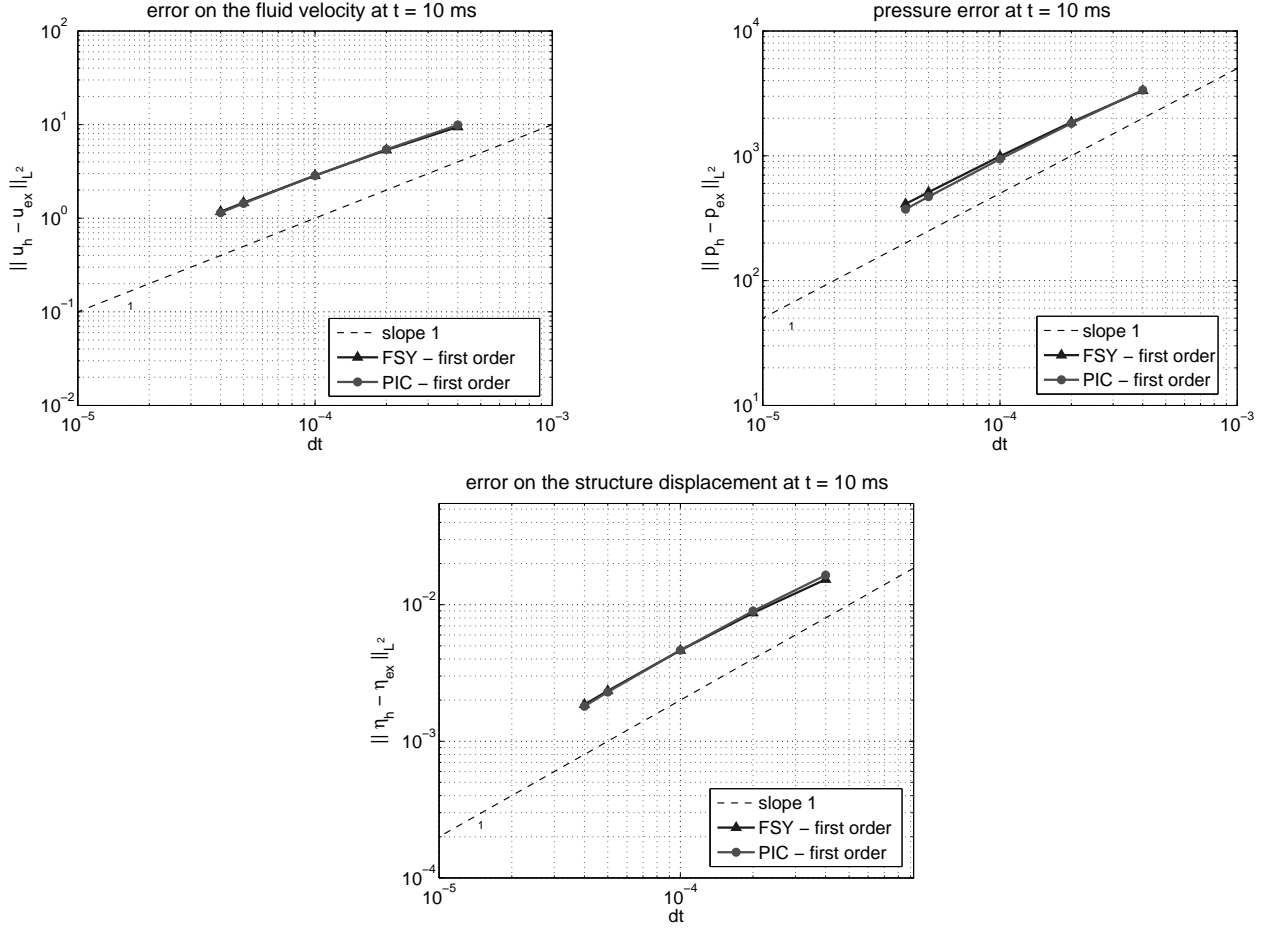


Figure 4.7: Convergence of the first order FSY and PIC schemes to the monolithic semi-implicit method.

remark that the “exact” solutions are different for the two grids, so it can happen that the errors on the fine mesh are bigger than the ones on the coarse grid, as in Fig. 4.8.

4.3.3 Splitting error for the FSY algorithm

The solution computed by the semi-implicit PIC or FSY methods is affected by three errors: the first one is due to the fact that nonlinearities of the FSI are explicitly treated, the second one is introduced by the discretization, and the third one derives from the splitting (i.e. approximation (3.15)). In Sections 4.3.1 and 4.3.2, we checked the first error and the sum of the second and the third ones, respectively. In this subsection, we evaluate the splitting error introduced by the first order FSY method. For this purpose, we compare at the different time steps the solution of our scheme with the solution of the semi-implicit

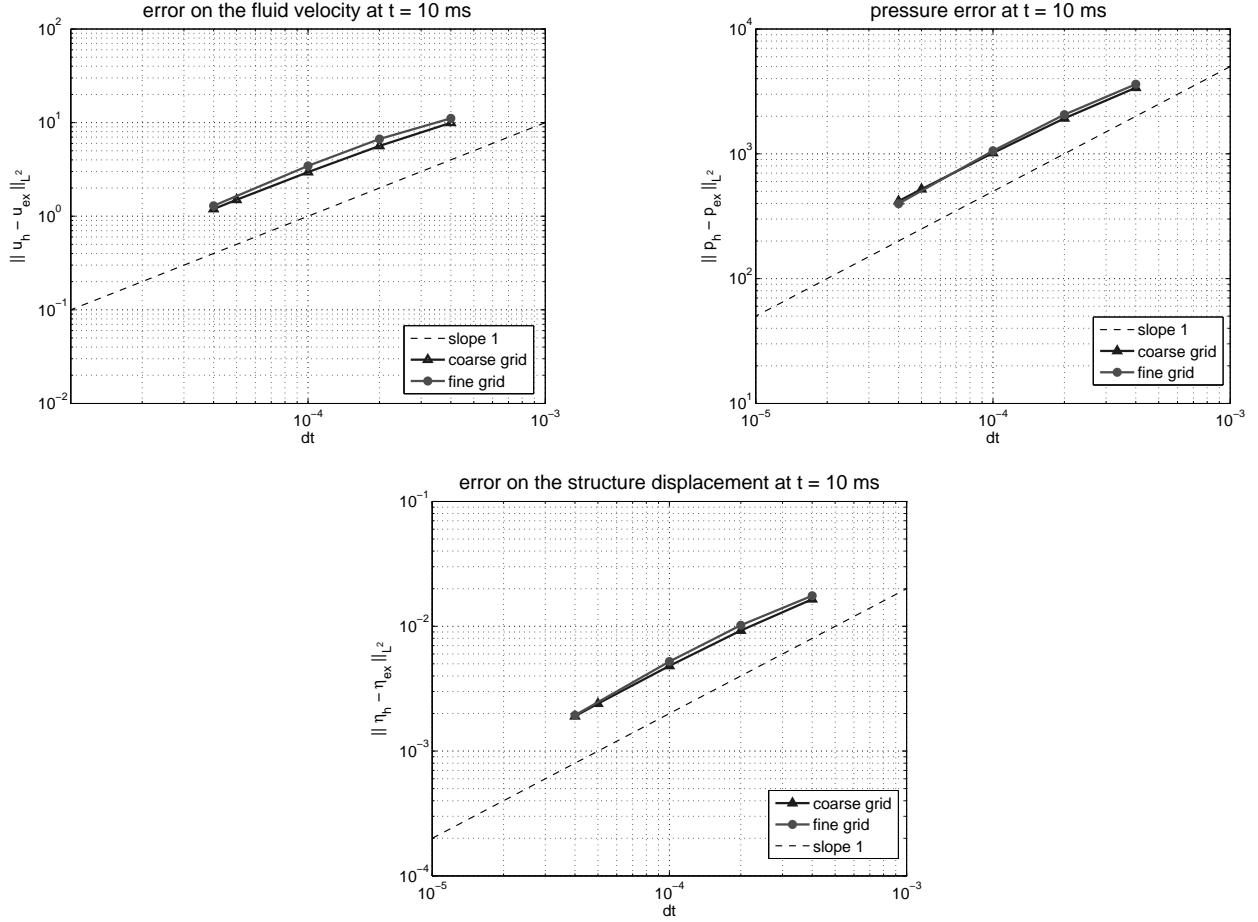


Figure 4.8: Convergence of the first order FSU scheme to the monolithic semi-implicit method on two different grids.

monolithic method, computed on the same mesh (Fig. 4.4) and with the same time step value. In Fig. 4.9, we report the splitting errors for fluid velocity, pressure, and structure displacement. The dashed line in each graph indicates slope 2.

As the time step gets refined, the FSU method introduces an error that behaves like δt^2 for all the three quantities. This means that the splitting error is smaller than the time discretization error. Thus, the global error in time for fluid velocity, pressure and structure displacement can be written as the sum of the three errors mentioned before

$$err(\delta t) = c_{SI} \delta t + c_{TD} \delta t + c_{Yos} \delta t^2, \quad (4.3)$$

where c_{SI} , c_{TD} , and c_{Yos} are two positive constants independent of δt . Formula (4.3) is empirical. In [67] the same behavior for the time discretization (TD) and the splitting error (Yos) is observed in the case of the Yosida method applied to Navier-Stokes in a

4.3. NUMERICAL EXPERIMENTS

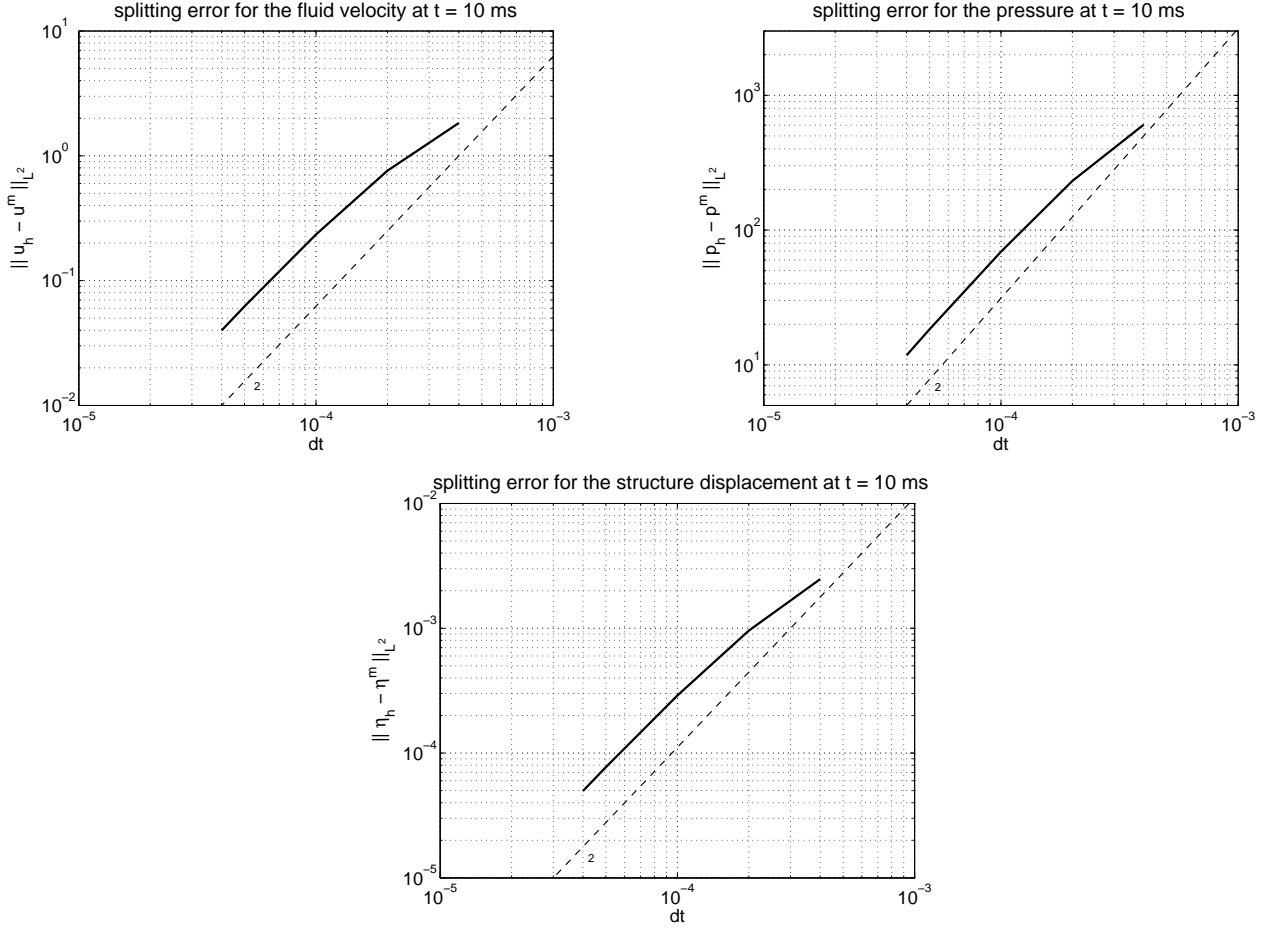


Figure 4.9: Splitting error on the fluid velocity, pressure, and structure displacement in the L^2 -norm at time $t = 10$ ms: difference between the solution of the first order FSY algorithm and the monolithic solution computed with the same time step.

fixed domain.

4.3.4 Convergence of predictor-corrector methods

The target is to analyze the convergence properties of predictor-corrector iterations with respect to the added-mass effect.

As commented in Section 3.3.3, since the pressure and structure problems remain coupled after the inexact factorization, the convergence of this method towards the monolithic solution must be added-mass effect independent.

We have plotted the average number of predictor-corrector iterations (in time) for different values of the structure density: $\rho_s = 500, 100, 50, 10, 5, 1$ g/cm³. We have

performed this test for two different time step values. Figure 4.10 shows that the average number of predictor-corrector subiterations keeps almost constant for all the values of ρ_s in both cases.

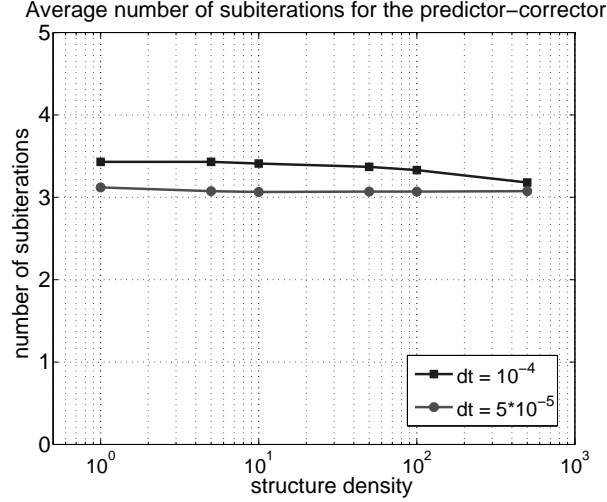


Figure 4.10: Average number of subiterations of the predictor corrector method as the structure density varies, for different time steps.

4.3.5 The added-mass effect and the pressure-interface system

The pressure-interface velocity system couples fluid and structure problems. In Section 3.6, we have discussed some possible alternatives for the solution of this linear system depending on modularity.

We want to evaluate how complicated it is to solve this system with respect to the added-mass effect. Again, we have solved the FSI test problem using different values of the structure density ($\rho_s = 500, 100, 50, 10, 5, 1 \text{ g/cm}^3$) and different time steps ($\delta t = 5 \cdot 10^{-4}, 10^{-4}, 5 \cdot 10^{-5}$). We have evaluated the condition number of the system matrix T , which involves the loss of modularity (Section 3.6.2). In Figure 4.11, we observe that the condition number of T decreases with respect to the added-mass effect. Therefore, the solution of the fluid-structure system (3.32) is made easier by the small condition number when the added-mass effect is more important. This behavior characterizes not only the simplified problem we are dealing with in this chapter, but also fully 3d problems as reported in Fig. 5.13. Therein, we have two PIC methods, PIC-GMRES and PIC-BiCGStab, depending on the solver used for system (3.32). The small condition number for $\rho_s = 1$, e.g., reflects in less GMRES iterations and, consequently, less CPU time.

On the other hand, we have evaluated the condition number of the interface system matrix (Section 3.6.3). As expected, due to the fact that this matrix is related to the interface problem, its condition number is much smaller. Moreover, the behavior with respect to the added-mass effect is opposite to the one for T : the condition number of this interface matrix increases when ρ_s approaches ρ_f .

We also notice that, keeping ρ_s fixed, in both cases the average condition number increases as the time step decreases.

As a conclusion, to lose modularity can be appealing when solving problems where the added-mass effect is critical. In Chapter 5, we further investigate non-modular algorithms and claim their efficiency in comparison to the DN-Richardson algorithm, a well known modular technique.

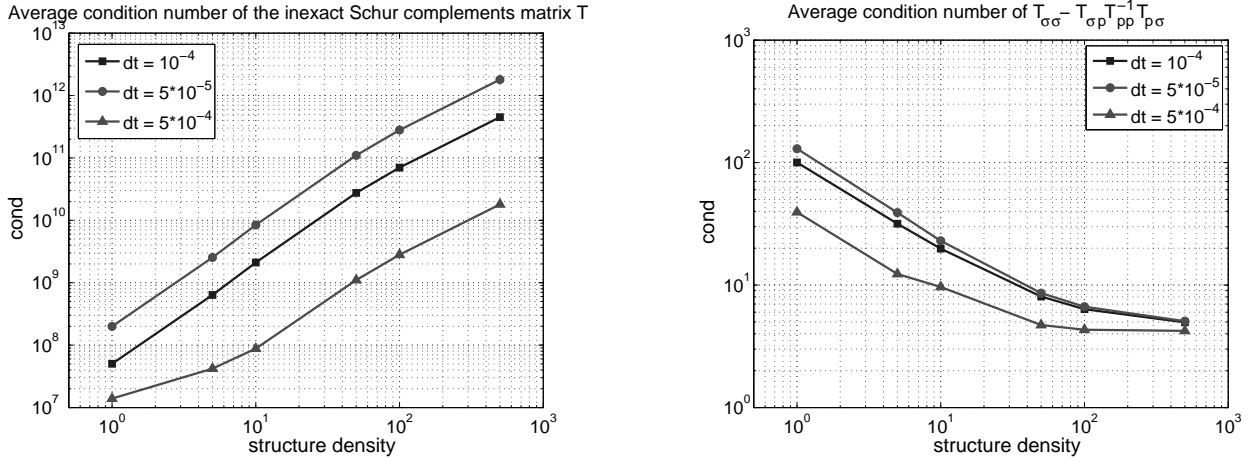


Figure 4.11: Average conditioning number for the inexact Schur complement matrices and its Schur complement for different structure densities and time steps.

4.3.6 Qualitative results

To highlight the propagative phenomena associated to FSI problems with large added-mass effect, we have computed average quantities on each vertical line \mathcal{S}_i of the mesh in Fig. 4.4 (see [104]), corresponding to the position $x_i = i \cdot h$, with $i = 0, \dots, 30$ and $h = 0.2$ cm. We calculated the diameter of the artery, the average pressure, and the flux at each time step:

$$d^n(x_i) = \text{meas}(\mathcal{S}_i^n), \quad \bar{p}^n(x_i) = \frac{1}{\mathcal{S}_i^n} \int_{\mathcal{S}_i^n} p_h^n \, dl, \quad Q^n(x_i) = \int_{\mathcal{S}_i^n} \mathbf{u}_h^n \cdot \mathbf{e}_x \, dl,$$

\mathbf{e}_x being the unit vector in the x direction, using different strategies and numerical parameters.

From Fig. 4.12, 4.14, and 4.13, it is evident that a propagative pulse is associated to all these three quantities.

In Figure 4.12, we report the comparison between the average pressure profiles computed every 2 milliseconds with the first order FSY scheme with two different time steps ($\delta t = 10^{-4}$ and $\delta t = 10^{-6}$). As expected, for larger time step values, the solution is slightly more dissipative.

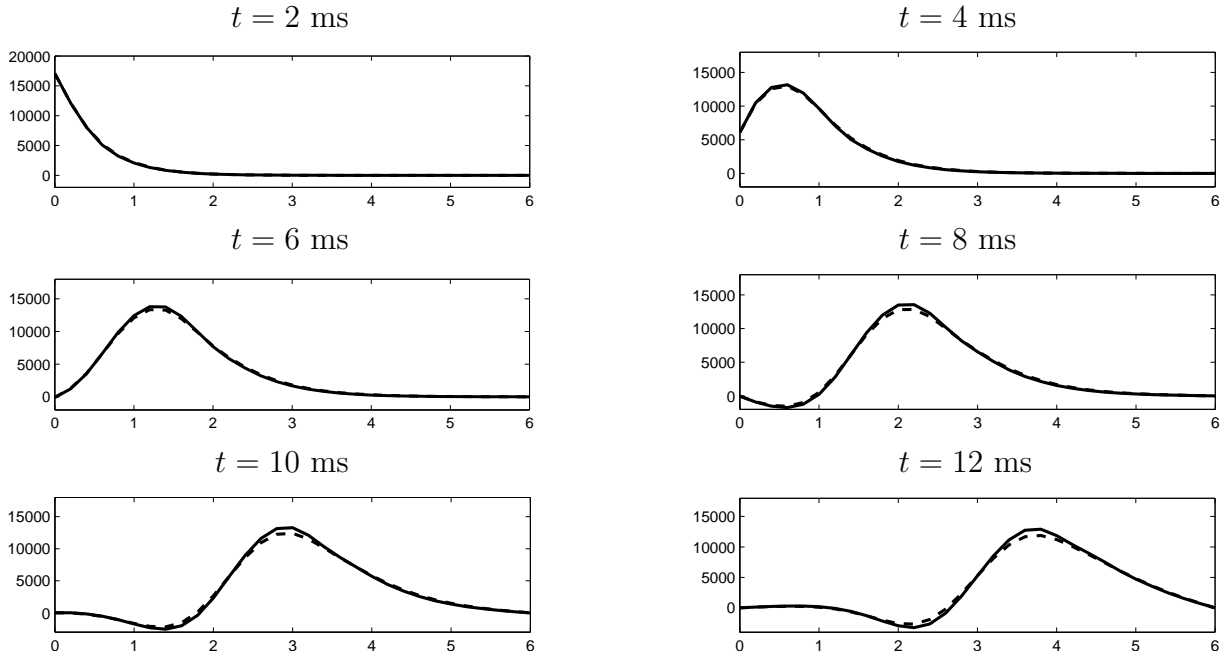


Figure 4.12: Average pressure profiles computed with the first order FSY method for $\delta t = 10^{-4}$ (dashed line) and for $\delta t = 10^{-6}$ (solid line). Comparison at different time levels.

In order to evaluate the influence of the spatial discretization on the numerical solution, we compare in Figure 4.13 the diameter of the artery section calculated with the first order PIC scheme on two different meshes: a coarse one ($31 \times 21 \mathbb{P}_1$ fluid nodes) and a fine one ($61 \times 26 \mathbb{P}_1$ fluid nodes). In both cases the time step is $\delta t = 10^{-4}$. We notice that the solution for the fine grid is slightly faster than the one computed on the coarse grid.

Finally, we compare, in a qualitative way, the flow rate of the monolithic scheme against those of PIC, FSY, and predictor-corrector methods for $\delta t = 5 \cdot 10^{-5}$. In all cases we consider semi-implicit procedures. We notice from Figure 4.14 that the difference between the flow rate profiles associated to all these solutions is very slight. Figure 4.15 shows a zoom of the flow rate profiles at $t = 12$ ms.

4.4. CONCLUSIONS

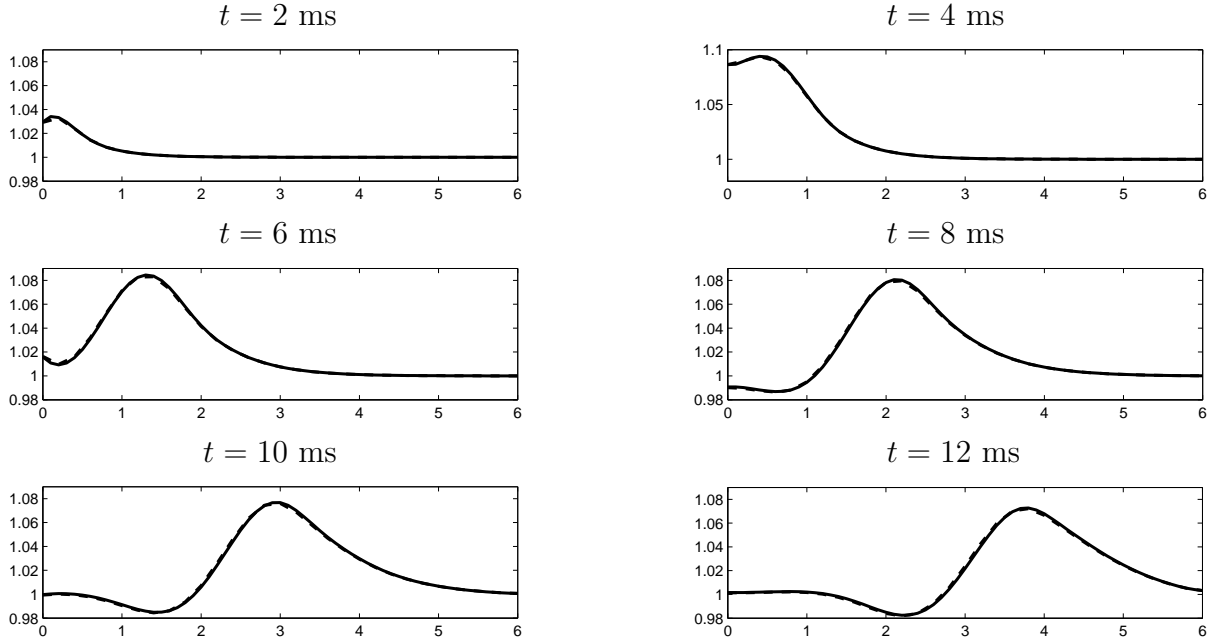


Figure 4.13: Diameter of the artery section along its axis computed with the first order PIC method on the coarse mesh (dashed line) and on the fine mesh (solid line). Comparison at different time levels.

4.4 Conclusions

In this chapter we applied to a simple test case the semi-implicit methods proposed in Chapter 3. Semi-implicit coupling methods, firstly introduced in [55], show good stability properties and low computational costs for FSI problems characterized by a strong added-mass effect. The basic idea behind them is to couple implicitly the pressure stress to the structure, while the nonlinearity due to convection and the geometrical nonlinearities are treated explicitly. In [55], the implicit-explicit splitting is performed through a Chorin-Temam scheme for the fluid.

In Chapter 3, we have proposed new schemes based on the inexact factorization of the linearized fluid-structure system, i.e. the procedure is split into explicit and implicit steps at the algebraic level. Two different methods have been designed: *pressure-interface correction* (PIC) and *fluid-structure Yosida* (FSY). In both cases, the perturbation error has been analyzed and the convergence properties of the methods have been checked through numerical experiments. In this chapter we show that, in the simulation of a pressure pulse propagation in an idealized blood flow vessel, the methods remained stable for a wide range of discretization and physical parameters. Qualitative results have turned out to be very similar to those achieved with the monolithic system.

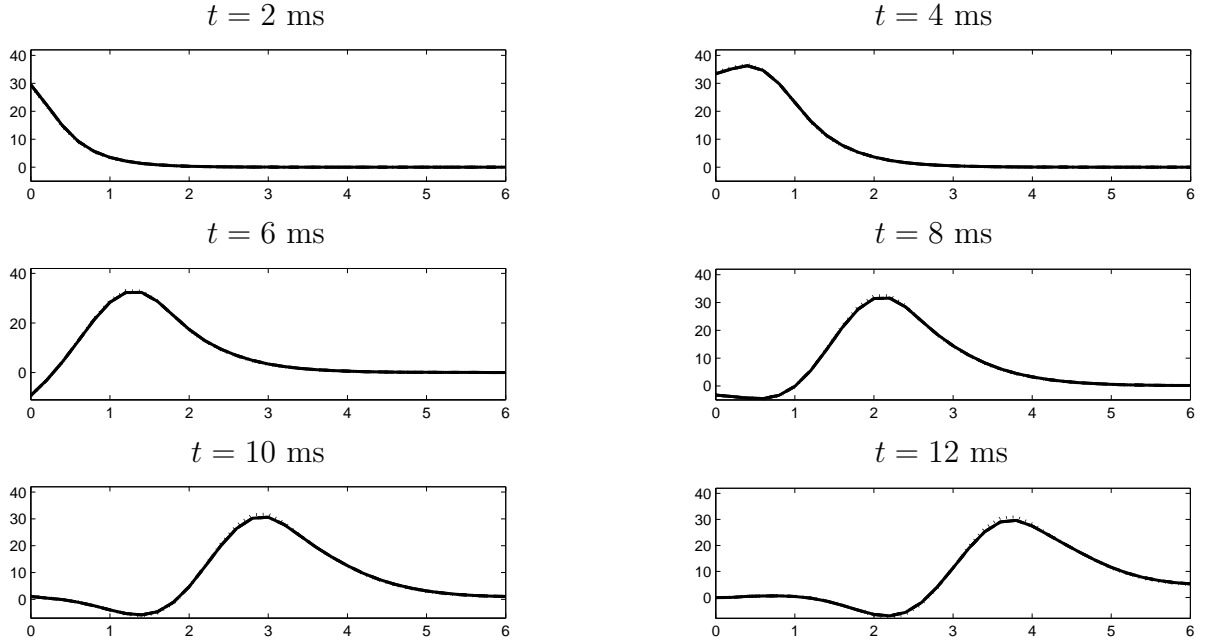


Figure 4.14: Flow rate profiles at different time levels: comparison between the solution of first order FSY (dashed line), first order PIC (solid line), predictor-corrector (dash-dot line) methods, all for $\delta t = 5 \cdot 10^{-5}$, and the “exact” solution (dotted line).

We have also proposed *predictor-corrector methods* that use inexact factors as preconditioners. The best feature of these procedures is that predictor-corrector iterations are independent of the added-mass effect. The solution of these methods converges to the one of the fully implicit monolithic system without introducing any perturbation. Therefore, these schemes are very well suited when there is an interest on implicit fluid-structure solutions. In this case, we can also consider *one-loop algorithms*, where nonlinearity and predictor-correction iterations are performed with only one loop.

The next step will concern the application of the algorithms presented here to three-dimensional problems. These more realistic cases would also enable us to evaluate the computational cost reduction allowed by the methods that we have introduced and tested in the previous and present chapters, respectively.

4.4. CONCLUSIONS

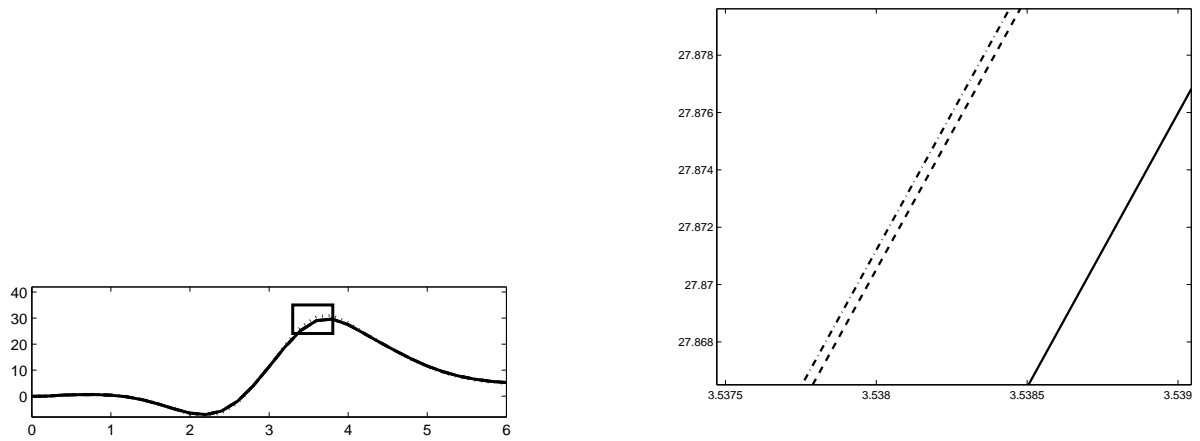


Figure 4.15: On the left the rectangle indicates the zoom area on the flow rate profiles for $t = 12$ ms. On the right there is the zoom.

CHAPTER 4. APPLICATION OF THE METHODS BASED ON INEXACT
FACTORIZATION TO BLOOD FLOW IN LARGE ARTERIES

Chapter 5

Comparison between modular and non-modular approaches

5.1 Introduction

In this chapter we aim at comparing the performances of the splitting technique based on an inexact block- LU factorization of the linear FSI system (Chapter 3) with those of other two approaches. These two approaches involve different preconditioners for the coupled system matrix obtained after space-time discretization and linearization of the FSI problem. The classical Dirichlet-Neumann preconditioner (Section 5.3) has the advantage of modularity because it allows to reuse existing fluid and structure codes with minimum effort (simple interface communication). Unfortunately, its performance is very poor in case of large added-mass effects. Alternatively, we consider a non-modular approach, detailed in Section 5.4. It consists in preconditioning the coupled system with a suitable diagonal scaling combined with an ILUT preconditioner. The system is then solved by a Krylov method. The drawback of this procedure is that the combination of fluid and structure codes to solve the coupled system is not straightforward.

Independently of the preconditioner, the efficiency of semi-implicit algorithms (i.e., those that treat geometric and fluid nonlinearities in an explicit way) is highlighted and their performance compared to the one of implicit algorithms. All the methods are tested on three-dimensional blood-vessel systems: a straight artery (Section 5.5) and the carotid bifurcation (Section 5.6). In Section 5.7, we draw some conclusions on the optimal range of applicability of the methods considered.

5.2 The domain decomposition approach

In this section we reformulate the fluid-structure problem in a domain decomposition approach, see e.g. [137, 44, 46, 45]. Our purpose is to introduce a framework for the next section by reporting a few theoretical concepts. We refer to [120] for an exhaustive exposition of the theory we just hint at.

We consider the time discretized version of (2.13) using a BDF scheme for the time integration at the step t^{n+1} . At the time step t^{n+1} , let us denote by $\boldsymbol{\eta}_\sigma$ the interface variable corresponding to the displacement on the fluid-structure interface $\boldsymbol{\eta}^{n+1}|_{\Sigma_{t^{n+1}}}$.

We define the *Steklov-Poincaré interface operator* (see [120]) for the fluid as follows: \mathcal{S}_f is the Dirichlet-to-Neumann map in $\Omega_{t^{n+1}}^f$ such that

$$\begin{aligned} \mathcal{S}_f & : (H^{1/2}(\Sigma_{t^{n+1}}))^d \longrightarrow (H^{-1/2}(\Sigma_{t^{n+1}}))^d \\ & \boldsymbol{\eta}_\sigma \longrightarrow \boldsymbol{\sigma}^f \cdot \boldsymbol{n}. \end{aligned}$$

This operator solves the fluid problem for a given value of the interface variable $\boldsymbol{\eta}_\sigma$ and recovers the stress on the interface $\boldsymbol{\sigma}^f \cdot \boldsymbol{n}$. Hence, this is a mapping between the trace of the structure displacement field $\boldsymbol{\eta}$ and the dual space of normal stresses exerted by the fluid.

We remark that the Steklov-Poincaré operator \mathcal{S}_f for the fluid is nonlinear, because of the shape nonlinearities and the nonlinearity due to the convective term of the fluid equations. As a consequence, the principle of superposition of effects does not hold and \mathcal{S}_f has to account also for forcing terms and non-homogeneous boundary conditions.

Likewise, we define the Steklov-Poincaré operator for the structure: \mathcal{S}_s is the Dirichlet-to-Neumann map in $\Omega_{t^{n+1}}^s$ such that

$$\begin{aligned} \mathcal{S}_s & : (H^{1/2}(\Sigma_{t^{n+1}}))^d \longrightarrow (H^{-1/2}(\Sigma_{t^{n+1}}))^d \\ & \boldsymbol{\eta}_\sigma \longrightarrow \boldsymbol{\sigma}^s \cdot \boldsymbol{n}. \end{aligned}$$

This operator solves the structure problem with $\boldsymbol{\eta}_\sigma$ as a Dirichlet boundary datum for $\boldsymbol{\eta}$ on $\Sigma_{t^{n+1}}$ and extracts the value of the interface stress $\boldsymbol{\sigma}^s \cdot \boldsymbol{n}$. Even if the structure equations are linear, this operator is nonlinear because of the shape nonlinearities. Its inverse \mathcal{S}_s^{-1} , called *Poincaré-Steklov interface operator*, is the Neumann-to-Dirichlet map in $\Omega_{t^{n+1}}^s$ such that:

$$\begin{aligned} \mathcal{S}_s^{-1} & : (H^{-1/2}(\Sigma_{t^{n+1}}))^d \longrightarrow (H^{1/2}(\Sigma_{t^{n+1}}))^d \\ & \boldsymbol{\sigma}^s \cdot \boldsymbol{n} \longrightarrow \boldsymbol{\eta}_\sigma. \end{aligned}$$

The operator \mathcal{S}_s^{-1} solves the structure problem with $\boldsymbol{\sigma}^s \cdot \boldsymbol{n}$ as Neumann boundary condition on the interface and recovers the displacement $\boldsymbol{\eta}_\sigma$.

Coupling condition (2.13e) can be rewritten in terms of the operators introduced above: find $\boldsymbol{\eta}_\sigma \in (H^{1/2}(\Sigma_{t^{n+1}}))^d$ such that

$$\mathcal{S}_f(\boldsymbol{\eta}_\sigma) + \mathcal{S}_s(\boldsymbol{\eta}_\sigma) = 0. \quad (5.1)$$

Thanks to the domain decomposition approach the FSI problem (2.13) has been reduced to interface equation (5.1).

If we apply the inverse of the Steklov-Poincaré operator \mathcal{S}_s^{-1} to equation (5.1), we obtain the following problem: find $\boldsymbol{\eta}_\sigma \in (H^{1/2}(\Sigma_{t^{n+1}}))^d$ such that

$$-\mathcal{S}_s^{-1}(\mathcal{S}_f(\boldsymbol{\eta}_\sigma)) = \boldsymbol{\eta}_\sigma. \quad (5.2)$$

Equation (5.2) can be easily solved through a fixed point algorithm. The iterative procedure reads: given $\boldsymbol{\eta}_\sigma^k$, find $\boldsymbol{\eta}_\sigma^{k+1}$ such that

$$\boldsymbol{\eta}_\sigma^{k+1} = -\mathcal{S}_s^{-1}(\mathcal{S}_f(\boldsymbol{\eta}_\sigma^k)). \quad (5.3)$$

Method (5.3) is referred to as *Dirichlet-Neumann*. In fact, given a value for the interface displacement $\boldsymbol{\eta}_\sigma^k$, we solve the fluid problem with a Dirichlet interface condition depending on $\boldsymbol{\eta}_\sigma^k$ and compute the stress $\boldsymbol{\sigma}^f \cdot \mathbf{n}$ on $\Sigma_{t^{n+1}}$. In this way, we have $\mathcal{S}_f(\boldsymbol{\eta}_\sigma^k)$. Then, we solve the structure problem with $\boldsymbol{\sigma}^s \cdot \mathbf{n} = \boldsymbol{\sigma}^f \cdot \mathbf{n}$ as Neumann interface condition and compute the new value of the interface displacement $\boldsymbol{\eta}_\sigma^{k+1}$. That corresponds to calculate $-\mathcal{S}_s^{-1}(\boldsymbol{\sigma}^f \cdot \mathbf{n})$. Notice that at every iteration of (5.3) the fluid domain must be updated. Thus, every iteration of the fixed point method deals with the fluid-structure coupling and the linearization of the geometrical nonlinearities.

The solution of the fluid problem in (5.3) needs nonlinear iterations. One possibility is to make use of nested loop: at every fixed point iteration nonlinear iterations are performed to linearize the convective term. Otherwise, we could replace $\mathcal{S}_f(\boldsymbol{\eta}_\sigma^k)$ in (5.3) by a linearized operator $\tilde{\mathcal{S}}_f(\mathbf{u}^*; \boldsymbol{\eta}_\sigma^k)$, where \mathbf{u}^* is the convective velocity adopted for the linearization. In this way, we deal with both nonlinearities (and the coupling) in the same loop.

Other widely used domain decomposition methods can be adopted to solve equation (5.1). In [46], the authors consider the following preconditioned Richardson method: given $\boldsymbol{\eta}_\sigma^k$, find $\boldsymbol{\eta}_\sigma^{k+1}$ such that

$$\mathcal{P}_k(\boldsymbol{\eta}_\sigma^{k+1} - \boldsymbol{\eta}_\sigma^k) = -\mathcal{S}_f(\boldsymbol{\eta}_\sigma^k) - \mathcal{S}_s(\boldsymbol{\eta}_\sigma^k), \quad (5.4)$$

where \mathcal{P}_k is a preconditioner for $\mathcal{S}_f(\boldsymbol{\eta}_\sigma^k) + \mathcal{S}_s(\boldsymbol{\eta}_\sigma^k)$. By choosing $\mathcal{P}_k = \mathcal{S}_s$, we recover the fixed point method (5.3). Thus, the classical Dirichlet-Neumann algorithm can be interpreted as a preconditioned Richardson method. For this reason, we denote it by DN-Richardson. Some alternative choices for \mathcal{P}_k are suggested in [46]. Moreover, relaxation is advisable to improve the convergence properties of (5.4).

In the next section, we consider the Dirichlet-Neumann method at the discrete level.

5.3 The Dirichlet-Neumann preconditioner

Let us reformulate the FSI system as an interface problem. This is achieved by writing system (3.4) only in terms of \mathbf{U}_σ^{n+1} thanks to the Schur complements of fluid and structure subproblems. The Schur complements represent the discrete Steklov-Poincaré operators introduced in Section 5.2. Omitting the time step superscript for simplicity, the interface problem is:

$$A_\sigma \mathbf{U}_\sigma = \tilde{\mathbf{b}}_\sigma,$$

with

$$\begin{aligned} A_\sigma &= \tilde{C}_\sigma + \tilde{N}_\sigma, \\ \tilde{C}_\sigma &= C_{\sigma\sigma} - \begin{bmatrix} C_{\sigma f} & G_\sigma^\tau \end{bmatrix} \begin{bmatrix} C_{ff} & G_f^\tau \\ D_f^\tau & L_p^\tau \end{bmatrix}^{-1} \begin{bmatrix} C_{f\sigma} \\ D_\sigma^\tau \end{bmatrix}, \\ \tilde{N}_\sigma &= N_{\sigma\sigma} - N_{\sigma s} N_{ss}^{-1} N_{s\sigma}, \\ \tilde{\mathbf{b}}_\sigma &= \mathbf{b}_\sigma - \begin{bmatrix} C_{\sigma f} & G_\sigma^\tau \end{bmatrix} \begin{bmatrix} C_{ff} & G_f^\tau \\ D_f^\tau & L_p^\tau \end{bmatrix}^{-1} \begin{bmatrix} \mathbf{b}_f \\ \mathbf{b}_p \end{bmatrix} - N_{\sigma s} N_{ss}^{-1} \mathbf{b}_s. \end{aligned} \tag{5.5}$$

The interface system preconditioned with the Dirichlet-Neumann preconditioner \tilde{N}_σ reads as follows:

$$\tilde{N}_\sigma^{-1} A_\sigma \mathbf{U}_\sigma = \tilde{N}_\sigma^{-1} \tilde{\mathbf{b}}_\sigma. \tag{5.6}$$

This Schur complement preconditioner can also be understood as an incomplete block- LU factorization of the FSI system matrix A (see [120]). Equation (5.6) is the algebraic counterpart of (5.2). This is more evident if we rewrite it like

$$-\tilde{N}_\sigma^{-1}(\tilde{C}_\sigma \mathbf{U}_\sigma - \tilde{\mathbf{b}}_\sigma) = \mathbf{U}_\sigma.$$

The preconditioned system must be solved with a matrix-free iterative solver. In the next two sections, we introduce two different choices.

Remark 5.1. *We defined the fluid and structure Schur complements in (5.6) for the case where the fluid equations are discretized with stabilized finite elements. Their definitions for the standard Galerkin formulation is easily retrieved from the associated FSI system (3.8).*

However, from now onwards, we consider the FSI system associated to the stabilized formulation. The numerical results reported in Section 5.5 and 5.6 refer to that formulation.

5.3.1 Richardson algorithm for the preconditioned interface system

One way to solve system (5.6) is by Richardson iterations:

$$\mathbf{U}_\sigma^{k+1} = \mathbf{U}_\sigma^k + \tilde{N}_\sigma^{-1}(\tilde{\mathbf{b}}_\sigma - A_\sigma \mathbf{U}_\sigma^k).$$

This equation corresponds to the discretized version of (5.4) with $\mathcal{P}_k = \mathcal{S}_s$ and it is the classical Dirichlet-Neumann algorithm.

We can easily infer that it is equivalent to the following iterative procedure:

- (i) Fluid problem (Dirichlet boundary condition)

$$\begin{bmatrix} C_{ff} & G_f^\tau \\ D_f^\tau & L_p^\tau \end{bmatrix} \begin{bmatrix} \mathbf{U}_f^{k+1} \\ \mathbf{P}^{k+1} \end{bmatrix} = \begin{bmatrix} \mathbf{b}_f - C_{f\sigma} \mathbf{U}_\sigma^k \\ \mathbf{b}_p - D_\sigma^\tau \mathbf{U}_\sigma^k \end{bmatrix} \quad (5.7a)$$

- (ii) Structure problem (Neumann boundary condition)

$$\begin{bmatrix} N_{\sigma\sigma} & N_{\sigma s} \\ N_{s\sigma} & N_{ss} \end{bmatrix} \begin{bmatrix} \mathbf{U}_\sigma^{k+1} \\ \mathbf{U}_s^{k+1} \end{bmatrix} = \begin{bmatrix} \mathbf{b}_\sigma^{k+1} - C_{\sigma\sigma} \mathbf{U}_\sigma^k - C_{\sigma f} \mathbf{U}_f^{k+1} - G_\sigma^\tau \mathbf{P}^{k+1} \\ \mathbf{b}_s^{k+1} \end{bmatrix}. \quad (5.7b)$$

This is the most appealing feature of the DN-Richardson method: every iteration of the algorithm can be performed by separate fluid and structure solvers. We only need to modify the boundary conditions.

The iterative process must be supplemented with an appropriate stopping criterion. For instance, for the numerical experiments in Sections 5.5 and 5.6 we use:

$$\frac{\|\mathbf{U}_\sigma^{k+1} - \mathbf{U}_\sigma^k\|}{\|\mathbf{U}_\sigma^0\|} \leq \epsilon. \quad (5.8)$$

Every iteration of the DN-Richardson algorithm is expensive, because it involves to solve one fluid and one structure problem. A cheaper preconditioner has been suggested in [149]. The fluid and structure problems are replaced by ILU-type preconditioners of the respective system matrices. This preconditioner is not modular and less effective than the original one, but the computational cost of every iteration is reduced.

5.3.2 GMRES algorithm for the preconditioned interface system

Instead of using Richardson iterations, we can apply the GMRES algorithm to the preconditioned interface problem (5.6). The resulting method is denoted by DN-GMRES. It is much faster and robust than DN-Richardson, because it involves orthonormal iterations.

Moreover, convergence is always assured, at worst after as many iterations as degrees of freedom at the interface (not practical for real applications). The GMRES method requires to compute and store the Krylov base associated to $Q = \tilde{N}_\sigma^{-1}A_\sigma$, starting from the preconditioned residual $\mathbf{r}^0 = \tilde{N}_\sigma^{-1}[\tilde{\mathbf{b}}_\sigma - A_\sigma\mathbf{U}_\sigma^0]$, where \mathbf{U}_σ^0 is the initial guess. The Krylov space generated for the m -th iteration of the GMRES method is

$$\mathcal{K}_m := \text{span}\{\mathbf{r}^0, Q\mathbf{r}^0, Q^2\mathbf{r}^0, \dots, Q^m\mathbf{r}^0\} = \text{span}\{\mathbf{z}^0, \mathbf{z}^1, \dots, \mathbf{z}^m\}.$$

Given \mathbf{z}^k , in order to get \mathbf{z}^{k+1} we must evaluate a matrix-vector product

$$\tilde{N}_\sigma^{-1}A_\sigma\mathbf{z}^k = \mathbf{z}^k + \tilde{N}_\sigma^{-1}\tilde{C}_\sigma\mathbf{z}^k$$

This algorithm can be rearranged in such a way that every matrix-vector product is evaluated by the DN-Richardson code, simply setting to zero the body force:

- (i) Given \mathbf{U}_σ^0 , solve one Richardson iteration of (5.7) to get \mathbf{U}_σ^1 and compute the initial residual as:

$$\mathbf{r}^0 = \mathbf{U}_\sigma^1 - \mathbf{U}_\sigma^0.$$

- (ii) Initialize the Krylov base with $\mathbf{z}^0 = \mathbf{r}^0/||\mathbf{r}^0||$ and at every GMRES iteration (see [127, Section 6.5]) obtain the matrix vector product $\mathbf{w} = Q\mathbf{z}^k$ as follows:

- (a) Fluid problem (Dirichlet boundary conditions and zero forcing term)

$$\begin{bmatrix} C_{ff} & G_f^\tau \\ D_f^\tau & L_p^\tau \end{bmatrix} \begin{bmatrix} \mathbf{v}_f \\ \mathbf{q} \end{bmatrix} = - \begin{bmatrix} C_{f\sigma}\mathbf{z}^k \\ D_\sigma^\tau\mathbf{z}^k \end{bmatrix}; \quad (5.9a)$$

- (b) Structure problem (Neumann boundary conditions and zero forcing term)

$$\begin{bmatrix} N_{\sigma\sigma} & N_{\sigma s} \\ N_{s\sigma} & N_{ss} \end{bmatrix} \begin{bmatrix} \mathbf{v}_\sigma \\ \mathbf{v}_s \end{bmatrix} = - \begin{bmatrix} C_{\sigma\sigma}\mathbf{z}^k + C_{\sigma f}\mathbf{v}_f + G_\sigma^\tau\mathbf{q} \\ \mathbf{0} \end{bmatrix}. \quad (5.9b)$$

- (c) Evaluate $\mathbf{w} = \mathbf{z}^k - \mathbf{v}_\sigma$.

Implementing the DN-GMRES method by reusing the DN-Richardson master allows to use separate fluid and structure solvers. Unluckily, the performance of the DN-GMRES algorithm is still negatively affected by the added-mass effect.

Remark 5.2. *At every GMRES iteration we get*

$$\mathbf{U}_\sigma^k = \arg \min_{\mathbf{y} \in \mathcal{K}_{k-1}} ||\tilde{N}_\sigma^{-1}[\tilde{\mathbf{b}}_\sigma - A_\sigma\mathbf{y}]||,$$

which can also be written as

$$\|\tilde{\mathbf{U}}_\sigma^{k+1} - \mathbf{U}_\sigma^k\|,$$

where $\tilde{\mathbf{U}}_\sigma^{k+1}$ is obtained from \mathbf{U}_σ^k by solving one iteration of the Richardson algorithm (5.7). By taking $\epsilon\|\mathbf{U}_\sigma^0\|$ as tolerance, we impose the same stopping criterion used for the DN-Richardson method. This is the choice adopted in the numerical experiments.

Remark 5.3. *The GMRES algorithm is performed over the interface unknowns. Therefore, the Krylov base elements only have the dimensions of \mathbf{U}_σ . The memory requirements are clearly reduced.*

Remark 5.4. *The DN-GMRES algorithm could be implemented in a modular way. The computation of the initial residual is nothing else but one iteration of the DN-Richardson algorithm and the rest of the matrix-vector products can be computed using (5.9), with separate fluid and structure evaluations. However, we must set to zero the right-hand side term in both sub-problems. Assuming that this can be done without modifying the source codes, the DN-GMRES would keep modularity. In any case, a modular DN-GMRES algorithm is extremely inefficient; fluid and structure matrices do not change in the iterative process and could be assembled only once. An efficient implementation of the DN-GMRES algorithm requires a master with access to fluid and structure blocks to perform the iterative process without reassembling matrices.*

5.3.3 The reduction factor for the residual norm of the DN-GMRES method for a model problem

The purpose of this subsection is to understand how the added-mass effect affects the convergence of the DN-GMRES algorithm. To fulfill it, we consider the simplified fluid-structure model proposed in [26].

We take a rectangular fluid domain $\Omega^f \subset \mathbb{R}^2$ of height R and length L (see Figure 5.1). The structure domain Ω^s is placed on the upper side of Ω^f and coincides with the interface (that is, $\overline{\Omega^s} = \Sigma$). Under the hypothesis of dealing with a thin structure, having a membrane behavior and neglecting all the displacements but the normal one, we derive the structure model:

$$\rho_s h_s \partial_{tt} \eta + a \eta - b \partial_{xx} \eta = f_\Sigma(x, t) \quad \text{in } \Omega^s \times (0, T).$$

This model derives from the generalized string model (4.1) by neglecting the viscoelastic contribution. So, $\eta = \eta(x, t)$ is the displacement in the direction of \mathbf{n}_f , $a = Eh_s/R^2(1-\nu^2)$, and $b = kGh_s$.

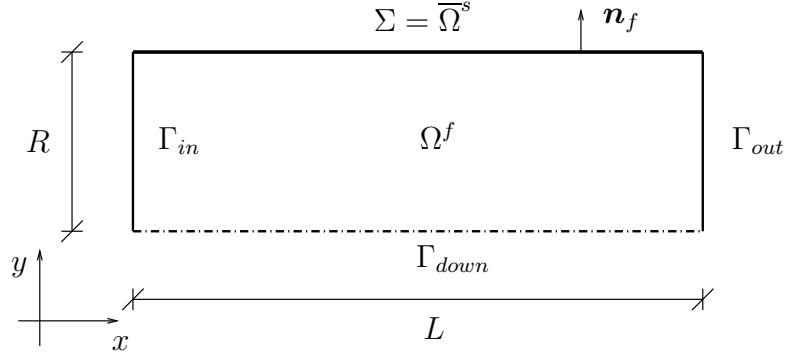


Figure 5.1: Domain for the simplified fluid-structure problem.

The model for the fluid is linear, incompressible, and inviscid. The deformation of the structure is assumed to be so small that the fluid domain Ω^f can be considered fixed. Hence, the fluid model is the following:

$$\rho_f \partial_t \mathbf{u} + \nabla p = \mathbf{0} \quad \text{in } \Omega^f \times (0, T), \quad (5.10a)$$

$$\nabla \cdot \mathbf{u} = 0 \quad \text{in } \Omega^f \times (0, T), \quad (5.10b)$$

$$u = \partial_t \eta \quad \text{on } \Sigma \times (0, T), \quad (5.10c)$$

with suitable boundary conditions on $\partial\Omega^f \setminus \Sigma$ and initial conditions; u denotes $\mathbf{u} \cdot \mathbf{n}_f$ on Σ .

For the time discretization of the FSI system we choose the implicit Euler scheme for the fluid problem and first order backward difference scheme for the structure one. The time-discrete problem reads:

$$\rho_f \delta_t \mathbf{u}^{n+1} + \nabla p^{n+1} = \mathbf{0} \quad \text{in } \Omega^f \times (0, T), \quad (5.11a)$$

$$\nabla \cdot \mathbf{u}^{n+1} = 0 \quad \text{in } \Omega_t^f \times (0, T), \quad (5.11b)$$

$$u = \delta_t \eta^{n+1} \quad \text{on } \Sigma \times (0, T), \quad (5.11c)$$

and

$$\rho_s h_s \frac{\eta^{n+1} - 2\eta^n + \eta^{n-1}}{\delta t^2} + a \eta^{n+1} - b \partial_{xx} \eta^{n+1} = p^{n+1} \quad \text{in } \Omega^s \times (0, T). \quad (5.12)$$

It can be shown [26, 6] that problem (5.11)-(5.12) corresponds to the following discrete added-mass problem for the structure:

$$(\rho_s h_s \mathcal{I} + \rho_f \mathcal{M}) \frac{\eta^{n+1} - 2\eta^n + \eta^{n-1}}{\delta t^2} + a \eta^{n+1} + b \mathcal{L} \eta^{n+1} = \hat{p}^{n+1} \quad \text{on } \Omega^s \times (0, T), \quad (5.13)$$

where \mathcal{I} denotes the identity operator, $\mathcal{M} : H^{-1/2}(\Sigma) \rightarrow H^{1/2}(\Sigma)$ stands for the added-mass operator and $\mathcal{L} = -\partial_{xx}$ is the Laplace operator. \hat{p}^{n+1} takes into account non-homogeneous

boundary conditions on $\partial\Omega^f \setminus \Sigma$. The added mass operator consists in: given $w \in H^{-1/2}(\Sigma)$ find $q \in H^1(\Omega^f)$ such that

$$\begin{aligned} -\Delta q &= 0 && \text{in } \Omega^f, \\ q &= 0 && \text{on } \Gamma_{in} \cup \Gamma_{out}, \\ \frac{\partial q}{\partial \mathbf{n}} &= 0 && \text{on } \Gamma_{down}, \\ \frac{\partial q}{\partial \mathbf{n}} &= w && \text{on } \Sigma, \end{aligned}$$

and extract the value of the solution q on Σ .

Let us indicate with \mathcal{Q} the linear, invertible, and continuous operator

$$\mathcal{Q} = \left(\frac{\rho_s h_s}{\delta t^2} + a \right) \mathcal{I} + b\mathcal{L} + \frac{\rho_f}{\delta t^2} \mathcal{M},$$

which can be split as $\mathcal{Q} = \mathcal{Q}_f + \mathcal{Q}_s$, where \mathcal{Q}_f and \mathcal{Q}_s are the linear operators associated to the fluid and structure subdomains:

$$\mathcal{Q}_f = \frac{\rho_f}{\delta t^2} \mathcal{M}, \quad \mathcal{Q}_s = \left(\frac{\rho_s h_s}{\delta t^2} + a \right) \mathcal{I} + b\mathcal{L}.$$

Solving (5.13) with the DN-GMRES algorithm means to solve the problem $\mathcal{Q}\eta^{n+1} = G$ (G accounting for η^n , η^{n-1} , and \hat{p}^{n+1}) with the GMRES method based on \mathcal{Q}_s as preconditioner. To analyze the DN-GMRES algorithm we express η as

$$\eta = \sum_{i=1}^{\infty} \eta_i g_i, \quad \text{with } g_i = \sqrt{\frac{2}{L}} \sin\left(i\pi \frac{x}{L}\right).$$

The functions g_i are eigenfunctions of both the added-mass and the Laplace operators. Let μ_i (see [26]) and λ_i (see [6]) be the respective eigenvalues:

$$\mu_i = \frac{L}{i\pi \tanh\left(i\pi \frac{R}{L}\right)}, \quad \text{and } \lambda_i = \left(\frac{i\pi}{L}\right)^2,$$

for $i = 1, \dots, \infty$. The operator \mathcal{Q}_s is continuous and coercive. Also \mathcal{Q}_f is continuous [26].

The reduction factor $\rho(m)$ with respect to the initial residual norm for the m -th iteration of the DN-GMRES method is defined as:

$$\|\mathbf{r}^{(m)}\| \leq \rho(m) \|\mathbf{r}^{(0)}\|,$$

where $\mathbf{r}^{(m)}$ is the residual vector at the m -th iteration. The most precise expression of the reduction factor depends on the iteration number (see [127, 50]). Asymptotically,

that estimate for $\mathbf{r}^{(m)}$, in the case of an operator \mathcal{R} characterized by real and positive eigenvalues, leads to

$$\lim_{m \rightarrow \infty} \rho = \frac{\sqrt{\sigma_{max}} - \sqrt{\sigma_{min}}}{\sqrt{\sigma_{max}} + \sqrt{\sigma_{min}}}, \quad (5.14)$$

where

$$\sigma_{min} = \inf_{\eta \neq 0} \frac{(\mathcal{R}\eta, \eta)}{(\eta, \eta)}, \quad \sigma_{max} = \sup_{\eta \neq 0} \frac{(\mathcal{R}\eta, \eta)}{(\eta, \eta)}.$$

In our case, we have $\mathcal{R} = \mathcal{Q}_s^{-1}\mathcal{Q}$, whose eigenvalues can easily be proved to be real and positive. However, always in the case of an operator with real and positive eigenvalues, a non-asymptotic and iteration-independent bound for the reduction factor is given by

$$\rho = \sqrt{1 - \frac{\sigma_{min}}{\sigma_{max}}}, \quad (5.15)$$

where, for our problem,

$$\sigma_{min} = \inf_{\eta \neq 0} \frac{(\mathcal{Q}_s^{-1}\mathcal{Q}\eta, \eta)}{(\eta, \eta)}, \quad \sigma_{max} = \sup_{\eta \neq 0} \frac{(\mathcal{Q}_s^{-1}\mathcal{Q}\eta, \eta)}{(\eta, \eta)}.$$

Estimate (5.15) is not as sharp as (5.14) but it is easier to compute.

We have:

$$\sigma_{min} = \inf_{\eta \neq 0} \frac{(\mathcal{Q}_s^{-1}(\mathcal{Q}_f + \mathcal{Q}_s)\eta, \eta)}{(\eta, \eta)} = 1 + \inf_{\eta \neq 0} \frac{(\mathcal{Q}_s^{-1}\mathcal{Q}_f\eta, \eta)}{(\eta, \eta)} = 1, \quad (5.16)$$

since the operator \mathcal{Q}_f is positive on $L^2(\Sigma)$ and $\mu_i \rightarrow 0$ and $\lambda_i \rightarrow \infty$ as $i \rightarrow \infty$. For the supremum we get:

$$\sigma_{max} = 1 + \sup_{\eta \neq 0} \frac{(\mathcal{Q}_s^{-1}\mathcal{Q}_f\eta, \eta)}{(\eta, \eta)} = 1 + \frac{\rho_f \mu_{max}}{\rho_s h_s + a\delta t^2 + \delta t^2 b \lambda_{min}}.$$

In [6], it is proved that the DN-Richardson algorithm applied to the simplified problem (5.13) converges to the monolithic solution only if the relaxation parameter $\omega \in (0, \omega_{max}]$, with

$$\omega_{max} = \frac{2}{1 + \frac{\rho_f \mu_1}{\rho_s h_s + a\delta t^2 + \delta t^2 b \lambda_1}}.$$

Thus, $\sigma_{max} = \frac{2}{\omega_{max}}$. Plugging this result and (5.16) into (5.15), we obtain

$$\begin{aligned} \rho &= \sqrt{1 - \frac{\omega_{max}}{2}} \\ &= \sqrt{\frac{\rho_f \mu_1}{\rho_f \mu_1 + \rho_s h_s + a\delta t^2 + \delta t^2 b \lambda_1}}. \end{aligned}$$

Since $0 < \rho < 1$, the advantage of the DN-GMRES algorithm is that convergence is always reached, whereas the DN-Richardson method has a constraint on the relaxation parameter. However, as the added-mass effect gets critical, $\omega_{max} \rightarrow 0$; so the reduction factor $\rho \rightarrow 1$ and convergence slows down.

5.4 ILU preconditioners

One of our goal in the present chapter is to show that non-modular algorithms for FSI should not be dismissed. In particular, we claim the efficiency of non-modular preconditioners for problems affected by a large added-mass effect. In this section we describe our monolithic strategy to solve system (3.4).

The basic aspects of our non-modular approach are the use of fluid and structure problems in terms of velocities, the use of a single finite element partition for the whole domain and the use of the same velocity finite element space for fluid and structure problems (that can easily be attained by using stabilization techniques). In this frame, the continuity of velocities is straightforward and the continuity of stresses is imposed weakly. For more details, see Section 3.2.1.

The first problem related to the monolithic FSI matrix is the discrepancy between the entries in the different blocks. In order to solve this issue, we consider a diagonal scaling of the matrix (applied on the left). The diagonal scaling we performed for the numerical simulations in Section 5.5 and 5.6 is the following. Let D be the diagonal matrix whose element are the diagonal coefficients of A (3.5). Instead of solving system (3.4), we solve:

$$\hat{A}\mathbf{X}^{n+1} = \hat{\mathbf{b}}^{n+1}$$

where $\hat{A} := D^{-1}A$ and $\hat{\mathbf{b}}^{n+1} := D^{-1}\mathbf{b}^{n+1}$. Note that the diagonal scaling can only be performed on matrix (3.5) and not on matrix (3.8).

The system matrix \hat{A} is preconditioned by an incomplete LU factorization P , the so-called ILUT preconditioner (see [127]). The ILUT preconditioner allows to fix a threshold (entries smaller than the threshold are discarded) and the level of fill-in (that defines the maximum number of non-zero entries per row). Again, we make use of left-preconditioning:

$$P^{-1}\hat{A}\mathbf{X}^{n+1} = P^{-1}\hat{\mathbf{b}}^{n+1} \quad (5.17)$$

This method is non-modular, in the sense that the whole monolithic matrix is needed to compute the preconditioner.

Remark 5.5. *An appropriate fluid formulation is important for the efficiency of ILU-type preconditioners applied to the FSI system. Inf-sup stable elements yield linear systems that are indefinite since they represent saddle-point problems. By using stabilized formulations the zero pressure block of these systems is replaced by a semi-positive definite matrix. This improves remarkably the efficiency of iterative solvers preconditioned with ILU-type preconditioners (see e.g. [135, 1, 59, 22]).*

In the non-modular approach, we aim at solving the FSI linear system through standard iterative methods. The preconditioned system is solved by a matrix-free Krylov

method. Because of the non-symmetric nature of the system, we consider the GMRES and BiCGStab algorithms. We denote this combination by ILUT-GMRES and ILUT-BiCGStab, respectively. Every iteration of the Krylov method requires to solve a linear system with the preconditioner as system matrix. The solution of this system is very simple and cheap thanks to the ILU structure of the preconditioner. This is a main difference with respect to the DN preconditioner, where the solution of the system with the preconditioner as system matrix involves expensive fluid and structure evaluations. Thus, for an equal number of outer Krylov method iterations, the non-modular approach is much faster.

The GMRES method is based on the minimization of the residual of the preconditioned system (5.17). This algorithm requires to store the Krylov base, where every element of the base is an array of size the number of unknowns. Due to memory constraints, the maximum number of Krylov elements that can be stored must be limited. When this limit is reached, the GMRES method must be re-started. The BiCGStab algorithm is based on a quasi-minimization of the residual that does not require to store the Krylov base, drastically reducing the memory usage. The GMRES algorithm (without re-starting) requires a lower number of iterations than BiCGStab; however, the latter performs better than the re-started GMRES.

5.5 Numerical results for the straight cylindrical pipe

Through our numerical experimentation we aim at analyzing how the added-mass effect affects the performance of the different FSI algorithms considered above and those described in Section 3.3. Our goal is to simulate the propagation of a pressure pulse in a straight pipe with deformable boundaries as the structure density varies. We consider both the fully $3d$ problem, whose fluid domain is a cylinder of radius $R_0 = 0.5$ cm and length $L = 6$ cm (Figure 5.2 (a)), and its $2d$ approximation, obtained by intersecting the pipe with a plane. The bi-dimensional problem differs from the one considered in Chapter 4 for the fact that here the structure is $2d$ too. The fluid and structure physical parameters used in the simulations are listed in Table 5.1: a double line separates the common ones from the ones of the $2d$ problem only (see [104]), which are separated also from the parameters of the $3d$ problem (see [45]).

On the inflow section we impose Neumann boundary (4.2), whereas on the outflow section a homogeneous Neumann condition has been imposed. The amplitude P_{in} of the pressure pulse has been taken equal to $2 \cdot 10^4$ dyne/cm² and the time duration of the pulse is 5 ms. We solve the problem over the time interval $[0, 0.012]$ s. Figure 5.3 displays the structure displacement vectors at $t = 2, 4, 6, 8$ ms.

For both problems we choose a conforming space discretization between fluid and structure: stabilized $\mathbb{P}_1 - \mathbb{P}_1$ finite elements for the fluid and \mathbb{P}_1 finite elements for the structure.

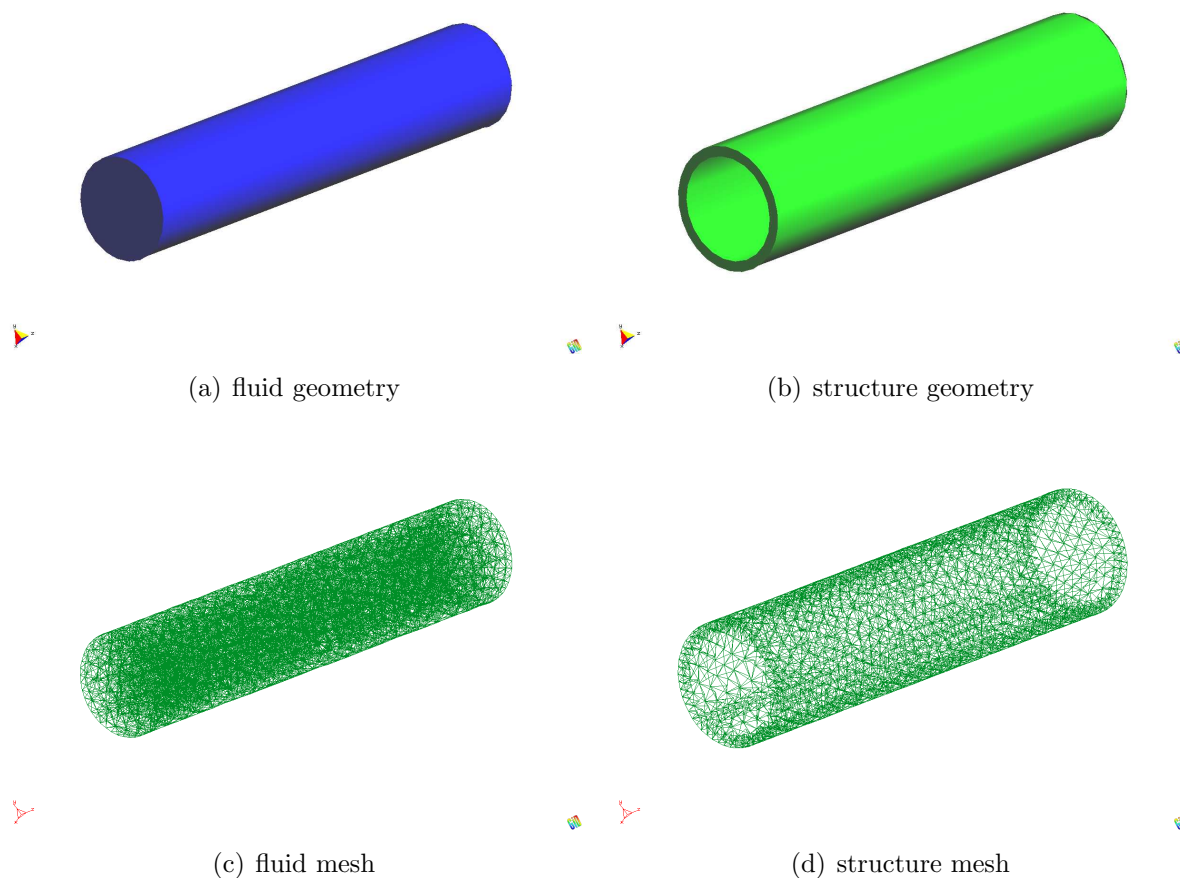


Figure 5.2: (a) Fluid and (b) structure geometries and the (c) fluid and (d) structure meshes used for the results in Section 5.5.3.

See Figure 5.2(c) and (d) for an example of fluid and structure meshes.

The software that has been used is ZEPHYR, a multi-physics finite element code written in Fortran and developed at CIMNE-UPC (Barcelona). For the ILUT preconditioner and iterative solvers, we have used SPARSKIT, developed by Saad (see [126]). All the simulations were performed on a 3.2 GHz Pentium 4 with 2 GB of RAM.

5.5.1 Comparison between the DN-Richardson and DN-GMRES methods

We solve the $2d$ problem with the two DN-Richardson and DN-GMRES algorithms (semi-implicit version) on a structured mesh of 61×21 fluid nodes and 61×4 structure nodes, with time step $\delta t = 2 \cdot 10^{-4}$ s. We consider different values of the structure density

CHAPTER 5. COMPARISON BETWEEN MODULAR AND NON-MODULAR APPROACHES

Fluid density: $\rho_f = 1.0 \text{ g/cm}^3$	Fluid viscosity: $\mu = 0.035 \text{ poise}$
Structure density: $\rho_s = 1.1 \text{ g/cm}^3$	Wall thickness: $h_s = 0.1 \text{ cm}$
Young modulus: $E = 7 \cdot 10^5 \text{ dyne/cm}^2$	Viscoelastic parameter: $\gamma = 10^{-1} \text{ dyne} \cdot \text{s}$
Shear modulus: $G = 2.5 \cdot 10^5 \text{ dyne/cm}^2$	Poisson coefficient: $\nu = 0.4$
Lamé constants: $\mu_\ell = 10^6 \text{ dyne/cm}^2$, $\lambda_\ell = 1.73 \cdot 10^6 \text{ dyne/cm}^2$	

Table 5.1: Fluid and structure physical properties for the numerical tests

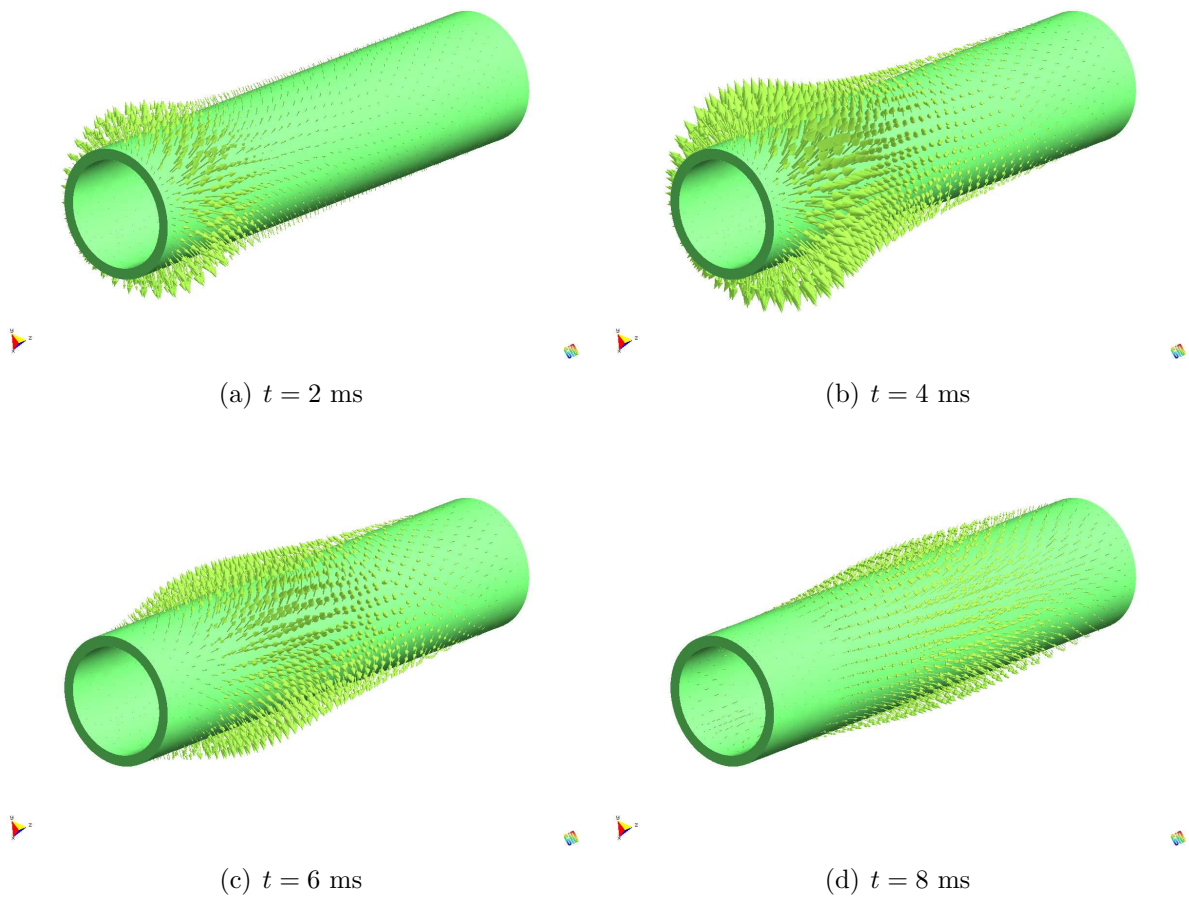


Figure 5.3: Structure displacement vectors as the pressure pulse moves from the inflow to the outflow section. Solution at every 2 ms.

$\rho_s = 500, 100, 50, 10, 5, 1 \text{ g/cm}^3$. Similar results have been reported in [26, 104] for inf-sup stable finite elements for the fluid and simplified structural models under the hypotheses of plane stress and membrane deformations.

We choose to adopt the explicit treatment of the nonlinearities in order to focus on the

fluid-structure coupling iterations.

Figure 5.4 shows the number of coupling iterations needed by the two algorithms to satisfy the stopping criterion ((5.8) with tolerance 10^{-4}) at each time step, for the different densities. The number of subiterations for the DN-Richardson algorithm increases dramatically as the structure density approaches the fluid one. Notice in the legend the relaxation parameter ω taken in each case: it corresponds to the highest value under which we have convergence of the coupling iterations. The relaxation parameter can be interpreted as an index of “stiffness” of the fluid-structure coupling. When using the DN-GMRES algorithm the number of subiterations increases only slightly as the structure density decreases. In fact, the two methods are almost equivalent in the case of high structure densities, but the advantage of employing GMRES instead of Richardson iterations becomes clear in presence of a strong added-mass effect. Moreover, no relaxation is needed for the convergence of the DN-GMRES algorithm.

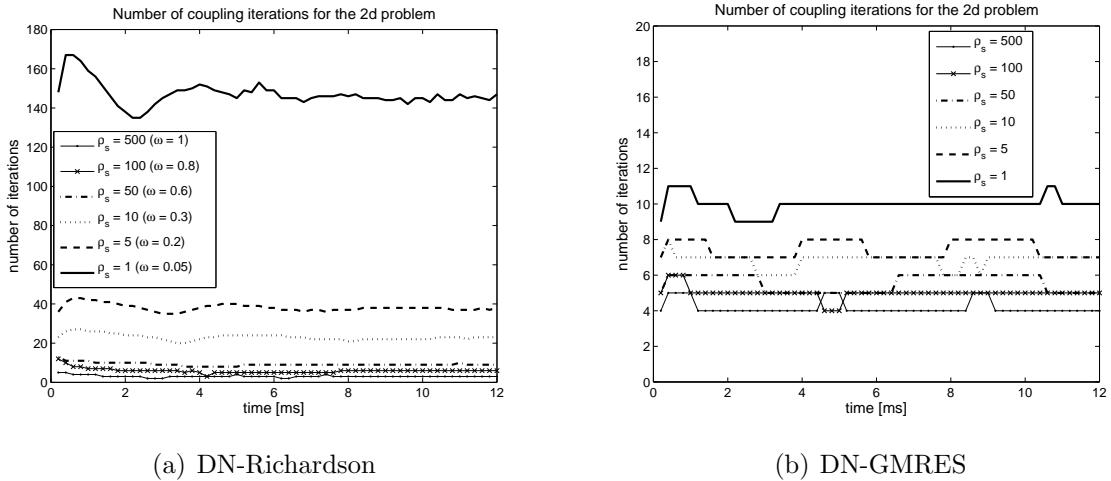


Figure 5.4: Number of coupling iterations needed to satisfy the convergence criterion at each time step for (a) the DN-Richardson and (b) DN-GMRES methods.

To better show the improvement of the DN-GMRES algorithm we report in Figure 5.5 the average number of coupling iterations over the time interval for the two methods as the structure density varies. Both methods are fairly insensitive to mesh size variations. The coarser structured mesh used for the comparison has 41×16 fluid nodes and 41×3 structure nodes.

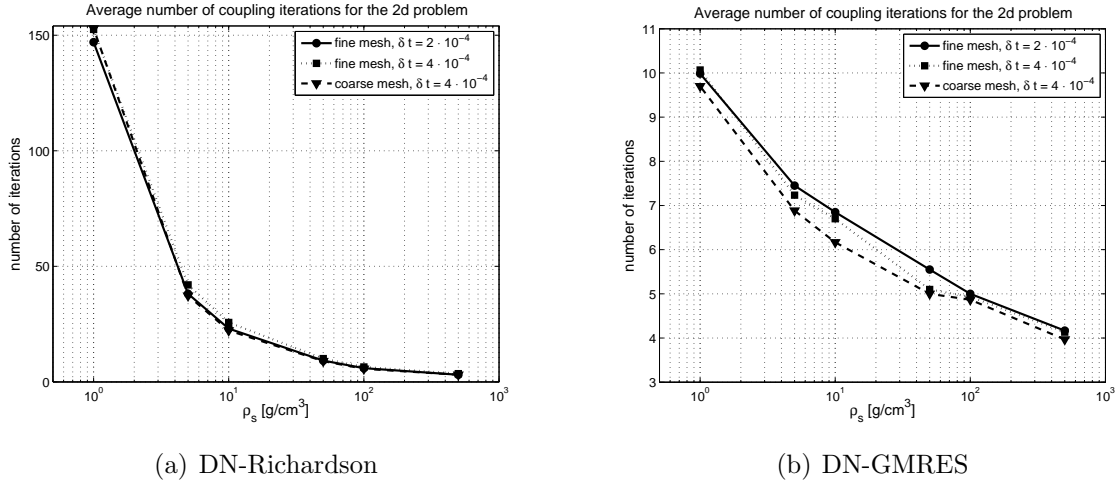


Figure 5.5: Average number of coupling iterations for (a) the DN-Richardson and (b) DN-GMRES methods as the structure density varies. Comparison for different meshes and different time step sizes.

5.5.2 The DN-GMRES method: implicit and semi-implicit versions

In order to check the computational savings allowed by the explicit treatment of the nonlinearities, we compare the implicit and semi-implicit versions of the DN-GMRES algorithm for the $2d$ problem.

Figure 5.6(a) shows the average number of nonlinear iterations of a fixed point algorithm for two different time step sizes, two different tolerances of the nonlinear loop, and for all the structure densities specified in Section 5.5.1. For high ρ_s the nonlinearity is mainly due to the convective term in the fluid equations, while as ρ_s decreases the domain nonlinearities become more important.

The implicit DN-GMRES method uses two nested loops: an external one dealing with the nonlinearity and an internal one solving every linearized system. Thus, the implicit method is computationally intensive, with a high number of fluid structure evaluations (loosely speaking, number of nonlinear iterations times number of average coupling iterations). We plot the cumulative number of iterations, i.e. the sum of the number of GMRES iterations required by every fixed point iteration, of the implicit DN-GMRES for the $2d$ test problem in Fig. 5.6(b). On the contrary, the DN-Richardson method allows to use only one loop that deals with both nonlinear and coupling iterations (see [4]). Even though the nonlinear iterations are not so ill-posed as the coupling iterations, the number of cumulative iterations increases a lot.

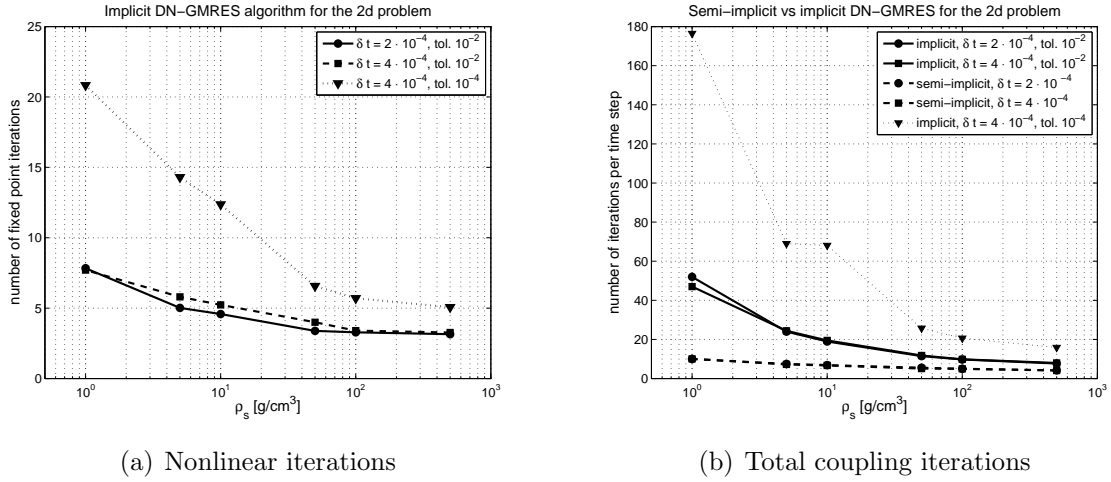


Figure 5.6: (a) Average number of fixed point iterations for the implicit version and (b) average number of total GMRES iterations per time step for the implicit and semi-implicit versions, for different structure densities and time step sizes.

Remark 5.6. *Although the use of one-loop algorithms can reduce the number of cumulative iterations, the matrix and right-hand side have to be updated at every iteration. When using nested loops, the matrix and right-hand side only need to be updated every nonlinear (external) iteration. The use of one-loop algorithms with DN-GMRES is not straightforward because the GMRES algorithm assumes the same system matrix during the iterative process. A way to get a one-loop algorithm is the use of a FGMRES method, that allows perturbations of the system matrix. FGMRES can only be used with right preconditioning, so the DN preconditioner must be applied to the right in this situation.*

In Figure 5.6(b), we compare the average number of GMRES iterations per time step for the implicit and semi-implicit versions of DN-GMRES, as ρ_s varies. In the case of a low density structure, an explicit treatment of the nonlinearity reduces drastically the CPU cost because no nonlinear iterations must be performed; when using the ALE formulation, every nonlinear iteration of the shape domain involves to compute a Laplacian problem. The difference between the CPU cost of semi-implicit and implicit schemes gets even bigger with a tighter tolerance, as expected. Therefore, in hemodynamics applications it is very appealing to deal explicitly with the geometrical and fluid nonlinearities, while keeping the fluid-structure system coupled.

The computational savings obtained by a semi-implicit treatment of the nonlinearity are also reported in Section 5.6.3 for a realistic 3d problem.

5.5.3 The ILUT-GMRES and ILUT-BiCGStab methods

We apply our non-modular approach to the $2d$ and $3d$ problems for the same values of ρ_s reported in Section 5.5.1. The preconditioners adopted are the incomplete LU factors of the scaled monolithic system with 20 non-zero entries per row and threshold 0.1. For the GMRES method, two different values for the maximum dimension of the Krylov space (20 and 50 for the $2d$ problem, 50 and 80 for the $3d$ one) are taken into account. Again, we consider the semi-implicit versions. The main goal of this section is not to compare re-started GMRES and BiCGStab iterative solvers; as commented in Section 5.4, the best choice will strongly depend on the available computer memory. Our purpose is rather to show how ILUT preconditioners behave as the structure density approaches the fluid one.

For the $2d$ problem, the meshes are the same ones used for the tests in Section 5.5.1. For the $3d$ case we considered two unstructured meshes: the coarse one with average element size $h = 0.14$ (4347 nodes and 21163 tetrahedra, see Figure 5.2(c) and (d)) and the fine one with average element size $h = 0.12$ (6452 nodes and 32190 tetrahedra). The tolerance on the normalized residual used for the iterative solvers is 10^{-4} .

In Figure 5.7 and 5.8, we observe the number of GMRES iterations for the bi-dimensional and three-dimensional problems, respectively, on two different meshes and with two different time step sizes ($\delta t = 2 \cdot 10^{-4}$ s and $\delta t = 4 \cdot 10^{-4}$ s). Refining the mesh causes an increase in the iterations number, while the number of iterations decreases with the time step. This can be explained by the fact that the starting point for the GMRES method is the solution at the previous time step. However, the difference in the number of iterations with respect to the mesh size and the time step reduces as the Krylov space dimension gets bigger and as the added-mass effect becomes important. For both problems increasing the maximum dimension of the Krylov space ensures faster convergence of the GMRES method, because it reduces the re-starting of the method. Furthermore, the algorithm shows better convergence properties for problems with large added-mass effect.

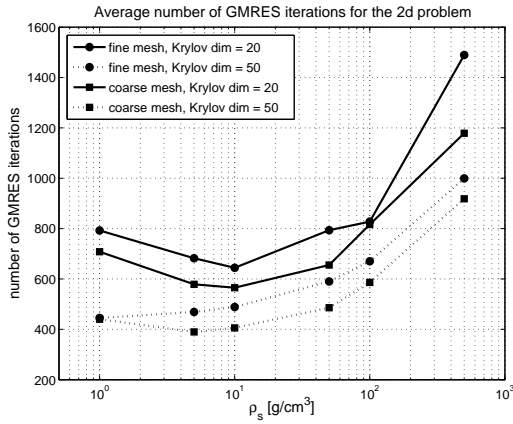
The convergence of the ILUT-BiCGStab algorithm for the $2d$ and $3d$ case is shown in Figures 5.9(a) and 5.9(b), respectively. ILUT-BiCGStab shows the same behavior than ILUT-GMRES in the $2d$ problem (Fig. 5.9(a)), while the trend is more irregular for the $3d$ test (Fig. 5.9(b)).

As a conclusion, non-modular ILUT preconditioners are suitable for large added-mass problems, because they do not exhibit the ill behavior of the DN preconditioner as ρ_s/ρ_f decreases (reported in Fig. 5.5).

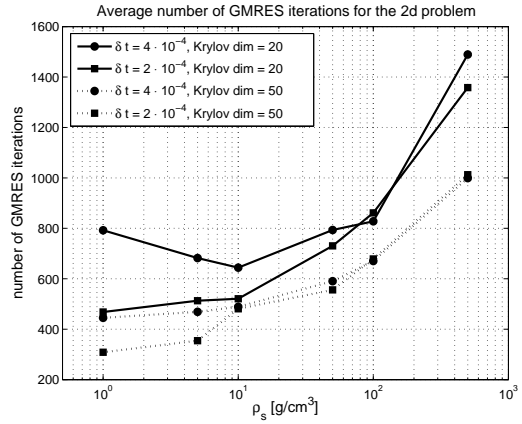
5.5.4 Comparison between the ILUT-solver and PIC-solver

We compare now CPU cost and number of iterations of the two non-modular approaches, the ILUT-solver and the PIC methods, with respect to the structure density for the $3d$

5.5. NUMERICAL RESULTS FOR THE STRAIGHT CYLINDRICAL PIPE

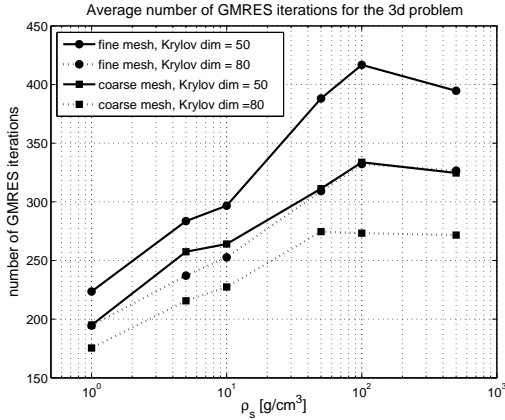


(a) Dependence with h

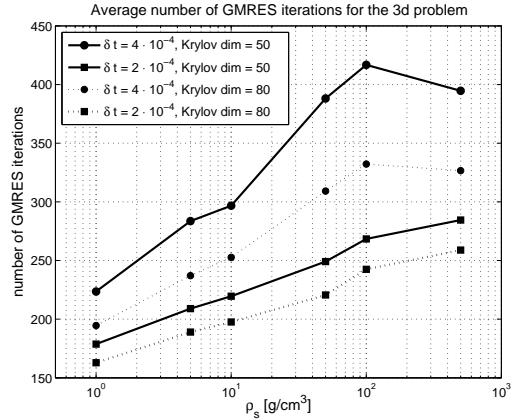


(b) Dependence with δt

Figure 5.7: Average number of GMRES iterations to solve the monolithic system for the $2d$ problem, for different ρ_s . Comparison for (a) different meshes and (b) different time step sizes.



(a) Dependence with h



(b) Dependence with δt

Figure 5.8: Average number of GMRES iterations to solve the monolithic system for the $3d$ problem, for different ρ_s . Comparison for (a) different meshes and (b) different time step sizes.

straight artery. Since we are interested in comparing the efficiency of different methods, in the numerical simulations we will only consider the PIC algorithm and not the FSY one. Indeed, the latter is more expensive in terms of computational time (see Section 3.3.2). For the solution of step 2 of the PIC method, we adopt the strategy described in Section 3.6.2.

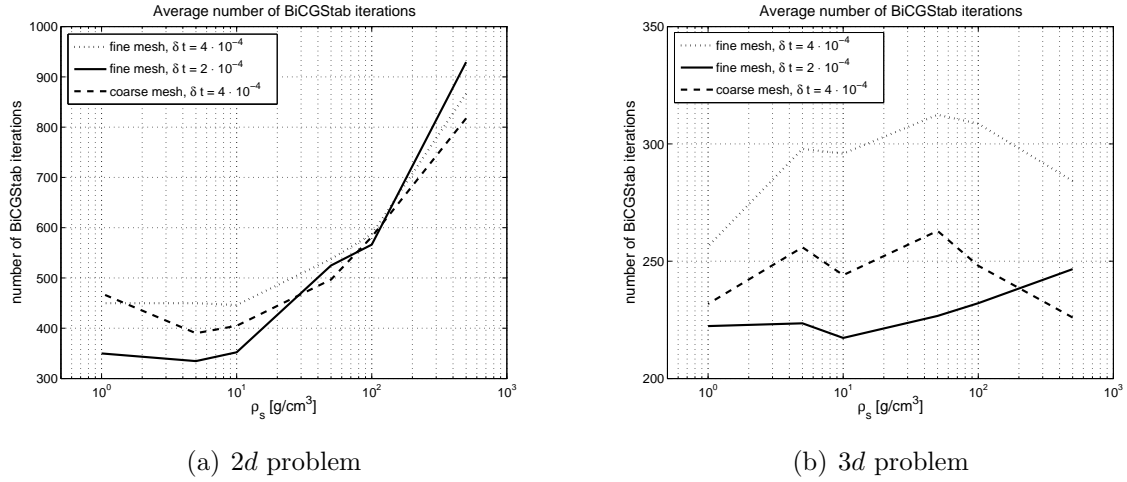


Figure 5.9: Average number of BiCGStab iterations to solve the monolithic system for the (a) 2d and (b) 3d problem, for different ρ_s , meshes and time step sizes.

In particular, for the solution of the pressure-structure system, we consider the GMRES and the BiCGStab algorithms. The corresponding PIC schemes are called PIC-GMRES and PIC-BiCGStab.

The solver iterations and CPU cost for the ILUT-GMRES and PIC-BiCGStab methods are reported in Fig. 5.10. For large added-mass effect, ILUT-GMRES requires less CPU cost whereas PIC-BiCGStab is cheaper for larger values of ρ_s . The CPU cost of ILUT-GMRES decreases as the added-mass effect becomes more important while the PIC-BiCGStab method exhibits a slight increase of CPU cost.

5.6 Numerical results for the carotid bifurcation

Our goal is now to simulate a pressure wave in the carotid bifurcation using the same fluid and solid properties as in the straight pipe case. The geometry is a realistic one first used in [83]. Figure 5.11(a) and 5.11(b) show the fluid and the structure geometries. The fluid and the structure are initially at rest and the same Neumann boundary conditions of the straight pipe are imposed at both the inlet and the outlet. The average inflow diameter is 0.67 cm, the time step used is $\delta t = 2 \cdot 10^{-4}$ s and the time interval is $[0, 0.012]$ s. Figure 5.12 shows the fluid pressure together with the structural deformation amplified by a factor 10 at time $t = 3, 6, 9, 12$ ms.

Again we choose a conforming space discretization between fluid and structure: stabilized $\mathbb{P}_1 - \mathbb{P}_1$ finite elements for the fluid and \mathbb{P}_1 finite elements for the structure. See Figure 5.11(c) and 5.11(d) for an example of fluid and structure meshes.

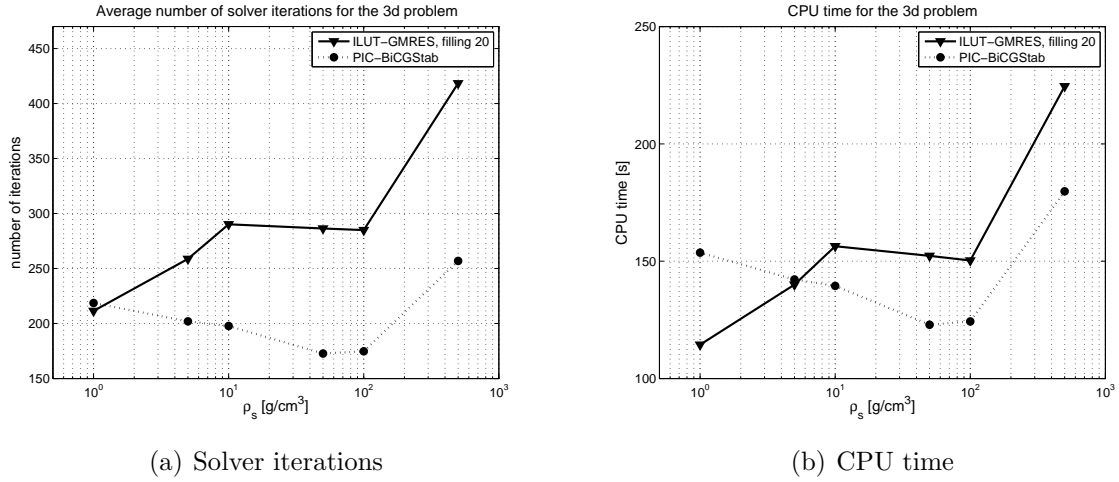


Figure 5.10: (a) Average number of solver iterations and (b) CPU time for the ILUT-solver and the PIC methods as the structure density varies.

5.6.1 Comparison between the ILUT-solver, PIC-solver, and DN-GMRES methods

We first compare the ILUT-solver and the PIC methods. In particular, we consider the ILUT-BiCGStab method, the ILUT-GMRES one with different fill-ins for the preconditioners, the PIC-GMRES and PIC-BiCGStab algorithms. The tolerance for the iterative method is 10^{-4} for all the schemes. When the GMRES method is adopted the maximum dimension of the Krylov base is set to 40. The unstructured mesh we used has diameter $h = 0.11$ (8737 nodes and 40814 tetrahedra) and is reported in Figure 5.11(c) and 5.11(d).

Fig. 5.13(a) shows the average number of solver iterations for the usual structure densities $\rho_s = 500, 100, 50, 10, 5, 1 \text{ g/cm}^3$. As already noticed in Sec. 5.5.3, the decreasing of the structure density improves the performances of the ILUT-GMRES method. Moreover, increasing the fill-in of the preconditioners reduces the number of GMRES iterations up to $\rho_s = 100$. This reduction in the number of iterations does not correspond to a decrease in the CPU time for $\rho_s > 1$, as it can be seen in Fig. 5.13(b). In fact, the more accurate ILU factorizations require fewer iterations to converge but the cost to compute the incomplete factors (and sometimes the overall CPU cost) increases. For low structure densities the ILUT-BiCGStab behaves worse than the ILUT-GMRES. In any case, both methods have very similar CPU cost for large-added mass effect problems. The choice of the iterative solver (GMRES vs. BiCGStab) will depend on the size of the problem and computer memory (see Section 5.4). While the PIC-BiCGStab method always converges in less iterations and faster than the PIC-GMRES.

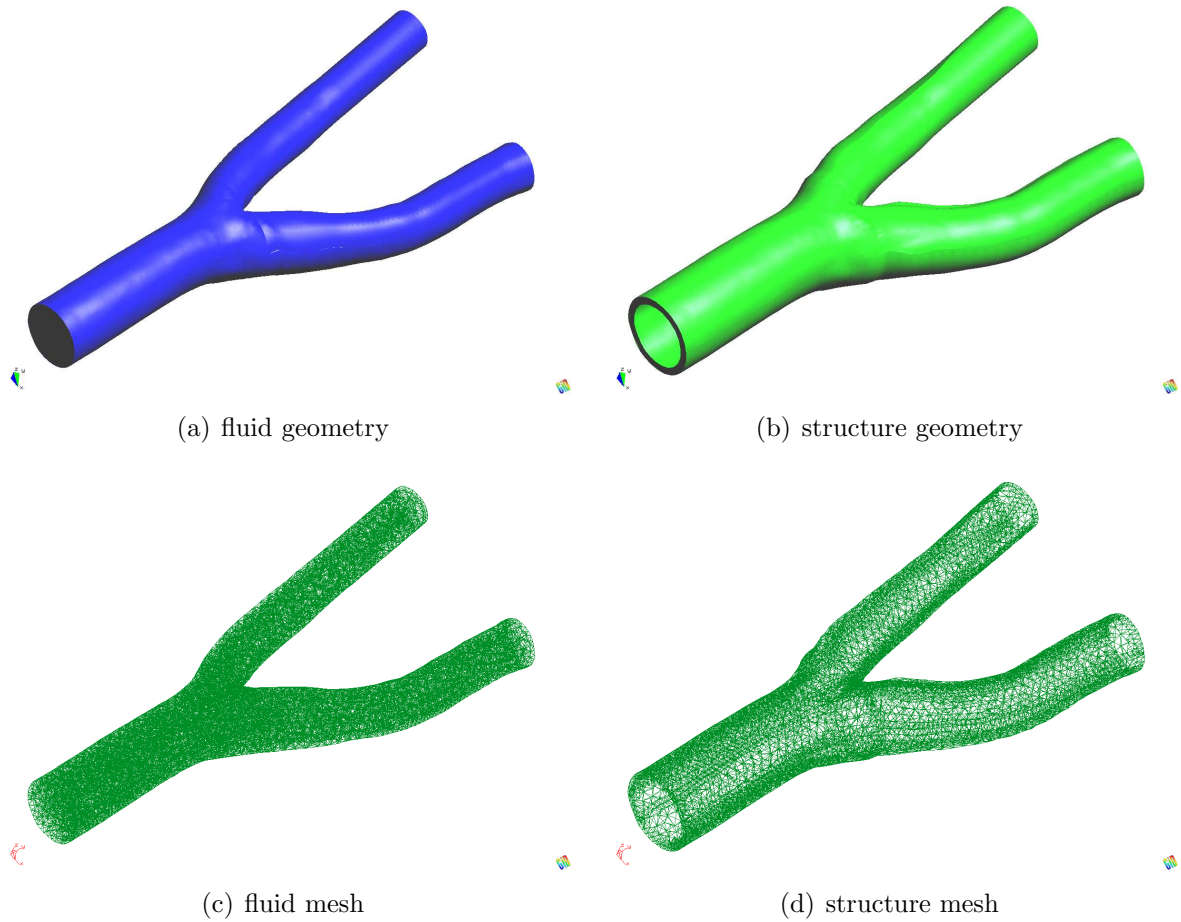


Figure 5.11: (a) Fluid and (b) structure geometries and the (c) fluid and (d) structure meshes used for the results in Section 5.6.1.

The PIC-solver methods whose results are reported in Fig. 5.13 employ the point-diagonal preconditioner to solve system (3.18b). We also considered the block-diagonal one. Obviously, this latter drastically reduces the number of solver iterations (Fig. 5.14(a)) but it is much more time consuming than the point-diagonal preconditioner (Fig. 5.14(b)).

The DN-GMRES algorithm is much more expensive in terms of CPU time than the other two methods. That is the reason why the results are not reported in the same graph but in a separated one (Fig. 5.15). Even though it represents an improvement with respect to the DN-Richardson algorithm, the DN-GMRES one is not competitive for realistic hemodynamics problem.

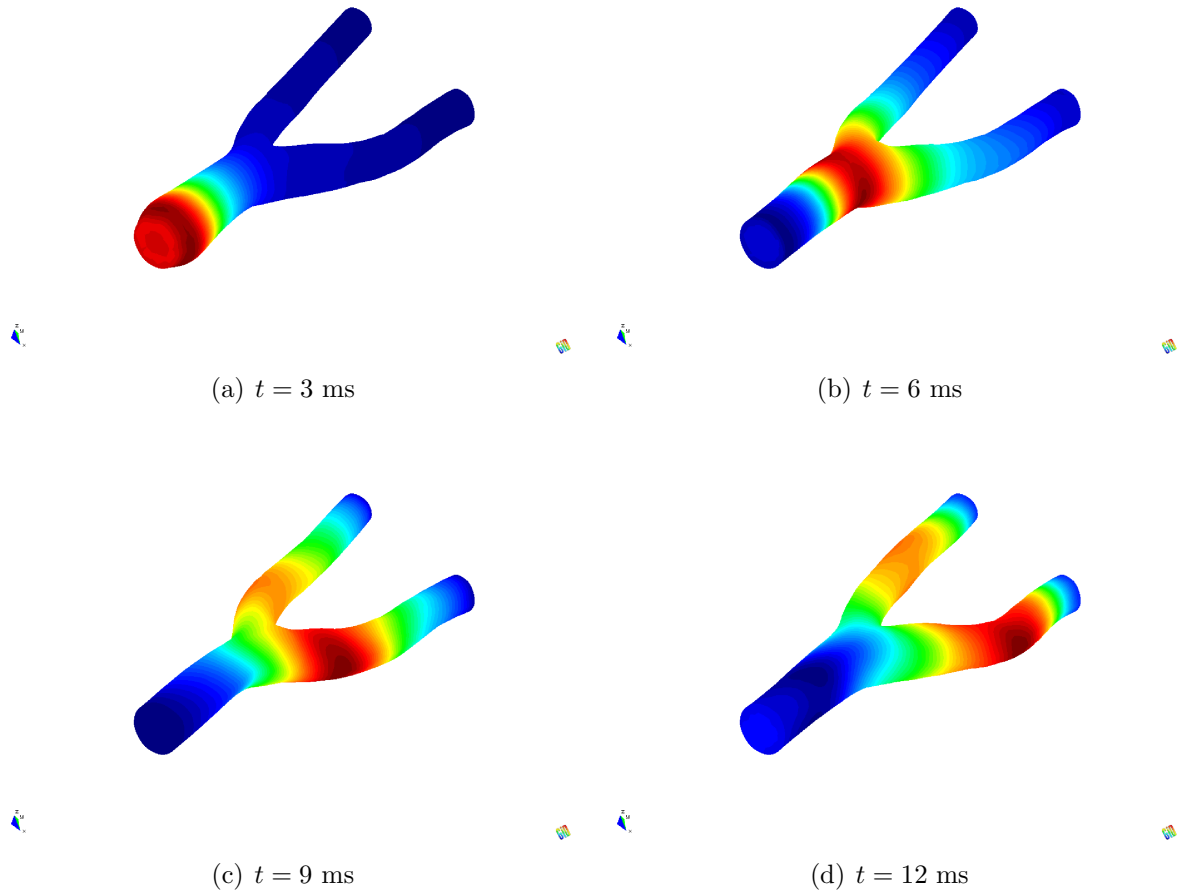


Figure 5.12: Propagation of the initial pressure pulse, moving from the inflow to the outflow section. Solution at every 3 ms.

5.6.2 The ILUT-GMRES and the PIC-BiCGStab methods for hemodynamics problems

Now we restrict our attention to the problem with the largest added-mass effect, i.e. we set $\rho_s = 1$. Fig. 5.16(a) reports the average number of solver iterations and Fig. 5.16(b) the CPU time required by the ILUT-GMRES and PIC-BiCGStab methods to solve the bifurcation problem on four different meshes. From the coarsest to the finest, the meshes we used have 6796, 8737, 13148, and 16402 nodes (31138, 40418, 62879, and 79528 tetrahedra, respectively). The PIC-BiCGStab method takes always more iterations to converge than the ILUT-GMRES one. The gap between the iterations number seems to increase with the refinement of the mesh. The CPU times needed by the two methods to complete the

CHAPTER 5. COMPARISON BETWEEN MODULAR AND NON-MODULAR APPROACHES

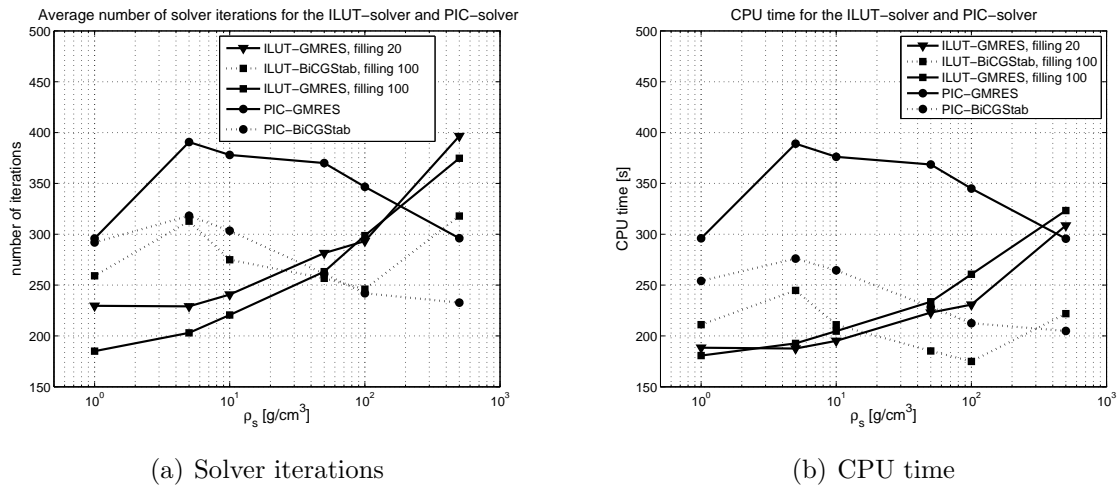


Figure 5.13: (a) Average number of solver iterations and (b) CPU time for the ILUT-solver and the PIC methods as the structure density varies.

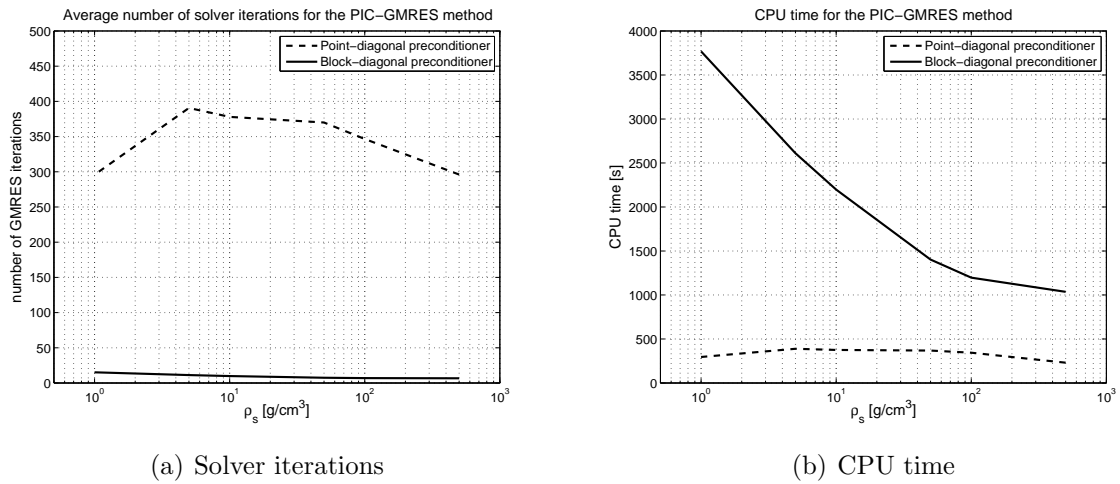


Figure 5.14: (a) Average number of GMRES iterations and (b) CPU time for the PIC-GMRES method with different preconditioners as the structure density varies.

simulation show the same tendency. Thus, the ILUT-GMRES algorithm remains the less time-consuming also when the size of the problem increases.

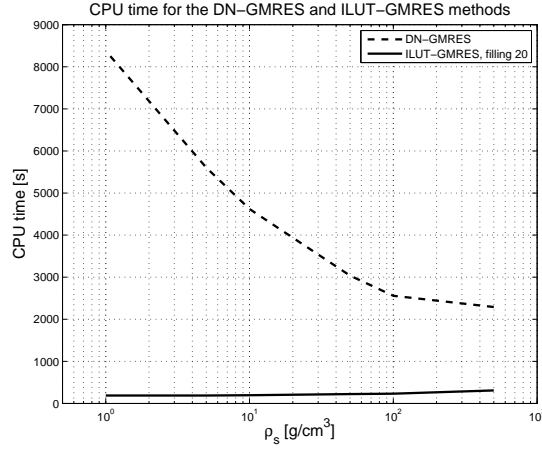
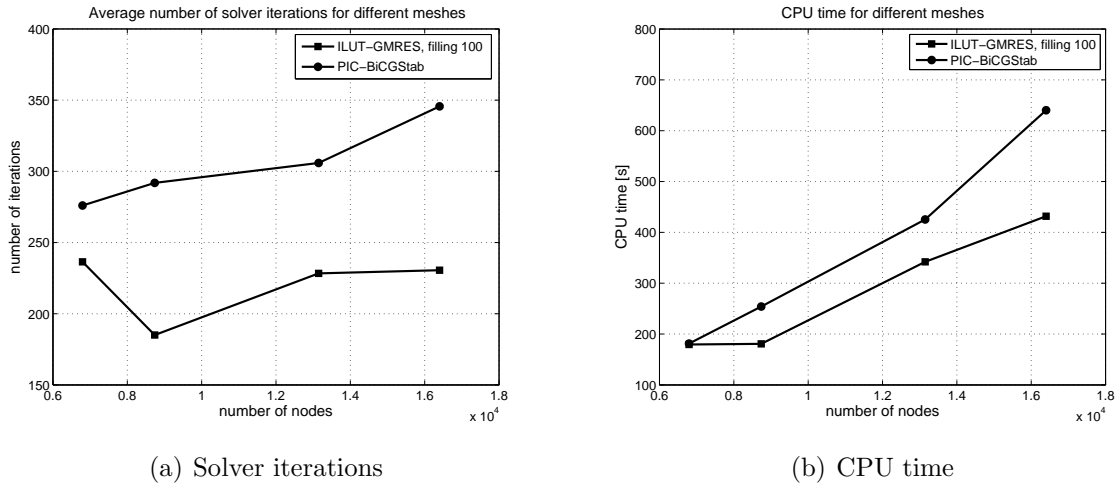


Figure 5.15: CPU time for the ILUT-GMRES and the DN-GMRES methods as the structure density varies.



(a) Solver iterations

(b) CPU time

Figure 5.16: (a) Average number of solver iterations and (b) CPU time for the ILUT-GMRES and the PIC-BiCGStab methods for different meshes.

5.6.3 The ILUT-solver: implicit and semi-implicit versions

As done in Section 5.5.2 for the DN-GMRES method and the $2d$ straight artery, we show the efficiency of a semi-implicit treatment of the nonlinearity for ILUT preconditioners. We solved the carotid bifurcation problem with ILUT-BiCGStab. We considered two different time step values and all the structure densities specified in Section 5.6.1. Fig. 5.17(a) shows the average number of fixed point iterations (with tolerance 10^{-2}) for the

implicit treatment of the nonlinearity. The CPU cost is reported in Figure 5.17(b). For the implicit algorithm, the number of nonlinear iterations is fairly insensitive to structure density variations whereas the CPU cost reduces when ρ_s increases. In any case, the computational savings associated to a semi-implicit treatment of the nonlinearity are clear in all situations.

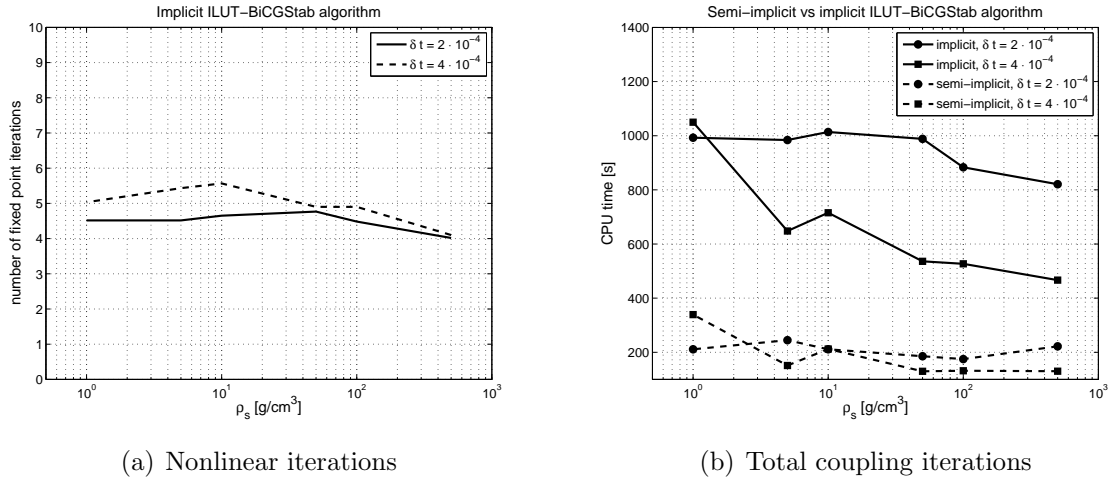


Figure 5.17: (a) Average number of fixed point iterations for the implicit version and (b) average CPU time per time step for the implicit and semi-implicit versions of the ILUT-BiCGStab method; values for different structure densities and time step sizes.

5.7 Conclusions

In this chapter, we took into account two different preconditioners for the coupled system obtained after linearization and full discretization of the FSI problem.

The first one is the classical Dirichlet-Neumann preconditioner. Two modular algorithms based on that preconditioner (the DN-Richardson and the DN-GMRES ones) have been considered. The reduction factor for the DN-GMRES method has been obtained for a model problem.

The second preconditioner is a non-modular ILUT preconditioner for the whole FSI system. We have introduced an appropriate monolithic formulation to be used with this preconditioner. Several aspects of this formulation have been also discussed in [137, 58].

The theoretical negative impact of the added-mass effect on the reduction factor agrees with the numerical experiments. The performances of DN-Richardson and DN-GMRES have been compared to those of two methods (ILUT-GMRES and ILUT-BiCGStab) yielded

by the non-modular ILUT preconditioner for the whole FSI system. Moreover, the DN algorithms and the ILUT-solver methods have been compared to another non-modular approach: the PIC scheme presented in Section 3.3.1. The difference with respect to the problem solved in Chapter 4 is that, in this chapter, we deal with d -dimensional structures and make use of stabilized finite elements methods.

The advantages of the explicit treatment for the nonlinearities of the FSI problem have been underlined once again. Thus, we dealt with the semi-implicit versions of all the methods mentioned above. This allowed us to focus on the fluid-structure coupling and on the effects of the added-mass.

We have carried out a broad set of numerical experiments. For problems with large added-mass effect we can draw the following conclusions:

- The DN-GMRES algorithm represents an improvement of the DN-Richardson one. However, they both perform well in case of high structure densities but suffer in case of critical added-mass effects.
- Unlike the DN-algorithms, the performance of the ILUT-solver methods is not deteriorated when the structure density approaches the fluid one. This good behavior in the large added-mass effect range pays off for the loss of modularity, also in the case of the PIC methods.
- The ILUT-solver method proved to be the least expensive in terms of CPU time for large problems. The PIC scheme is very competitive for smaller problems. Anyways, both non-modular preconditioners prove to be much more efficient than the modular DN-algorithm approach for the applications under consideration.
- A clear reduction of the CPU cost can be attained by considering a semi-implicit treatment of the nonlinearities.

CHAPTER 5. COMPARISON BETWEEN MODULAR AND NON-MODULAR
APPROACHES

Chapter 6

The interaction between a fluid and a poroelastic structure

6.1 Introduction

Let us take a closer look at the anatomy of the artery wall (see Figure 4.1, on the left). The intima is the innermost layer separated from the media layer by internal elastic lamina (IEL). It is made of a single layer of the endothelial cells. The endothelium is a cell layer with clefts among the cells which exchange water and solute between the arterial lumen and the intima. The media layer mainly contains smooth muscle cells and elastic fibers. The adventita is the outermost layer of the artery wall comprised of connective tissue and fibroblast. The blood from the arterial lumen enters the intima by crossing the endothelial cells. It passes through the intima and enters the media after crossing the IEL to serve the adventita and implanted smooth muscle cells.

Neglecting the porosity of the artery wall means to disregard an important feature of its nature. Thus, for a more realistic modeling of the fluid-structure problem appearing in hemodynamics, we switch from a purely elastic model for the artery wall to a poroelastic one. Modeling the poroelastic behavior of the artery wall represents a step forward towards the numerical simulations of complex clinical problems, such as the development and treatment of atherosclerosis.

It is believed that accumulation of low density lipoproteins (LDL) leads to the initiation of atherosclerosis. The LDL concentration is affected by the filtration flow through the endothelial layer. In turn, the velocity of this flow is affected by the deformation of the artery wall. Assuming for simplicity that the LDL concentration has no effect on the motion of the artery (or blood flow solution), a coupled fluid-poroelastic structure model needs to be developed to simulate this problem. Then, the transfer of LDL would be simulated by an advection-diffusion problem which uses the fluid velocities (inside both

the lumen and the wall) as advective velocities.

Nano-sized delivery vehicles are emerging as powerful tools for treating and imaging cardiovascular disease (see, e.g., [57]). One method that has been proposed to treat vulnerable plaques and diffuse atherosclerosis in the large arteries involves injecting a drug compound into the bloodstream with a catheter to transport the drug to the surrounding tissue. The simulation of these phenomena requires as well a coupled FSI methodology where blood is modeled as a Newtonian incompressible fluid and the artery wall is modeled as a linear, isotropic, and poroelastic medium.

The classic fluid-structure interaction problem in hemodynamics (Navier-Stokes/elasticity for thin structures coupling) has been broadly studied, see Section 2.5. Many works have been devoted also to the Navier-Stokes/Darcy coupling (see Section 6.2.2) to simulate mass transport from the arterial lumen to the arterial walls and inside the walls, which are supposed to be rigid. Up to our knowledge, the fluid-poroelastic structure interaction (FPSI) appearing in hemodynamics has been investigated in a very limited number of works [84, 25]. In [84], the Navier-Stokes equations for an incompressible fluid are coupled to the Biot equations, which govern the motion of a saturated poroelastic medium. The coupled system is linearized by Newton's method and solved by a monolithic solver. A monolithic approach is adopted also in [25], where the structure is described by a simplified poroelastic model.

We extend to FPSI problems some of the strategies proposed for fluid-elastic structure interactions in the previous chapters. Unlike [84, 25], we choose a fixed point method for the linearization of the Navier-Stokes/Biot coupled system. In this way, it is easy to consider the semi-implicit versions of all the algorithms, i.e. only one fixed point iteration is performed per time step. Semi-implicit methods enable us to better understand the Navier-Stokes/Biot coupling because nonlinearities are explicitly treated. To solve the linear FPSI system, we propose to apply both the monolithic approach introduced in Section 5.4 and partitioned procedures. It is the first time that a modular approach is adopted for FPSI problems. Among all the partitioned procedures derived from a domain decomposition viewpoint, we focus our attention on the Dirichlet-Neumann, Robin-Neumann, and Robin-Robin algorithms. We show again that, although the monolithic approach solves a problem whose size is bigger than that of the single subproblems, it proves to be efficient for the combination of physical parameters which maximizes the added-mass effect. On the other side, the Robin-Neumann scheme exhibits the best performances among the partitioned procedures in terms of robustness to parameters variations.

In Section 6.2 we state the Navier-Stokes/Biot coupled problem in its differential form, specifying the coupling conditions which lead to a mathematically well-posed problem. The variational formulation of the coupled problem is tackled in Section 6.3. The space and time discretization of the FPSI problem is challenging due to the fact that a double

inf-sup condition needs to be satisfied: one for the fluid subproblem and the other for the poroelastic system. While there exists a great variety of stabilization techniques for the incompressible Navier-Stokes equations, only a few works deal with stabilization for the incompressibility in poroelastic structures (see, e.g., [64] in case of using the finite difference method for the space discretization). For this reason, Section 6.4 is devoted to the derivation of a simple stabilized formulation for the structure subproblem. The matrix form associated to the fully discretized and linearized (Section 6.5) is detailed in Section 6.6. Sections 6.7 and 6.8 present our monolithic approach and the partitioned procedures we apply to solve the linear system. Finally, in Section 6.9 we carry out some numerical experiments on simplified $2d$ problems representing blood-vessel systems.

6.2 Problem setting

Suppose that the bounded, polyhedral, and moving domain $\Omega_t \subset \mathbb{R}^d$ ($d=2, 3$, being the space dimension, and $t \in [0, T]$ the time) is made up of two regions, Ω_t^f and Ω_t^p , separated by a common interface $\Sigma_t = \partial\Omega_t^f \cap \partial\Omega_t^p$. The first region Ω_t^f is occupied by an incompressible and Newtonian fluid (see Chapter 1), and the second one Ω_t^p is occupied by a fully-saturated elastic porous matrix. As for the FSI problem in Chapter 2, both domains depend on time. Here, we denote by \mathbf{n} the unit normal vector on the boundary $\partial\Omega_t^f$, directed outwards into Ω_t^p , and by \mathbf{t} the unit tangential vector orthogonal to \mathbf{n} . We assume the boundary $\partial\Omega_t$ (and so \mathbf{n} and \mathbf{t}) to be regular enough.

6.2.1 The Biot system

A porous medium is defined as a mixture of a solid material, called *skeleton* or *matrix*, and connecting *pores* filled with fluid (see Figure 6.1). The fluid and the solid are assumed

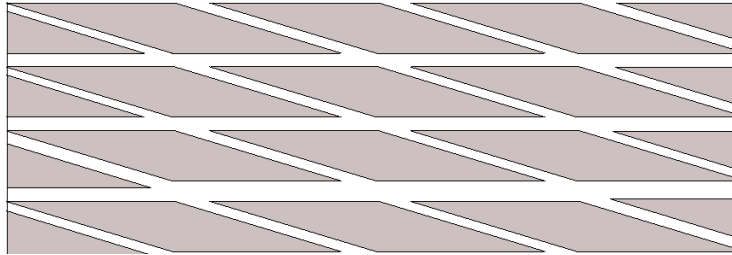


Figure 6.1: Schematic representation of the artery wall as a porous medium: matrix (dark) and connecting pores (blank).

to be incompressible. The dynamics of such a medium are described by the Biot system

[13, 14, 15]:

$$\rho_p D_t \mathbf{u}_s + \rho_d D_t \mathbf{q} - \nabla \cdot \boldsymbol{\sigma}_s^E(\boldsymbol{\eta}) + \nabla p_p = \mathbf{f}_s \quad \text{in } \Omega_t^p \times (0, T), \quad (6.1a)$$

$$\rho_d D_t \mathbf{u}_s + \rho_d D_t \frac{\mathbf{q}}{\phi} + K_D^{-1} \mathbf{q} + \nabla p_p = \mathbf{f}_d \quad \text{in } \Omega_t^p \times (0, T), \quad (6.1b)$$

$$\nabla \cdot (\mathbf{u}_s + \mathbf{q}) = 0 \quad \text{in } \Omega_t^p \times (0, T), \quad (6.1c)$$

consisting of the momentum equation for the balance of the total forces (6.1a), the momentum conservation equation for the fluid phase only (6.1b), and the constraint of incompressibility (6.1c). In system (6.1), ρ_d is the density of the fluid in the pores, and $\rho_p = \rho_s(1 - \phi) + \rho_d\phi$ is the density of the saturated porous medium, ρ_s being the density of the solid material and ϕ being the *porosity*. The porosity is the ratio of the pore volume over the total volume (pore + skeleton). We denote by $\mathbf{u}_s = \partial_t \boldsymbol{\eta}$ the velocity of the skeleton and by \mathbf{q} the filtration velocity, i.e. the relative velocity of the fluid phase with respect to the solid one, $\mathbf{q} = \phi(\mathbf{u}_d - \mathbf{u}_s)$. Here, \mathbf{u}_d is the velocity of the fluid in the porous medium. The hydraulic conductivity tensor is indicated with K_D . The effective Cauchy stress tensor of the matrix is $\boldsymbol{\sigma}_s^E$ and it is related to the displacement of the porous structure $\boldsymbol{\eta}$ by a suitable constitutive law. The pressure of the fluid in the pore is given by p_p . We define the total Cauchy stress for the poroelastic structure as

$$\boldsymbol{\sigma}_s = -p_p \mathbf{I} + \boldsymbol{\sigma}_s^E.$$

The right-hand side vectors \mathbf{f}_s and \mathbf{f}_d account for external body forces.

In the subsequent discussion, the values of densities, porosity, and hydraulic conductivity are constant in space and time.

The Biot system (6.1) is widely employed to model geotechnical problems. For that kind of applications the time derivative $D_t \mathbf{q}$ is extremely small. Therefore, it is neglected in (6.1a) and (6.1b). As for the moment, we keep it for hemodynamics applications. In fact, the only work [84] that employs equations (6.1) to model the arterial wall takes derivative $D_t \mathbf{q}$ into account.

Also when dealing with a poroelastic structure, we adopt a purely Lagrangian approach (See Section 2.1.1). However, we avoid to cast system (6.1) into the reference domain Ω_0^p , in order not to introduce additional variables and complicate the notation.

In order for system (6.1) to be well-posed, proper initial and boundary conditions must be imposed. In the following, the boundary conditions on $\partial\Omega_t^p \setminus \Sigma_t$ are chosen in a classical simple form, since they play no essential role in the interaction. On the exterior boundary of the porous medium we shall impose *drained conditions* $p_p = 0$ on the pressure and *clamped conditions* $\mathbf{u}_s = \mathbf{0}$ on the structure velocity at the inlet and outlet. In Fig. 6.2, we specify the boundary conditions imposed on $\partial\Omega_t$ for the 2d simulation of the Navier-Stokes/Biot system in Section 6.9.

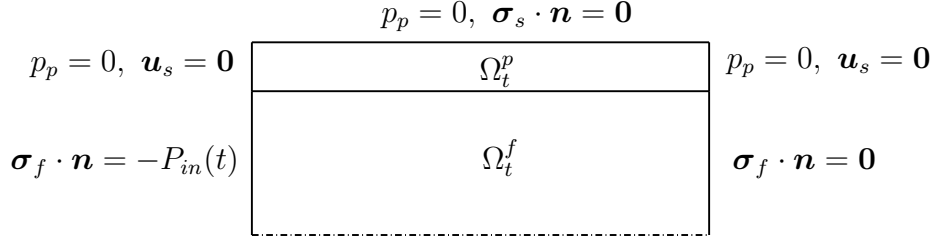


Figure 6.2: Boundary conditions imposed on the physical boundary of the $2d$ problem in Section 6.9.

6.2.2 The coupling conditions and the Biot/Navier-Stokes system

The objective of this subsection is to identify a physically consistent set of interface conditions which couple the Biot system (6.1) to the incompressible Navier-Stokes equations. The variational statement of the resulting problem must lead to a mathematically well-posed initial-boundary-value problem.

In Section 2.1.2 we saw that the natural transmission conditions at the interface of a fluid and an impervious elastic solid consist of continuity of velocity (2.13d) and stresses (2.13e). In order to understand the coupling between the fluid and a deformable and porous medium, we review the transmission relations for a fluid in contact with a rigid but porous solid matrix. In that case, we have two distinct scales of hydrodynamics: the first one is represented by the Navier-Stokes system and the second one by the Darcy equations

$$K_D^{-1} \mathbf{q} + \nabla p_p = \mathbf{f}_d \quad \text{in } \Omega^p, \quad (6.2a)$$

$$\nabla \cdot \mathbf{q} = 0 \quad \text{in } \Omega^p. \quad (6.2b)$$

Fluid mass conservation is a natural requirement at the interface, and continuity of pressure or vanishing tangential velocity of the viscous fluid are other classically assumed conditions [52, 88]. However, these issues have been controversial, see [133]. In fact, the location itself of the interface is uncertain, since the porous medium is a mixture of fluid and solid. Furthermore, Beavers and Joseph [10] discovered that a fluid in contact with a porous medium flows faster along the interface than a fluid in contact with a solid surface. This means that there is a slip of the fluid at the interface with a porous medium. To represent it, they proposed that the normal derivative of the tangential component of the fluid velocity $\mathbf{u}_f \cdot \mathbf{t}$ satisfy

$$\frac{\partial(\mathbf{u}_f \cdot \mathbf{t})}{\partial n} = \frac{\gamma}{\sqrt{K_D}} (\mathbf{u}_f \cdot \mathbf{t} - \mathbf{q} \cdot \mathbf{t}),$$

where γ is the slip rate coefficient. This condition was developed further in [128, 82]. A rigorous analysis of such interface conditions can be found in [79, 80]. See [103, 95] for

insights on those interface conditions, [130, 63, 86, 47] for numerical works, and [108] for dependence on related problems.

Any model of fluid in contact with a deformable and porous medium contains the filtration velocity, in addition to the displacement (or velocity) and stress variations of the porous matrix. These must be coupled to the Navier-Stokes flow in the ALE formulation

$$\rho_f \partial_t \mathbf{u}_f|_{\mathbf{x}_0} + \rho_f (\mathbf{u}_f - \mathbf{w}) \cdot \nabla \mathbf{u}_f - \nabla \cdot \boldsymbol{\sigma}_f^V + \nabla p_f = \mathbf{f}_f \quad \text{in } \Omega_t^f \times (0, T), \quad (6.3a)$$

$$\nabla \cdot \mathbf{u}_f = 0 \quad \text{in } \Omega_t^f \times (0, T), \quad (6.3b)$$

$$\rho_p D_t \mathbf{u}_s + \rho_d D_t \mathbf{q} - \nabla \cdot \boldsymbol{\sigma}_s^E + \nabla p_p = \mathbf{f}_s \quad \text{in } \Omega_t^p \times (0, T), \quad (6.3c)$$

$$\rho_d D_t \mathbf{u}_s + \rho_d D_t \frac{\mathbf{q}}{\phi} + K_D^{-1} \mathbf{q} + \nabla p_p = \mathbf{f}_d \quad \text{in } \Omega_t^p \times (0, T), \quad (6.3d)$$

$$\nabla \cdot (\mathbf{u}_s + \mathbf{q}) = 0 \quad \text{in } \Omega_t^p \times (0, T), \quad (6.3e)$$

via suitable interface conditions. The fluid velocity and pressure in Ω_t^f are now denoted by \mathbf{u}_f and p_f , respectively. The tensor $\boldsymbol{\sigma}_f^V = 2\mu_f \boldsymbol{\epsilon}(\mathbf{u}_f)$ stands for the viscous contribution to the Cauchy stress tensor $\boldsymbol{\sigma}_f$ for a Newtonian fluid (1.2):

$$\boldsymbol{\sigma}_f = -p_f \mathbf{I} + \boldsymbol{\sigma}_f^V.$$

For a discussion on the coupling between a Stokes flow and a poroelastic medium, see [98, 99, 134]. Following [134], we begin with the mass-conservation requirement that the normal fluid flux must be continuous across the interface. Thus, the solution of (6.3) is required to satisfy the *admissibility constraint*:

$$\mathbf{u}_f \cdot \mathbf{n} = (\mathbf{u}_s + \mathbf{q}) \cdot \mathbf{n}. \quad (6.4a)$$

For the balance of the normal stresses in the fluid phase across Σ_t , we have

$$\mathbf{n} \cdot (\boldsymbol{\sigma}_f \cdot \mathbf{n}) = -p_p. \quad (6.4b)$$

The conservation of momentum requires that the total stress of the porous medium is balanced by the total stress of the fluid:

$$\boldsymbol{\sigma}_s \cdot \mathbf{n} = \boldsymbol{\sigma}_f \cdot \mathbf{n}. \quad (6.4c)$$

Finally, the fluid tangential stress (which is equal to the one of the solid phase) is assumed to be proportional to the slip rate according to the Beavers-Joseph-Saffman condition:

$$\mathbf{t} \cdot (\boldsymbol{\sigma}_f \cdot \mathbf{n}) = -\frac{\gamma}{\sqrt{K_D}} (\mathbf{u}_f - \mathbf{u}_s) \cdot \mathbf{t}. \quad (6.4d)$$

We shall show next that interface conditions (6.4) suffice to precisely couple the Biot system (6.3c)-(6.3d)-(6.3e) in Ω_t^p to the Navier Stokes one (6.3a)-(6.3b) in Ω_t^f .

Equations (6.3) are written in terms of structure velocity (rather than deformation). The motivations for this choice are discussed in Section 3.2.1.

6.3 Weak formulation

The purpose of this section is to construct an appropriate variational formulation of the Navier-Stokes/Biot system (6.3) coupled by interface conditions (6.4). To accomplish it, for any given $t \in [0, T)$, we define the following spaces

$$\begin{aligned}\hat{R} &= \{ \hat{\mathbf{v}} : \Omega_0^p \rightarrow \mathbb{R}^d, \hat{\mathbf{v}} \in (H(\operatorname{div}, \Omega_0^p))^d \}, \\ R(t) &= \left\{ \mathbf{v} : \Omega_t^p \rightarrow \mathbb{R}^d, \mathbf{v} = \hat{\mathbf{v}} \circ (\mathcal{L}_t)^{-1}, \hat{\mathbf{v}} \in \hat{R} \right\}, \\ Q^p(t) &= \left\{ q : \Omega_t^p \rightarrow \mathbb{R}, q = \hat{q} \circ (\mathcal{L}_t)^{-1}, \hat{q} \in L^2(\Omega_0^p) \right\},\end{aligned}$$

where \mathcal{L}_t is the Lagrangian mapping describing the motion of the porous medium. It coincides with (2.2) upon replacement of Ω_0^s and Ω_t^s with Ω_0^p and Ω_t^p . When it is not otherwise specified, homogeneous conditions are imposed on the physical boundary, for the sake of simplicity.

We seek a solution in the spaces

$$\mathbf{u}_f \in V^f(t), \quad p_f \in Q^f(t), \quad \mathbf{u}_s \in V^s(t), \quad \mathbf{q} \in R(t), \quad p_p \in Q^p(t).$$

Spaces $V^f(t)$ and $V^s(t)$ are defined in Section 2.2, and $Q^f(t)$ coincides with $Q(t)$ introduced therein. The functions of $V^f(t)$, $V^s(t)$, and $Q^p(t)$ have a well defined trace on the external boundary and on the interface, and those from $R(t)$ have a normal trace. Furthermore, we define the following space

$$V_0^f(t) = \{ \mathbf{v} \in V^f(t), \mathbf{v} \cdot \mathbf{n}|_{\Sigma_t} = 0 \}.$$

We test the Navier-Stokes/Biot system (6.3) with test functions $(\mathbf{v}^f, q_f, \mathbf{v}^s, \mathbf{r}, q_p) \in V^f(t) \times Q^f(t) \times V^s(t) \times R(t) \times Q^p(t)$; after integration by parts we get

$$\rho_f(\partial_t \mathbf{u}_f|_{x_0}, \mathbf{v}^f)_{\Omega_t^f} + \mathcal{N}(\mathbf{u}_f - \mathbf{w}; \mathbf{u}_f, p_f, \mathbf{v}^f, q_f)_{\Omega_t^f} - (\boldsymbol{\sigma}_f \cdot \mathbf{n}, \mathbf{v}^f)_{\Sigma_t} = \langle \mathbf{f}_f, \mathbf{v}^f \rangle_{\Omega_t^f}, \quad (6.5a)$$

$$\rho_p(\mathbf{D}_t \mathbf{u}_s, \mathbf{v}^s)_{\Omega_t^p} + \rho_d(\mathbf{D}_t \mathbf{q}, \mathbf{v}^s)_{\Omega_t^p} + (\boldsymbol{\sigma}_s, \nabla \mathbf{v}^s)_{\Omega_t^p} + (\boldsymbol{\sigma}_s \cdot \mathbf{n}, \mathbf{v}^s)_{\Sigma_t} = \langle \mathbf{f}_s, \mathbf{v}^s \rangle_{\Omega_t^p}, \quad (6.5b)$$

$$\begin{aligned}\rho_d(\mathbf{D}_t \mathbf{u}_s, \mathbf{r})_{\Omega_t^p} + \frac{\rho_d}{\phi}(\mathbf{D}_t \mathbf{q}, \mathbf{r})_{\Omega_t^p} + K_D^{-1}(\mathbf{q}, \mathbf{r})_{\Omega_t^p} - (p_p, \nabla \cdot \mathbf{r})_{\Omega_t^p} \\ - (p_p, \mathbf{r} \cdot \mathbf{n})_{\Sigma_t} = \langle \mathbf{f}_d, \mathbf{r} \rangle_{\Omega_t^p},\end{aligned} \quad (6.5c)$$

$$(\nabla \cdot (\mathbf{u}_s + \mathbf{q}), q_p)_{\Omega_t^p} = 0. \quad (6.5d)$$

None of the coupling conditions (6.4) has been imposed yet.

Let us sum up equations (6.5) and consider only the interface integrals

$$I_{\Sigma_t} = -(\boldsymbol{\sigma}_f \cdot \mathbf{n}, \mathbf{v}^f)_{\Sigma_t} + (\boldsymbol{\sigma}_s \cdot \mathbf{n}, \mathbf{v}^s)_{\Sigma_t} - (p_p, \mathbf{r} \cdot \mathbf{n})_{\Sigma_t}. \quad (6.6)$$

For each triple of test function $\mathbf{v}^f, \mathbf{v}^s, \mathbf{r}$ satisfying the admissibility constraint (6.4a), the interface integral (6.6) becomes

$$I_{\Sigma_t} = -(\boldsymbol{\sigma}_f \cdot \mathbf{n}, \mathbf{v}^f)_{\Sigma_t} + (\boldsymbol{\sigma}_s \cdot \mathbf{n}, \mathbf{v}^s)_{\Sigma_t} - (p_p, \mathbf{v}_f \cdot \mathbf{n})_{\Sigma_t} + (p_p, \mathbf{v}_s \cdot \mathbf{n})_{\Sigma_t}.$$

Decomposing the stress terms into their normal and tangential components, we obtain

$$\begin{aligned} I_{\Sigma_t} = & -(\mathbf{n} \cdot (\boldsymbol{\sigma}_f \cdot \mathbf{n}) + p_p, \mathbf{v}^f \cdot \mathbf{n})_{\Sigma_t} + (\mathbf{n} \cdot (\boldsymbol{\sigma}_s \cdot \mathbf{n}) + p_p, \mathbf{v}^s \cdot \mathbf{n})_{\Sigma_t} \\ & - (\mathbf{t} \cdot (\boldsymbol{\sigma}_f \cdot \mathbf{n}), \mathbf{v}^f \cdot \mathbf{t})_{\Sigma_t} + (\mathbf{t} \cdot (\boldsymbol{\sigma}_s \cdot \mathbf{n}), \mathbf{v}^s \cdot \mathbf{t})_{\Sigma_t}. \end{aligned}$$

The first two terms are equal to zero thanks to interface conditions (6.4b) and (6.4c). Moreover, coupling conditions (6.4c) and (6.4d) yield

$$I_{\Sigma_t} = \frac{\gamma}{\sqrt{K_D}} ((\mathbf{u}_f - \mathbf{u}_s) \cdot \mathbf{t}, (\mathbf{v}^f - \mathbf{v}^s) \cdot \mathbf{t})_{\Sigma_t}. \quad (6.7)$$

We define the space of admissible solutions

$$W(t) = \{(\mathbf{v}^f, \mathbf{v}^s, \mathbf{r}) \in V^f(t) \times V^s(t) \times R(t), \quad \mathbf{v}^f \cdot \mathbf{n} = (\mathbf{v}^s + \mathbf{r}) \cdot \mathbf{n} \text{ on } \Sigma_t\},$$

or, equivalently,

$$\begin{aligned} W(t) = & \{(\mathbf{v}^f, \mathbf{v}^s, \mathbf{0}) \in V^f(t) \times V^s(t) \times R(t), \quad \mathbf{v}^f \cdot \mathbf{n} = \mathbf{v}^s \cdot \mathbf{n} \text{ on } \Sigma_t\} \\ & \oplus \{(\mathbf{v}^f, \mathbf{0}, \mathbf{r}) \in V^f(t) \times V^s(t) \times R(t), \quad \mathbf{v}^f \cdot \mathbf{n} = \mathbf{r} \cdot \mathbf{n} \text{ on } \Sigma_t\}. \end{aligned}$$

Then, summing equations (6.5) and taking into account expression (6.7) for the interface integrals, the variational formulation reads: Given $t \in (0, T)$, find $(\mathbf{u}_f, \mathbf{u}_s, \mathbf{q}, p_f, p_p) \in W(t) \times Q^f(t) \times Q^p(t)$ such that

$$\begin{aligned} & \rho_f (\partial_t \mathbf{u}_f|_{\mathbf{x}_0}, \mathbf{v}^f)_{\Omega_t^f} + \mathcal{N}(\mathbf{u}_f - \mathbf{w}; \mathbf{u}_f, p_f, \mathbf{v}^f, q_f)_{\Omega_t^f} + \rho_p (\mathbf{D}_t \mathbf{u}_s, \mathbf{v}^s)_{\Omega_t^p} + \rho_d (\mathbf{D}_t \mathbf{q}, \mathbf{v}^s)_{\Omega_t^p} \\ & + \langle \boldsymbol{\sigma}_s, \nabla \mathbf{v}^s \rangle_{\Omega_t^p} + \rho_d (\mathbf{D}_t \mathbf{u}_s, \mathbf{r})_{\Omega_t^p} + \frac{\rho_d}{\phi} (\mathbf{D}_t \mathbf{q}, \mathbf{r})_{\Omega_t^p} + K_D^{-1} (\mathbf{q}, \mathbf{r})_{\Omega_t^p} - (p_p, \nabla \cdot \mathbf{r})_{\Omega_t^p} \\ & + \frac{\gamma}{\sqrt{K_D}} ((\mathbf{u}_f - \mathbf{u}_s) \cdot \mathbf{t}, (\mathbf{v}^f - \mathbf{v}^s) \cdot \mathbf{t})_{\Sigma_t} + (\nabla \cdot (\mathbf{u}_s + \mathbf{q}), q_p)_{\Omega_t^p} = \langle \mathbf{f}_f, \mathbf{v}^f \rangle_{\Omega_t^f} \\ & + \langle \mathbf{f}_s, \mathbf{v}^s \rangle_{\Omega_t^p} + \langle \mathbf{f}_d, \mathbf{r} \rangle_{\Omega_t^p}, \end{aligned} \quad (6.8)$$

for all $(\mathbf{v}^f, \mathbf{v}^s, \mathbf{r}, q_f, q_p) \in W(t) \times Q^f(t) \times Q^p(t)$. This is a preliminary weak form which makes use of space $W(t)$ to show how to rewrite the interface integrals (6.6) thanks to coupling conditions (6.4). However, space $W(t)$ is not appropriate from the discretization point of view, since basis and test functions fulfilling the normal continuity requirement would be too cumbersome.

In Section 2.2.2, we remarked that the continuity of stresses between the fluid and the elastic structure can be imposed in a weak way. This choice yields several advantages from

the computational point of view. Hence, we enforce interface conditions (6.4b)-(6.4c)-(6.4d) in the following weak way

$$((\boldsymbol{\sigma}^s - \boldsymbol{\sigma}^f) \cdot \mathbf{n}, \boldsymbol{\xi})_{\Sigma_t} = 0, \quad \forall \boldsymbol{\xi} \in H^{1/2}(\Sigma_t), \quad (6.9a)$$

$$\left(\boldsymbol{\sigma}^f \cdot \mathbf{n} + p_p \mathbf{n} + \frac{\gamma}{\sqrt{K_D}} (\mathbf{u}_f \cdot \mathbf{t} - \mathbf{u}_s \cdot \mathbf{t}) \mathbf{t}, \boldsymbol{\xi} \right)_{\Sigma_t} = 0, \quad \forall \boldsymbol{\xi} \in H^{1/2}(\Sigma_t). \quad (6.9b)$$

By defining three arbitrary extension operators \mathcal{E}_t^f , \mathcal{E}_t^s , and \mathcal{E}_t^d from $H^{1/2}(\Sigma_t)$ to $V^f(t)$, $V^s(t)$, and $R(t)$, respectively, we have the following equalities:

$$\begin{aligned} (\boldsymbol{\sigma}^f \cdot \mathbf{n}, \boldsymbol{\xi})_{\Sigma_t} &= \rho_f (\partial_t \mathbf{u}_f|_{\mathbf{x}_0}, \mathcal{E}_t^f(\boldsymbol{\xi}))_{\Omega_t^f} + \mathcal{N}(\mathbf{u}_f - \mathbf{w}; \mathbf{u}_f, p_f, \mathcal{E}_t^f(\boldsymbol{\xi}), q_f)_{\Omega_t^f} - \langle \mathbf{f}_f, \mathcal{E}_t^f(\boldsymbol{\xi}) \rangle_{\Omega_t^f} \\ &= - \left\langle \mathcal{R}_f(\mathbf{u}_f, p_f), \mathcal{E}_t^f(\boldsymbol{\xi}) \right\rangle_{\Omega_t^f}, \\ (\boldsymbol{\sigma}^s \cdot \mathbf{n}, \boldsymbol{\xi})_{\Sigma_t} &= \langle \mathbf{f}_s, \mathcal{E}_t^s(\boldsymbol{\xi}) \rangle_{\Omega_t^s} - \rho_p (\mathbf{D}_t \mathbf{u}_s, \mathcal{E}_t^s(\boldsymbol{\xi}))_{\Omega_t^s} - \rho_d (\mathbf{D}_t \mathbf{q}, \mathcal{E}_t^s(\boldsymbol{\xi}))_{\Omega_t^s} - (\boldsymbol{\sigma}_s, \nabla \mathcal{E}_t^s(\boldsymbol{\xi}))_{\Omega_t^s} \\ &= \langle \mathcal{R}_s(\mathbf{u}_s, \mathbf{q}, p_p), \mathcal{E}_t^s(\boldsymbol{\xi}) \rangle_{\Omega_t^s}, \\ (p_p \mathbf{n}, \boldsymbol{\xi})_{\Sigma_t} &= \rho_d (\mathbf{D}_t \mathbf{u}_s, \mathcal{E}_t^d(\boldsymbol{\xi}))_{\Omega_t^s} + \frac{\rho_d}{\phi} (\mathbf{D}_t \mathbf{q}, \mathcal{E}_t^d(\boldsymbol{\xi}))_{\Omega_t^s} + K_D^{-1} (\mathbf{q}, \mathcal{E}_t^d(\boldsymbol{\xi}))_{\Omega_t^s} - (p_p, \nabla \cdot \mathcal{E}_t^d(\boldsymbol{\xi}))_{\Omega_t^s} \\ &\quad - \langle \mathbf{f}_d, \mathcal{E}_t^d(\boldsymbol{\xi}) \rangle_{\Omega_t^s} = - \left\langle \mathcal{R}_d(\mathbf{u}_s, \mathbf{q}, p_p), \mathcal{E}_t^d(\boldsymbol{\xi}) \right\rangle_{\Omega_t^s}. \end{aligned}$$

Thus, conditions (6.9) can be rewritten as

$$\begin{aligned} &- \left\langle \mathcal{R}_f(\mathbf{u}_f, p_f), \mathcal{E}_t^f(\boldsymbol{\xi}) \right\rangle_{\Omega_t^f} - \langle \mathcal{R}_s(\mathbf{u}_s, \mathbf{q}, p_p), \mathcal{E}_t^s(\boldsymbol{\xi}) \rangle_{\Omega_t^s} = 0, \\ &- \left\langle \mathcal{R}_f(\mathbf{u}_f, p_f), \mathcal{E}_t^f(\boldsymbol{\xi}) \right\rangle_{\Omega_t^f} - \langle \mathcal{R}_d(\mathbf{u}_s, \mathbf{q}, p_p), \mathcal{E}_t^d(\boldsymbol{\xi}) \rangle_{\Omega_t^s} \\ &\quad + \left(\frac{\gamma}{\sqrt{K_D}} (\mathbf{u}_f \cdot \mathbf{t} - \mathbf{u}_s \cdot \mathbf{t}) \mathbf{t}, \boldsymbol{\xi} \right)_{\Sigma_t} = 0, \end{aligned}$$

for all $\boldsymbol{\xi} \in H^{1/2}(\Sigma_t)$.

Notice that in general one might expect that $\mathbf{q} \cdot \mathbf{n} \in H^{-1/2}(\Sigma_t)$ because $\mathbf{q} \in R(t)$, while $\mathbf{u}_f \cdot \mathbf{n} \in H^{1/2}(\Sigma_t)$ and $\mathbf{u}_s \cdot \mathbf{n} \in H^{1/2}(\Sigma_t)$, since $\mathbf{u}_f \in V^f(t)$ and $\mathbf{u}_s \in V^s(t)$. However, it can be proved that $\mathbf{q} \cdot \mathbf{n} \in H^{1/2}(\Sigma_t)$ due to the coupling.

By imposing conditions (6.4b)-(6.4c)-(6.4d) weakly, we could write the variational formulation of the coupled Navier-Stokes/Biot system in another way with respect to (6.8). This other variational formulation makes use of function spaces better suited to be approximated by finite element spaces (they get rid of normal continuity requirement). That is,

given $t \in (0, T)$, find $(\mathbf{u}_f, \mathbf{u}_s, \mathbf{q}, p_f, p_p) \in V^f(t) \times V^s(t) \times R(t) \times Q^f(t) \times Q^p(t)$ such that

$$\begin{aligned} \rho_f(\partial_t \mathbf{u}_f|_{\mathbf{x}_0}, \mathbf{v}^f)_{\Omega_t^f} + \mathcal{N}(\mathbf{u}_f - \mathbf{w}; \mathbf{u}_f, p_f, \mathbf{v}^f, q_f)_{\Omega_t^f} \\ - \left(\frac{\gamma}{\sqrt{K_D}} (\mathbf{u}_f \cdot \mathbf{t} - \mathbf{u}_s \cdot \mathbf{t}) \mathbf{t}, \mathbf{v}^f \right)_{\Sigma_t} = \langle \mathbf{f}_f, \mathbf{v}^f \rangle_{\Omega_t^f}, \end{aligned} \quad (6.10a)$$

$$\begin{aligned} \rho_p(\mathbf{D}_t \mathbf{u}_s, \mathbf{v}^s)_{\Omega_t^p} + \rho_d(\mathbf{D}_t \mathbf{q}, \mathbf{v}^s)_{\Omega_t^p} + (\boldsymbol{\sigma}_s^E - p_p \mathbf{I}, \nabla \mathbf{v}^s)_{\Omega_t^p} - \left\langle \mathcal{R}_f(\mathbf{u}_f, p_f), \mathcal{E}_t^f(\mathbf{v}^s|_{\Sigma_t}) \right\rangle_{\Omega_t^f} \\ = \langle \mathbf{f}_s, \mathbf{v}^s \rangle_{\Omega_t^p}, \end{aligned} \quad (6.10b)$$

$$\begin{aligned} \rho_d(\mathbf{D}_t \mathbf{u}_s, \mathbf{r})_{\Omega_t^p} + \frac{\rho_d}{\phi} (\mathbf{D}_t \mathbf{q}, \mathbf{r})_{\Omega_t^p} + K_D^{-1}(\mathbf{q}, \mathbf{r})_{\Omega_t^p} - (p_p, \nabla \cdot \mathbf{r})_{\Omega_t^p} \\ + \left\langle (\mathcal{R}_f(\mathbf{u}_f, p_f) \cdot \mathbf{n}) \mathbf{n}, \mathcal{E}_t^f(\mathbf{r}|_{\Sigma_t}) \right\rangle_{\Omega_t^f} = \langle \mathbf{f}_d, \mathbf{r} \rangle_{\Omega_t^p}, \end{aligned} \quad (6.10c)$$

$$(\nabla \cdot (\mathbf{u}_s + \mathbf{q}), q_p)_{\Omega_t^p} = 0, \quad (6.10d)$$

$$\langle \mathbf{u}_f \cdot \mathbf{n}, \mathbf{v}^f|_{\Sigma_t} \rangle = \langle (\mathbf{q} + \mathbf{u}_s) \cdot \mathbf{n}, \mathbf{v}^f|_{\Sigma_t} \rangle, \quad (6.10e)$$

for all $(\mathbf{v}^f, \mathbf{v}^s, \mathbf{r}, q_f, q_p) \in V_0^f(t) \times V^s(t) \times R(t) \times Q^f(t) \times Q^p(t)$. In (6.10), the fluid problem is supplemented with Dirichlet interface condition (6.4a) for the normal component of the velocity (imposed weakly by (6.10e)) and a Robin interface condition (6.4d). The poroelastic subproblem is endowed with Neumann interface conditions (6.4b)-(6.4c).

6.4 Space and time discretization of the poroelastic problem

The full discretization of the fluid subproblem has been analyzed in Section 1.4. In this section we focus on the space and time discretization of the poroelastic subproblem (6.1).

Let $\hat{V}_h^s \subset (H^1(\Omega_0^p))^d$, $\hat{R}_h \subset (H(\text{div}, \Omega_0^p))^d$, and $\hat{Q}_h^p \subset L^2(\Omega_0^p)$ be the finite element spaces approximating $V^s(0)$, $R(0)$, and $Q^p(0)$ at the reference configuration, respectively. The finite element spaces for a given time level t^n can be defined using the domain map (2.2), e.g. $V_h^s(t^n) = \mathcal{L}_{t^n}(\hat{V}_h^s)$. From now on, we omit the time label t^n from the finite element spaces names.

The standard Galerkin approximation of the poroelastic problem (6.1) may fail because pressure stability can only be obtained for suitable filtration velocity-pressure finite element pairs (see Section 6.4.3). An alternative is to resort to stabilized methods. As already pointed out in Section 1.4.2, the idea is to strengthen the classical variational formulation so that discrete approximations, which would otherwise be unstable, become stable and convergent. Thus, the coupling of an incompressible fluid to a poroelastic structure, instead of an elastic one, shows an additional difficulty: stabilization (or inf-sup stable finite elements) is needed not only for the fluid subproblem, but also for the structure one.

In [84], there is no mention to the stabilization method adopted for the structure subproblem. We aim at finding a simple way to stabilize the Biot system (6.1). In view of that, we consider first the Darcy and the generalized Darcy problems. The stabilization we propose for the Darcy problem is a simple generalization of the method in [92], whereas the stabilization for the generalized Darcy and Biot equations are introduced for the first time.

In subsection 6.4.1, we propose a stabilization for the Darcy problem based on the work of Masud ad Hughes [92]. In subsection 6.4.2, we generalize it for the generalized Darcy problem. We extend the same approach to the poroelastic system (6.1) in subsection 6.4.3. In subsection 6.4.4 we treat a limit case and numerical results are reported in the last subsection.

6.4.1 Stabilization of the Darcy problem

The Darcy problem can be regarded as a particular case of the Biot system, when \mathbf{u}_s and $D_t \mathbf{q}$ are negligible. That is, the porous medium is no more deformable (we denote the domain by Ω^p), the problem is steady, and $\mathbf{q} = \phi \mathbf{u}_d$. Hence, equation (6.1a) is disregarded and the system (6.1) reduces to (6.2). There are two different approaches to solve equations (6.2): one involves a primal, single-field formulation for the pressure, while the other employs a mixed two-field formulation in which the variables are both velocity and pressure.

The primal formulation requires the solution of a Poisson problem for the pressure with a coefficient equal to the hydraulic permeability K_D . This can be done with adequate accuracy through existing finite element formulations (standard Galerkin method). However, the derived flux is obtained by taking the gradient of the pressure and multiplying it by K_D . This process involves loss of accuracy and, moreover, mass conservation is not guaranteed. Consequently, this approach has not proved suitable for practical applications.

For the Navier-Stokes/Biot system, the coupling conditions are written in terms of velocity, which is a postprocess quantity. Thus, losing accuracy in computing the velocity is not acceptable.

We adopt the mixed formulation. The classical mixed variational formulation is well-posed in terms of the functional spaces $L^2(\Omega^p)$ and $(H(\text{div}, \Omega^p))^d$ for the pressure and velocity, respectively (see [21]). Finite element approximations of those spaces, which satisfy the inf-sup condition, can be found in [122, 145, 101, 20, 102, 19, 18]. These discrete spaces attain good accuracy for both velocity and pressure, and mass conservation is achieved locally (i.e. element-wise) as well as globally. The price to pay for this is the complexity of the approach. Different interpolations are required for pressure and velocity and implementation is particularly involved in three dimensions. To avoid this drawback, we propose a stabilized variational formulation stemming from [92].

Let us consider a slightly different Darcy problem, replacing equation (6.2b) with

$$\nabla \cdot \mathbf{q} = g \quad \text{in } \Omega^p, \quad (6.11)$$

where g is the volumetric flow rate source or sink. The incompressible case is recovered simply by setting $g = 0$. Problem (6.2a)-(6.11) must be supplemented with either Neumann ($p_p = p_N$, with p_N a given function) or Dirichlet ($\mathbf{q} \cdot \mathbf{n} = q_D$, q_D known) boundary conditions. For the moment, we restrict our attention to the case of homogeneous boundary conditions. To this purpose, we introduce the space

$$R_0(t) = \{\mathbf{v} \in R(t), \mathbf{v} \cdot \mathbf{n}|_{\partial\Omega^p} = 0\}.$$

The classical weak formulation associated to equations (6.2a)-(6.11) reads: Find $\mathbf{q} \in R_0$ and $p_p \in Q^p$ such that

$$K_D^{-1}(\mathbf{q}, \mathbf{r})_{\Omega^p} - (p_p, \nabla \cdot \mathbf{r})_{\Omega^p} = (\mathbf{f}_d, \mathbf{r})_{\Omega^p}, \quad (6.12a)$$

$$(\nabla \cdot \mathbf{q}, q_p)_{\Omega^p} = (g, q_p)_{\Omega^p}, \quad (6.12b)$$

for all $(\mathbf{r}, q_p) \in R_0 \times Q^p$. For sufficiently regular data, this variational formulation is known to possess a unique solution if the spaces R_0 and Q^p satisfy the following compatibility conditions: there exists $\beta > 0$ such that

$$\inf_{q \in Q^p} \sup_{\mathbf{v} \in R_0} \frac{|\int_{\Omega^p} \nabla \cdot \mathbf{v} q \, d\Omega|}{\|\mathbf{v}\|_{H(\text{div}; \Omega^p)} \|q\|_{L^2(\Omega^p)}} \geq \beta. \quad (6.13)$$

The Galerkin approximation of this problem consists of: Find $\mathbf{q}_h \in R_{0,h}$ and $p_{p,h} \in Q_h^p$ such that

$$K_D^{-1}(\mathbf{q}_h, \mathbf{r}_h)_{\Omega^p} - (p_{p,h}, \nabla \cdot \mathbf{r}_h)_{\Omega^p} = (\mathbf{f}_d, \mathbf{r}_h)_{\Omega^p}, \quad (6.14a)$$

$$(\nabla \cdot \mathbf{q}_h, q_{p,h})_{\Omega^p} = (g, q_{p,h})_{\Omega^p}, \quad (6.14b)$$

for all $(\mathbf{r}_h, q_{p,h}) \in R_{0,h} \times Q_h^p$. Only certain combinations of velocity and pressure interpolations are stable. In fact, the solution of (6.14) is unique provided the discrete counterpart of (6.13) is satisfied, i.e. there exists $\beta_d > 0$, independent of h , such that

$$\inf_{q_h \in Q_h^p} \sup_{\mathbf{v}_h \in R_{0,h}} \frac{|\int_{\Omega^p} \nabla \cdot \mathbf{v}_h q_h \, d\Omega|}{\|\mathbf{v}_h\|_{H(\text{div}; \Omega^p)} \|q_h\|_{L^2(\Omega^p)}} \geq \beta_d. \quad (6.15)$$

To circumvent this restriction, we adopt a stabilization technique based on the variational multiscale (VMS) approach, originally introduced in [75]. The key idea of the formulation is a multiscale splitting of the variable of interest into resolved (grid) scale and unresolved (subgrid) scales. This decomposition acknowledges that certain components of the solution

cannot be captured by the finite element mesh. This approach has been successfully applied to a variety of problems (see, e.g., [76, 35, 106, 77, 36]).

Let us decompose the filtration velocity as follows

$$\mathbf{q} = \mathbf{q}_h + \tilde{\mathbf{q}}, \quad (6.16)$$

where $\mathbf{q}_h \in R_{0,h}$ is the finite element approximation and $\tilde{\mathbf{q}} \in \tilde{R}_0$ is the subgrid scale. Decomposition (6.16) is unique if one can express the original function space R_0 as the direct sum of two spaces $R_0 = R_{0,h} \oplus \tilde{R}_0$. The space of subgrid scales \tilde{R}_0 is the infinite-dimensional space that completes $R_{0,h}$ in R_0 . It is the role of the subgrid model to provide a successful approximation of the subgrid scales space. This is the theoretical foundation from which stabilization methods such as the algebraic subgrid scales (ASGS, see [75]) and the orthogonal subgrid scales (OSS, see [37]) are derived. Splitting (6.16) helps understand the origins of those stabilization methods which are known to be effective.

We neglect the subgrid pressure component \tilde{p}_p because condition (6.15) can be proved with the subgrid velocity component $\tilde{\mathbf{q}}$ only.

By plugging (6.16) into the variational formulation (6.12) and invoking the same decomposition into finite element approximation and subgrid scale for the test function, we get the multiscale system

$$K_D^{-1}(\mathbf{q}_h, \mathbf{r}_h)_{\Omega^p} + K_D^{-1}(\tilde{\mathbf{q}}, \mathbf{r}_h)_{\Omega^p} - (p_{p,h}, \nabla \cdot \mathbf{r}_h)_{\Omega^p} = (\mathbf{f}_d, \mathbf{r}_h)_{\Omega^p}, \quad (6.17a)$$

$$K_D^{-1}(\mathbf{q}_h, \tilde{\mathbf{r}})_{\Omega^p} + K_D^{-1}(\tilde{\mathbf{q}}, \tilde{\mathbf{r}})_{\Omega^p} + (\nabla p_{p,h}, \tilde{\mathbf{r}})_{\Omega^p} = (\mathbf{f}_d, \tilde{\mathbf{r}})_{\Omega^p}, \quad (6.17b)$$

$$(\nabla \cdot \mathbf{q}_h, q_{p,h})_{\Omega^p} - (\tilde{\mathbf{q}}, \nabla q_{p,h})_{\Omega^p} = (g, q_{p,h})_{\Omega^p}. \quad (6.17c)$$

To solve this problem is as difficult as the original one. Further simplifications are required, in order to get a computationally feasible numerical method. The subgrid equation (6.17b) motivates an expression for the subgrid component $\tilde{\mathbf{q}}$ in terms of the finite element components $(\mathbf{q}_h, p_{p,h})$:

$$K_D^{-1} \tilde{\mathbf{q}} = -\mathcal{P}(\nabla p_{p,h} + K_D^{-1} \mathbf{q}_h - \mathbf{f}_d), \quad (6.18)$$

where \mathcal{P} is the L^2 projection operator onto the subgrid space. This approximation is known as the *modeling for the subscales*. The residual of the finite element components is at the right-hand-side of (6.18). Thus, this kind of methods are known as *residual-based*. By plugging (6.18) into (6.17a) and (6.17c), we find

$$K_D^{-1}(\mathbf{q}_h, \mathbf{r}_h)_{\Omega^p} - (\mathcal{P}(\nabla p_{p,h} + K_D^{-1} \mathbf{q}_h - \mathbf{f}_d), \mathbf{r}_h)_{\Omega^p} - (p_{p,h}, \nabla \cdot \mathbf{r}_h)_{\Omega^p} = (\mathbf{f}_d, \mathbf{r}_h)_{\Omega^p}, \quad (6.19a)$$

$$K_D^{-1}(\nabla \cdot \mathbf{q}_h, q_{p,h})_{\Omega^p} + (\mathcal{P}(\nabla p_{p,h} + K_D^{-1} \mathbf{q}_h - \mathbf{f}_d), \nabla q_{p,h})_{\Omega^p} = K_D^{-1}(g, q_{p,h})_{\Omega^p}. \quad (6.19b)$$

We multiply (6.19a) by K_D^{-1} and sum it to (6.19b) to get

$$\begin{aligned} & K_D^{-2}(\mathbf{q}_h, \mathbf{r}_h)_{\Omega^p} - K_D^{-1}(p_{p,h}, \nabla \cdot \mathbf{r}_h)_{\Omega^p} + K_D^{-1}(\nabla \cdot \mathbf{q}_h, q_{p,h})_{\Omega^p} \\ & - (\mathcal{P}(\nabla p_{p,h} + K_D^{-1} \mathbf{q}_h - \mathbf{f}_d), K_D^{-1} \mathbf{r}_h - \nabla q_{p,h})_{\Omega^p} = K_D^{-1}(\mathbf{f}_d, \mathbf{r}_h)_{\Omega^p} + K_D^{-1}(g, q_{p,h})_{\Omega^p}. \end{aligned}$$

Notice that the stabilization term in this equation (first term in the second row) can be written as

$$(\mathcal{P}(\mathcal{L}\mathbf{Q} - \mathbf{f}_d), -\mathcal{S}\mathbf{R})_{\Omega^p}, \quad (6.20)$$

where we have used the abridged notation

$$\mathbf{Q} = \begin{bmatrix} \mathbf{q}_h \\ p_{p,h} \end{bmatrix}, \quad \mathbf{R} = \begin{bmatrix} \mathbf{r}_h \\ q_{p,h} \end{bmatrix}, \quad (6.21)$$

and

$$\begin{aligned} \mathcal{L}\mathbf{Q} &= K_D^{-1} \mathbf{q}_h + \nabla p_{p,h}, \\ \mathcal{S}\mathbf{R} &= K_D^{-1} \mathbf{r}_h - \nabla q_{p,h}. \end{aligned}$$

In [92], stabilization term (6.20) is approximated by

$$\frac{1}{2}(\mathcal{L}\mathbf{Q} - \mathbf{f}_d, -\mathcal{S}\mathbf{R})_{\Omega^p}. \quad (6.22)$$

We remark that $\mathcal{L}\mathbf{Q}$ and $\mathcal{S}\mathbf{R}$ belong to the same space. For instance, if \mathbf{q}_h and $p_{p,h}$ are both continuous piecewise linear functions, this space is the space of discontinuous piecewise linear functions. Should \mathbf{f}_d be approximated by a function belonging to the same space of $\mathcal{L}\mathbf{Q}$ and $\mathcal{S}\mathbf{R}$, (6.22) would be equivalent to take \mathcal{P} in (6.20) as the identity immersion operator in $L^2(\Omega^p)$. Otherwise, operator \mathcal{P} is approximated by the projection operator onto the space of $\mathcal{S}\mathbf{R}$. Let us approximate stabilization term (6.20) by

$$\alpha(\mathcal{L}\mathbf{Q} - \mathbf{f}_d, -\mathcal{S}\mathbf{R})_{\Omega^p},$$

with $0 < \alpha < 1$. By setting $\alpha = 1/2$, we recover the method suggested in [92]. Then, the stabilized momentum conservation equation is

$$(1 - \alpha)K_D^{-1}(\mathbf{q}_h, \mathbf{r}_h)_{\Omega^p} - (1 - \alpha)(p_{p,h}, \nabla \cdot \mathbf{r}_h)_{\Omega^p} = (1 - \alpha)(\mathbf{f}_d, \mathbf{r}_h)_{\Omega^p},$$

which implies

$$K_D^{-1} \mathbf{q}_h = -\Pi(\nabla p_{p,h} - \mathbf{f}_d), \quad \text{and} \quad K_D^{-1} \tilde{\mathbf{q}} = -\alpha \Pi^{\perp}(\nabla p_{p,h} - \mathbf{f}_d).$$

As in Section 1.4.2, $\Pi(\cdot)$ is the L^2 projection onto the velocity finite element space and $\Pi^\perp(\cdot) = \mathcal{I}(\cdot) - \Pi(\cdot)$ the L^2 orthogonal projection onto the velocity finite element space. Notice that the stabilized momentum balance equation is simply equation (6.14a) times a constant factor.

By exploiting (6.18) and integrating by parts the second term in (6.17c), the mass conservation equation reads

$$\begin{aligned} & (1 - \alpha)K_D^{-1}(\nabla \cdot \mathbf{q}_h, q_{p,h})_{\Omega^p} + \alpha(\nabla p_{p,h}, \nabla q_{p,h})_{\Omega^p} \\ & = K_D^{-1}(g, q_{p,h})_{\Omega^p} + \alpha(\mathbf{f}_d, \nabla q_{p,h})_{\Omega^p}, \end{aligned}$$

or, equivalently,

$$\begin{aligned} & (1 - \alpha)(\Pi(\nabla p_{p,h}), \nabla q_{p,h})_{\Omega^p} + \alpha(\nabla p_{p,h}, \nabla q_{p,h})_{\Omega^p} \\ & = K_D^{-1}(g, q_{p,h})_{\Omega^p} + (\Pi(\mathbf{f}_d), \nabla q_{p,h})_{\Omega^p} + \alpha(\Pi^\perp(\mathbf{f}_d), \nabla q_{p,h})_{\Omega^p}. \end{aligned} \quad (6.23)$$

Thus, the stabilized Galerkin formulation reads: Find $(\mathbf{q}_h, p_{p,h}) \in R_{0,h} \times Q_h^p$ such that

$$\mathcal{A}_d(\mathbf{q}_h, p_{p,h}; \mathbf{r}_h, q_{p,h})_{\Omega^p} = b_d(\mathbf{r}_h, q_{p,h})_{\Omega^p}, \quad \forall (\mathbf{r}_h, q_{p,h}) \in R_{0,h} \times Q_h^p, \quad (6.24)$$

with

$$\begin{aligned} \mathcal{A}_d(\mathbf{q}_h, p_{p,h}; \mathbf{r}_h, q_{p,h}) & = (1 - \alpha)K_D^{-1}(\mathbf{q}_h, \mathbf{r}_h)_{\Omega^p} - (1 - \alpha)(p_{p,h}, \nabla \cdot \mathbf{r}_h)_{\Omega^p} \\ & \quad + (1 - \alpha)K_D^{-1}(\nabla \cdot \mathbf{q}_h, q_{p,h})_{\Omega^p} + \alpha(\nabla p_{p,h}, \nabla q_{p,h})_{\Omega^p}, \end{aligned}$$

and

$$b_d(\mathbf{r}_h, q_{p,h})_{\Omega^p} = K_D^{-1}(g, q_{p,h})_{\Omega^p} + (1 - \alpha)(\mathbf{f}_d, \mathbf{r}_h)_{\Omega_t^p} + \alpha(\mathbf{f}_d, \nabla q_{p,h})_{\Omega^p}.$$

Notice that

$$\mathcal{A}_d(\mathbf{q}_h, p_{p,h}; K_D^{-1}\mathbf{q}_h, p_{p,h}) = (1 - \alpha)K_D^{-2}\|\mathbf{q}_h\|_{L^2(\Omega^p)}^2 + \alpha\|\nabla p_{p,h}\|_{L^2(\Omega^p)}^2.$$

Hence, the kernel of \mathcal{A}_d contains only the zero vector and problem (6.24) possesses a unique solution satisfying inequality

$$(1 - \alpha)K_D^{-2}\|\mathbf{q}_h\|_{L^2(\Omega^p)}^2 + \frac{\alpha}{2}\|\nabla p_{p,h}\|_{L^2(\Omega^p)}^2 \leq 2C_{\Omega^p}^2 \frac{K_D^{-2}}{\alpha}\|g\|_{L^2(\Omega^p)}^2 + \|\mathbf{f}_d\|_{L^2(\Omega^p)}^2. \quad (6.25)$$

The positive constant C_{Ω^p} is the Poincaré constant (1.8) appearing in

$$\|p_{p,h}\|_{L^2(\Omega^p)} \leq C_{\Omega^p}\|\nabla p_{p,h}\|_{L^2(\Omega^p)}.$$

Remark 6.1. *Let us roughly denote with M , G , D , and L the mass, gradient, divergence, and Laplacian matrices, respectively. The Galerkin approximation of the primal formulation requires the solution of system*

$$L\mathbf{P} = K_D^{-1}\mathbf{G} - D\mathbf{F}_d, \quad (6.26)$$

where \mathbf{P} , \mathbf{G} , and \mathbf{F}_d are the arrays of nodal values for pressure, g , and \mathbf{f}_d . On the other side, the Galerkin mixed formulation leads to the pressure Poisson equation

$$(DM^{-1}G)\mathbf{P} = K_D^{-1}\mathbf{G} - D\mathbf{F}_d. \quad (6.27)$$

System matrix $DM^{-1}G$ is non-singular only for finite elements spaces satisfying the inf-sup condition (6.15). The algebraic formulation of the stabilized problem (6.23) is

$$((1 - \alpha)DM^{-1}G + \alpha L)\mathbf{P} = K_D^{-1}\mathbf{G} - D\mathbf{F}_d,$$

which is a linear combination of (6.26) and (6.27).

Remark 6.2. *The OSS method would use $\mathcal{P} = \alpha\Pi^\perp$, which is analogous to the previous approach. Therefore, the ASGS and the OSS approach are equivalent for the Darcy problem.*

6.4.2 Stabilization of the generalized Darcy problem

The generalized Darcy problem in its strong form reads as

$$\frac{\rho_d}{\phi}D_t\mathbf{q} + K_D^{-1}\mathbf{q} + \nabla p_p = \mathbf{f}_d \quad \text{in } \Omega^p \times (0, T), \quad (6.28a)$$

$$\nabla \cdot \mathbf{q} = g \quad \text{in } \Omega^p \times (0, T). \quad (6.28b)$$

It corresponds to system (6.1) when \mathbf{u}_s is vanishing. As for the Darcy problem, the domain (denoted by Ω^p) is not deformable, but, unlike it, the inertia term $D_t\mathbf{q}$ is no more negligible.

For the moment, let us consider homogeneous boundary conditions. Thus, the classical variational formulation requires to find $\mathbf{q} \in R_0$ and $p_p \in Q^p$ such that

$$\begin{aligned} \left(\frac{\rho_d}{\phi}D_t\mathbf{q} + K_D^{-1}\mathbf{q}, \mathbf{r} \right)_{\Omega^p} - (p_p, \nabla \cdot \mathbf{r})_{\Omega^p} &= (\mathbf{f}_d, \mathbf{r})_{\Omega^p}, \\ (\nabla \cdot \mathbf{q}, p_p)_{\Omega^p} &= (g, p_p)_{\Omega^p}, \end{aligned}$$

for all $(\mathbf{r}, q_p) \in R_0 \times Q^p$.

We choose the BDF1 scheme for the time discretization. The Galerkin approximation of this problem through conforming finite element spaces consists of: Given \mathbf{q}_h^n , for $n \geq 0$ find $\mathbf{q}_h^{n+1} \in R_{0,h}$ and $p_{p,h}^{n+1} \in Q_{p,h}^p$ such that

$$\left(\frac{\rho_d}{\phi}d_t\mathbf{q}_h^{n+1} + K_D^{-1}\mathbf{q}_h^{n+1}, \mathbf{r}_h \right)_{\Omega^p} - (p_{p,h}^{n+1}, \nabla \cdot \mathbf{r}_h)_{\Omega^p} = (\mathbf{f}_d^{n+1}, \mathbf{r}_h)_{\Omega^p}, \quad (6.29a)$$

$$(\nabla \cdot \mathbf{q}_h^{n+1}, q_{p,h})_{\Omega^p} = (g^{n+1}, q_{p,h})_{\Omega^p}, \quad (6.29b)$$

for all $(\mathbf{r}_h, q_{p,h}) \in R_{0,h} \times Q_h^p$. We assume that $\mathbf{q}_h^0 \in R_{0,h}$ and $(\nabla \cdot \mathbf{q}_h^0, q_{p,h})_{\Omega^p} = (g^0, q_{p,h})_{\Omega^p}$. We denote by d_t the discrete material derivative. To overcome the necessity of employing conforming finite elements, we resort to the same approach adopted for the Darcy problem. Being the problem time dependent, we can employ either the dynamic [40, 41] or the quasi-static subscales for the velocity. We choose the former. Thus, we have

$$\left(\frac{\rho_d}{\phi} d_t \mathbf{q}_h^{n+1} + K_D^{-1} \mathbf{q}_h^{n+1}, \mathbf{r}_h \right)_{\Omega^p} + \left(\frac{\rho_d}{\phi} d_t \tilde{\mathbf{q}}^{n+1} + K_D^{-1} \tilde{\mathbf{q}}^{n+1}, \mathbf{r}_h \right)_{\Omega^p} - (p_{p,h}^{n+1}, \nabla \cdot \mathbf{r}_h)_{\Omega^p} = (\mathbf{f}_d^{n+1}, \mathbf{r}_h)_{\Omega^p}, \quad (6.30a)$$

$$\left(\frac{\rho_d}{\phi} d_t \mathbf{q}_h^{n+1} + K_D^{-1} \mathbf{q}_h^{n+1}, \tilde{\mathbf{r}} \right)_{\Omega^p} + \left(\frac{\rho_d}{\phi} d_t \tilde{\mathbf{q}}^{n+1} + K_D^{-1} \tilde{\mathbf{q}}^{n+1}, \tilde{\mathbf{r}} \right)_{\Omega^p} + (\nabla p_{p,h}^{n+1}, \tilde{\mathbf{r}})_{\Omega^p} = (\mathbf{f}_d^{n+1}, \tilde{\mathbf{r}})_{\Omega^p}, \quad (6.30b)$$

$$(\nabla \cdot \mathbf{q}_h^{n+1}, q_{p,h})_{\Omega^p} - (\tilde{\mathbf{q}}^{n+1}, \nabla q_{p,h})_{\Omega^p} = (g^{n+1}, q_{p,h})_{\Omega^p}. \quad (6.30c)$$

From (6.30b), it follows that

$$\frac{\rho_d}{\phi} d_t \tilde{\mathbf{q}}^{n+1} + K_D^{-1} \tilde{\mathbf{q}}^{n+1} = -\mathcal{P} \left(\frac{\rho_d}{\phi} d_t \mathbf{q}_h^{n+1} + K_D^{-1} \mathbf{q}_h^{n+1} + \nabla p_{p,h}^{n+1} - \mathbf{f}_d^{n+1} \right). \quad (6.31)$$

Let us approximate \mathcal{P} as in Section 6.4.1. Thus, the stabilized momentum conservation equation is

$$(1 - \alpha) \left(\frac{\rho_d}{\phi} d_t \mathbf{q}_h^{n+1} + K_D^{-1} \mathbf{q}_h^{n+1}, \mathbf{r}_h \right)_{\Omega^p} - (1 - \alpha) (p_{p,h}^{n+1}, \nabla \cdot \mathbf{r}_h)_{\Omega^p} = (1 - \alpha) (\mathbf{f}_d^{n+1}, \mathbf{r}_h)_{\Omega^p},$$

which implies that

$$\frac{\rho_d}{\phi} d_t \mathbf{q}_h^{n+1} + K_D^{-1} \mathbf{q}_h^{n+1} = -\Pi(\nabla p_{p,h}^{n+1} - \mathbf{f}_d^{n+1}),$$

and

$$\frac{\rho_d}{\phi} d_t \tilde{\mathbf{q}}^{n+1} + K_D^{-1} \tilde{\mathbf{q}}^{n+1} = -\alpha \Pi^\perp(\nabla p_{p,h}^{n+1} - \mathbf{f}_d^{n+1}).$$

Again, the stabilized momentum balance equation is the unstabilized equation (6.29a) times constant $(1 - \alpha)$.

By taking the time derivative of both sides of (6.30c) and combining it linearly with equation (6.30c) itself in order to exploit (6.31), we get

$$\begin{aligned} & \left(\nabla \cdot \left(\frac{\rho_d}{\phi} d_t \mathbf{q}_h^{n+1} + K_D^{-1} \mathbf{q}_h^{n+1} \right), q_{p,h} \right)_{\Omega^p} - \left(\frac{\rho_d}{\phi} d_t \tilde{\mathbf{q}}^{n+1} + K_D^{-1} \tilde{\mathbf{q}}^{n+1}, \nabla q_{p,h} \right)_{\Omega^p} \\ &= \left(\frac{\rho_d}{\phi} d_t g^{n+1} + K_D^{-1} g^{n+1}, q_{p,h} \right)_{\Omega^p}, \end{aligned}$$

which leads to

$$(1 - \alpha)(\Pi(\nabla p_{p,h}^{n+1}), \nabla q_{p,h})_{\Omega^p} + \alpha(\nabla p_{p,h}^{n+1}, \nabla q_{p,h})_{\Omega^p} = \left(\frac{\rho_d}{\phi} d_t g^{n+1} + K_D^{-1} g^{n+1}, q_{p,h} \right)_{\Omega^p} + (\Pi(\mathbf{f}_d^{n+1}), \nabla q_{p,h})_{\Omega^p} + \alpha(\Pi^\perp(\mathbf{f}_d^{n+1}), \nabla q_{p,h})_{\Omega^p}. \quad (6.32)$$

The stabilized Galerkin formulation reads: Given \mathbf{q}_h^n , for $n \geq 0$ find $(\mathbf{q}_h^{n+1}, p_{p,h}^{n+1}) \in R_{0,h} \times Q_h^p$ such that

$$\mathcal{A}_{gd}(\mathbf{q}_h^{n+1}, p_{p,h}^{n+1}; \mathbf{r}_h, q_{p,h})_{\Omega^p} = b_{gd}(\mathbf{r}_h, q_{p,h})_{\Omega^p}, \quad \forall (\mathbf{r}_h, q_{p,h}) \in R_{0,h} \times Q_h^p,$$

with

$$\begin{aligned} \mathcal{A}_{gd}(\mathbf{q}_h^{n+1}, p_{p,h}^{n+1}; \mathbf{r}_h, q_{p,h})_{\Omega^p} = & (1 - \alpha) \left(\frac{\rho_d}{\phi} d_t \mathbf{q}_h^{n+1} + K_D^{-1} \mathbf{q}_h^{n+1}, \mathbf{r}_h \right)_{\Omega^p} - (1 - \alpha)(p_{p,h}^{n+1}, \nabla \cdot \mathbf{r}_h)_{\Omega^p} \\ & + (1 - \alpha) \left(\nabla \cdot \left(\frac{\rho_d}{\phi} d_t \mathbf{q}_h^{n+1} + K_D^{-1} \mathbf{q}_h^{n+1} \right), q_{p,h} \right)_{\Omega^p} \\ & + \alpha(\nabla p_{p,h}^{n+1}, \nabla q_{p,h})_{\Omega^p}, \end{aligned}$$

and

$$b_{gd}(\mathbf{r}_h, q_{p,h})_{\Omega^p} = \left(\frac{\rho_d}{\phi} d_t g^{n+1} + K_D^{-1} g^{n+1}, q_{p,h} \right)_{\Omega^p} + (1 - \alpha)(\mathbf{f}_d^{n+1}, \mathbf{r}_h)_{\Omega^p} + (\mathbf{f}_d^{n+1}, \nabla q_{p,h})_{\Omega^p}.$$

Concerning stability, we have

$$\begin{aligned} \mathcal{A}_{gd}(\mathbf{q}_h^{n+1}, p_{p,h}^{n+1}; \frac{\rho_d}{\phi} d_t \mathbf{q}_h^{n+1} + K_D^{-1} \mathbf{q}_h^{n+1}, p_{p,h}^{n+1}) = & (1 - \alpha) \left\| \frac{\rho_d}{\phi} d_t \mathbf{q}_h^{n+1} + K_D^{-1} \mathbf{q}_h^{n+1} \right\|_{L^2(\Omega^p)}^2 \\ & + \alpha \left\| \nabla p_{p,h}^{n+1} \right\|_{L^2(\Omega^p)}^2. \end{aligned}$$

Since the kernel of \mathcal{A}_{gd} contains only the zero vector, the stabilized formulation has a unique solution which satisfies the following inequality

$$\begin{aligned} (1 - \alpha) \left(\frac{\rho_d}{\phi \delta t} \right) K_D^{-1} \left(\left\| \mathbf{q}_h^{n+1} \right\|_{L^2(\Omega^p)}^2 - \left\| \mathbf{q}_h^n \right\|_{L^2(\Omega^p)}^2 \right) + (1 - \alpha) K_D^{-2} \left\| \mathbf{q}_h^{n+1} \right\|_{L^2(\Omega^p)}^2 \\ + \frac{\alpha}{2} \left\| \nabla p_{p,h}^{n+1} \right\|_{L^2(\Omega^p)}^2 \leq 2 \frac{C_{\Omega^p}}{\alpha} \left\| \frac{\rho_d}{\phi} d_t g^{n+1} + K_D^{-1} g^{n+1} \right\|_{L^2(\Omega^p)}^2 + 2(1 + C_{\Omega^p}) \left\| \mathbf{f}_d^{n+1} \right\|_{L^2(\Omega^p)}^2. \end{aligned} \quad (6.33)$$

By summing inequality (6.33) over n , for $n \geq 0$, we obtain the estimate

$$\begin{aligned} (1 - \alpha) \left(\frac{\rho_d}{\phi \delta t} \right) K_D^{-1} \left\| \mathbf{q}_h^{n+1} \right\|_{L^2(\Omega^p)}^2 + (1 - \alpha) K_D^{-2} \sum_{i=0}^n \left\| \mathbf{q}_h^{i+1} \right\|_{L^2(\Omega^p)}^2 + \frac{\alpha}{2} \sum_{i=0}^n \left\| \nabla p_{p,h}^{i+1} \right\|_{\Omega^p}^2 \\ \leq (1 - \alpha) \left(\frac{\rho_d}{\phi \delta t} \right) K_D^{-1} \left\| \mathbf{q}_h^0 \right\|_{L^2(\Omega^p)}^2 + 2 \frac{C_{\Omega^p}}{\alpha} \sum_{i=0}^n \left\| \frac{\rho_d}{\phi} d_t g^{i+1} + K_D^{-1} g^{i+1} \right\|_{L^2(\Omega^p)}^2 \\ + 2(1 + C_{\Omega^p}) \sum_{i=0}^n \left\| \mathbf{f}_d^{i+1} \right\|_{L^2(\Omega^p)}^2. \end{aligned} \quad (6.34)$$

Remark 6.3. We use the same notation of Remark 6.1. The algebraic form of equation (6.32) is

$$((1 - \alpha)DM^{-1}G + \alpha L)\mathbf{P}^{n+1} = \frac{\rho_d}{\phi}d_t\mathbf{G}^{n+1} + K_D^{-1}\mathbf{G}^{n+1} - D\mathbf{F}_d.$$

The system matrix is unchanged with respect to the Darcy problem.

Remark 6.4. Also for the generalized Darcy problem the ASGS and OSS approaches are equivalent (see Remark 6.2).

Remark 6.5. The use of quasi-static subscales differs from that of the dynamic subscales for the fact that $d_t\tilde{\mathbf{q}}^{n+1}$ in (6.30a) and (6.30b) is assumed to be negligible.

6.4.3 The stabilized Biot system

Let us consider a slight variant of the Biot system (6.1) replacing (6.1c) with

$$\nabla \cdot (\mathbf{u}_s + \mathbf{q}) = g \quad \text{in } \Omega_t^p \times (0, T). \quad (6.35)$$

Again, we start by focusing on the case of homogeneous boundary conditions. To this purpose, we introduce the space

$$V_0^s(t) = \{\mathbf{v} \in V^s(t), \mathbf{v}|_{\partial\Omega_t^p} = 0\}.$$

The classical variational formulation reads: Find $(\mathbf{u}_s, \mathbf{q}, p_p) \in V_0^s \times R_0 \times Q^p$ such that

$$\begin{aligned} \rho_s(1 - \phi)(D_t\mathbf{u}_s, \mathbf{v}^s)_{\Omega_t^p} + \rho_d\phi(D_t\mathbf{u}_s, \mathbf{v}^s)_{\Omega_t^p} + \rho_d(D_t\mathbf{q}, \mathbf{v}^s)_{\Omega_t^p} \\ + (\boldsymbol{\sigma}_s^E(\boldsymbol{\eta}), \nabla\mathbf{v}^s)_{\Omega_t^p} - (p_p, \nabla \cdot \mathbf{v}^s)_{\Omega_t^p} = \langle \mathbf{f}_s, \mathbf{v}^s \rangle_{\Omega_t^p}, \end{aligned} \quad (6.36a)$$

$$\rho_d(D_t\mathbf{u}_s, \mathbf{r})_{\Omega_t^p} + \frac{\rho_d}{\phi}(D_t\mathbf{q}, \mathbf{r})_{\Omega_t^p} + K_D^{-1}(\mathbf{q}, \mathbf{r})_{\Omega_t^p} - (p_p, \nabla \cdot \mathbf{r})_{\Omega_t^p} = \langle \mathbf{f}_d, \mathbf{r} \rangle_{\Omega_t^p}, \quad (6.36b)$$

$$(\nabla \cdot (\mathbf{u}_s + \mathbf{q}), q_p)_{\Omega_t^p} = (g, q_p)_{\Omega_t^p}. \quad (6.36c)$$

for all $(\mathbf{v}^s, \mathbf{r}, q_p) \in V_0^s \times R_0 \times Q^p$.

In order to understand the well-posedness of the weak problem, we consider the fully homogeneous problem, i.e. we set to zero the forcing terms \mathbf{f}_s , \mathbf{f}_d , and g . Moreover, we take $\mathbf{v}^s = \mathbf{u}_s$, $\mathbf{r} = \mathbf{q}$, and $q_p = p_p$ in (6.36), and sum the resulting equations to get

$$\begin{aligned} \rho_s(1 - \phi)(D_t\mathbf{u}_s, \mathbf{u}_s)_{\Omega_t^p} + \rho_d\phi(D_t\mathbf{u}_s, \mathbf{u}_s)_{\Omega_t^p} + \rho_d(D_t\mathbf{q}, \mathbf{u}_s)_{\Omega_t^p} \\ + (\boldsymbol{\sigma}_s^E, \nabla\mathbf{u}_s)_{\Omega_t^p} + \rho_d(D_t\mathbf{u}_s, \mathbf{q})_{\Omega_t^p} + \frac{\rho_d}{\phi}(D_t\mathbf{q}, \mathbf{q})_{\Omega_t^p} + K_D^{-1}(\mathbf{q}, \mathbf{q})_{\Omega_t^p} = 0. \end{aligned}$$

This equation is equivalent to

$$\begin{aligned} \rho_s(1 - \phi)(D_t\mathbf{u}_s, \mathbf{u}_s)_{\Omega_t^p} + \rho_d\phi \left(D_t \left(\mathbf{u}_s + \frac{\mathbf{q}}{\phi} \right), \mathbf{u}_s + \frac{\mathbf{q}}{\phi} \right)_{\Omega_t^p} \\ + (\boldsymbol{\sigma}_s^E, \nabla\mathbf{u}_s)_{\Omega_t^p} + K_D^{-1}(\mathbf{q}, \mathbf{q})_{\Omega_t^p} = 0, \end{aligned} \quad (6.37)$$

where we recognize the fluid velocity in the porous medium $\mathbf{u}_d = \mathbf{u}_s + \frac{\mathbf{q}}{\phi}$ in the second term. We integrate equation (6.37) over the time interval $[0, T]$ to obtain

$$\begin{aligned} & K_D^{-1} \int_0^T \|\mathbf{q}(t)\|_{L^2(\Omega_t^p)}^2 dt + \int_0^T (\boldsymbol{\sigma}_s^E(\boldsymbol{\eta}(t)), \nabla \mathbf{u}_s(t))_{\Omega_t^p} dt + \rho_s(1-\phi) \frac{1}{2} \left(\|\mathbf{u}_s(T)\|_{L^2(\Omega_T^p)}^2 \right. \\ & \left. - \|\mathbf{u}_s(0)\|_{L^2(\Omega_0^p)}^2 \right) + \rho_d \phi \frac{1}{2} \left(\left\| \mathbf{u}_s(T) + \frac{\mathbf{q}(T)}{\phi} \right\|_{L^2(\Omega_T^p)}^2 - \left\| \mathbf{u}_s(0) + \frac{\mathbf{q}(0)}{\phi} \right\|_{L^2(\Omega_0^p)}^2 \right) = 0. \end{aligned}$$

In order to have pressure stability, we need to satisfy condition (6.13) under the assumption that $\phi > c > 0$.

For the time discretization of the problem we adopt the BDF1 scheme. The fully discrete problem reads: Given $\mathbf{u}_{s,h}^n$ and \mathbf{q}_h^n , for $n \geq 0$ find $(\mathbf{u}_{s,h}^{n+1}, \mathbf{q}_h^{n+1}, p_{p,h}^{n+1}) \in V_{0,h}^s \times R_{0,h} \times Q_h^p$ such that

$$\begin{aligned} & \rho_s(1-\phi)(d_t \mathbf{u}_{s,h}^{n+1}, \mathbf{v}_h^s)_{\Omega_{t^{n+1}}^p} + \rho_d \phi (d_t \mathbf{u}_{s,h}^{n+1}, \mathbf{v}_h^s)_{\Omega_{t^{n+1}}^p} + \rho_d (d_t \mathbf{q}_h^{n+1}, \mathbf{v}_h^s)_{\Omega_{t^{n+1}}^p} \\ & \quad + (\boldsymbol{\sigma}_s^E(\boldsymbol{\eta}_h^{n+1}), \nabla \mathbf{v}_h^s)_{\Omega_{t^{n+1}}^p} - (p_{p,h}^{n+1}, \nabla \cdot \mathbf{v}_h^s)_{\Omega_{t^{n+1}}^p} = \langle \mathbf{f}_s^{n+1}, \mathbf{v}_h^s \rangle_{\Omega_{t^{n+1}}^p}, \\ & \rho_d (d_t \mathbf{u}_{s,h}^{n+1}, \mathbf{r}_h)_{\Omega_{t^{n+1}}^p} + \frac{\rho_d}{\phi} (d_t \mathbf{q}_h^{n+1}, \mathbf{r}_h)_{\Omega_{t^{n+1}}^p} + K_D^{-1} (\mathbf{q}_h^{n+1}, \mathbf{r}_h)_{\Omega_t^p} \\ & \quad - (p_{p,h}^{n+1}, \nabla \cdot \mathbf{r}_h)_{\Omega_{t^{n+1}}^p} = (\mathbf{f}_d^{n+1}, \mathbf{r}_h)_{\Omega_{t^{n+1}}^p}, \\ & (\nabla \cdot (\mathbf{u}_{s,h}^{n+1} + \mathbf{q}_h^{n+1}), q_{p,h})_{\Omega_{t^{n+1}}^p} = (g^{n+1}, q_{p,h})_{\Omega_{t^{n+1}}^p}, \end{aligned}$$

for all $(\mathbf{v}_h^s, \mathbf{r}_h, q_{p,h}) \in V_{0,h}^s \times R_{0,h} \times Q_h^p$. Conforming finite elements for the generalized Darcy problem would lead to a stable discretization of the problem provided $\phi > c > 0$.

In order to write the stabilized version of the problem, we repeat the same procedure we followed for the Darcy and the generalized Darcy problems. By using the dynamic subscales for $\tilde{\mathbf{q}}$ (we neglect $\tilde{\mathbf{u}}_s$) and introducing the stability for the generalized Darcy problem only, we have

$$\begin{aligned} & \left(\frac{\rho_d}{\phi} d_t \mathbf{q}_h^{n+1} + K_D^{-1} \mathbf{q}_h^{n+1}, \mathbf{r}_h \right)_{\Omega_{t^{n+1}}^p} + \left(\frac{\rho_d}{\phi} d_t \tilde{\mathbf{q}}^{n+1} + K_D^{-1} \tilde{\mathbf{q}}^{n+1}, \mathbf{r}_h \right)_{\Omega_{t^{n+1}}^p} \\ & \quad + \rho_d (d_t \mathbf{u}_{s,h}^{n+1}, \mathbf{r}_h)_{\Omega_{t^{n+1}}^p} - (p_{p,h}^{n+1}, \nabla \cdot \mathbf{r}_h)_{\Omega_{t^{n+1}}^p} = (\mathbf{f}_d^{n+1}, \mathbf{r}_h)_{\Omega_{t^{n+1}}^p}, \end{aligned} \quad (6.38a)$$

$$\begin{aligned} & \left(\frac{\rho_d}{\phi} d_t \mathbf{q}_h^{n+1} + K_D^{-1} \mathbf{q}_h^{n+1}, \tilde{\mathbf{r}} \right)_{\Omega_{t^{n+1}}^p} + \left(\frac{\rho_d}{\phi} d_t \tilde{\mathbf{q}}^{n+1} + K_D^{-1} \tilde{\mathbf{q}}^{n+1}, \tilde{\mathbf{r}} \right)_{\Omega_{t^{n+1}}^p} \\ & \quad + \rho_d (d_t \mathbf{u}_{s,h}^{n+1}, \tilde{\mathbf{r}})_{\Omega_{t^{n+1}}^p} + (\nabla p_{p,h}^{n+1}, \tilde{\mathbf{r}})_{\Omega_{t^{n+1}}^p} = (\mathbf{f}_d^{n+1}, \mathbf{r}_h)_{\Omega_{t^{n+1}}^p}, \end{aligned} \quad (6.38b)$$

$$(\nabla \cdot (\mathbf{u}_{s,h}^{n+1} + \mathbf{q}_h^{n+1}), q_{p,h})_{\Omega_t^p} - (\tilde{\mathbf{q}}^{n+1}, \nabla q_{p,h})_{\Omega_t^p} = (g^{n+1}, q_{p,h})_{\Omega_t^p}. \quad (6.38c)$$

From the subgrid equation (6.38b), we derive the expression for the velocity subscale

$$\frac{\rho_d}{\phi} d_t \tilde{\mathbf{q}}^{n+1} + K_D^{-1} \tilde{\mathbf{q}}^{n+1} = -\mathcal{P} \left(\frac{\rho_d}{\phi} d_t \mathbf{q}_h^{n+1} + K_D^{-1} \mathbf{q}_h^{n+1} + \rho_d d_t \mathbf{u}_{s,h}^{n+1} + \nabla p_{p,h} - \mathbf{f}_d^{n+1} \right). \quad (6.39)$$

By plugging (6.39) into (6.38a) and approximating \mathcal{P} as in Section 6.4.1, the momentum conservation equation becomes

$$(1 - \alpha) \left(\frac{\rho_d}{\phi} \mathbf{d}_t \mathbf{q}_h^{n+1} + K_D^{-1} \mathbf{q}_h^{n+1}, \mathbf{r}_h \right)_{\Omega_{t^{n+1}}^p} + (1 - \alpha) \rho_d (\mathbf{d}_t \mathbf{u}_{s,h}^{n+1}, \mathbf{r}_h)_{\Omega_{t^{n+1}}^p} - (1 - \alpha) (p_{p,h}^{n+1}, \nabla \cdot \mathbf{r}_h)_{\Omega_{t^{n+1}}^p} = (1 - \alpha) (\mathbf{f}_d^{n+1}, \mathbf{r}_h)_{\Omega_{t^{n+1}}^p}, \quad (6.40)$$

from which it follows that

$$\frac{\rho_d}{\phi} \mathbf{d}_t \mathbf{q}_h^{n+1} + K_D^{-1} \mathbf{q}_h^{n+1} = -\Pi(\nabla p_{p,h}^{n+1} + \rho_d \mathbf{d}_t \mathbf{u}_{s,h}^{n+1} - \mathbf{f}_d^{n+1}),$$

and

$$\frac{\rho_d}{\phi} \mathbf{d}_t \tilde{\mathbf{q}}^{n+1} + K_D^{-1} \tilde{\mathbf{q}}^{n+1} = -\alpha \Pi^\perp(\nabla p_{p,h}^{n+1} + \rho_d \mathbf{d}_t \mathbf{u}_{s,h}^{n+1} - \mathbf{f}_d^{n+1}).$$

By taking the time derivative of both sides in (6.38c) and combining it linearly with equation (6.38c) itself in order to exploit (6.39), we obtain

$$\begin{aligned} & \left(\nabla \cdot \left(\frac{\rho_d}{\phi} \mathbf{d}_t \mathbf{q}_h^{n+1} + K_D^{-1} \mathbf{q}_h^{n+1} \right), q_{p,h} \right)_{\Omega_{t^{n+1}}^p} - \left(\frac{\rho_d}{\phi} \mathbf{d}_t \tilde{\mathbf{q}}^{n+1} + K_D^{-1} \tilde{\mathbf{q}}^{n+1}, \nabla q_{p,h} \right)_{\Omega_{t^{n+1}}^p} \\ & + \left(\nabla \cdot \left(\frac{\rho_d}{\phi} \mathbf{d}_t \mathbf{u}_{s,h}^{n+1} + K_D^{-1} \mathbf{u}_{s,h}^{n+1} \right), q_{p,h} \right)_{\Omega_{t^{n+1}}^p} = \left(\frac{\rho_d}{\phi} \mathbf{d}_t g^{n+1} + K_D^{-1} g^{n+1}, q_{p,h} \right)_{\Omega_{t^{n+1}}^p}, \end{aligned}$$

or, equivalently,

$$\begin{aligned} & (1 - \alpha) (\Pi(\nabla p_{p,h}), \nabla q_{p,h})_{\Omega_{t^{n+1}}^p} + \alpha (\nabla p_{p,h}, \nabla q_{p,h})_{\Omega_{t^{n+1}}^p} + (1 - \alpha) \rho_d (\nabla \cdot \Pi(\mathbf{d}_t \mathbf{u}_{s,h}^{n+1}), q_{p,h})_{\Omega_{t^{n+1}}^p} \\ & + \alpha \rho_d (\nabla \cdot (\mathbf{d}_t \mathbf{u}_{s,h}^{n+1}), q_{p,h})_{\Omega_{t^{n+1}}^p} + \left(\nabla \cdot \left(\frac{\rho_d}{\phi} \mathbf{d}_t \mathbf{u}_{s,h}^{n+1} + K_D^{-1} \mathbf{u}_{s,h}^{n+1} \right), q_{p,h} \right)_{\Omega_{t^{n+1}}^p} \\ & = \left(\frac{\rho_d}{\phi} \mathbf{d}_t g^{n+1} + K_D^{-1} g^{n+1}, q_{p,h} \right)_{\Omega_{t^{n+1}}^p} + (\Pi(\mathbf{f}_d^{n+1}), \nabla q_{p,h})_{\Omega_{t^{n+1}}^p} + \alpha (\Pi^\perp(\mathbf{f}_d^{n+1}), \nabla q_{p,h})_{\Omega_{t^{n+1}}^p}. \end{aligned}$$

The stabilized Galerkin formulation reads: Given $\mathbf{u}_{s,h}^n$ and \mathbf{q}_h^n , for $n \geq 0$ find $(\mathbf{u}_{s,h}^{n+1}, \mathbf{q}_h^{n+1}, p_{p,h}^{n+1}) \in V_{0,h}^s \times R_{0,h} \times Q_h^p$ such that

$$\mathcal{A}_p(\mathbf{u}_{s,h}^{n+1}, \mathbf{q}_h^{n+1}, p_{p,h}^{n+1}; \mathbf{v}_h^s, \mathbf{r}_h, q_{p,h})_{\Omega_{t^{n+1}}^p} = b_p(\mathbf{v}_h^s, \mathbf{r}_h, q_{p,h})_{\Omega_{t^{n+1}}^p}, \quad (6.41)$$

for all $(\mathbf{v}_h^s, \mathbf{r}_h, q_{p,h}) \in V_{0,h}^s \times R_{0,h} \times Q_h^p$, with

$$\begin{aligned}
\mathcal{A}_p(\mathbf{u}_{s,h}^{n+1}, \mathbf{q}_h^{n+1}, p_{p,h}^{n+1}; \mathbf{v}_h^s, \mathbf{r}_h, q_{p,h})_{\Omega_{t^{n+1}}^p} &= \rho_p(\mathbf{d}_t \mathbf{u}_{s,h}^{n+1}, \mathbf{v}_h^s)_{\Omega_{t^{n+1}}^p} + \rho_d(\mathbf{d}_t \mathbf{q}_h^{n+1}, \mathbf{v}_h^s)_{\Omega_{t^{n+1}}^p} \\
&+ (\boldsymbol{\sigma}_s^E(\boldsymbol{\eta}_h^{n+1}), \nabla \mathbf{v}_h^s)_{\Omega_{t^{n+1}}^p} - (p_{p,h}^{n+1}, \nabla \cdot \mathbf{v}_h^s)_{\Omega_{t^{n+1}}^p} + (1 - \alpha) \left(\frac{\rho_d}{\phi} \mathbf{d}_t \mathbf{q}_h^{n+1} + K_D^{-1} \mathbf{q}_h^{n+1}, \mathbf{r}_h \right)_{\Omega_{t^{n+1}}^p} \\
&+ (1 - \alpha) \rho_d(\mathbf{d}_t \mathbf{u}_{s,h}^{n+1}, \mathbf{r}_h)_{\Omega_{t^{n+1}}^p} - (1 - \alpha) (p_{p,h}^{n+1}, \nabla \cdot \mathbf{r}_h)_{\Omega_{t^{n+1}}^p} + \alpha (\nabla p_{p,h}, \nabla q_{p,h})_{\Omega_{t^{n+1}}^p} \\
&+ (1 - \alpha) \left(\nabla \cdot \left(\frac{\rho_d}{\phi} \mathbf{d}_t \mathbf{q}_h^{n+1} + K_D^{-1} \mathbf{q}_h^{n+1} \right), q_{p,h} \right)_{\Omega_{t^{n+1}}^p} + K_D^{-1} (\nabla \cdot \mathbf{u}_{s,h}^{n+1}, q_{p,h})_{\Omega_{t^{n+1}}^p} \\
&+ \rho_d \left(\frac{1}{\phi} - \alpha \right) (\nabla \cdot (\mathbf{d}_t \mathbf{u}_{s,h}^{n+1}), q_{p,h})_{\Omega_{t^{n+1}}^p}
\end{aligned} \tag{6.42}$$

and

$$\begin{aligned}
b_p(\mathbf{v}_h^s, \mathbf{r}_h, q_{p,h})_{\Omega_{t^{n+1}}^p} &= \left(\frac{\rho_d}{\phi} \mathbf{d}_t \mathbf{g}^{n+1} + K_D^{-1} \mathbf{g}^{n+1}, q_{p,h} \right)_{\Omega_{t^{n+1}}^p} + \langle \mathbf{f}_s^{n+1}, \mathbf{v}_h^s \rangle_{\Omega_{t^{n+1}}^p} \\
&+ (1 - \alpha) (\mathbf{f}_d^{n+1}, \mathbf{r}_h)_{\Omega_{t^{n+1}}^p} + \alpha (\mathbf{f}_d^{n+1}, \nabla q_{p,h})_{\Omega_{t^{n+1}}^p}.
\end{aligned} \tag{6.43}$$

The algebraic form associated to (6.41) will be discussed in Section 6.6.

6.4.4 A limit case

The hydraulic conductivity K_D is the ratio between the Darcy permeability κ and the viscosity μ_p . The values of those parameters in hemodynamics have been evaluated experimentally in [151] and used for applications in [154, 112]. Precisely, realistic values are $\kappa = 2 \cdot 10^{-14} \text{ cm}^2$ and $\mu_p = 0.72 \cdot 10^{-2} \text{ g}/(\text{cm s})$, thus $K_D \sim 10^{-12} \text{ (cm}^3 \text{ s)}/\text{g}$. For those values of hydraulic conductivity, the orders of magnitude of the two velocities \mathbf{u}_s and \mathbf{q} are very different and the stabilization method described in Section 6.4.3 fails. In fact, it stabilizes the Darcy problem only.

Let us denote with an overline adimensional variables. System (6.1) in its adimensional form reads

$$\mathbf{d}_{\bar{t}} \bar{\mathbf{u}}_s + \frac{\rho_d Q}{\rho_p U_s} \mathbf{d}_{\bar{t}} \bar{\mathbf{q}} - \frac{1}{\rho_p U_s} \bar{\nabla} \cdot \boldsymbol{\sigma}_s^E(\bar{\boldsymbol{\eta}}) + \bar{\nabla} \bar{p}_p = \frac{1}{\rho_p U_s} \mathbf{f}_s \quad \text{in } \Omega_t^p \times (0, T), \tag{6.44a}$$

$$\mathbf{d}_{\bar{t}} \bar{\mathbf{u}}_s + \frac{1}{\phi U_s} \mathbf{d}_{\bar{t}} \bar{\mathbf{q}} + \frac{1}{\varepsilon Re_p} \bar{\mathbf{q}} + \bar{\nabla} \bar{p}_p = \frac{1}{\rho_d U_s} \mathbf{f}_d \quad \text{in } \Omega_t^p \times (0, T), \tag{6.44b}$$

$$\bar{\nabla} \cdot \bar{\mathbf{u}}_s + \frac{Q}{U_s} \bar{\nabla} \cdot \bar{\mathbf{q}} = 0 \quad \text{in } \Omega_t^p \times (0, T), \tag{6.44c}$$

where Q, U_s , and T are characteristic values for filtration velocity, structure velocity, and time, respectively. The Reynolds number $Re_p = \delta_p Q / \nu_p$ (see [48]), δ_p being a characteristic pore size and $\nu_p = \mu_p / \rho_d$ the fluid kinematic viscosity, is an adimensional quantity.

Moreover, ε in (6.44b) is equal to δ_p/L , where L is a characteristic length of the structure problem.

For $K_D \sim 10^{-12}$, the ratio Q/U_s is “small” and the terms in (6.44) multiplied by this ratio become negligible with respect to the others. Thus, equations (6.44a)-(6.44c) model an incompressible solid and equation (6.44b) recovers the filtration velocity \mathbf{q} once \mathbf{u}_s and p_p are computed. Thanks to this simplification, instead of stabilizing equations (6.44b)-(6.44c) as presented in the previous subsection, we stabilize equations (6.44a)-(6.44c) using the method proposed in [29]. Therein, a stabilization technique based on the orthogonal subscales method is presented to solve incompressibility in solid mechanics.

As done for all the previous problems, we consider homogeneous boundary conditions. We choose the BDF1 scheme for the time discretization. The Galerkin approximation of the simplified problem written in terms of structure displacement $\boldsymbol{\eta}$ reads: Given $\boldsymbol{\eta}_h^n$ and $\boldsymbol{\eta}_h^{n-1}$, for $n \geq 0$ find $\boldsymbol{\eta}_h^{n+1} \in V_{0,h}^s$ and $p_{p,h}^{n+1} \in Q_h^p$ such that

$$\begin{aligned} \rho_p (\mathbf{d}_{tt}\boldsymbol{\eta}_h^{n+1}, \mathbf{v}_h^s)_{\Omega_{t^{n+1}}^p} + (\boldsymbol{\sigma}_s^E(\boldsymbol{\eta}_h^{n+1}), \nabla \mathbf{v}_h^s)_{\Omega_{t^{n+1}}^p} - (p_{p,h}^{n+1}, \nabla \cdot \mathbf{v}_h^s)_{\Omega_{t^{n+1}}^p} &= (\mathbf{f}_s^{n+1}, \mathbf{v}_h^s)_{\Omega_{t^{n+1}}^p}, \\ (\nabla \cdot \boldsymbol{\eta}_h^{n+1}, q_{p,h})_{\Omega_{t^{n+1}}^p} &= (g^{n+1}, q_{p,h})_{\Omega_{t^{n+1}}^p}, \end{aligned}$$

for all $(\mathbf{v}_h^s, q_{p,h}) \in V_{0,h}^s \times Q_h^p$. We assume that $\boldsymbol{\eta}_h^0 \in V_{0,h}^s$ and $(\nabla \cdot \boldsymbol{\eta}_h^0, q_{p,h})_{\Omega_{t^{n+1}}^p} = (g^0, q_{p,h})_{\Omega_{t^{n+1}}^p}$.

Let us take $\boldsymbol{\sigma}_s^E(\boldsymbol{\eta}_h^{n+1}) = \mu_\ell \nabla \boldsymbol{\eta}$. We employ the quasi-static subscales for $\boldsymbol{\eta}$ to circumvent the necessity of conforming finite elements. Invoking the decomposition into finite element approximation and subgrid scale for both $\boldsymbol{\eta}^{n+1}$ and \mathbf{v}^s , we have

$$\begin{aligned} \rho_p (\mathbf{d}_{tt}\boldsymbol{\eta}_h^{n+1}, \mathbf{v}_h^s)_{\Omega_{t^{n+1}}^p} + (\boldsymbol{\sigma}_s^E(\boldsymbol{\eta}_h^{n+1}), \nabla \mathbf{v}_h^s)_{\Omega_{t^{n+1}}^p} - (\tilde{\boldsymbol{\eta}}^{n+1}, \boldsymbol{\sigma}_{s,h}^{E*}(\nabla \mathbf{v}_h^s))_{\Omega_{t^{n+1}}^p} \\ - (p_{p,h}^{n+1}, \nabla \cdot \mathbf{v}_h^s)_{\Omega_{t^{n+1}}^p} = (\mathbf{f}_s^{n+1}, \mathbf{v}_h^s)_{\Omega_{t^{n+1}}^p}, \end{aligned} \quad (6.45a)$$

$$\begin{aligned} \rho_p (\mathbf{d}_{tt}\boldsymbol{\eta}_h^{n+1}, \tilde{\mathbf{v}}^s)_{\Omega_{t^{n+1}}^p} - (\nabla \cdot \boldsymbol{\sigma}_s^E(\boldsymbol{\eta}_h^{n+1}), \tilde{\mathbf{v}}^s)_{\Omega_{t^{n+1}}^p} - (\nabla \cdot \boldsymbol{\sigma}_s^E(\tilde{\boldsymbol{\eta}}^{n+1}), \tilde{\mathbf{v}}^s)_{\Omega_{t^{n+1}}^p} \\ + (\nabla p_{p,h}^{n+1}, \tilde{\mathbf{v}}^s)_{\Omega_{t^{n+1}}^p} = (\mathbf{f}_s^{n+1}, \tilde{\mathbf{v}}^s)_{\Omega_{t^{n+1}}^p}, \end{aligned} \quad (6.45b)$$

$$(\nabla \cdot \boldsymbol{\eta}_h^{n+1}, q_{p,h})_{\Omega_{t^{n+1}}^p} - (\tilde{\boldsymbol{\eta}}^{n+1}, \nabla q_{p,h})_{\Omega_{t^{n+1}}^p} = (g^{n+1}, q_{p,h})_{\Omega_{t^{n+1}}^p}, \quad (6.45c)$$

where $\boldsymbol{\sigma}_{s,h}^{E*}(\cdot)$ is the formal adjoint operator of $\boldsymbol{\sigma}_s^E(\cdot)$ evaluated element-wise, neglecting inter-element jumps.

An approximation in (6.45b) is required in order to be able to find an expression for the subscale $\tilde{\boldsymbol{\eta}}^{n+1}$ in terms of $(\boldsymbol{\eta}_h^{n+1}, p_{p,h}^{n+1})$. The following simplification (see [36, 29, 5]) could be considered

$$-\nabla \cdot \boldsymbol{\sigma}_s^E(\tilde{\boldsymbol{\eta}}^{n+1}) \approx \tau^{-1} \tilde{\boldsymbol{\eta}}^{n+1}, \quad (6.46)$$

where τ is a stabilization parameter defined within each element. In solid mechanics, it can be taken as

$$\tau = c \left(\frac{2\mu_\ell}{h^2} \right)^{-1},$$

where c is a numerical constant and h is a characteristic length of the element. The subgrid component $\tilde{\boldsymbol{\eta}}^{n+1}$ is localized to the element by replacing the Laplacian operator at the left-hand-side of (6.46) with a differential operator which evaluates the Laplacian only on the interior of the finite elements (thus neglecting inter-element jumps).

Simplification (6.46) allows us to write from (6.45b) the equation for the subscale

$$\begin{aligned} \tau^{-1} \tilde{\boldsymbol{\eta}}^{n+1} &= -\mathcal{P} \left(\rho_p \mathbf{d}_{tt} \boldsymbol{\eta}_h^{n+1} - \nabla \cdot \boldsymbol{\sigma}_s^E(\boldsymbol{\eta}_h^{n+1}) + \nabla p_{p,h}^{n+1} - \mathbf{f}_s^{n+1} \right) \\ &\simeq -\mathcal{P} \left(\rho_p \mathbf{d}_{tt} \boldsymbol{\eta}_h^{n+1} + \nabla p_{p,h}^{n+1} - \mathbf{f}_s^{n+1} \right). \end{aligned} \quad (6.47)$$

The terms $\nabla \cdot \boldsymbol{\sigma}_s^E(\boldsymbol{\eta}_h^{n+1})$ and $\boldsymbol{\sigma}_{s,h}^{E*}(\nabla \mathbf{v}_h^s)$ involve second derivatives of finite elements functions which vanish in case of linear elements. Since for the results in Section 6.9 we employ linear elements and for the sake of simplicity, those terms will be neglected in what follows. However, we remark that, when higher order elements and the ASGS method are used, $\nabla \cdot \boldsymbol{\sigma}_s^E(\boldsymbol{\eta}_h^{n+1})$ and $\boldsymbol{\sigma}_{s,h}^{E*}(\nabla \mathbf{v}_h^s)$ are needed in order to keep consistency.

In our case, the stabilization term of the momentum conservation equation (6.45a) is negligible.

By invoking (6.47) in equation (6.45c) and considering the usual approximation for \mathcal{P} , we obtain

$$\begin{aligned} (\nabla \cdot \boldsymbol{\eta}_h^{n+1}, q_{p,h})_{\Omega_{t^{n+1}}^p} + \alpha \tau ((\rho_p \mathbf{d}_{tt} \boldsymbol{\eta}_h^{n+1} + \nabla p_{p,h}^{n+1}), \nabla q_{p,h})_{\Omega_{t^{n+1}}^p} &= (g^{n+1}, q_{p,h})_{\Omega_{t^{n+1}}^p} \\ &+ \alpha \tau (\mathbf{f}_s^{n+1}, \nabla q_{p,h})_{\Omega_{t^{n+1}}^p}. \end{aligned}$$

This stabilization allows pressure stability in case of “small” K_D .

Remark 6.6. *If we use the dynamic subscales, instead of the quasi-static ones, equation (6.45a) is replaced by*

$$\begin{aligned} \rho_p (\mathbf{d}_{tt} \boldsymbol{\eta}_h^{n+1}, \mathbf{v}_h^s)_{\Omega_{t^{n+1}}^p} + (\boldsymbol{\sigma}_s^E(\boldsymbol{\eta}_h^{n+1}), \nabla \mathbf{v}_h^s)_{\Omega_{t^{n+1}}^p} + \rho_p (\mathbf{d}_{tt} \tilde{\boldsymbol{\eta}}^{n+1}, \mathbf{v}_h^s)_{\Omega_{t^{n+1}}^p} \\ - (\tilde{\boldsymbol{\eta}}^{n+1}, \boldsymbol{\sigma}_{s,h}^{E*}(\nabla \mathbf{v}_h^s))_{\Omega_{t^{n+1}}^p} - (p_{p,h}^{n+1}, \nabla \cdot \mathbf{v}_h^s)_{\Omega_{t^{n+1}}^p} = (\mathbf{f}_s^{n+1}, \mathbf{v}_h^s)_{\Omega_{t^{n+1}}^p}. \end{aligned} \quad (6.48)$$

Since the time derivative of the subscale is no more considered to be negligible, the equation for $\tilde{\boldsymbol{\eta}}^{n+1}$ is the following

$$\rho_p \mathbf{d}_{tt} \tilde{\boldsymbol{\eta}}^{n+1} + \tau^{-1} \tilde{\boldsymbol{\eta}}^{n+1} = -\mathcal{P} \left(\rho_p \mathbf{d}_{tt} \boldsymbol{\eta}_h^{n+1} + \nabla p_{p,h}^{n+1} - \mathbf{f}_s^{n+1} \right),$$

instead of (6.47). The difficulty associated to the dynamic subscales is that it is impossible to write problem (6.48)-(6.45c) only in terms of the finite element approximations $(\boldsymbol{\eta}_h^{n+1}, p_{p,h}^{n+1})$. We would need to track in time the subscales (see [41]). Because of this complication, we prefer to adopt the quasi-static subscales approach.

Now, our goal is to find a stabilized formulation for the Biot system that could be used independently of the value of K_D . To this purpose, let us stabilize system (6.1a)-(6.1b)-(6.35) with the stabilization of both the generalized Darcy problem and the incompressible elasticity. We make use of the quasi-static subscales for both problems. Thus, we have

$$\begin{aligned} \rho_p(\mathrm{d}_{tt}\boldsymbol{\eta}_h^{n+1}, \mathbf{v}_h^s)_{\Omega_{t^{n+1}}^p} + \rho_d(\mathrm{d}_t\mathbf{q}_h^{n+1}, \mathbf{v}_h^s)_{\Omega_{t^{n+1}}^p} + (\boldsymbol{\sigma}_s^E(\boldsymbol{\eta}_h^{n+1}), \nabla\mathbf{v}_h^s)_{\Omega_{t^{n+1}}^p} \\ - (\tilde{\boldsymbol{\eta}}^{n+1}, \boldsymbol{\sigma}_{s,h}^{E*}(\nabla\mathbf{v}_h^s))_{\Omega_{t^{n+1}}^p} - (p_{p,h}^{n+1}, \nabla \cdot \mathbf{v}_h^s)_{\Omega_{t^{n+1}}^p} = (\mathbf{f}_s^{n+1}, \mathbf{v}_h^s)_{\Omega_{t^{n+1}}^p}, \end{aligned} \quad (6.49a)$$

$$\begin{aligned} \rho_p(\mathrm{d}_{tt}\boldsymbol{\eta}_h^{n+1}, \tilde{\mathbf{v}}^s)_{\Omega_{t^{n+1}}^p} + \rho_d(\mathrm{d}_t\mathbf{q}_h^{n+1}, \tilde{\mathbf{v}}^s)_{\Omega_{t^{n+1}}^p} - (\nabla \cdot \boldsymbol{\sigma}_s^E(\boldsymbol{\eta}_h^{n+1}), \tilde{\mathbf{v}}^s)_{\Omega_{t^{n+1}}^p} \\ - (\nabla \cdot \boldsymbol{\sigma}_s^E(\tilde{\boldsymbol{\eta}}^{n+1}), \tilde{\mathbf{v}}^s)_{\Omega_{t^{n+1}}^p} + (\nabla p_{p,h}^{n+1}, \tilde{\mathbf{v}}^s)_{\Omega_{t^{n+1}}^p} = (\mathbf{f}_s^{n+1}, \tilde{\mathbf{v}}^s)_{\Omega_{t^{n+1}}^p}, \end{aligned} \quad (6.49b)$$

$$\begin{aligned} \rho_d(\mathrm{d}_t\mathbf{u}_{s,h}^{n+1}, \mathbf{r}_h)_{\Omega_{t^{n+1}}^p} + \frac{\rho_d}{\phi}(\mathrm{d}_t\mathbf{q}_h^{n+1}, \mathbf{r}_h)_{\Omega_{t^{n+1}}^p} + K_D^{-1}(\mathbf{q}_h^{n+1}, \mathbf{r}_h)_{\Omega_{t^{n+1}}^p} \\ + K_D^{-1}(\tilde{\mathbf{q}}^{n+1}, \mathbf{r}_h)_{\Omega_{t^{n+1}}^p} - (p_{p,h}^{n+1}, \nabla \cdot \mathbf{r}_h)_{\Omega_{t^{n+1}}^p} = (\mathbf{f}_d^{n+1}, \mathbf{r}_h)_{\Omega_{t^{n+1}}^p}, \end{aligned} \quad (6.49c)$$

$$\begin{aligned} \rho_d(\mathrm{d}_t\mathbf{u}_{s,h}^{n+1}, \tilde{\mathbf{r}})_{\Omega_{t^{n+1}}^p} + \frac{\rho_d}{\phi}(\mathrm{d}_t\mathbf{q}_h^{n+1}, \tilde{\mathbf{r}})_{\Omega_{t^{n+1}}^p} + K_D^{-1}(\mathbf{q}_h^{n+1}, \tilde{\mathbf{r}})_{\Omega_{t^{n+1}}^p} \\ + K_D^{-1}(\tilde{\mathbf{q}}^{n+1}, \tilde{\mathbf{r}})_{\Omega_{t^{n+1}}^p} + (\nabla p_{p,h}^{n+1}, \tilde{\mathbf{r}})_{\Omega_{t^{n+1}}^p} = (\mathbf{f}_d^{n+1}, \tilde{\mathbf{r}})_{\Omega_{t^{n+1}}^p}, \end{aligned} \quad (6.49d)$$

$$(\nabla \cdot (\mathbf{u}_{s,h}^{n+1} + \mathbf{q}_h^{n+1}), q_{p,h})_{\Omega_{t^{n+1}}^p} - (\tilde{\mathbf{u}}_s^{n+1} + \tilde{\mathbf{q}}^{n+1}, \nabla q_{p,h})_{\Omega_{t^{n+1}}^p} = (g^{n+1}, q_{p,h})_{\Omega_{t^{n+1}}^p}, \quad (6.49e)$$

with $\tilde{\mathbf{u}}_s^{n+1} = \delta_t \tilde{\boldsymbol{\eta}}^{n+1}$. From (6.49b), thanks to simplification (6.46) and neglecting the term $\nabla \cdot \boldsymbol{\sigma}_s^E(\boldsymbol{\eta}_h^{n+1})$, it follows that

$$\tau^{-1}\tilde{\boldsymbol{\eta}}^{n+1} = -\mathcal{P}(\rho_p \mathrm{d}_{tt}\boldsymbol{\eta}_h^{n+1} + \rho_d \mathrm{d}_t\mathbf{q}_h^{n+1} + \nabla p_{p,h}^{n+1} - \mathbf{f}_s^{n+1}),$$

and so

$$\tau^{-1}\tilde{\mathbf{u}}_s^{n+1} = -\mathcal{P}(\rho_p \mathrm{d}_{tt}\mathbf{u}_{s,h}^{n+1} + \rho_d \mathrm{d}_{tt}\mathbf{q}_h^{n+1} + \nabla(\mathrm{d}_t p_{p,h}^{n+1}) - \mathrm{d}_t \mathbf{f}_s^{n+1}).$$

From equation (6.49d), we get

$$K_D^{-1}\tilde{\mathbf{q}}^{n+1} = -\mathcal{P}\left(\rho_d \mathrm{d}_t\mathbf{u}_{s,h}^{n+1} + \frac{\rho_d}{\phi}\mathrm{d}_t\mathbf{q}_h^{n+1} + K_D^{-1}\mathbf{q}_h^{n+1} + \nabla p_{p,h}^{n+1} - \mathbf{f}_d^{n+1}\right).$$

The stabilization term in equation (6.49a) is neglected because it involves $\boldsymbol{\sigma}_{s,h}^{E*}(\nabla\mathbf{v}_h^s)$, while equation (6.49c) becomes (6.40).

Plugging the expressions for the subscales of structure and filtration velocity into equation (6.49e), the stabilized continuity equation is as follows

$$\begin{aligned}
& (\nabla \cdot \mathbf{u}_{s,h}^{n+1}, q_{p,h})_{\Omega_{t^{n+1}}^p} - \alpha \tau \rho_p (\nabla \cdot \mathbf{d}_{tt} \mathbf{u}_{s,h}^{n+1}, q_{p,h})_{\Omega_{t^{n+1}}^p} - \alpha K_D \rho_d (\nabla \cdot \mathbf{d}_t \mathbf{u}_{s,h}^{n+1}, q_{p,h})_{\Omega_{t^{n+1}}^p} \\
& + (1 - \alpha) (\nabla \cdot \mathbf{q}_h^{n+1}, q_{p,h})_{\Omega_{t^{n+1}}^p} - \alpha \tau \rho_d (\nabla \cdot \mathbf{d}_{tt} \mathbf{q}_h^{n+1}, q_{p,h})_{\Omega_{t^{n+1}}^p} - \alpha K_D \frac{\rho_d}{\phi} (\nabla \cdot \mathbf{d}_t \mathbf{q}_h^{n+1}, q_{p,h})_{\Omega_{t^{n+1}}^p} \\
& + \alpha \tau (\nabla (\mathbf{d}_t p_{p,h}^{n+1}), \nabla q_{p,h})_{\Omega_{t^{n+1}}^p} + \alpha K_D (\nabla p_{p,h}^{n+1}, \nabla q_{p,h})_{\Omega_{t^{n+1}}^p} = (g^{n+1}, q_{p,h})_{\Omega_{t^{n+1}}^p} \\
& + \alpha \tau (\mathbf{d}_t \mathbf{f}_s^{n+1}, \nabla q_{p,h})_{\Omega_{t^{n+1}}^p} + \alpha K_D (\mathbf{f}_d^{n+1}, \nabla q_{p,h})_{\Omega_{t^{n+1}}^p}. \tag{6.50}
\end{aligned}$$

Finally, the stabilized Galerkin formulation reads: Given $\mathbf{u}_{s,h}^n$ and \mathbf{q}_h^n , for $n \geq 0$ find $(\mathbf{u}_{s,h}^{n+1}, \mathbf{q}_h^{n+1}, p_{p,h}^{n+1}) \in V_h^s \times R_h \times Q_h^p$ such that (6.41) holds, with

$$\begin{aligned}
\mathcal{A}_p(\mathbf{u}_{s,h}^{n+1}, \mathbf{q}_h^{n+1}, p_{p,h}^{n+1}; \mathbf{v}_h^s, \mathbf{r}_h, q_{p,h})_{\Omega_{t^{n+1}}^p} &= \rho_p (\mathbf{d}_t \mathbf{u}_{s,h}^{n+1}, \mathbf{v}_h^s)_{\Omega_{t^{n+1}}^p} + \rho_d (\mathbf{d}_t \mathbf{q}_h^{n+1}, \mathbf{v}_h^s)_{\Omega_{t^{n+1}}^p} \\
&+ (\boldsymbol{\sigma}_s^E(\boldsymbol{\eta}_h^{n+1}), \nabla \mathbf{v}_h^s)_{\Omega_{t^{n+1}}^p} - (p_{p,h}^{n+1}, \nabla \cdot \mathbf{v}_h^s)_{\Omega_{t^{n+1}}^p} + (1 - \alpha) \left(\frac{\rho_d}{\phi} \mathbf{d}_t \mathbf{q}_h^{n+1} + K_D^{-1} \mathbf{q}_h^{n+1}, \mathbf{r}_h \right)_{\Omega_{t^{n+1}}^p} \\
&+ (1 - \alpha) \rho_d (\mathbf{d}_t \mathbf{u}_{s,h}^{n+1}, \mathbf{r}_h)_{\Omega_{t^{n+1}}^p} - (1 - \alpha) (p_{p,h}^{n+1}, \nabla \cdot \mathbf{r}_h)_{\Omega_{t^{n+1}}^p} + (\nabla \cdot \mathbf{u}_{s,h}^{n+1}, q_{p,h})_{\Omega_{t^{n+1}}^p} \\
&- \alpha \tau \rho_p (\nabla \cdot \mathbf{d}_{tt} \mathbf{u}_{s,h}^{n+1}, q_{p,h})_{\Omega_{t^{n+1}}^p} - \alpha K_D \rho_d (\nabla \cdot \mathbf{d}_t \mathbf{u}_{s,h}^{n+1}, q_{p,h})_{\Omega_{t^{n+1}}^p} + (1 - \alpha) (\nabla \cdot \mathbf{q}_h^{n+1}, q_{p,h})_{\Omega_{t^{n+1}}^p} \\
&- \alpha \tau \rho_d (\nabla \cdot \mathbf{d}_{tt} \mathbf{q}_h^{n+1}, q_{p,h})_{\Omega_{t^{n+1}}^p} - \alpha K_D \frac{\rho_d}{\phi} (\nabla \cdot \mathbf{d}_t \mathbf{q}_h^{n+1}, q_{p,h})_{\Omega_{t^{n+1}}^p} + \alpha \tau (\nabla (\mathbf{d}_t p_{p,h}^{n+1}), \nabla q_{p,h})_{\Omega_{t^{n+1}}^p} \\
&+ \alpha K_D (\nabla p_{p,h}^{n+1}, \nabla q_{p,h})_{\Omega_{t^{n+1}}^p} \tag{6.51}
\end{aligned}$$

and

$$\begin{aligned}
b_p(\mathbf{v}_h^s, \mathbf{r}_h, q_{p,h})_{\Omega_{t^{n+1}}^p} &= (\mathbf{f}_s^{n+1}, \mathbf{v}_h^s)_{\Omega_{t^{n+1}}^p} + (1 - \alpha) (\mathbf{f}_d^{n+1}, \mathbf{r}_h)_{\Omega_{t^{n+1}}^p} + (g^{n+1}, q_{p,h})_{\Omega_{t^{n+1}}^p} \\
&+ \alpha \tau (\mathbf{f}_s^{n+1}, \nabla q_{p,h})_{\Omega_{t^{n+1}}^p} + \alpha K_D (\mathbf{f}_d^{n+1}, \nabla q_{p,h})_{\Omega_{t^{n+1}}^p}. \tag{6.52}
\end{aligned}$$

This stabilization can be adopted for every value of the hydraulic conductivity.

6.4.5 Numerical results

We present first the results for the Darcy problem (6.2a)-(6.11). To study the convergence rates we consider a test problem taken from [92]. The domain is a square with side length one. The exact pressure solution is given by:

$$p = \sin(2\pi x) \sin(2\pi y).$$

The velocity field \mathbf{q} is computed from equation (6.2a), after setting $\mathbf{f}_d = \mathbf{0}$. Then, g is calculated from (6.11) by taking the divergence of the velocity field. The problem is supplemented with Dirichlet conditions $\mathbf{q} \cdot \mathbf{n} = q_D$ on $\partial\Omega^p$. The datum q_D is computed by taking the normal component of the velocity.

We consider linear triangular elements. The elliptic meshes employed consist of 200, 800, 3200 and 128000 elements. The element mesh parameter h is taken to be the short-edge length.

For the results in Fig. 6.3 and Fig. 6.4, we considered the OSS stabilized formulation reported in Section 6.4.1. Fig. 6.3 shows the L^2 -norm of the velocity and pressure errors for $K_D = 1$ for different choices of the parameter α : $\alpha = 1, 0.95, 0.5$. For $\alpha = 0.5$, the OSS approach is equivalent to the ASGS approach (see Section 6.4.1) and we recover the same rates shown in [92]. The choice $\alpha = 1$ corresponds to solving a Poisson problem for the pressure and recovering the velocity through $\mathbf{q}_h = \Pi^0(\nabla p_{p,h} - \text{Ext}_h(q_D))$. Here, Π^0 is the projection onto the velocity finite element space with boundary conditions. In this case (and for values of α close to 1, like $\alpha = 0.95$), the L^2 -rate of convergence for the velocity is no more optimal, as expected.

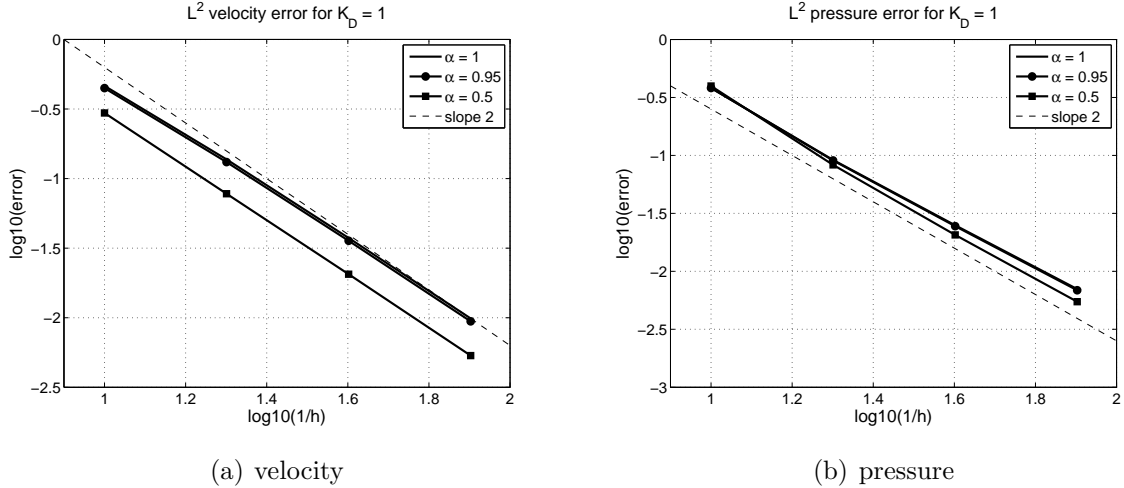


Figure 6.3: Darcy problem: convergence rate for the (a) velocity and (b) pressure, for $K_D = 1$.

The same simulations are performed for $K_D = 0.01$. The convergence rates for velocity and pressure show the same behavior of the $K_D = 1$ case for all the values of α (see Fig. 6.4).

To test the robustness of the stabilized formulation for the Darcy problem, we solve a quarter of the five-spot problem (see [92]). Again the domain under consideration is a square of side length one. Velocity is prescribed at the source (the lower left-hand corner) and at the sink (the upper right-hand corner), see Fig. 6.5(a). The divergence of the velocity field g is assumed to be a Dirac delta function acting at the source and sink, with strength $+1/4$ and $-1/4$, respectively. Since the problem is symmetric, zero normal flow is prescribed along the boundaries. To solve the problem, we calculate an equivalent

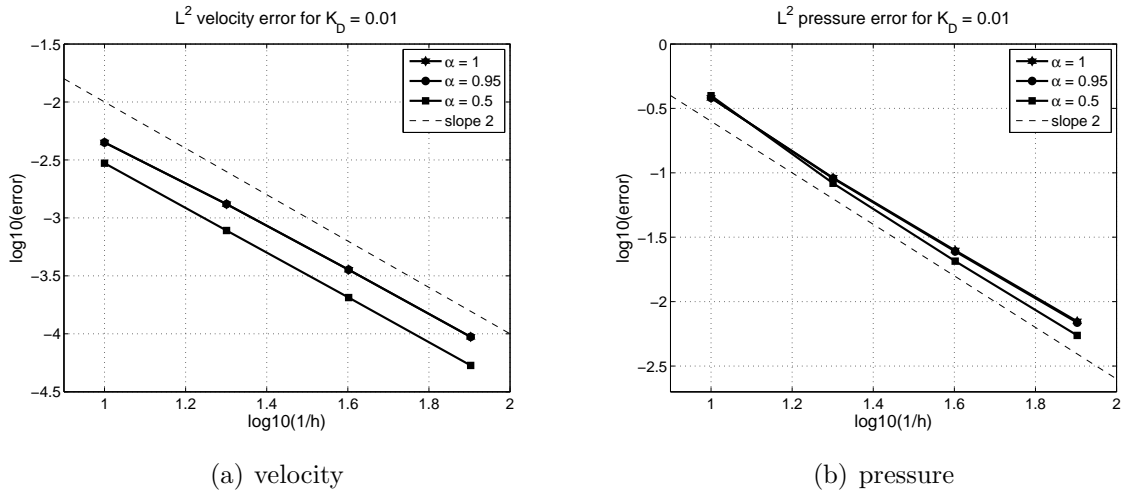


Figure 6.4: Darcy problem: convergence rate for the (a) velocity and (b) pressure, for $K_D = 0.01$.

distribution of normal velocity q_D , setting $g = 0$. We assume a linear distribution of q_D along the external edges of the corner elements, which is zero at the nodes adjacent to the corner ones and $1/4h$ at the corner nodes (see Fig. 6.5(b)). We take $K_D = 0.5$.

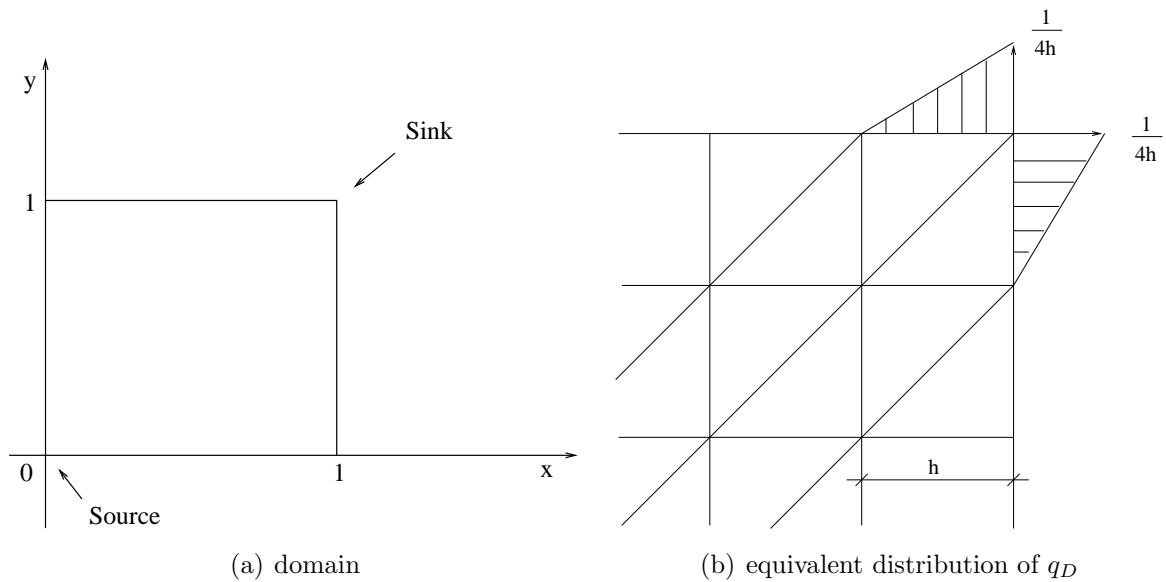


Figure 6.5: (a) Five-spot problem domain and (b) equivalent distribution of q_D along the corner elements at the sink.

Fig. 6.6(a) presents the pressure distribution along the diagonal for the different values

of the stabilization parameter $\alpha = 1, 0.95, 0.5$. The domain has been discretized with an elliptic mesh consisting of 800 triangular elements. In all the cases, the singular behavior of the exact solution at the source and sink is captured. For the results in Fig. 6.6(b), we fixed $\alpha = 0.5$ and we solved the problem on all the meshes used for the previous simulation. The pressure distributions along the diagonal show that the singularities in the pressure field are always captured, proving the robustness of the stabilized formulation.

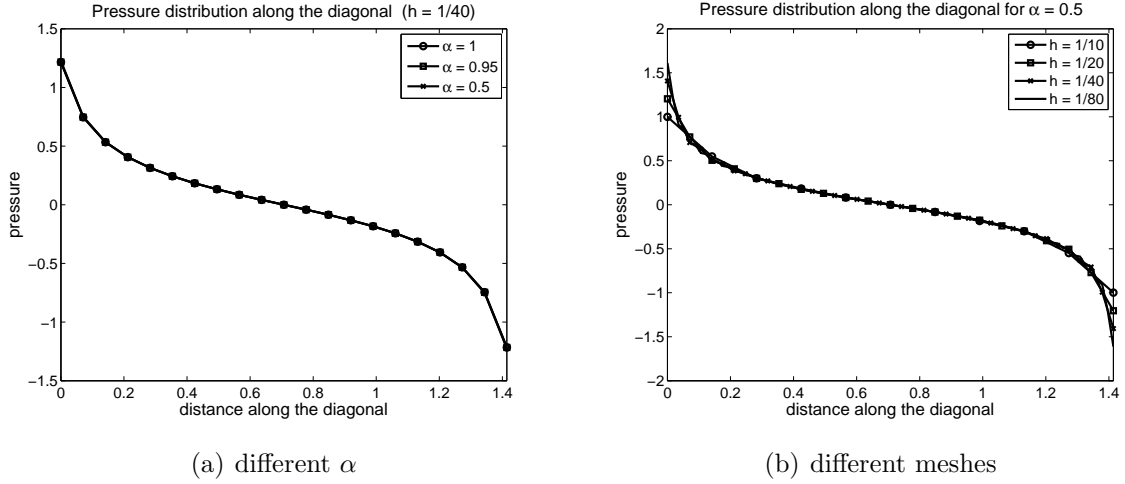


Figure 6.6: Five-spot problem: (a) pressure distribution along the diagonal for different value of the stabilization parameter α and (b) for different meshes.

Now, let us deal with the generalized Darcy problem (6.28). In order to check the convergence rates, we propose a test problem inspired by the one used for the Darcy equations. In a square of side length one, we consider the following exact velocity solution:

$$\mathbf{q} = \begin{bmatrix} -2\pi \cos(2\pi x) \sin(2\pi y)t \\ -2\pi \sin(2\pi x) \cos(2\pi y)t \end{bmatrix}.$$

The pressure field is computed from equation (6.28a) by setting $\mathbf{f}_d = 0$, while g is calculated from (6.28b). Dirichlet boundary conditions are imposed on the four sides.

We consider linear triangular elements and the same meshes as for the Darcy problem. Again, the mesh parameter h refers to the short-edge length of the elements. The time interval under consideration is $[0, 1]$ s.

For the results in Fig. 6.7, we considered the stabilized formulation introduced in Section 6.4.2 with the same three choices for α of the Darcy problem. The time step value we employed is $\delta t = 0.1$ s. Fig. 6.7 shows the L^2 -norm of the velocity and pressure errors for $\phi K_D^{-1} = 1$ and $\rho_d = 1$, at time $t = 1$ s. Also for the generalized Darcy problem, if $\alpha = 1$ or the value of α is close to one, the L^2 -rate of convergence for the velocity is less than 2.

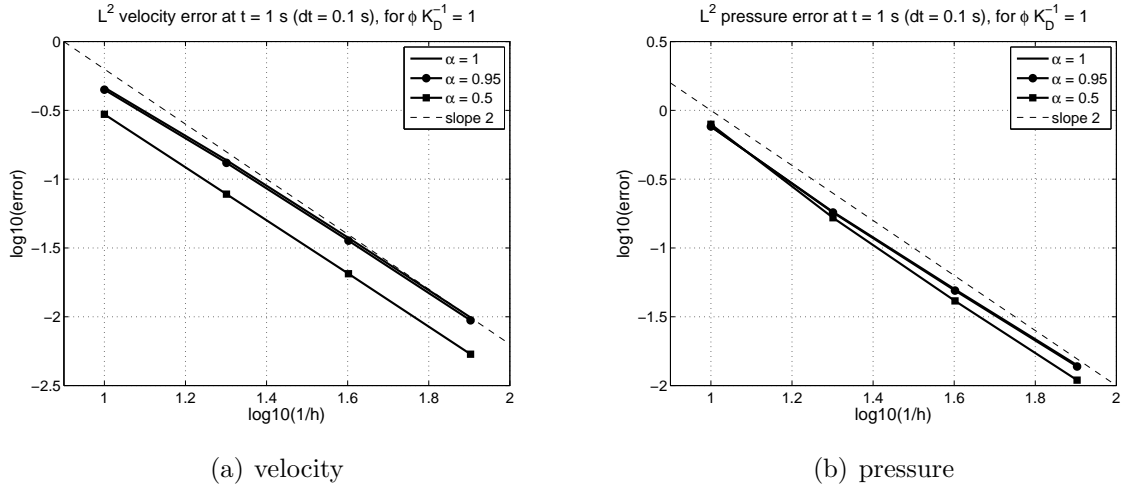


Figure 6.7: Generalized Darcy problem: convergence rate for the (a) velocity and (b) pressure, for $\phi K_D^{-1} = 1$, $\rho_d = 1$.

To check the order of convergence in time, we deal with the exact velocity:

$$\mathbf{q} = \begin{bmatrix} -\sin(t) \\ -\sin(t) \end{bmatrix}.$$

Thus, the exact pressure solution is $p_p = \left(\frac{\rho_d}{\phi} \cos(t) + K_D^{-1} \sin(t)\right)(x + y)$, and $g = 0$. Dirichlet boundary conditions are imposed on the four sides.

The square of size length one is discretized with an elliptic mesh of 800 triangles. Four time step values are considered ($\delta t = 0.1, 0.05, 0.025, 0.0125$ s) and all the errors are calculated at time $t = 1$ s. Fig. 6.8 shows that first order convergence in time is attained, as expected.

Finally, we perform a convergence test for the Biot system (6.1a)-(6.1b)-(6.35). The domain under consideration is again the biunit square and we impose forcing terms \mathbf{f}_s and \mathbf{f}_d such that the exact solution is

$$\mathbf{u}_s = \begin{bmatrix} -2\pi \sin(2\pi x) \cos(2\pi y) \\ -2\pi \cos(2\pi x) \sin(2\pi y) \end{bmatrix}, \quad \mathbf{q} = \phi \begin{bmatrix} -2\pi \cos(2\pi x) \sin(2\pi y)t + 2\pi \sin(2\pi x) \cos(2\pi y) \\ -2\pi \sin(2\pi x) \cos(2\pi y)t + 2\pi \cos(2\pi x) \sin(2\pi y) \end{bmatrix},$$

and

$$p = (\rho_d + K_D^{-1}\phi t) \sin(2\pi x) \sin(2\pi y) + K_D^{-1}\phi \cos(2\pi x) \cos(2\pi y) - K_D^{-1}\phi.$$

We impose Dirichlet conditions on the four sides both for \mathbf{u}_s and $\mathbf{q} \cdot \mathbf{n}$. The Dirichlet data for \mathbf{u}_s and \mathbf{q} are easily computed from the exact solution.

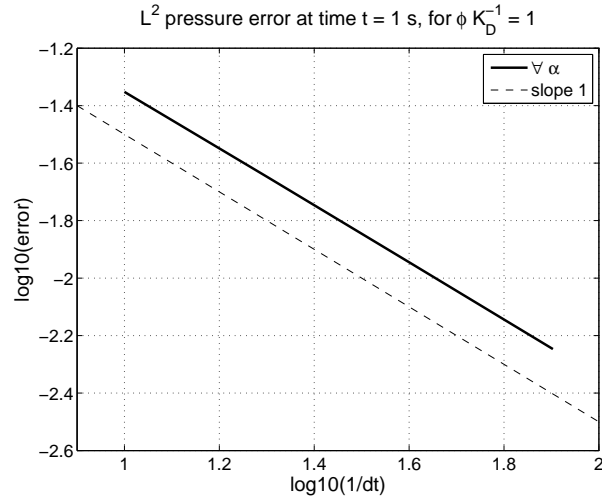


Figure 6.8: Generalized Darcy problem: order of convergence in time for $\phi K_D^{-1} = 1$, $\rho_d = 1$.

Meshes, time interval, and time step are the same ones used for the convergence test of the generalized Darcy problem. Fig. 6.9 shows the L^2 -norm of the pressure, structure and filtration velocity errors at time $t = 1$ s for $K_D = 1$, $\rho_d = 1$, $\rho_s = 1.2$, and $\phi = 0.2$. For these results, we adopted the stabilized formulation reported in Section 6.4.3 and chose $\alpha = 1, 0.5$. The same convergence rate of the Darcy and generalized Darcy problem is recovered.

If we repeat the same test for $K_D \sim 10^{-12}$, the pressure shows instabilities. Hence, for such a small value of the hydraulic conductivity, pressure stability cannot be achieved.

Concluding, the stabilization method introduced in Section 6.4.3 works well for values of K_D typical of previous or semi-pervious media, whereas for very small values an alternative is needed. For the numerical experiments in Section 6.9, we used the alternative stabilization proposed in Section 6.4.4. It guaranteed pressure stability for the wide range of parameters we tested.

6.5 The fully discrete problem

Let us consider matching partitions for the fluid and structure subdomain, as in Section 2.4.

For the fluid subproblem, we consider the BDF1 scheme and a stabilized finite element formulation for the time and space discretization, respectively. The fully discretized fluid-structure problem couples this discrete fluid subproblem to the discrete poroelastic subproblem (6.41). Thus, it reads

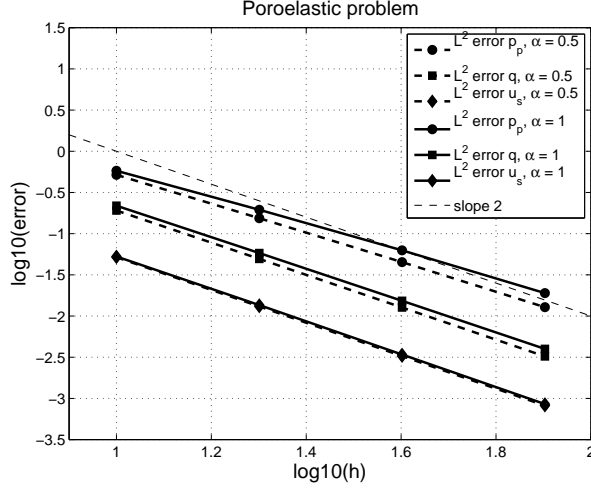


Figure 6.9: Biot problem: convergence rate for the pressure, structure, and filtration velocity.

1. Geometry problem: Find the fluid domain displacement as in (2.19).
2. Fluid-structure problem: Find $(\mathbf{u}_{f,h}^{n+1}, p_{f,h}^{n+1}, \mathbf{u}_{s,h}^{n+1}, \mathbf{q}_h^{n+1}, p_{p,h}^{n+1}) \in V_h^f \times Q_h^f \times V_h^s \times R_h \times Q_{0,h}^p$ such that

$$\begin{aligned} & \rho_f \left(\delta_t \mathbf{u}_{f,h}^{n+1} |_{\mathbf{x}_0}, \mathbf{v}_h^f \right)_{\Omega_{t^{n+1}}^f} + \mathcal{N}_s \left(\mathbf{u}_{f,h}^{n+1} - \mathbf{w}_h^{n+1}; \mathbf{u}_{f,h}^{n+1}, p_{f,h}^{n+1}, \mathbf{v}_h^f, q_{f,h} \right)_{\Omega_{t^{n+1}}^f} \\ & - \left(\frac{\gamma}{\sqrt{K_D}} (\mathbf{u}_{f,h}^{n+1} \cdot \mathbf{t} - \mathbf{u}_{s,h}^{n+1} \cdot \mathbf{t}) \mathbf{t}, \mathbf{v}_h^f \right)_{\Sigma_{t^{n+1}}} = \left\langle \mathbf{f}_f^{n+1}, \mathbf{v}_h^f \right\rangle_{\Omega_{t^{n+1}}^f}, \end{aligned} \quad (6.53a)$$

$$\begin{aligned} & \mathcal{A}_p(\mathbf{u}_{s,h}^{n+1}, \mathbf{q}_h^{n+1}, p_{p,h}^{n+1}; \mathbf{v}_h^s, \mathbf{r}_h, q_{p,h})_{\Omega_{t^{n+1}}^p} = b_p(\mathbf{v}_h^s, \mathbf{r}_h, q_{p,h})_{\Omega_{t^{n+1}}^p} \\ & - \left\langle \mathcal{R}_f(\mathbf{u}_{f,h}^{n+1}, p_{f,h}^{n+1}), \mathcal{E}_h^f(\mathbf{v}_h^s |_{\Sigma_{t^{n+1}}}) \right\rangle_{\Omega_{t^{n+1}}^f} \\ & - (1 - \alpha) \left\langle (\mathcal{R}_f(\mathbf{u}_{f,h}^{n+1}, p_{f,h}^{n+1}) \cdot \mathbf{n}), \mathcal{E}_h^f(\mathbf{r}_h |_{\Sigma_{t^{n+1}}}) \right\rangle_{\Omega_{t^{n+1}}^f} \end{aligned} \quad (6.53b)$$

$$\langle \mathbf{u}_{f,h}^{n+1} \cdot \mathbf{n}, \mathbf{v}_h^f |_{\Sigma_{t^{n+1}}} \rangle = \langle (\mathbf{q}_h^{n+1} + \mathbf{u}_{s,h}^{n+1}) \cdot \mathbf{n}, \mathbf{v}_h^f |_{\Sigma_{t^{n+1}}} \rangle, \quad (6.53c)$$

for all $(\mathbf{v}_h^f, q_{f,h}, \mathbf{v}_h^s, \mathbf{r}_h, q_{p,h}) \in V_{0,h}^f \times Q_h^f \times V_h^s \times R_h \times Q_{0,h}^p$.

Form \mathcal{A}_p and functional b_p are defined either by (6.42) and (6.43), in case of pervious and semi-pervious porous media, or by (6.51) and (6.52), for any kind of porous media.

Like the FSI problem (2.19)-(2.20), problem (2.19)-(6.53) is nonlinear. Also in this case, we consider a fixed point method for the linearization of both the geometrical nonlinearity and the one due to the convective term. It consists of: given the predictions $\tilde{\boldsymbol{\eta}}_h^{n+1}$ and $\tilde{\mathbf{u}}_{f,h}^{n+1}$

- Step 1: Compute the fluid domain displacement as in (2.19) but replacing the first equation with (2.22).
- Step 2: Solve the fluid-structure problem as in (6.53) replacing the fluid momentum equation (6.53a) by its linearized version:

$$\begin{aligned} & \rho_f \left(\delta_t \mathbf{u}_{f,h}^{n+1} |_{\mathbf{x}_0}, \mathbf{v}_h^f \right)_{\Omega_{t^{n+1}}^f} + \mathcal{N}_s \left(\tilde{\mathbf{u}}_{f,h}^{n+1} - \mathbf{w}_h^{n+1}; \mathbf{u}_{f,h}^{n+1}, p_{f,h}^{n+1}, \mathbf{v}_h^f, q_{f,h} \right)_{\Omega_{t^{n+1}}^f} \\ & - \left(\frac{\gamma}{\sqrt{K_D}} (\mathbf{u}_{f,h}^{n+1} \cdot \mathbf{t} - \mathbf{u}_{s,h}^{n+1} \cdot \mathbf{t}) \mathbf{t}, \mathbf{v}_h^f \right)_{\Sigma_{t^{n+1}}} = \left\langle \mathbf{f}_f^{n+1}, \mathbf{v}_h^f \right\rangle_{\Omega_{t^{n+1}}^f}. \end{aligned} \quad (6.54)$$

- Step 3: Check the stopping criterion. If it is not satisfied, update $\tilde{\boldsymbol{\eta}}_h^{n+1} = \hat{\boldsymbol{\eta}}_h^{n+1}$ (we recall that $\hat{\boldsymbol{\eta}}_h^{n+1} = \boldsymbol{\eta}_h^{n+1} \circ \mathcal{L}_{t^{n+1}}$), $\tilde{\mathbf{u}}_{f,h}^{n+1} = \mathbf{u}_{f,h}^{n+1}$ and go to Step 1.

The fully discretized and linearized fluid-structure problem we obtain at step 2 can be solved by a linear solver. Different strategies for the solution of this system are tackled in Sections 6.7 and 6.8.

When using inf-sup stable finite elements for the fluid subproblem, the only difference is that the form \mathcal{N}_s has to be replaced by \mathcal{N}_h in (6.53a) and (6.54).

6.6 The linear fluid-structure system

The purpose of this section is to write the linear system that has to be solved at every iteration of the fixed point method (6.54)-(6.53b)-(6.53c). For the moment, we consider \mathcal{A}_p and b_p in (6.53b) as defined by (6.42) and (6.43).

Like it has been done in Section 1.4.4 for fluid problems in rigid domains and in Section 3.2 for the interaction between a fluid and an elastic structure, we start by introducing the Lagrange basis associated to the finite element spaces. We denote by $\{\phi_i\}_{\mathcal{N}_f} \oplus \{\phi_j^\sigma\}_{\mathcal{N}_\sigma}$, $\{\psi_i\}_{\mathcal{N}_s} \oplus \{\psi_j^\sigma\}_{\mathcal{N}_\sigma}$, $\{\varphi_i\}_{\mathcal{N}_q} \oplus \{\varphi_j^\sigma\}_{\mathcal{N}_\sigma}$, $\{\pi_i\}_{\mathcal{N}_{pf}}$, and $\{\xi_i\}_{\mathcal{N}_{pp}}$, the basis for V_h^f , V_h^s , R_h , Q_h^f , and $Q_{0,h}^p$, respectively. The sets of pressure nodes in the fluid and structure subdomain are indicated by \mathcal{N}_{pf} and \mathcal{N}_{pp} . As in Section 3.2, \mathcal{N}_f , \mathcal{N}_s , and \mathcal{N}_σ refer to the set of fluid inner nodes, structure inner nodes for \mathbf{u}_s and velocity nodes on the interface, respectively. In addition, we have \mathcal{N}_q , the set of structure inner nodes for the filtration velocity. The time evolution of the finite element shape functions depends on the maps (2.2)-(2.8) as explained in Section 3.2.

We remind that, since we focused on the case of geometrical conforming grids, the nodes \mathcal{N}_σ belong to the grids of both subdomains. Hence, $\mathcal{E}_h^f(\psi_i^\sigma) = \phi_i^\sigma$ and $\mathcal{E}_h^d(\phi_i^\sigma) = \varphi_i^\sigma$, for $i \in \mathcal{N}_\sigma$.

The finite element approximation of all the velocities is easily written:

$$\begin{aligned} \mathbf{u}_{f,h}^{n+1}(\mathbf{x}, t^{n+1}) &= \sum_{i \in \mathcal{N}_f} \phi_i(\mathbf{x}, t^{n+1})(\mathbf{U}_{ff}^{n+1}(t^{n+1}))_i + \sum_{j \in \mathcal{N}_\sigma} \phi_j^\sigma(\mathbf{x}, t^{n+1})(\mathbf{U}_{f\sigma}^{n+1}(t^{n+1}))_j, \\ \mathbf{u}_{s,h}^{n+1}(\mathbf{x}, t^{n+1}) &= \sum_{i \in \mathcal{N}_s} \psi_i(\mathbf{x}, t^{n+1})(\mathbf{U}_{ss}^{n+1}(t^{n+1}))_i + \sum_{j \in \mathcal{N}_\sigma} \psi_j^\sigma(\mathbf{x}, t^{n+1})(\mathbf{U}_{s\sigma}^{n+1}(t^{n+1}))_j, \\ \mathbf{q}_h^{n+1}(\mathbf{x}, t^{n+1}) &= \sum_{i \in \mathcal{N}_q} \varphi_i(\mathbf{x}, t^{n+1})(\mathbf{Q}_q^{n+1}(t^{n+1}))_i + \sum_{j \in \mathcal{N}_\sigma} \varphi_j^\sigma(\mathbf{x}, t^{n+1})(\mathbf{Q}_\sigma^{n+1}(t^{n+1}))_j. \end{aligned}$$

\mathbf{U}_{ff}^{n+1} , \mathbf{U}_{ss}^{n+1} , and \mathbf{Q}_q^{n+1} are the arrays of nodal values for the velocities on the inner nodes of the respective subdomain, whereas the arrays $\mathbf{U}_{f\sigma}^{n+1}$, $\mathbf{U}_{s\sigma}^{n+1}$, and \mathbf{Q}_σ^{n+1} are related to the interface nodes.

The finite element approximation of the two pressures is

$$\begin{aligned} p_{f,h}^{n+1}(\mathbf{x}) &= \sum_{k \in \mathcal{N}_{pf}} \pi_k(\mathbf{x}, t^{n+1})(\mathbf{P}_f^{n+1}(t^{n+1}))_k, \\ p_{p,h}^{n+1}(\mathbf{x}) &= \sum_{k \in \mathcal{N}_{pp}} \xi_k(\mathbf{x}, t^{n+1})(\mathbf{P}_p^{n+1}(t^{n+1}))_k, \end{aligned}$$

where \mathbf{P}_f^{n+1} and \mathbf{P}_p^{n+1} are the arrays of nodal values for the pressure in $\Omega_{t^{n+1}}^f$ and $\Omega_{t^{n+1}}^p$, respectively.

Usually, the arrays of nodal values for the velocities are arranged for Cartesian components, e.g. in $2d$

$$\mathbf{U}_f^{n+1} = \begin{bmatrix} \mathbf{U}_{f,x}^{n+1} \\ \mathbf{U}_{f,y}^{n+1} \end{bmatrix}.$$

Here, \mathbf{U}_{ff}^{n+1} , \mathbf{U}_{ss}^{n+1} , and \mathbf{Q}_q^{n+1} are arranged in this way, whereas a rotation is required for $\mathbf{U}_{f\sigma}^{n+1}$, $\mathbf{U}_{s\sigma}^{n+1}$, and \mathbf{Q}_σ^{n+1} in order to impose interface conditions (6.4a) and (6.4d). In fact, the usual methods of treating a constrained degree of freedom are no longer applicable when we wish to specify the normal or tangential component of a variable at a boundary which is not parallel to the x or y axis. For a $2d$ problem, we need to pass from

$$\mathbf{U}_{f\sigma}^{n+1} = \begin{bmatrix} \mathbf{U}_{f\sigma,x}^{n+1} \\ \mathbf{U}_{f\sigma,y}^{n+1} \end{bmatrix} \quad \text{to} \quad \tilde{\mathbf{U}}_{f\sigma}^{n+1} = \begin{bmatrix} \tilde{\mathbf{U}}_{f\sigma,t}^{n+1} \\ \tilde{\mathbf{U}}_{f\sigma,n}^{n+1} \end{bmatrix}.$$

The tilde overscript indicates the rotation to the tangent-normal system.

In order to write the fully discretized coupled problem for a given time value t^{n+1} , we need the matrices and the notation for the submatrices introduced in Section 3.2. As a consequence of the rotation for the interface variables, all the matrices multiplied by them

must be rotated. To this purpose, we adopt the method described in [53]. So, for instance, we rotate matrix

$$C_{\sigma\sigma} = \begin{bmatrix} C_{\sigma\sigma,xx} & C_{\sigma\sigma,xy} \\ C_{\sigma\sigma,yx} & C_{\sigma\sigma,yy} \end{bmatrix} \quad \text{to} \quad \tilde{C}_{\sigma\sigma} = \begin{bmatrix} \tilde{C}_{\sigma\sigma,xt} & \tilde{C}_{\sigma\sigma,xn} \\ \tilde{C}_{\sigma\sigma,yt} & \tilde{C}_{\sigma\sigma,yn} \end{bmatrix}.$$

Let us define a few additional matrices to compact the notation for the fluid-structure linear system. Those related to the C -matrices are:

$$\begin{aligned} C_{\sigma f}^x &= \begin{bmatrix} C_{\sigma f,xx} & C_{\sigma f,xy} \\ 0 & 0 \end{bmatrix}, \quad C_{\sigma f}^y = \begin{bmatrix} 0 & 0 \\ C_{\sigma f,yx} & C_{\sigma f,yy} \end{bmatrix}, \\ \tilde{C}_{\sigma\sigma}^x &= \begin{bmatrix} \tilde{C}_{\sigma\sigma,xt} & \tilde{C}_{\sigma\sigma,xn} \\ 0 & 0 \end{bmatrix}, \quad \tilde{C}_{\sigma\sigma}^y = \begin{bmatrix} 0 & 0 \\ \tilde{C}_{\sigma\sigma,yt} & \tilde{C}_{\sigma\sigma,yn} \end{bmatrix}. \end{aligned} \quad (6.55)$$

Since there are divergence and gradient matrices in both subdomains, we need an additional subscript to specify the subdomain, e.g. in $G_{\beta\delta}$, β corresponds to the subdomain ($\beta = f$ or $\beta = p$) and δ to the set of nodes. In plus, we define matrices

$$G_{f\sigma}^{\tau,x} = \begin{bmatrix} G_{f\sigma,x}^{\tau} \\ 0 \end{bmatrix} \quad \text{and} \quad G_{f\sigma}^{\tau,y} = \begin{bmatrix} 0 \\ G_{f\sigma,y}^{\tau} \end{bmatrix}. \quad (6.56)$$

To impose coupling conditions (6.4a) and (6.4d), we introduce other two matrices:

$$R = \begin{bmatrix} \frac{\gamma}{\sqrt{K_D}} \tilde{M}_{\Sigma} & 0 \\ 0 & \tilde{M}_{\Sigma} \end{bmatrix} \quad \text{and} \quad B = \begin{bmatrix} 0 & 0 \\ 0 & \tilde{M}_{\Sigma} \end{bmatrix},$$

where we have indicated with \tilde{M}_{Σ} the rotated interface mass matrix.

Finally, for the stabilized continuity equation, we define matrices

$$\begin{aligned} E &= -a\tilde{D}_{s\sigma} - \alpha \frac{\rho_d}{\delta t} \begin{bmatrix} 0 & \tilde{M}_{\Sigma} \end{bmatrix}, \\ F &= -(1-\alpha)c\tilde{D}_{s\sigma} - \alpha c \begin{bmatrix} 0 & \tilde{M}_{\Sigma} \end{bmatrix}, \end{aligned}$$

where $a = \frac{\rho_d}{\delta t} \left(\frac{1}{\phi} - \alpha \right) + K_D^{-1}$ and $c = \frac{\rho_d}{\delta t} + K_D^{-1}$.

At a given time value t^{n+1} , equations (6.54)-(6.53b)-(6.53c) can be written in matrix form as:

$$A\mathbf{X}^{n+1} = \mathbf{b}^{n+1}, \quad (6.57)$$

where

$$A = \begin{bmatrix} C_{ff} & G_{ff}^\tau & \tilde{C}_{f\sigma} & 0 & 0 & 0 & 0 & 0 \\ D_{ff}^\tau & L^\tau & \tilde{D}_{f\sigma}^\tau & 0 & 0 & 0 & 0 & 0 \\ C_{\sigma f}^x & G_{f\sigma}^{\tau,x} & \tilde{C}_{\sigma\sigma}^x + R & -R & 0 & -B & 0 & 0 \\ C_{\sigma f} & G_{f\sigma}^\tau & \tilde{C}_{\sigma\sigma} & \tilde{N}_{\sigma\sigma} & N_{\sigma s} & \frac{\rho_d}{\delta t} \tilde{M}_{\sigma\sigma}^s & \frac{\rho_d}{\delta t} M_{\sigma q}^s & G_{p\sigma} \\ 0 & 0 & 0 & \tilde{N}_{s\sigma} & N_{ss} & \frac{\rho_d}{\delta t} \tilde{M}_{s\sigma}^s & \frac{\rho_d}{\delta t} M_{sq}^s & G_{ps} \\ C_{\sigma f}^y & G_{f\sigma}^{\tau,y} & \tilde{C}_{\sigma\sigma}^y & \frac{\rho_d}{\delta t} \tilde{M}_{\sigma\sigma}^s & \frac{\rho_d}{\delta t} M_{\sigma s}^s & c \tilde{M}_{\sigma\sigma}^s & c M_{\sigma q}^s & G_{p\sigma} \\ 0 & 0 & 0 & \frac{\rho_d}{\delta t} \tilde{M}_{q\sigma}^s & \frac{\rho_d}{\delta t} M_{qs}^s & c \tilde{M}_{q\sigma}^s & c M_{qq}^s & G_{pq} \\ 0 & 0 & 0 & E & -a D_{ps} & F & -(1-\alpha) c D_{pq} & \alpha L_p \end{bmatrix}, \quad (6.58)$$

and

$$\mathbf{X}^{n+1} = \begin{bmatrix} \mathbf{U}_{ff}^{n+1} \\ \mathbf{P}_f^{n+1} \\ \tilde{\mathbf{U}}_{f\sigma}^{n+1} \\ \tilde{\mathbf{U}}_{s\sigma}^{n+1} \\ \mathbf{U}_{ss}^{n+1} \\ \tilde{\mathbf{Q}}_\sigma^{n+1} \\ \mathbf{Q}_q^{n+1} \\ \mathbf{P}_p^{n+1} \end{bmatrix}, \quad \mathbf{b}^{n+1} = \begin{bmatrix} \mathbf{b}_{ff}^{n+1} \\ \mathbf{b}_{pf}^{n+1} \\ \mathbf{b}_{f\sigma}^{n+1} \\ \mathbf{b}_{s\sigma}^{n+1} \\ \mathbf{b}_{ss}^{n+1} \\ \mathbf{b}_{d\sigma}^{n+1} \\ \mathbf{b}_{dq}^{n+1} \\ \mathbf{b}_{pp}^{n+1} \end{bmatrix}.$$

Matrix L_p is defined as $L_p^{i,j} = (\nabla \xi_i, \nabla \xi_j)$, with $i, j \in \mathcal{N}_{pp}$. As for (3.4), the right-hand-side terms account for body forces, time integration and stabilization terms, and the structure terms related to the fact that the structure equation is stated in terms of velocities.

Once $\tilde{\mathbf{U}}_{f\sigma}^{n+1}$, $\tilde{\mathbf{U}}_{s\sigma}^{n+1}$, and $\tilde{\mathbf{Q}}_\sigma^{n+1}$ are computed, we obtain $\mathbf{U}_{f\sigma}^{n+1}$, $\mathbf{U}_{s\sigma}^{n+1}$, and \mathbf{Q}_σ^{n+1} by applying the inverse rotation.

Remarks 3.1, 3.3, and 3.4 hold also for fluid-poroelastic structure interaction problems.

Remark 6.7. *In case we use inf-sup stable finite elements for the fluid subproblem, submatrices G_{ff}^τ , $G_{f\sigma}^\tau$, D_{ff}^τ , $D_{f\sigma}^\tau$, and L^τ in (6.58) are replaced by G_{ff} , $G_{f\sigma}$, D_{ff} , $D_{f\sigma}$, and 0, respectively. Furthermore, vector \mathbf{b}_{pf}^{n+1} at the right-hand-side is equal to zero.*

Remark 6.8. *To derive matrix (6.58), we have adopted the stabilization method described in Section 6.4.3. If form \mathcal{A}_p and functional b_p were defined by (6.51) and (6.52), instead of (6.42) and (6.43), the only difference in the system matrix (6.58) would be in the last line.*

Let N_e denote the number of elements of \mathcal{T}_h , the triangulation for $\Omega_{t^{n+1}}^p$, and let K_e^k , with

$k = 1, \dots, N_e$, indicate the generic element. Once matrices

$$\begin{aligned}
 D_{p\delta}^{\tau,ij} &= \sum_{k=1}^{N_e} (\tau^k \nabla \cdot \boldsymbol{\psi}_i, \xi_j)_{K_e^k}, & i \in \mathcal{N}_\delta, j \in \mathcal{N}_{pp}, & \text{with } \delta = s, \sigma, \\
 D_{p\delta}^{\tau,ij} &= \sum_{k=1}^{N_e} (\tau^k \nabla \cdot \boldsymbol{\varphi}_i, \xi_j)_{K_e^k}, & i \in \mathcal{N}_\delta, j \in \mathcal{N}_{pp}, & \text{with } \delta = q, \sigma, \\
 L_p^{\tau,ij} &= \sum_{k=1}^{N_e} (\tau^k \nabla \xi_i, \nabla \xi_j)_{K_e^k}, & i \in \mathcal{N}_{pp}, j \in \mathcal{N}_{pp}. &
 \end{aligned}$$

are defined, the matrix form associated to the continuity equation stabilized as in (6.51) is easily written.

Remark 6.9. Matrix (6.58) has been written for a 2d problem for the sake of simplicity. In a 3d case, we would transform variables and matrices from the Cartesian coordinate system x - y - z to the tangent-normal-binormal system. Details about this rotation can be found in [53].

6.7 The monolithic approach

In Chapter 5 we showed the efficiency of non-modular methods for FSI problems affected by large added-mass effect. Thus, the first approach we take into consideration for the solution of system (6.57) is the monolithic one.

Because of the similar way in which they were derived, monolithic systems (6.57) and (3.4) share many features. In both cases, we rely on a single partition of the entire domain and make use of the same finite element space for fluid and structure velocities. Moreover, since we adopt a stabilized formulation for the poroelastic structure, the same finite element interpolation space can be used for its pressure p_p . In case of using stabilized finite elements for the fluid, we can use the same space for pressure p_f , too.

Thanks to these choices, the continuity of the stresses is easily imposed. In fact, the weak transmission of stresses arises from the fact that the shape functions on the interface nodes have a support on both fluid and structure subdomains. The remaining coupling conditions, i.e. the admissibility condition and the Beavers-Joseph-Saffman condition, are easily enforced, once the interface mass matrix M_Σ is computed (see the third line of matrix (6.58)).

We recall that the ILUT-solver approach presented in Section 5.4 combines the diagonal scaling of the system matrix with the ILUT preconditioner. The resulting system is solved by a matrix-free Krylov method. The diagonal scaling of system matrix (6.58), as it is described in Section 5.4, can only be performed if a stabilized formulation is used for the

fluid problem. If this is not the case, one option is not to apply any scaling and fix a smaller threshold for the computation of the incomplete LU factors (entries smaller than the threshold are set to zero). In this way, convergence is not compromised despite the discrepancy between the entries of the different blocks of matrix (6.58). Another possibility is to replace the zero pressure block with the identity matrix and let D (see Section 5.4) be the diagonal matrix whose elements are the diagonal ones of this modified matrix.

At time step t^{n+1} , the stopping criterion for the iterative procedure is based on the relative residual:

$$\frac{\|\mathbf{r}^{k+1}\|}{\|\mathbf{b}^{n+1}\|} = \frac{\|\mathbf{b}^{n+1} - A\mathbf{X}^{n+1,k+1}\|}{\|\mathbf{b}^{n+1}\|} < \epsilon. \quad (6.59)$$

As already pointed out, the monolithic approach solves a problem whose size is bigger than those of the two subproblems. However, it has the advantage of robustness, in particular when the added-mass effect is critical (see Section 6.9.1).

The monolithic approach described in this section differs from those used in [84, 25]. We solve the monolithic system derived from the linearization by a fixed point iterative algorithm, while in [84, 25] the FPSI system is linearized by Newton's method. We ask specific requirements for meshes and interpolations spaces to ease the imposition of coupling conditions. Moreover, we make precise choices for the preconditioners to speed up the algorithm convergence. In [84, 25], the authors do not comment on the preconditioner and the linear solver adopted.

6.8 The domain decomposition approach

The second approach we consider for the solution of the FPSI problems consists in the iterative procedures arising from a domain decomposition viewpoint. The Dirichlet-Neumann (DN) method presented in Section 5.3 is just one of these procedures, but there are many others. The Neumann-Dirichlet (ND) and the Neumann-Neumann (NN) algorithms are other domain decomposition methods that have already been proposed for hemodynamics problems [45]. None of those two clearly outperforms the DN method. Recently, partitioned procedures based on Robin transmission conditions have been suggested in [6, 7]. We remind that all the domain decomposition algorithms derive from the solution of the FSI system, reformulated as an interface problem, by preconditioned Richardson iterations. The preconditioner gives the name to the method. For simplicity, at the moment we do not consider the possibility of replacing Richardson iterations with GMRES ones.

To our knowledge, this is the first attempt to apply domain decomposition methods to FPSI problems.

A boundary condition of Robin type is a linear combination of a Dirichlet and a Neumann boundary condition. Referring, for instance, to the FSI problem (2.13), the fluid

and structure subproblems would be supplemented with the following Robin transmission conditions

$$\begin{aligned}\alpha_f \mathbf{u}^{n+1} + \boldsymbol{\sigma}^{f,n+1} \cdot \mathbf{n}_f &= \alpha_f \mathbf{u}_s^{n+1} - \boldsymbol{\sigma}^{s,n+1} \cdot \mathbf{n}_s, \\ \alpha_s \mathbf{u}_s^{n+1} + \boldsymbol{\sigma}^{s,n+1} \cdot \mathbf{n}_s &= \alpha_s \mathbf{u}^{n+1} - \boldsymbol{\sigma}^{f,n+1} \cdot \mathbf{n}_f,\end{aligned}$$

respectively. We used the notation $\boldsymbol{\sigma}^{f,n+1} = \boldsymbol{\sigma}^f(\mathbf{u}^{n+1}, p^{n+1})$ and $\boldsymbol{\sigma}^{s,n+1} = \boldsymbol{\sigma}^s(\boldsymbol{\eta}^{n+1})$. Concerning FSI problem (6.3), the Robin coupling condition for the fluid subproblem is slightly different

$$\alpha_f \mathbf{u}_f^{n+1} \cdot \mathbf{n} + \mathbf{n} \cdot (\boldsymbol{\sigma}_f^{n+1} \cdot \mathbf{n}) = \alpha_f (\mathbf{u}_s^{n+1} + \mathbf{q}^{n+1}) \cdot \mathbf{n} + \mathbf{n} \cdot (\boldsymbol{\sigma}_s^{n+1} \cdot \mathbf{n}), \quad (6.60a)$$

$$\alpha_f \mathbf{u}_f^{n+1} \cdot \mathbf{t} + \left(1 + \alpha_f \frac{\sqrt{K_D}}{\gamma}\right) \mathbf{t} \cdot (\boldsymbol{\sigma}_f^{n+1} \cdot \mathbf{n}) = \alpha_f \mathbf{u}_s^{n+1} \cdot \mathbf{t} + \mathbf{t} \cdot (\boldsymbol{\sigma}_s^{n+1} \cdot \mathbf{n}), \quad (6.60b)$$

and so is the one for the structure

$$\alpha_s (\mathbf{u}_s^{n+1} + \mathbf{q}^{n+1}) \cdot \mathbf{n} - \mathbf{n} \cdot (\boldsymbol{\sigma}_s^{n+1} \cdot \mathbf{n}) = \alpha_s \mathbf{u}_f^{n+1} \cdot \mathbf{n} - \mathbf{n} \cdot (\boldsymbol{\sigma}_f^{n+1} \cdot \mathbf{n}), \quad (6.61a)$$

$$\alpha_s \mathbf{u}_s^{n+1} \cdot \mathbf{t} - \mathbf{t} \cdot (\boldsymbol{\sigma}_s^{n+1} \cdot \mathbf{n}) = \alpha_s \mathbf{u}_f^{n+1} \cdot \mathbf{t} + \left(\alpha_s \frac{\sqrt{K_D}}{\gamma} - 1\right) \mathbf{t} \cdot (\boldsymbol{\sigma}_f^{n+1} \cdot \mathbf{n}), \quad (6.61b)$$

$$\alpha_s (\mathbf{q}^{n+1} + \mathbf{u}_s^{n+1}) \cdot \mathbf{n} + p_p^{n+1} = \alpha_s \mathbf{u}_f^{n+1} \cdot \mathbf{n} - \mathbf{n} \cdot (\boldsymbol{\sigma}_f^{n+1} \cdot \mathbf{n}). \quad (6.61c)$$

Notice that (6.60a) is coupling condition (6.4a) times α_f plus the normal component of equation (6.4c), whereas (6.60b) is transmission condition (6.4d) times α_f plus the tangential component of condition (6.4c). Similarly, (6.61c) and (6.61a) come from the multiplication of condition (6.4a) by α_s minus (6.4b) and the normal component of (6.4c), respectively. Finally, (6.61b) combines linearly (6.4d) to the tangential component of (6.4c).

The combination parameters must satisfy $\alpha_f \neq -\alpha_s$. Furthermore, we assume $\alpha_f, \alpha_s > 0$ in order for the problem to be well posed. Robin interface conditions motivate new partitioned procedures, some of which feature better convergence than the DN method. Notice that the classical DN and ND algorithms can be recovered with particular values of the combination parameters ($\alpha_f = \infty, \alpha_s = 0$ for the former, and $\alpha_f = 0, \alpha_s = \infty$ for the latter). Other particular cases, studied in [6], are the Neumann-Robin ($\alpha_f = 0$), Robin-Neumann ($\alpha_s = 0$), Dirichlet-Robin ($\alpha_f = \infty$), and Robin-Dirichlet ($\alpha_s = \infty$) schemes.

Remark 6.10. *If we choose $\alpha_f = \infty, \alpha_s = 0$ in (6.60) and (6.61), we do not recover a Dirichlet-Neumann algorithm, strictly speaking. In fact, while a Dirichlet condition is imposed on the normal component of the velocity, a Robin condition is imposed on the tangential one. However, the structure problem is endowed with a Neumann interface*

condition. In the same way, if we set $\alpha_f = 0$, $\alpha_s = \infty$, the resulting method is not properly a Neumann-Dirichlet one. Nevertheless, we will address to those schemes as DN and ND ones.

The main issue in using Robin transmission conditions is the evaluation of appropriate combination parameters α_f and/or α_s capable of improving the convergence properties of the classical DN method. Robin-Robin methods have been adopted for other applications (see, e.g., [49] for the Stokes-Darcy coupling) and they proved to be successful only for the right choices of the combination parameters. In [6], effective values are provided by simplified models for the fluid and the structure. For the fluid-poroelastic structure interaction, we employ the same simplified fluid model (see problem (5.10)) to derive α_s . On the other hand, a new simplified structure model needs to be studied to get a suitable value for α_f .

In the following, we restrict our attention to the Dirichlet-Neumann, Robin-Neumann (RN), and Robin-Robin (RR) algorithms for the solution of problem (6.57). We expect the RN method to be the best one. In fact, from [6, 7] it is clear that the RN is the optimal choice.

6.8.1 Block Gauss-Seidel interpretation

In Section 5.3.1, we saw that the so-called DN-Richardson algorithm is equivalent to the sequential solution of a fluid problem with a Dirichlet interface condition (5.7a) and a structure problem with a Neumann boundary condition (5.7b). Thus, it can be seen as a block Gauss-Seidel iterative method applied to the FSI system.

In general, all the partitioned procedures arising from a domain decomposition framework can be written as a block Gauss-Seidel iterative solver for the preconditioned FSI system

$$PAX^{n+1} = P\mathbf{b}^{n+1},$$

where P is a permutation matrix depending on the partitioned procedure. The idea is to choose the blocks of system matrix (6.58) in such a way that the Gauss-Seidel method is modular. Hence, we consider the following partition of the unknowns vector \mathbf{X}^{n+1} :

$$\mathbf{X}_f^{n+1} = \begin{bmatrix} \mathbf{U}_{ff}^{n+1} \\ \mathbf{P}_f^{n+1} \\ \tilde{\mathbf{U}}_{f\sigma}^{n+1} \end{bmatrix}, \quad \mathbf{X}_p^{n+1} = \begin{bmatrix} \tilde{\mathbf{U}}_{s\sigma}^{n+1} \\ \mathbf{U}_{ss}^{n+1} \\ \tilde{\mathbf{Q}}_{\sigma}^{n+1} \\ \mathbf{Q}_q^{n+1} \\ \mathbf{P}_p^{n+1} \end{bmatrix}.$$

which separates the fluid block from the structure one. This variable splitting induces a block structure in PA and $P\mathbf{b}^{n+1}$:

$$PA = \begin{bmatrix} (PA)_{ff} & (PA)_{fp} \\ (PA)_{pf} & (PA)_{pp} \end{bmatrix}, \quad P\mathbf{b}^{n+1} = \begin{bmatrix} (P\mathbf{b}^{n+1})_f \\ (P\mathbf{b}^{n+1})_p \end{bmatrix}.$$

The general Gauss-Seidel solver for the solution of system (6.57) requires, at each time step t^{n+1} and given $\mathbf{X}^{n+1,k}$, to iterate over

$$\begin{aligned} (PA)_{ff}\mathbf{X}_f^{n+1,k+1} &= (P\mathbf{b}^{n+1})_f - (PA)_{fp}\mathbf{X}_p^{n+1,k}, \\ (PA)_{pp}\mathbf{X}_p^{n+1,k+1} &= (P\mathbf{b}^{n+1})_p - (PA)_{pf}\mathbf{X}_f^{n+1,k+1}, \end{aligned}$$

until convergence. The stopping criterion for the iterative procedure is the following:

$$\frac{\|\mathbf{r}^{k+1}\|}{\|\mathbf{r}^0\|} = \frac{\|\mathbf{b}^{n+1} - A\mathbf{X}^{n+1,k+1}\|}{\|\mathbf{b}^{n+1} - A\mathbf{X}^{n+1,0}\|} < \epsilon, \quad (6.62)$$

where ϵ is a specified tolerance.

The appropriate choice of the permutation matrix allows us to recover the DN, RR, and RN schemes. The DN algorithm is obtained by taking the identity matrix as permutation matrix ($P_{DN} = I$). To define the permutation matrix P_{RR} , we introduce matrix

$$I_n = \begin{bmatrix} 0 & 0 \\ 0 & I \end{bmatrix},$$

where I is the identity matrix. Then, the permutation matrix to get the RR method is

$$P_{RR} = \begin{bmatrix} I & 0 & 0 & 0 & 0 & 0 & 0 & 0 \\ 0 & I & 0 & 0 & 0 & 0 & 0 & 0 \\ 0 & 0 & \alpha_f I & I & 0 & 0 & 0 & 0 \\ 0 & 0 & \alpha_s I & -I & 0 & 0 & 0 & 0 \\ 0 & 0 & 0 & 0 & I & 0 & 0 & 0 \\ 0 & 0 & \alpha_s I_n & 0 & 0 & -I & 0 & 0 \\ 0 & 0 & 0 & 0 & 0 & 0 & I & 0 \\ 0 & 0 & 0 & 0 & 0 & 0 & 0 & I \end{bmatrix}.$$

The permutation matrix to retrieve the RN algorithm is obtained by taking $\alpha_s = 0$ in P_{RR} .

6.8.2 A simplified fluid-structure model

In order to analyze the convergence properties of the DN, RR, and RN algorithms for the FPSI problem, we introduce a simplified fluid-structure model.

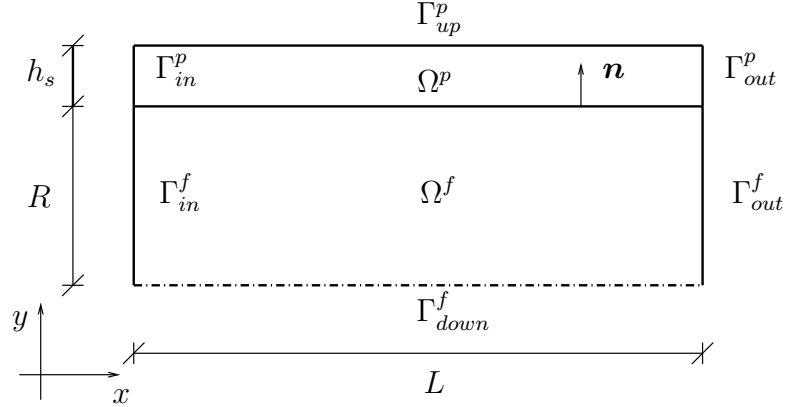


Figure 6.10: Domain for the simplified fluid-poroelastic structure problem.

We take a rectangular fluid domain $\Omega^f \subset \mathbb{R}^2$ of height R and length L . The structure domain $\Omega^s \subset \mathbb{R}^2$ is a rectangle of length L and height h_s , placed on the upper side of Ω^f (see Figure 6.10). The difference with the simplified structure subproblem in Section 5.3.3 is that the structure domain coincides no more with the interface.

In Ω^f we consider a potential fluid flow (see (5.10)), which, rewritten according to the FPSI notation, is

$$\rho_f \partial_t \mathbf{u}_f + \nabla p_f = \mathbf{0} \quad \text{in } \Omega^f \times (0, T), \quad (6.63a)$$

$$\nabla \cdot \mathbf{u}_f = 0 \quad \text{in } \Omega^f \times (0, T), \quad (6.63b)$$

$$u_f = \partial_t \eta + q \quad \text{on } \Sigma \times (0, T), \quad (6.63c)$$

$$p_f = \bar{p}_f \quad \text{on } \Gamma_{in}^f \cup \Gamma_{out}^f, \quad (6.63d)$$

$$u_f = 0 \quad \text{on } \Gamma_{down}^f, \quad (6.63e)$$

with suitable initial conditions. The non-bold variable refers to the normal component of the associated vector, e.g. $q = \mathbf{q} \cdot \mathbf{n}$. Thanks to the definition of the added-mass operator \mathcal{M} (see Section 5.3.3), we have

$$p_f = \hat{p}_f - \rho_f \mathcal{M}(\partial_{tt} \eta + \partial_t q), \quad (6.64)$$

where \hat{p}_f accounts for possible non-homogeneous boundary conditions on $\partial\Omega^f \setminus \Sigma$.

For the structure subproblem, we deal with the limit case described in Section 6.4.4. Moreover, we neglect the term $\nabla \cdot \boldsymbol{\sigma}_s^E(\boldsymbol{\eta})$ in the structure momentum balance equation, i.e. we assume negligible shear deformations. Hence, the structure model written in terms

of displacement $\boldsymbol{\eta}$ (instead of velocity \mathbf{u}_s) is governed by equations

$$\rho_p \partial_{tt} \boldsymbol{\eta} + a \boldsymbol{\eta} + \nabla p_p = \mathbf{0} \quad \text{in } \Omega^p \times (0, T), \quad (6.65a)$$

$$\rho_d \partial_{tt} \boldsymbol{\eta} + K_D^{-1} \mathbf{q} + \nabla p_p = \mathbf{0} \quad \text{in } \Omega^p \times (0, T), \quad (6.65b)$$

$$\nabla \cdot \boldsymbol{\eta} = 0 \quad \text{in } \Omega^p \times (0, T), \quad (6.65c)$$

$$p_p = p_f \quad \text{on } \Sigma \times (0, T), \quad (6.65d)$$

$$p_p = 0 \quad \text{on } \Gamma_{in}^p \cup \Gamma_{out}^p \cup \Gamma_{up}^p, \quad (6.65e)$$

where $a = E/(1 - \nu^2)R^2$, E being the Young modulus and ν the Poisson ratio of the matrix. The reaction term in (6.65a) represents the transversal membrane effects appearing when the structure equations are written in axisymmetric form. Problem (6.65) must be supplemented with initial conditions. Moreover, drained conditions (6.65e) have been imposed on $\partial\Omega^p \setminus \Sigma$.

Equation (6.65a) for the normal component η can be written as

$$\rho_p \partial_{tt} \eta + a \eta + \frac{\partial p_p}{\partial \mathbf{n}} \Big|_{\Sigma} = 0. \quad (6.66)$$

By taking the divergence of (6.65a) and exploiting (6.65c), system (6.65) may be reformulated as follows

$$-\Delta p_p = 0 \quad \text{in } \Omega^p, \quad (6.67a)$$

$$p_p = p_f \quad \text{on } \Sigma, \quad (6.67b)$$

$$p_p = 0 \quad \text{on } \Gamma_{in}^p \cup \Gamma_{out}^p \cup \Gamma_{up}^p. \quad (6.67c)$$

For any $p_f \in H^{1/2}(\Sigma)$, equations (6.67) compute a pressure $p_p \in H^1(\Omega^p)$. Then, $\boldsymbol{\eta}$ and \mathbf{q} are recovered by (6.65a) and (6.65b), respectively. Let us define the operator $\mathcal{M}_p^{-1} : H^{1/2}(\Sigma) \rightarrow H^{-1/2}(\Sigma)$ by

$$\mathcal{M}_p^{-1} p_f = -\frac{\partial p_p}{\partial \mathbf{n}} \Big|_{\Sigma}. \quad (6.68)$$

The Dirichlet-to-Neumann map \mathcal{M}_p^{-1} can be seen as a sort of inverse added-mass operator for the structure. By plugging (6.64) into (6.68), we obtain

$$\frac{\partial p_p}{\partial \mathbf{n}} \Big|_{\Sigma} = \rho_f \mathcal{D} \partial_{tt} \eta + \rho_f \mathcal{D} \partial_t q - \mathcal{M}_p^{-1} \hat{p}_f,$$

where we called $\mathcal{D} : H^{-1/2}(\Sigma) \rightarrow H^{-1/2}(\Sigma)$ the operator deriving from the composition of \mathcal{M} with \mathcal{M}_p^{-1} , i.e. $\mathcal{D}(\cdot) = \mathcal{M}_p^{-1}(\mathcal{M}(\cdot))$. Using this result in (6.66), we find that the FPSI model problem (6.63)-(6.65) is equivalent to: find η and q such that

$$(\rho_p \mathcal{I} + \rho_f \mathcal{D}) \partial_{tt} \eta + a \eta + \rho_f \mathcal{D} \partial_t q = \mathcal{M}_p^{-1} \hat{p}_f, \quad (6.69a)$$

$$(\rho_d \mathcal{I} + \rho_f \mathcal{D}) \partial_{tt} \eta + K_D^{-1} q + \rho_f \mathcal{D} \partial_t q = \mathcal{M}_p^{-1} \hat{p}_f. \quad (6.69b)$$

Remark 6.11. Equation (6.69a) looks like structure equation (6.66) with an extra operator in front of the second order time derivative and a term in $\partial_t q$. When a fluid interacts with a poroelastic structure, it acts like an “added-mass” on the structure, as in the interaction with a purely elastic structure. Moreover, an additional inertial term related to the filtration velocity appears in the structure equation.

For the subsequent mathematical analysis, it is important to estimate the maximum eigenvalue of operator \mathcal{D} , denoted by $\mu_{max}^{\mathcal{D}}$. Note that, like the maximum eigenvalue of \mathcal{M} $\mu_{max}^{\mathcal{M}}$ (see [26]), it is a purely geometric quantity. When dealing with a generic geometry, a closed expression for $\mu_{max}^{\mathcal{D}}$ cannot be found, but in the case of the simple geometry in Fig. 6.10 it is possible.

We consider the following reformulation of fluid problem (6.63)

$$\begin{aligned} -\Delta p_f &= 0 && \text{in } \Omega^f \\ \partial_y p_f &= g && \text{on } \Sigma, \\ p_f &= 0 && \text{on } \Gamma_{in}^f \cup \Gamma_{out}^f, \\ \partial_y p_f &= 0 && \text{on } \Gamma_{down}^f. \end{aligned}$$

coupled to the model structure problem (6.67). By expressing function g as

$$g(x) = \sum_{k \geq 1} g_k \sin\left(k\pi \frac{x}{L}\right),$$

we compute the fluid pressure $p_f(x, y)$ (see [26]) and extract its value at the interface $y = R$

$$p_f(x)|_{\Sigma} = \mathcal{M}g = \sum_{k \geq 1} g_k \frac{L \cosh\left(k\pi \frac{R}{L}\right)}{k\pi \sinh\left(k\pi \frac{R}{L}\right)} \sin\left(k\pi \frac{x}{L}\right) = \sum_{k \geq 1} p_{f,k}.$$

Plugging this function in (6.67b) allows us to compute the pressure $p_p(x, y)$ in the poroelastic medium

$$p_p(x, y) = \sum_{k \geq 1} g_k \frac{L \cosh\left(k\pi \frac{R}{L}\right)}{k\pi \sinh\left(k\pi \frac{R}{L}\right)} \frac{1}{\sinh\left(k\pi \frac{h_s}{L}\right)} \sin\left(k\pi \frac{x}{L}\right) \sinh\left(k\pi \frac{R + h_s - y}{L}\right).$$

Then, since \mathbf{n} indicates the y direction, we can write

$$\begin{aligned} \mathcal{D}g &= -\frac{\partial p_p}{\partial \mathbf{n}} \Big|_{\Sigma} = \sum_{k \geq 1} g_k \frac{\cosh\left(k\pi \frac{R}{L}\right) \cosh\left(k\pi \frac{h_s}{L}\right)}{\sinh\left(k\pi \frac{R}{L}\right) \sinh\left(k\pi \frac{h_s}{L}\right)} \sin\left(k\pi \frac{x}{L}\right) \\ &= \sum_{k \geq 1} p_{f,k} \frac{k\pi}{L} \frac{1}{\tanh\left(k\pi \frac{h_s}{L}\right)}. \end{aligned} \tag{6.70}$$

Finding the eigenvalues $\mu_k^{\mathcal{D}}$, $k = 1, 2, \dots$, of \mathcal{D} associated to the eigenvector $g = g_k \sin(k\pi \frac{x}{L})$ means to solve the eigenvalue problem

$$\mathcal{D}g = \mu_k^{\mathcal{D}} g,$$

which implies

$$\mu_k^{\mathcal{D}} = \frac{1}{\tanh(k\pi \frac{R}{L}) \tanh(k\pi \frac{h_s}{L})}.$$

Thus, the maximum eigenvalue is for $k = 1$

$$\mu_{max}^{\mathcal{D}} = \frac{1}{\tanh(\pi \frac{R}{L}) \tanh(\pi \frac{h_s}{L})}.$$

Figures 6.11(a) and 6.11(b) show the value of $\mu_{max}^{\mathcal{D}}$ varying the fluid and the structure geometry, i.e. L and R , and L and h_s , respectively.

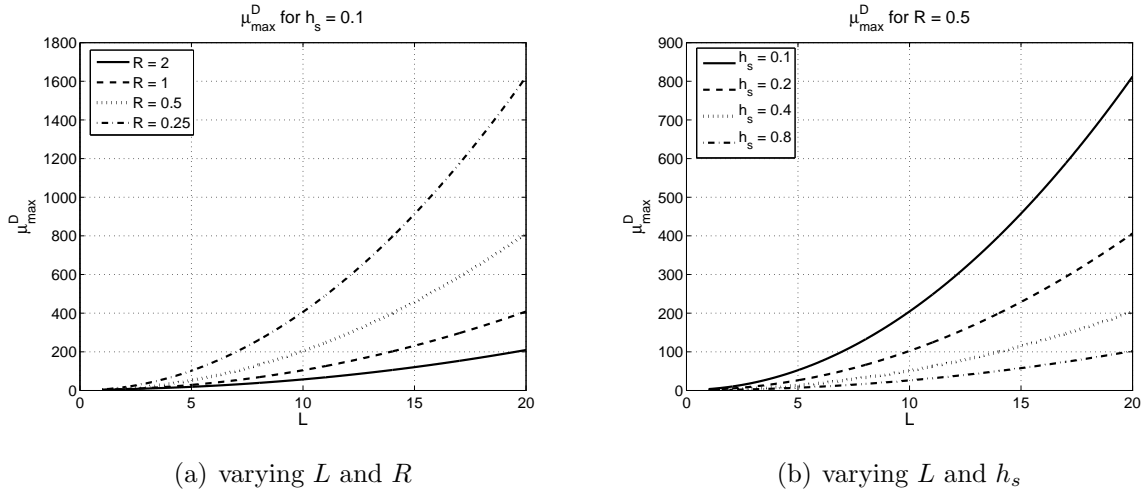


Figure 6.11: Largest eigenvalue of operator \mathcal{D} as a function of (a) fluid domain length L and height H and (b) structure domain length L and thickness h_s .

6.8.3 The Dirichlet-Neumann algorithm

In this subsection, we aim at analyzing the convergence properties of the DN method applied to the simplified FPSI problem (6.63)-(6.65).

We discretize in time problem (6.63)-(6.65) with the BDF1 scheme for both fluid and structure equations. The Dirichlet-Neumann algorithm supplemented with a relaxation technique reads: at time step t^{n+1} and iteration $k + 1$, with $n, k > 0$, given \mathbf{u}_f^n , $\boldsymbol{\eta}^n$, and $\boldsymbol{\eta}^{n-1}$, solve

(i) Fluid problem (Dirichlet boundary condition): Find $\mathbf{u}_f^{k+1}, p_f^{k+1}$ such that

$$\rho_f \delta_t \mathbf{u}_f^{k+1} + \nabla p_f^{k+1} = \mathbf{0} \quad \text{in } \Omega^f, \quad (6.71a)$$

$$\nabla \cdot \mathbf{u}_f^{k+1} = 0 \quad \text{in } \Omega^f, \quad (6.71b)$$

$$u_f^{k+1} = \delta_t \eta^k + q^k \quad \text{on } \Sigma, \quad (6.71c)$$

$$p_f^{k+1} = \bar{p}_f \quad \text{on } \Gamma_{in}^f \cup \Gamma_{out}^f, \quad (6.71d)$$

$$u_f^{k+1} = 0 \quad \text{on } \Gamma_{down}^f. \quad (6.71e)$$

(ii) Structure problem (Neumann boundary condition): Find $\tilde{\boldsymbol{\eta}}^{k+1}, \tilde{\mathbf{q}}^{k+1}, p_p^{k+1}$ such that

$$\rho_p \delta_{tt} \tilde{\boldsymbol{\eta}}^{k+1} + a \tilde{\boldsymbol{\eta}}^{k+1} + \nabla p_p^{k+1} = \mathbf{0} \quad \text{in } \Omega^p, \quad (6.72a)$$

$$\rho_d \delta_{tt} \tilde{\boldsymbol{\eta}}^{k+1} + K_D^{-1} \tilde{\mathbf{q}}^{k+1} + \nabla p_p^{k+1} = \mathbf{0} \quad \text{in } \Omega^p, \quad (6.72b)$$

$$\nabla \cdot \tilde{\boldsymbol{\eta}}^{k+1} = 0 \quad \text{in } \Omega^p, \quad (6.72c)$$

$$p_p^{k+1} = p_f^{k+1} \quad \text{on } \Sigma, \quad (6.72d)$$

$$p_p^{k+1} = 0 \quad \text{on } \Gamma_{in}^p \cup \Gamma_{out}^p \cup \Gamma_{up}^p. \quad (6.72e)$$

(iii) Relaxation step

$$\eta^{k+1} = \omega \tilde{\eta}^{k+1} + (1 - \omega) \eta^k, \quad (6.73a)$$

$$q^{k+1} = \omega \tilde{q}^{k+1} + (1 - \omega) q^k. \quad (6.73b)$$

(iv) Convergence test: if the stopping criterion is satisfied, then set $\mathbf{u}_f^{n+1} = \mathbf{u}_f^{k+1}, p_f^{n+1} = p_f^{k+1}, \boldsymbol{\eta}^{n+1} = \boldsymbol{\eta}^{k+1}, \mathbf{q}^{n+1} = \mathbf{q}^{k+1}$, and $p_p^{n+1} = p_p^{k+1}$.

The relaxation parameter might be necessary to guarantee the convergence of the method.

Theorem 6.1. *The Dirichlet-Neumann iterative method applied to the solution of the FPSI test problem (6.63)-(6.65) converges to the “monolithic” solution provided the following condition on the relaxation parameter is satisfied*

$$0 < \omega \leq \frac{2(\rho_p + a\delta t^2)}{(\rho_p + a\delta t^2 + 2\rho_f \mu_{max}^D)}. \quad (6.74)$$

Proof. Let us introduce the normal component of the structure velocity $\tilde{u}_s^{k+1} = (\tilde{\boldsymbol{\eta}}^{k+1} - \boldsymbol{\eta}^n) / \delta t$. The DN algorithm (6.71)-(6.72) is equivalent to: find \tilde{u}_s^{k+1} and \tilde{q}^{k+1}

$$\begin{aligned} \frac{\rho_p}{\delta t} (\tilde{u}_s^{k+1} - u_s^n) + a \delta t \tilde{u}_s^{k+1} + \frac{\rho_f}{\delta t} \mathcal{D} (q^k - q^n + u_s^k - u_s^n) &= \mathcal{M}_p^{-1} \hat{p}_f^{n+1} - a \eta^n, \\ \frac{\rho_d}{\delta t} (\tilde{u}_s^{k+1} - u_s^n) + K_D^{-1} \tilde{q}^{k+1} + \frac{\rho_f}{\delta t} \mathcal{D} (q^k - q^n + u_s^k - u_s^n) &= \mathcal{M}_p^{-1} \hat{p}_f^{n+1}. \end{aligned} \quad (6.75)$$

From relaxation step (6.73), it follows that

$$\tilde{u}_s^{k+1} = \frac{1}{\omega} u_s^{k+1} - \frac{1-\omega}{\omega} u_s^k, \quad \text{and} \quad \tilde{q}^{k+1} = \frac{1}{\omega} q^{k+1} - \frac{1-\omega}{\omega} q^k.$$

Then, the previous system is equivalent to

$$\begin{aligned} \frac{1}{\omega} \left[\left(\frac{\rho_p}{\delta t} + a\delta t \right) \mathcal{I} \right] u_s^{k+1} - \left[\frac{1-\omega}{\omega} \left(\frac{\rho_p}{\delta t} + a\delta t \right) \mathcal{I} - \frac{\rho_f}{\delta t} \mathcal{D} \right] u_s^k + \frac{\rho_f}{\delta t} \mathcal{D} q^k &= f(u_s^n, q^n, \hat{p}_f^{n+1}), \\ \frac{1}{\omega} \frac{\rho_d}{\delta t} u_s^{k+1} + \frac{K_D^{-1}}{\omega} q^{k+1} - \left[\frac{1-\omega}{\omega} \frac{\rho_d}{\delta t} \mathcal{I} - \frac{\rho_f}{\delta t} \mathcal{D} \right] u_s^k - \left[\frac{1-\omega}{\omega} K_D^{-1} \mathcal{I} - \frac{\rho_f}{\delta t} \mathcal{D} \right] q^k &= g(u_s^n, q^n, \hat{p}_f^{n+1}), \end{aligned}$$

for suitable functions f and g . In turn, this corresponds to iterative method

$$u_s^{k+1} = \left[(1-\omega) \mathcal{I} - \omega \frac{\rho_f}{\rho_p + a\delta t^2} \mathcal{D} \right] u_s^k - \omega \frac{\rho_f}{\rho_p + a\delta t^2} \mathcal{D} q^k + \tilde{f}(u_s^n, q^n, \hat{p}_f^{n+1}), \quad (6.76a)$$

$$\begin{aligned} q^{k+1} = & \omega K_D \left(\frac{\rho_d}{\rho_p + a\delta t^2} - 1 \right) \frac{\rho_f}{\delta t} \mathcal{D} u_s^k + \left[(1-\omega) \mathcal{I} + \omega K_D \left(\frac{\rho_d}{\rho_p + a\delta t^2} - 1 \right) \frac{\rho_f}{\delta t} \mathcal{D} \right] q^k \\ & + \tilde{g}(u_s^n, q^n, \hat{p}_f^{n+1}), \end{aligned} \quad (6.76b)$$

for suitable functions \tilde{f} and \tilde{g} .

The solution of the DN method coincides with the fixed point of the iterative method (6.76). Sufficient conditions for the convergence of that fixed point method are

$$\begin{aligned} \left| (1-\omega) - \omega \frac{\rho_f \mu_i^{\mathcal{D}}}{\rho_p + a\delta t^2} \right| + \left| \omega \frac{\rho_f \mu_i^{\mathcal{D}}}{\rho_p + a\delta t^2} \right| &< 1, \\ \left| \omega K_D \left(\frac{\rho_d}{\rho_p + a\delta t^2} - 1 \right) \frac{\rho_f}{\delta t} \mu_i^{\mathcal{D}} \right| + \left| (1-\omega) + \omega K_D \left(\frac{\rho_d}{\rho_p + a\delta t^2} - 1 \right) \frac{\rho_f}{\delta t} \mu_i^{\mathcal{D}} \right| &< 1, \end{aligned}$$

which lead to

$$0 < \omega \leq \frac{2(\rho_p + a\delta t^2)}{(\rho_p + a\delta t^2 + 2\rho_f \mu_{max}^{\mathcal{D}})}, \quad (6.77a)$$

$$0 < \omega \leq \frac{2}{1 + 2K_D \frac{\rho_f}{\delta t} \left(1 - \frac{\rho_d}{\rho_p + a\delta t^2} \right) \mu_{max}^{\mathcal{D}}}. \quad (6.77b)$$

For the values of K_D which allow us to derive model problem (6.65), condition (6.77b) is far less restrictive than condition (6.77a). Thus, the convergence of the DN algorithm (6.71)-(6.72)-(6.73) depends only on the latter. Numerical experiments reported in Section 6.9.1 confirm this result. \square

6.8.4 The Robin-Robin and the Robin-Neumann algorithms

The Robin-Robin algorithm for the time discrete version of problem (6.63)-(6.65) reads: at time step t^{n+1} and iteration $k + 1$, with $n, k > 0$, given \mathbf{u}_f^n , $\boldsymbol{\eta}^n$, and $\boldsymbol{\eta}^{n-1}$, solve

- (i) Fluid problem (Robin boundary condition): Find \mathbf{u}_f^{k+1} , p_f^{k+1} as in (6.71) but replacing interface condition (6.71c) with

$$\alpha_f u_f^{k+1} - p_f^{k+1} = \alpha_f (\delta_t \eta^k + q^k) - p_p^k \quad \text{on } \Sigma. \quad (6.78)$$

- (ii) Structure problem (Robin boundary condition): Find $\tilde{\boldsymbol{\eta}}^{k+1}$, $\tilde{\mathbf{q}}^{k+1}$, p_p^{k+1} as in (6.72) but replacing interface condition (6.72d) with

$$\alpha_s (u_s^{k+1} + q^{k+1}) + p_p^{k+1} = \alpha_s u_f^{k+1} + p_f^{k+1} \quad \text{on } \Sigma.$$

Steps (iii) and (iv) are common to the DN algorithm.

As already highlighted, a central role in the convergence of the Robin-Robin algorithm is played by the combination parameters α_f and α_s . We adopt the α_s computed in [6], i.e.

$$\alpha_s = \frac{\rho_f}{\delta t} \mu_{max}^{\mathcal{M}}, \quad (6.79)$$

where $\mu_{max}^{\mathcal{M}}$ is the largest eigenvalue of the added-mass operator (see Section 5.3.3). To derive a possible value for α_f , we consider simplified model (6.65). We consider the normal component of equations (6.65a)-(6.65b), discretize them in time with the BDF1 scheme and plug (6.70) into them to get

$$\rho_p \delta_t u_s^{n+1} + a \delta t u_s^{n+1} - \sum_{k \geq 1} p_{f,k}^{n+1} \frac{k\pi}{L} \frac{1}{\tanh(k\pi \frac{h_s}{L})} = -a \eta^n, \quad (6.80a)$$

$$\rho_d \delta_t u_s^{n+1} + K_D^{-1} q^{n+1} - \sum_{k \geq 1} p_{f,k}^{n+1} \frac{k\pi}{L} \frac{1}{\tanh(k\pi \frac{h_s}{L})} = 0. \quad (6.80b)$$

If we truncate the sum at the first element, (6.80) becomes

$$\begin{aligned} \left(\frac{\rho_p}{\delta t} + a \delta t \right) u_s^{n+1} &= \left(\frac{\pi}{L} \frac{1}{\tanh(\pi \frac{h_s}{L})} \right) p_{f,1}^{n+1} + \frac{\rho_p}{\delta t} u_s^n - a \eta^n, \\ \frac{\rho_d}{\delta t} u_s^{n+1} + K_D^{-1} q^{n+1} &= \left(\frac{\pi}{L} \frac{1}{\tanh(\pi \frac{h_s}{L})} \right) p_{f,1}^{n+1} + \frac{\rho_d}{\delta t} u_s^n, \end{aligned}$$

which is equivalent to

$$u_s^{n+1} = \frac{1}{\frac{\rho_p}{\delta t} + a \delta t} \left(\frac{\pi}{L} \frac{1}{\tanh(\pi \frac{h_s}{L})} \right) p_{f,1}^{n+1} + \frac{\rho_p}{\rho_p + a \delta t^2} u_s^n - \frac{a \delta t}{\rho_p + a \delta t^2} \eta^n, \quad (6.81a)$$

$$q^{n+1} = K_D \left(1 - \frac{\rho_d}{\rho_p + a \delta t^2} \right) \left(\frac{\pi}{L} \frac{1}{\tanh(\pi \frac{h_s}{L})} \right) p_{f,1}^{n+1} + K_D \frac{a \delta t}{\rho_p + a \delta t^2} (\delta t u_s^n + \eta^n). \quad (6.81b)$$

By summing (6.81a) to (6.81b) and thanks to the admissibility condition (6.4a), we find

$$\begin{aligned} u_f^{n+1} &= \frac{\pi}{L} \frac{1}{\tanh\left(\pi \frac{h_s}{L}\right)} \frac{1}{\rho_p + a\delta t^2} [\delta t + K_D(\rho_p - \rho_d + a\delta t^2)] p_{f,1}^{n+1} \\ &\quad + \frac{\rho_p + K_D a\delta t^2}{\rho_p + a\delta t^2} u_s^n - \frac{a\delta t}{\rho_p + a\delta t^2} (1 - K_D) \eta^n. \end{aligned} \quad (6.82)$$

If $p_{f,1}^{n+1}$ is a good approximation for p_f^{n+1} , this equation suggests the use of the following combination parameter

$$\alpha_f = (\rho_p + a\delta t^2) \frac{L}{\pi} \tanh\left(\pi \frac{h_s}{L}\right) \frac{1}{\delta t + K_D(\rho_p - \rho_d + a\delta t^2)} \quad (6.83)$$

in Robin transmission condition (6.78). For the values of K_D which allow us to derive model problem (6.65), α_f could be simplified in the following way

$$\alpha_f \sim \left(\frac{\rho_p}{\delta t} + a\delta t\right) \tanh\left(\pi \frac{h_s}{L}\right) \frac{L}{\pi}. \quad (6.84)$$

Even though (6.82) prescribes an interface condition only on the normal component of the velocity, we impose the Robin condition with the same α_f also for the tangential component. Moreover, the same value of α_f can be used even for more general structure models, whose behavior is similar to the one predicted by (6.66).

The Robin-Neumann algorithm is recovered from the Robin-Robin method by choosing α_f as in (6.83) and $\alpha_s = 0$. In the classical FSI problems, the RN algorithm proves to be the best in terms of convergence properties, see [6, 7]. For this reason, we check its performance when applied to FPSI problems.

The following theorem states the convergence properties of the RN algorithm.

Theorem 6.2. *The Robin-Neumann iterative method applied to the solution of the FPSI test problem (6.63)-(6.65) converges to the “monolithic” solution provided the following condition on the relaxation parameter is satisfied*

$$0 < \omega \leq 2. \quad (6.85)$$

Proof. By discretizing in time (6.64) with the BDF1 scheme and using the admissibility constraint, we know that

$$u_f^{k+1} = -\frac{\delta t}{\rho_f} \mathcal{M}^{-1} p_f^{k+1} + u_f^n + \frac{\delta t}{\rho_f} \mathcal{M}^{-1} \hat{p}_f.$$

If we approximate p_f^{k+1} in this inequality with $p_{f,1}^{k+1}$ and invoke it in (6.82), we get

$$\left(\alpha_f \frac{\delta t}{\rho_f} \mathcal{M}^{-1} + 1\right) p_{f,1}^{k+1} = f(u_s^n, u_f^n, \eta^n), \quad (6.86)$$

where α_f is defined by (6.83) and f is a suitable function. Combining (6.86) to the fixed point method associated to (6.81)

$$\begin{aligned}\tilde{u}_s^{k+1} &= \frac{1}{\frac{\rho_p}{\delta t} + a\delta t} \left(\frac{\pi}{L} \frac{1}{\tanh\left(\pi \frac{h_s}{L}\right)} \right) p_{f,1}^{k+1} + \frac{\rho_p}{\rho_p + a\delta t^2} u_s^n - \frac{a\delta t}{\rho_p + a\delta t^2} \eta^n, \\ \tilde{q}^{k+1} &= K_D \left(1 - \frac{\rho_d}{\rho_p + a\delta t^2} \right) \left(\frac{\pi}{L} \frac{1}{\tanh\left(\pi \frac{h_s}{L}\right)} \right) p_{f,1}^{k+1} + K_D \frac{a\delta t}{\rho_p + a\delta t^2} (\delta t u_s^n + \eta^n),\end{aligned}$$

we obtain

$$\begin{aligned}\tilde{u}_s^{k+1} &= g(u_s^n, u_f^n, \eta^n), \\ \tilde{q}^{k+1} &= h(u_s^n, u_f^n, \eta^n),\end{aligned}$$

for suitable functions g and h . A sufficient condition for the convergence of such a fixed point method is

$$|1 - \omega| < 1, \tag{6.87}$$

from which (6.85) follows. □

Remark 6.12. *The value of α_f has been calculated for the simple domain in Fig. 6.10. When the geometry is more complicated (e.g. a stenotic artery) and it is impossible to find a closed expression for μ_{max}^D , the RN algorithm becomes less effective. A possible solution is to replace the Richardson iterations of the RN scheme by GMRES ones which are less sensitive to the value of α_s (see [7]).*

6.9 Numerical results

We aim at analyzing how the performance of the methods described in Sections 6.7 and 6.8 are affected by the variation of the different parameters involved in FPSI problem (6.3). Our goal is again to simulate the propagation of a pressure pulse in a straight pipe with deformable porous boundaries. We consider only the 2d (bi-dimensional fluid and structure) approximation of this problem. We use the fluid and structure physical parameters listed in Table 5.1, unless otherwise specified. The other parameters of the poroelastic structure will be indicated each time, except for the slip rate coefficient γ which is always taken equal to 1.

We impose the usual Neumann condition (4.2), with $P_{in} = 2 \cdot 10^4$ dyne/cm², at the inlet, while a homogeneous Neumann condition is imposed at the outlet.

We choose a conforming space discretization between fluid and structure: ($\mathbb{P}_1 iso \mathbb{P}_2$) - \mathbb{P}_1 finite elements for the fluid and stabilized $\mathbb{P}_1 - \mathbb{P}_1$ finite elements for the structure.

6.9.1 Comparison between the ILUT-GMRES and the DN methods

The purpose of this subsection is to compare the non-modular approach described in Section 6.7 and the modular DN algorithm.

We solve the FPSI problem on a structured grid of 31×11 \mathbb{P}_1 fluid nodes and 61×4 structure nodes. The structure mesh nodes at the interface correspond to the \mathbb{P}_1 iso \mathbb{P}_2 degrees of freedom for the fluid velocity. We set the structure density $\rho_s = 100$ g/cm³ and the pores fluid density $\rho_d = 1$ g/cm³. Notice that the effective density of the poroelastic structure is $\rho_p = \rho_s(1 - \phi) + \rho_d\phi$ and the added-mass effect increases with the ratio ρ_f/ρ_p . Hence, varying the porosity makes the added-mass effect more or less critical.

We choose to adopt the explicit treatment of the nonlinearities in order to focus on the fluid-structure coupling iterations.

Let us consider first the non-modular ILUT-GMRES approach. The preconditioners adopted are the incomplete LU factors of the (either scaled or unscaled) monolithic system with threshold 10^{-5} . The choice of such a small value is due to the fact that it was the largest one to allow convergence in all the cases we considered, even when the diagonal scaling is not performed. Thanks to the small size of the problem, we can apply the GMRES method without restart. The tolerance used in (6.59) to stop the GMRES iteration is 10^{-4} .

In addition to the relative residual in (6.59), here denoted simply by \mathbf{r} , we define the relative residuals \mathbf{r}_f , \mathbf{r}_σ , and \mathbf{r}_p as the residuals of the equations for the inner fluid, interface, and inner structure nodes, respectively. We aim at checking how all those residuals decrease with the iteration number, either with or without applying the diagonal scaling to system matrix (6.58). Figures 6.12 report this study for two different values of ϕ ($\phi = 0.15$ and $\phi = 0.95$) and time step ($\delta t = 2.5 \cdot 10^{-4}$ s and $\delta t = 10^{-4}$ s). The diagonal scaling allows to reduce the number of ILUT-GMRES iterations in all the cases. However, this reduction gets less important as ϕ decreases (i.e. as the added-mass effect gets less critical) and as the time step becomes small. We notice that \mathbf{r}_σ is always slightly bigger than \mathbf{r}_f and \mathbf{r}_p . The porosity being fixed, the number of iterations increases as the time step value decreases. Moreover, GMRES converges faster for small ρ_p . This confirms what found in Section 5.5.3: the ILUT-GMRES algorithm shows better convergence properties for problems with large added-mass effect.

To highlight this aspect, we plot in Figure 6.13(a) the average number of GMRES iterations to solve monolithic system (6.57) for different porosities ($\phi = 0.15, 0.35, 0.55, 0.75, 0.95$), hydraulic conductivities ($K_D \sim 10^{-6}, 10^{-8}, 10^{-10}, 10^{-12}$ (cm³ s)/g), and time step values ($\delta t = 5 \cdot 10^{-4}, 2.5 \cdot 10^{-4}$ s). The larger the added-mass effect is, the fewer iterations the GMRES method requires to converge. This tendency (unaffected by the value of K_D) is opposite to what happens with the DN algorithm, as it was already shown in Section 5.5.1

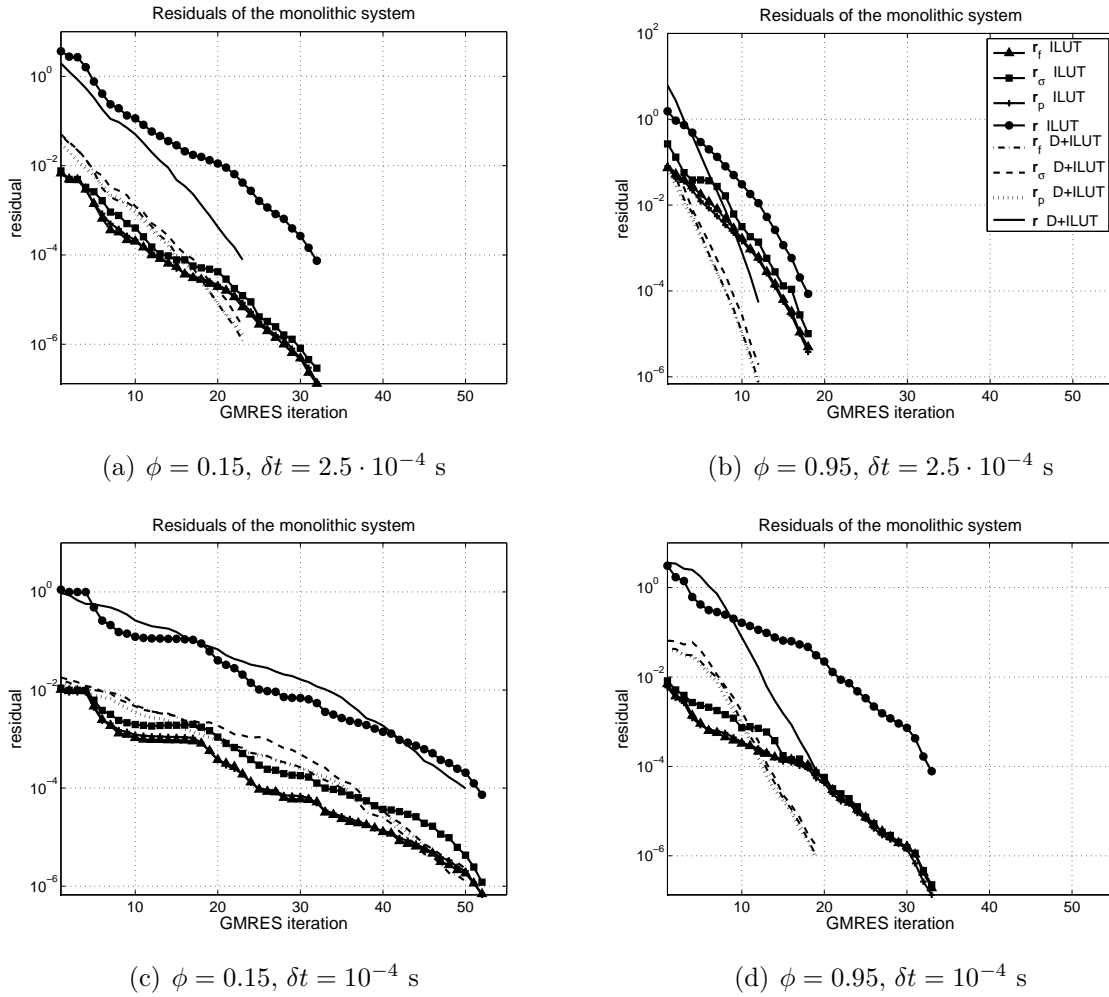


Figure 6.12: Residuals \mathbf{r} , \mathbf{r}_f , \mathbf{r}_σ , and \mathbf{r}_p associated to the monolithic system, with and without scaling, for different different values of ϕ and δt . The legend in (b) is common to the four graphs.

and Fig. 6.13(b) confirms. The DN method whose results are reported in Fig. 6.13(b) uses an Aitken relaxation procedure (see [44]).

Variations in the order of magnitude of K_D cause only small differences in the number of average iterations for both methods.

6.9.2 Comparison between the DN and the RN algorithms

In this subsection, we intend to compare two modular procedures. The first one is the DN method whose advantages and drawbacks have already been discussed in the previous

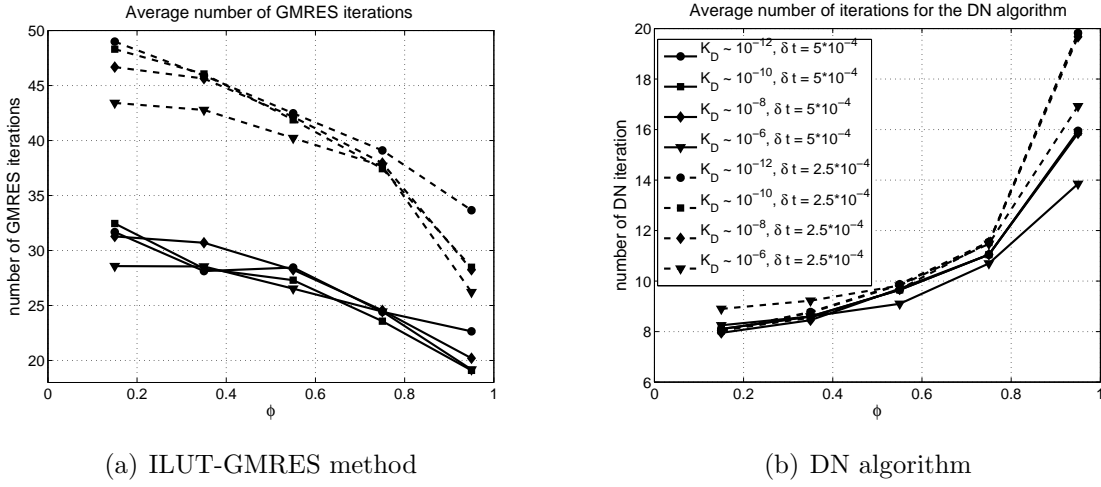


Figure 6.13: (a) Average number of GMRES iterations to solve the monolithic system and (b) average number of iterations for the DN algorithm for different values of ϕ , K_D , and δt . The legend in (b) is common to the two figures.

chapter. The second one is the RN algorithm which exhibits an excellent behavior for classical FSI problems appearing in hemodynamics.

As in the previous subsection the focus is on coupling iterations. Hence, the nonlinearities are explicitly treated. We compare the two schemes by studying their sensitivity to some physical and discretization parameters. Out of the numerous parameters involved in FPSI problems, only a few have a meaningful impact on the performances of the partitioned procedures. For instance, in the previous subsection we remarked that variations of the hydraulic conductivity produce minor changes in the number of iterations, unlike variations of the porosity.

For all the simulations, we took $\rho_d = 1 \text{ g/cm}^3$ and $K_D \sim 10^{-12} \text{ (cm}^3 \text{ s)/g}$, and we used the same mesh of Section 6.9.1. Figures 6.14(a), 6.14(b), and 6.14(c) show the sensitivity to the time step, porosity, and Young's modulus, respectively. For the results in Fig. 6.14(a) and Fig. 6.14(c), we choose the physiological values $\rho_s = 1.1 \text{ g/cm}^3$, $\phi = 0.15$, while for those in Fig. 6.14(b) $\rho_s = 100 \text{ g/cm}^3$. The reason of this non-physiological value is that, if ρ_d and ρ_s are of the same order of magnitude, varying ϕ does not change the criticality of the added-mass effect. In fact, the effect of porosity on the convergence properties of partitioned procedures is simply related to the reduction of the effective structure density. In Fig. 6.14, we report the results of the RN scheme (with α_f prescribed by (6.83)), without relaxation and with an Aitken relaxation procedure, and those of the DN algorithm with Aitken acceleration parameters.

We let the time step take four different values, $\delta t = 10^{-3}, 5 \cdot 10^{-4}, 2.5 \cdot 10^{-4}, 1.25 \cdot 10^{-4} \text{ s}$

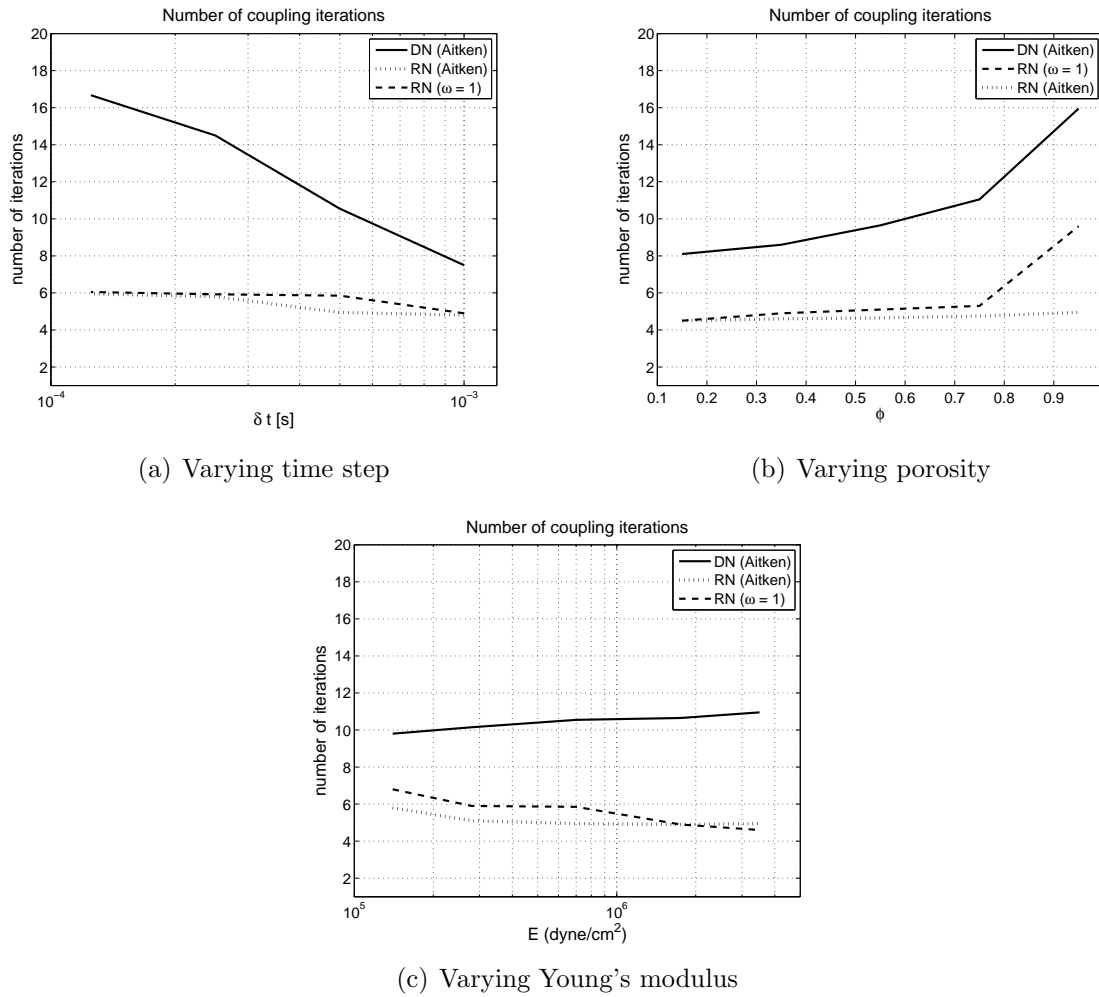


Figure 6.14: Average number of coupling iterations for the DN and RN schemes varying (a) time step δt , (b) porosity ϕ , and (c) Young's modulus E .

and report the results in Fig. 6.14(a), whereas for those in Fig. 6.14(b) and 6.14(c) we set $\delta t = 5 \cdot 10^{-4}$. The porosity in Fig. 6.14(b) takes all the values used for Fig. 6.13. Finally, the results reported in Fig. 6.14(c) we refer to the Young's modulus in Table 5.1 times a factor β , with $\beta = 1/5, 1/2.5, 1, 2.5, 5$.

Figures 6.14 confirm that the RN scheme converges always without relaxation. Furthermore, it is quite insensitive to parameters variations. The insensitivity is even more evident when an Aitken acceleration technique is employed. On the other side, the convergence of the DN algorithm deteriorates as the time step decreases and the porosity increases.

Concluding, the RN algorithm proves to be faster and more robust than the DN scheme also when dealing with FPSI problems.

δt [s]	ω_{max}	ϕ	ω_{max}	β	ω_{max}
10^{-3}	0.71	0.15	1.12	1/5	0.26
$5 \cdot 10^{-4}$	0.26	0.35	1	1/2.5	0.26
$2.5 \cdot 10^{-4}$	0.09	0.55	0.85	1	0.26
$1.25 \cdot 10^{-4}$	0.04	0.75	0.65	2.5	0.26
		0.95	0.35	5	0.25

Table 6.1: Maximum relaxation parameter ω_{max} allowed by the DN algorithm for different values of time step δt , porosity ϕ , and Young’s modulus factor β .

Figures 6.14 display only the results of the DN algorithm with an Aitken relaxation method because the algorithm with a constant acceleration parameter becomes dramatically slow for small time step values and large added-mass effects. To give an idea of how slow the convergence of the DN scheme can become we report in Table 6.1 the maximum relaxation parameter ω_{max} allowed for all the cases reported in Fig. 6.14.

Remark 6.13. *The DN scheme adopted for the results presented in this subsection is not a Dirichlet-Neumann algorithm strictly speaking (see Remark 6.10). In order to impose a Dirichlet interface condition on both components of the fluid velocity at the $(k + 1)$ -th iteration, we could replace condition*

$$\mathbf{u}_f^{k+1} \cdot \mathbf{t} + \frac{\sqrt{K_D}}{\gamma} \mathbf{t} \cdot (\boldsymbol{\sigma}_f^{k+1} \cdot \mathbf{n}) = \mathbf{u}_s^k \cdot \mathbf{t},$$

by

$$\mathbf{u}_f^{k+1} \cdot \mathbf{t} = \mathbf{u}_s^k \cdot \mathbf{t} - \frac{\sqrt{K_D}}{\gamma} \mathbf{t} \cdot (\boldsymbol{\sigma}_f^k \cdot \mathbf{n}),$$

where we omitted the reference to the time level t^{n+1} . We tested also this “proper” DN method but its performance is even worse than that of the “improper” DN scheme. Thus, we disregarded it.

6.9.3 The RR algorithm

We aim at checking the convergence properties of the RR algorithm with an explicit treatment of the nonlinearities.

In [6], it is pointed out that the estimate of α_s given by (6.79) does not allow a better performance with respect to the RN method. The reason is that fluid model problem (6.63) is far too simplified. Hence, instead of choosing the combination factor α_s as in (6.79), we take $\bar{\alpha}_s = \beta \alpha_s$. Figure 6.15 shows the number of average coupling iterations for factor β

spanning from 10^{-4} to 1. The results refer to the FPSI problem in hemodynamics: $\rho_s = 1.1$ g/cm³, $\rho_d = 1$ g/cm³, $\phi = 0.15$, $K_D \sim 10^{-12}$ (cm³ s)/g. The mesh is the same used for the simulations in Section 6.9.1 and the time step is taken equal to $\delta t = 5 \cdot 10^{-4}$. From Fig. 6.15, we see that for no factor β the RR algorithm outperforms the RN one. A better estimate for α_s should be studied in order to make the RR method more competitive.

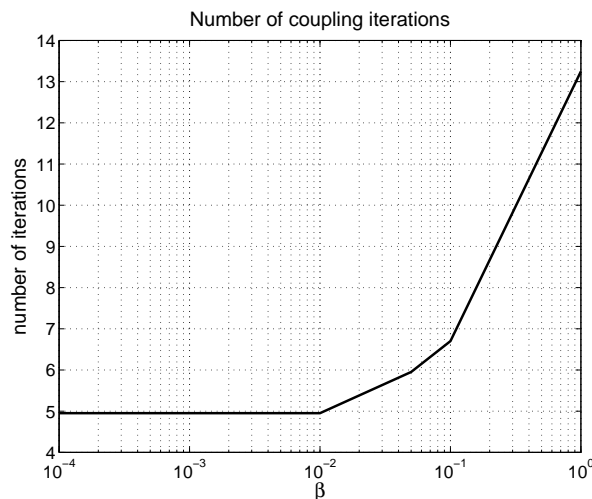


Figure 6.15: Number of iterations for the RR scheme for different values of factor β .

6.9.4 Qualitative results

Solving FPSI problems in hemodynamics could help understand how LDL deposit, leading to the formation of atherosclerotic plaques. Atherosclerosis localizes at a bend and/or bifurcation of an artery, where the LDL can accumulate. Therefore, we consider a $2d$ model obtained by intersecting a bended, stenotic artery with a plane. The geometry we consider (see Fig. 6.16) is idealized. However, it serves the purpose of showing qualitatively how important it is to account for wall deformation as well as filtration flow.

We impose the same boundary conditions as for the straight artery. We solve both the Navier-Stokes/generalized Darcy and the Navier-Stokes/Biot coupled problems. The former accounts for filtration flow only, neglecting the compliance of the artery wall, whereas the latter models both. The meshes we used are reported in Fig. 6.16. The fluid and structure meshes consist of 596 \mathbb{P}_1 fluid nodes and 1698 structure nodes, respectively. As for the straight artery, the structure mesh nodes at the interface correspond to the \mathbb{P}_1 iso \mathbb{P}_2 degrees of freedom for the fluid velocity. The parameters are those typical of hemodynamics, i.e. the ones listed in Table 5.1 plus $\rho_d = 1$ g/cm³, $K_D \sim 10^{-12}$ (cm³ s)/g, and

$\phi = 0.15$. In the two cases, we adopted a monolithic approach and an explicit treatment of the nonlinearities.

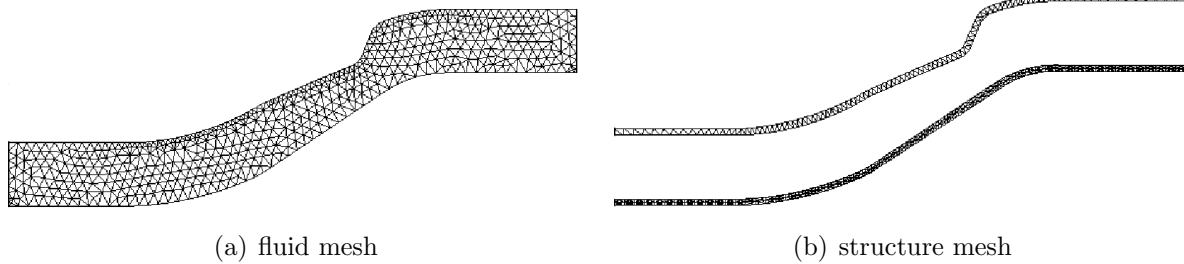


Figure 6.16: (a) Fluid and (b) structure meshes used for an idealized bended, stenotic artery.

Figure 6.17 shows the fluid pressure p_f and the pressure of the porous structure p_p every 4 ms in case the structure is governed by the generalized Darcy system. Being the fluid incompressible and the structure rigid, the pressure pulse imposed at the inlet does not propagate. Both pressures return to zero when the pulse is over, i.e. after 5 ms. The blood and structure dynamics change completely when the porous medium is deformable, see Fig. 6.18. The pressure pulse enters the lumen and the poroelastic structure and propagates from the upstream section to the downstream one. Supposing that blood flow and wall movement dictate the transport of the LDL, it is clear that a diffusion-advection model will give significantly different LDL distributions if it uses the solution of the Navier-Stokes/generalized Darcy or the Navier-Stokes/Biot system.

6.10 Conclusions

In this chapter we described a new methodology for modeling the fluid-structure problems in hemodynamics. The novelty consists in employing a poroelastic model for the artery wall. The necessary mathematical theory was developed in order to couple a linear poroelastic solid with the nonlinear Navier-Stokes fluid model. Special attention was paid to the stabilization of the poroelastic subproblem.

Modular and non-modular solution techniques used for fluid-elastic structure interaction problems have been extended to these more complex interactions. The non-modular approach is based on the ILUT preconditioner for the whole FPSI system. The modular algorithms make use of classical domain decomposition preconditioners: the Dirichlet-Neumann, the Robin-Robin, and the Robin-Neumann ones. Robin conditions are linear combinations of Dirichlet and Neumann conditions. Effective combinations coefficients for

the Robin interface conditions have been suggested thanks to simplified fluid and structure models. The convergence properties of the partitioned procedures were analyzed through simplified blood-vessel systems. Also in the case of FPSI problems, the Robin-Neumann algorithm converges always without relaxation and it is fairly insensitive to the added-mass effect, unlike the Dirichlet-Neumann scheme. In the case of a poroelastic structure, the added-mass effect is dictated by the porosity: the bigger the porosity value is, the smaller the effective structure density becomes.

Since there was an interest in the fluid-structure coupling, we dealt with the semi-implicit versions of all the methods mentioned above. This allowed us to focus on the effects of physical and discretization parameters variations on the “stiffness” of the coupling.

Numerical experiments on a straight $2d$ artery agree with the theoretical results found for the partitioned procedures. The monolithic approach confirmed its efficiency in presence of critical added-mass effects. Moreover, we used an idealized bended, stenotic $2d$ artery to show how important it is to adopt the poroelastic model for the simulation of complex problems, such the LDL transport and accumulation in the artery wall.

6.10. CONCLUSIONS

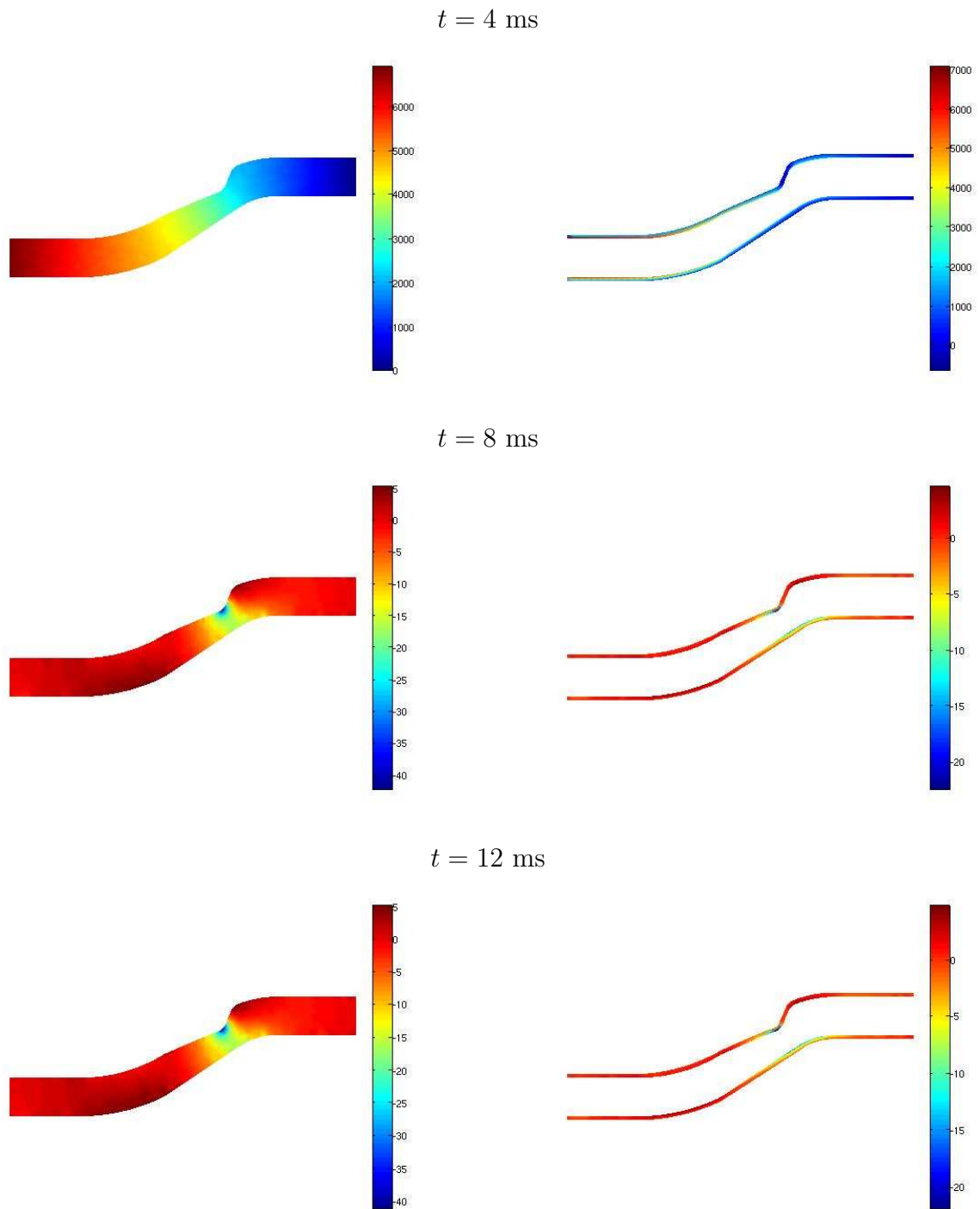


Figure 6.17: Pressure solution every 4 ms in the fluid and in the rigid porous structure.

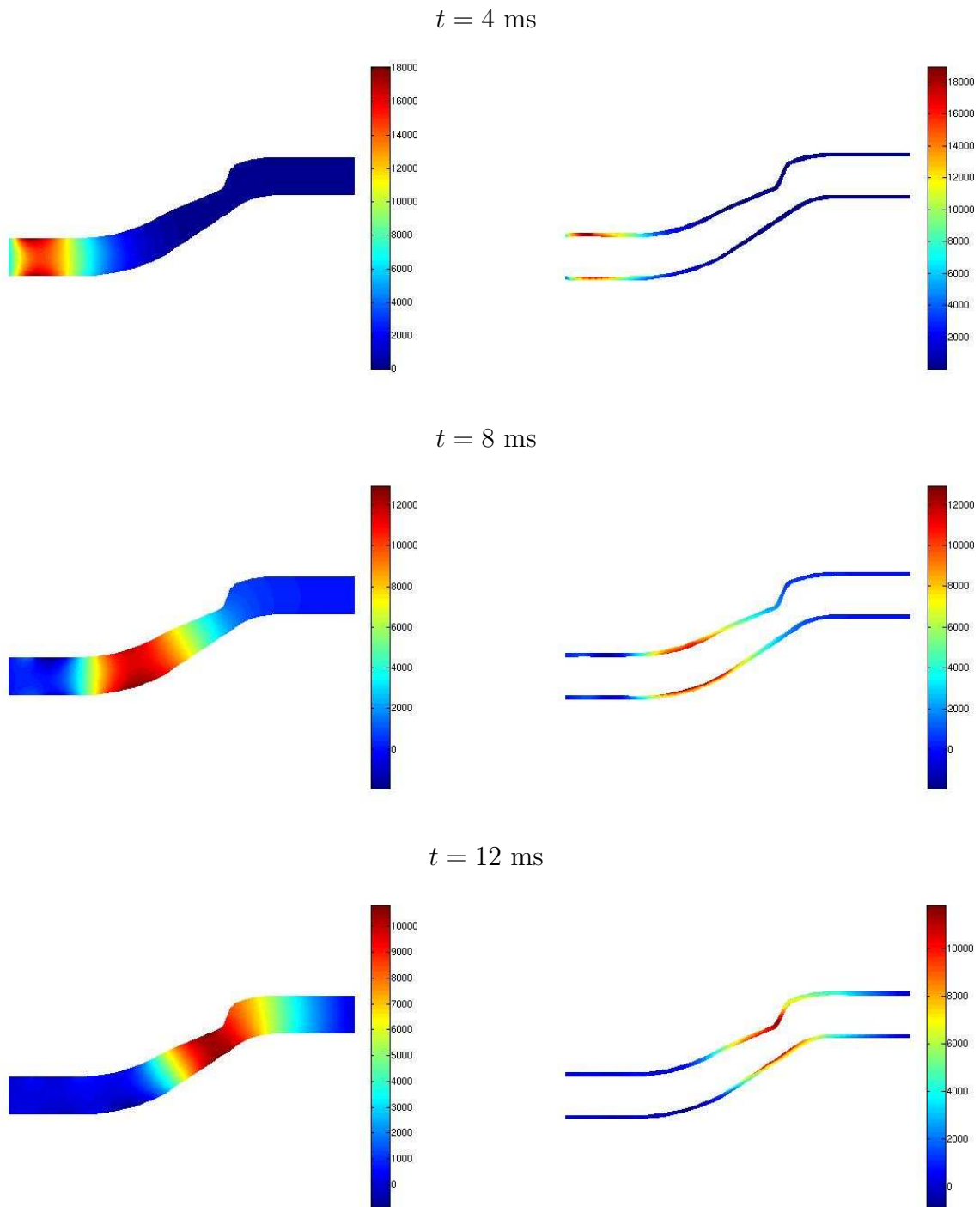


Figure 6.18: Propagation of the initial pressure pulse in the fluid and in the poroelastic structure. Solution at every 4 ms.

Conclusions

In this thesis we have focused on the numerical simulation of fluid-structure interaction problems arising in hemodynamics. The first way to model this kind of problems is to treat blood as an incompressible fluid and represent the artery wall as an elastic structure. The setting up of efficient algorithms for the solution of these coupled problems is difficult and classical iterative procedures fail or are too slow due to the large added-mass effect.

In such situations, good stability properties and low computational costs are featured by semi-implicit coupling methods. Their distinguishing property is to couple implicitly the pressure stress to the structure, while the nonlinearity due to convection and the geometrical nonlinearities are treated explicitly. We have proposed new schemes based on the inexact factorization of the linearized fluid-structure system, i.e. the procedure is split into explicit and implicit steps at the algebraic level. Two different methods have been designed: pressure-interface correction (PIC) and fluid-structure Yosida (FSY) algorithms. In both cases, the perturbation error has been analyzed and the convergence properties of the methods have been checked through numerical experiments. We showed that, in the simulation of a pressure pulse propagation in an idealized blood flow vessel, the methods remained stable for a wide range of discretization and physical parameters. Qualitative results have turned out to be very similar to those achieved with the monolithic system.

We have also proposed predictor-corrector methods that use inexact factors as preconditioners. The best feature of these procedures is that predictor-corrector iterations are independent of the added-mass effect. The solution of these methods converges to the one of the fully implicit monolithic system without introducing any perturbation.

The schemes derived from inexact factorization have been compared with other methods based on two preconditioners for the FSI system. The first one is the classical Dirichlet-Neumann preconditioner. Two modular algorithms based on that preconditioner (the DN-Richardson and the DN-GMRES ones) have been considered. The reduction factor for the DN-GMRES method has been obtained for a model problem. The second preconditioner is a non-modular ILUT preconditioner for the whole FSI system. We have introduced an appropriate monolithic formulation to be used with this preconditioner.

The advantages of the explicit treatment for the nonlinearities of the FSI problem have

been underlined, independently of the scheme used. Thus, we dealt with the semi-implicit versions of all the methods mentioned above. We have carried out a broad set of numerical experiments to compare the algorithms. For problems with critical added-mass effect we can conclude that the ILUT-solver method is the least expensive in terms of CPU time for large problems. The PIC scheme is very competitive for smaller problems. Anyways, both non-modular approaches prove to be much more efficient than the modular DN-algorithms for the applications under consideration.

A better way to model fluid-structure interaction problems in hemodynamics is to represent the vessel wall as a poroelastic medium. The necessary mathematical theory was developed in order to couple a linear poroelastic solid with the nonlinear Navier-Stokes fluid model. Special attention was paid to the stabilization of the poroelastic subproblem.

Modular and non-modular solution techniques used for fluid-elastic structure interaction problems have been extended to these more complex interactions. The non-modular approach is based on the ILUT preconditioner for the whole FPSI system. The modular algorithms make use of classical domain decomposition preconditioners: the Dirichlet-Neumann, the Robin-Robin, and the Robin-Neumann ones. Robin conditions are linear combinations of Dirichlet and Neumann conditions. Effective combinations coefficients for the Robin interface conditions have been suggested thanks to simplified fluid and structure models. The convergence properties of the partitioned procedures were analyzed through simplified blood-vessel systems. Also in the case of FPSI problems, the Robin-Neumann algorithm converges always without relaxation and it is fairly insensitive to the added-mass effect, unlike the Dirichlet-Neumann scheme. Numerical experiments on a straight $2d$ artery agree with the theoretical results found for the partitioned procedures. The monolithic approach confirmed its efficiency in presence of critical added-mass effects.

Fluid-poroelastic structure interactions have been less investigated than classical fluid-structure interactions. More efficient monolithic approach could be proposed, e.g. exploiting more powerful preconditioners for the FPSI system than the ILUT one. Concerning partitioned procedures, we considered Richardson iterations preconditioned by classical domain decomposition preconditioners. The next step will be to replace Richardson iterations with GMRES ones to improve robustness and efficiency. Furthermore, all those algorithms should be applied to realistic three-dimensional problems. Then, if the final goal is to simulate LDL transport or drug delivery, a mass transfer code which uses the solutions of the FPSI problem shall be implemented.

Bibliography

- [1] J. Atanga and D. Silvester. Iterative methods for stabilized mixed velocity-pressure finite elements. *Internat. J. Numer. Methods Fluids*, 14:71–81, 1992.
- [2] I. Babuška. Error bounds for the finite element method. *Numer. Math.*, 16:322–333, 1971.
- [3] S. Badia and R. Codina. Analysis of a stabilized finite element approximation of the transient convection-diffusion equation using an ALE framework. *SIAM J. Numer. Anal.*, 44(5):2159–2197, 2006.
- [4] S. Badia and R. Codina. On some fluid-structure iterative algorithms using pressure segregation methods. Application to aeroelasticity. *Internat. J. Numer. Methods Engrg.*, 72:46–71, 2007.
- [5] S. Badia and R. Codina. On a multiscale approach to the transient Stokes problem. Dynamic subscales and anisotropic space-time discretization. *Appl. Math. Comput.*, in press, 2008.
- [6] S. Badia, F. Nobile, and C. Vergara. Fluid-structure partitioned procedures based on Robin transmission conditions. *J. Comp. Phys*, 227:7027–7051, 2008.
- [7] S. Badia, F. Nobile, and C. Vergara. Robin-Robin preconditioned Krylov methods for fluid-structure interaction. Technical Report 19/2008, MOX, Politecnico di Milano, 2008.
- [8] S. Badia, A. Quaini, and A. Quarteroni. Modular vs. non-modular preconditioners for fluid-structure systems with large added-mass effect. *Comput. Methods Appl. Mech. Engrg.*, 197(49-50):4216–4232, 2008.
- [9] S. Badia, A. Quaini, and A. Quarteroni. Splitting methods based on algebraic factorization for fluid-structure interaction. *SIAM J. Sci. Comput.*, 30(4):1778–1805, 2008.

BIBLIOGRAPHY

- [10] G. S. Beavers and D. D. Joseph. Boundary conditions at a naturally permeable wall. *J. Fluid Mech.*, 30:197–207, 1967.
- [11] H. Beirao da Veiga. On the existence of strong solutions to a coupled fluid-structure evolution problem. *J. Math. Fluid Mech.*, 6:21–52, 2004.
- [12] F. Ben Belgacem. The mortar finite element method with Lagrange multipliers. *Numer. Math.*, 84:173–197, 1999.
- [13] M. A. Biot. General theory of three-dimensional consolidation. *J. Appl. Phys.*, 12:155–164, 1941.
- [14] M. A. Biot. Theory of elasticity and consolidation for a porous anisotropic solid. *J. Appl. Phys.*, 25:182–185, 1955.
- [15] M. A. Biot. Theory of finite deformations of porous solids. *Indiana Univ. Math. J.*, 21:597–620, 1971/72.
- [16] J. Blasco and R. Codina. Space and time error estimates for a first order, pressure stabilized finite element method for the incompressible Navier-Stokes equations. *Appl. Numer. Math.*, 38:475–497, 2001.
- [17] F. Brezzi. On the existence, uniqueness and approximation of saddle point problems arising from Lagrange multipliers. *RAIRO Anal. Numer.*, 8:129–151, 1974.
- [18] F. Brezzi, J. Douglas, R. Duran, and M. Fortin. Mixed finite elements for second order elliptic problems in three variables. *Numer. Math.*, 51:237–250, 1987.
- [19] F. Brezzi, J. Douglas, M. Fortin, and L. D. Marini. Efficient rectangular mixed finite elements in two and three spaces variables. *RAIRO Modél. Math. Anal. Numér.*, 21:581–604, 1987.
- [20] F. Brezzi, J. Douglas, and L. D. Marini. Two families of mixed finite elements for second order elliptic problems. *Numer. Math.*, 47:217–235, 1985.
- [21] F. Brezzi and M. Fortin. *Mixed and Hybrid Finite Element Methods*. Springer Verlag, 1991.
- [22] F. Brezzi, M. Fortin, and L.D. Marini. Error analysis of constant pressure approximations of Darcy’s law. *Comput. Methods Appl. Mech. Engrg.*, 195:1547–1559, 2006.
- [23] F. Brezzi, T.J.R. Hughes, and E. Süli. Variational approximation of flux in conforming finite element methods for elliptic partial differential equations: a model problem. *Rend. Mat. Acc. Lincei s. 9*, 12:167–183, 2001.

- [24] E. Burman and M.A. Fernández. Stabilized explicit coupling for fluid-structure interaction using Nitsche’s method. *C. R. Acad. Sci. Paris Sér. I Math.*, 345:467–472, 2007.
- [25] V. M. Calo, N. F. Brasher, Y. Bazilevs, and T. J. R. Hughes. Multiphysics model for blood flow and drug transport with application to patient-specific coronary artery flow. *Comput. Mech.*, 43(1):161–177, 2008.
- [26] P. Causin, J.F. Gerbeau, and F. Nobile. Added-mass effect in the design of partitioned algorithms for fluid-structure problems. *Comput. Methods Appl. Mech. Engrg.*, 194(42-44):4506–4527, 2005.
- [27] A. Chambolle, B. Desjardins, M. Esteban, and C. Grandmont. Existence of weak solutions of an unsteady fluid-plate interaction problem. *J. Math. Fluid Mech.*, 7(3):368–404, 2004.
- [28] C. H. A. Cheng, D. Coutand, and S. Shkoller. Navier-Stokes equations interacting with a nonlinear elastic biofluid shell. *SIAM J. Math. Anal.*, 39:742–800, 2007.
- [29] M. Chiumenti, Q. Valverde, C. Agelet de Saracibar, and M. Cervera. A stabilized formulation for incompressible elasticity using linear displacement and pressure interpolations. *Comput. Methods Appl. Mech. Engrg.*, 191:5253–5264, 2002.
- [30] A.J. Chorin. A numerical method for solving incompressible viscous problems. *J. Comp. Phys*, 2:12–26, 1967.
- [31] A.J. Chorin. The numerical solution of the Navier–Stokes equations for an incompressible fluid. AEC Research and Development Report, NYO-1480-82. New York University, New York, 1967.
- [32] A.J. Chorin. Numerical solution of the Navier–Stokes equations. *Math. Comp.*, 22:745–762, 1968.
- [33] A.J. Chorin. On the convergence of discrete approximation to the Navier–Stokes equations. *Math. Comp.*, 23, 1969.
- [34] P.G. Ciarlet. *Mathematical Elasticity. Vol. I.* Studies in mathematics and its applications. North-Holland Publishing, Amsterdam, 1988.
- [35] R. Codina. Comparison of some finite element methods for solving the diffusion-convection-reaction equation. *Comput. Methods Appl. Mech. Engrg.*, 156:185–210, 1998.

- [36] R. Codina. A stabilized finite element method for generalized stationary incompressible flows. *Comput. Methods Appl. Mech. Engrg.*, 190:2681–2706, 2001.
- [37] R. Codina. Stabilized finite element approximation of transient incompressible flows using orthogonal subscales. *Comput. Methods Appl. Mech. Engrg.*, 191:4295–4321, 2002.
- [38] R. Codina and S. Badia. On some pressure segregation methods of fractional-step type for the finite element approximation of incompressible flow problems. *Comput. Methods Appl. Mech. Engrg.*, 195:2900–2918, 2006.
- [39] R. Codina and J. Blasco. Analysis of a pressure-stabilized finite element approximation of the stationary Navier-Stokes equations. *Numer. Math.*, 87:59–81, 2000.
- [40] R. Codina and J. Principe. Dynamic subscales in the finite element approximation of thermally coupled incompressible flow. *Int. J. Numer. Meth. Fluids*, 54:707–730, 2007.
- [41] R. Codina, J. Principe, O. Guasch, and S. Badia. Time dependent subscales in the stabilized finite element approximation of incompressible flow problems. *Comput. Methods Appl. Mech. Engrg.*, 196:2413–2430, 2007.
- [42] R. Codina and O. Soto. Approximation of the incompressible Navier–Stokes equations using orthogonal–subscale stabilization and pressure segregation on anisotropic finite element meshes. *Comput. Methods Appl. Mech. Engrg.*, 193:1403–1419, 2004.
- [43] G. de Rham. *Variétés Différentiables Formes, Courants, Formes Harmoniques*. Paris Hermann, 1973.
- [44] S. Deparis. *Numerical Analysis of Axisymmetric Flows and Methods for Fluid-Structure Interaction Arising in Blood Flow Simulation*. PhD thesis, École Polytechnique Fédérale de Lausanne, 2004.
- [45] S. Deparis, M. Discacciati, G. Fourestey, and A. Quarteroni. Fluid-structure algorithms based on Steklov-Poincaré operators. *Comput. Methods Appl. Mech. Engrg.*, 195(41-43):5797–5812, 2006.
- [46] S. Deparis, M. Discacciati, and A. Quarteroni. A domain decomposition framework for fluid-structure interaction problems. In C. Groth and D. W. Zingg, editors, *Proceedings of the Third International Conference of Computational Fluid Dynamics (ICCFD3) 2004*, Toronto, 2006.

- [47] M. Discacciati. *Domain Decomposition Methods for the Coupling of Surface and Groundwater Flows*. PhD thesis, École Polytechnique Fédérale de Lausanne, 2004.
- [48] M. Discacciati. Iterative methods for Stokes/Darcy coupling. *Domain Decomposition Methods in Science and Engineering, Lecture Notes in Computational Science and Engineering*, No. 40. Springer-Verlag, Berlin and Heidelberg, 2004.
- [49] M. Discacciati, A. Quarteroni, and A. Valli. Robin-Robin domain decomposition methods for the Stokes-Darcy coupling. *SIAM J. Numer. Anal.*, 45(3):1246–1268, 2007.
- [50] H. Elman, D. Silvester, and A. Wathen. *Finite Elements and Fast Iterative Solvers*. Oxford Science Publications, 2005.
- [51] H.C. Elman. Preconditioners for saddle point problems arising in computational fluid dynamics. *Appl. Numer. Math.*, 43:75–89, 2002.
- [52] H. I. Ene and E. Sánchez-Palencia. Équations et phénomènes de surface pour l'écoulement dans un modèle de milieu poreux. *J. Mécanique*, 14:73–108, 1975.
- [53] M.S. Engelman, R.L. Sani, and P. Gresho. The implementation of normal and/or tangential boundary conditions in finite element codes for incompressible fluid flow. *Internat. J. Numer. Methods Fluids*, 2:225–238, 1982.
- [54] C. Farhat, P. Geuzaine, and G. Brown. Application of a three-field nonlinear fluid-structure formulation to the prediction of the aeroelastic parameters of an F-16 fighter. *Comput. & Fluids*, 32:3–29, 2003.
- [55] M.A. Fernández, J.F. Gerbeau, and C. Grandmont. A projection semi-implicit scheme for the coupling of an elastic structure with an incompressible fluid. *Internat. J. Numer. Methods Engrg.*, 69(4):794–821, 2007.
- [56] M.A. Fernández and M. Moubachir. A Newton method using exact Jacobians for solving fluid-structure coupling. *Comput. & Structures*, 83(2-3):127–142, 2005.
- [57] M. Ferrari. Cancer nanotechnology: opportunities and challenges. *Nature Reviews Cancer*, 3(5):161–171, 2005.
- [58] C. Figueroa, I. Vignon-Clementel, K. Jansen, T. Hughes, and C. Taylor. A coupled momentum method for modeling blood flow in three-dimensional deformable arteries. *Comput. Methods Appl. Mech. Engrg.*, 195:5685–5706, 2006.

BIBLIOGRAPHY

- [59] B. Fisher, A. Ramage, D.J. Silvester, and A.J. Wathen. On parameter choice and iterative convergence for stabilised discretisations of advection-diffusion problems. *Comput. Methods Appl. Mech. Engrg.*, 179:179–195, 1999.
- [60] L. Formaggia, J.-F. Gerbeau, F. Nobile, and A. Quarteroni. On the coupling of 3D and 1D Navier-Stokes equations for flow problems in compliant vessels. *Comput. Methods Appl. Mech. Engrg.*, 191(6-7):561–582, 2001.
- [61] L. Formaggia, A. Quarteroni, and A. Veneziani. *Cardiovascular Mathematics*, volume 1 of *Modeling, Simulation and Applications*. Springer, 2009.
- [62] H. Fujita and N. Sauer. On existence of weak solutions of the Navier-Stokes equations in regions with moving boundaries. *J. Fac. Sci. Univ. Tokyo, sect. 1A*, 17:403–420, 1970.
- [63] D. K. Gartling, C. E. Hickox, and R. C. Givler. Simulation of coupled viscous and porous flow problems. *Comp. Fluid Dynamics*, 7:23–48, 1996.
- [64] F.J. Gaspar, F. Lisbona, and C.W. Oosterlee. A stabilized difference scheme for deformable porous media and its numerical resolution by multigrid methods. *Comput. Vis. Sci.*, 11:67–76, 2008.
- [65] A. Gauthier, F. Saleri, and A. Veneziani. A fast preconditioner for the incompressible Navier-Stokes equations. *Comput. Vis. Sci.*, 6(2-3):105–112, 2004.
- [66] J.F. Gerbeau and M. Vidrascu. A quasi-Newton algorithm based on a reduced model for fluid-structure interaction problems in blood flows. *M2AN Math. Model. Numer. Anal.*, 37(4):631–648, 2003.
- [67] P. Gervasio, F. Saleri, and A. Veneziani. Algebraic fractional-step schemes with spectral methods for the incompressible Navier-Stokes equations. *J. Comp. Phys*, 214(1):347–365, 2006.
- [68] R. Glowinski. Splitting methods for the numerical solution of the incompressible Navier-Stokes equations. In *Vistas in applied mathematics*, pages 57–95, New York, 1986.
- [69] P.M. Gresho. On the theory of semi-implicit projection methods for viscous incompressible flow and its implementation via a finite element method that also introduces a nearly consistent mass matrix. Part I: Theory. *Internat. J. Numer. Methods Fluids*, 11:587–620, 1990.

- [70] J.L. Guermond, P. Mineev, and J. Shen. An overview of projection methods for incompressible flows. *Comput. Methods Appl. Mech. Engrg.*, 195:6011–6045, 2006.
- [71] G. Guidoboni, R. Glowinski, N. Cavallini, S. Canic, and S. Lapin. Kinematically coupled time-splitting scheme for fluid-structure interaction in blood flow. *Appl. Math. Lett.*, Accepted for publication, 2008.
- [72] M. Heil. An efficient solver for the fully coupled solution of large-displacement fluid-structure interaction problems. *Comput. Methods Appl. Mech. Engrg.*, 193:1–23, 2004.
- [73] M. O. Henriksen and J. Holmen. Algebraic splitting for incompressible Navier-Stokes equations. *J. Comput. Phys.*, 175(2):438–453, 2002.
- [74] E. Hopf. Über die Anfangswertaufgabe für die hydrodynamischen Grundgleichungen. *Math. Nachr.*, 4:213–231, 1951.
- [75] T.J.R. Hughes. Multiscale phenomena: Green’s function, the Dirichlet-to-Neumann formulation, subgrid scale models, bubbles and the origins of stabilized formulations. *Comput. Methods Appl. Mech. Engrg.*, 127:387–401, 1995.
- [76] T.J.R. Hughes, G.R. Feijóo, L. Mazzei, and J.B. Quincy. The variational multiscale method—A paradigm for computational mechanics. *Comput. Methods Appl. Mech. Engrg.*, 166:3–24, 1998.
- [77] T.J.R. Hughes, L. Mazzei, and K.E. Jansen. Large eddy simulation and the variational multiscale method. *Computing and Visualization in Science*, 3:47–59, 2000.
- [78] A. Inoue and M. Wakimoto. On existence of solutions of the Navier-Stokes equations in a time dependent domain. *J. Fac. Sci. Univ. Tokyo, sect. 1A*, 24:303–319, 1977.
- [79] W. Jäger and A. Mikelić. On the boundary conditions at the contact interface between a porous medium and a free fluid. *Ann. Scuola Norm. Sup. Pisa Cl. Sci.*, 23(3):403–465, 1996.
- [80] W. Jäger and A. Mikelić. On the interface boundary condition Beavers, Joseph, and Saffman. *SIAM J. Appl. Math.*, 60(4):1111–1127, 2000.
- [81] D. Jaubert and V. Moreau. Fluid-structure interaction: applications in the context of a flow in arterial medium. *CRS4 Tech. Rep. 97/15*, 1997.
- [82] I. P. Jones. Low Reynolds number flow past a porous spherical shell. *Proc. Camb. Phil. Soc.*, 73:231–238, 1973.

BIBLIOGRAPHY

- [83] G. Karner, K. Perktold, M. Hofer, and D. Liepsch. Flow characteristics in an anatomically realistic compliant carotid artery bifurcation model. *Methods in Biomechanics and Biomedical Engineering*, 2(39–41):171–185, 1999.
- [84] N. Koshiba, J. Ando, X. Chen, and T. Hisada. Multiphysics simulation of blood flow and LDL transport in a porohyperelastic arterial wall model. *J. of Biomech. Eng.*, 129:374–385, 2007.
- [85] O. Ladyzhenskaya. *The Mathematical Theory of Viscous Incompressible Flow*. Gordon and Breach, New York, 1969.
- [86] W. J. Layton, F. Schieweck, and I. Yotov. Coupling fluid flow with porous media flow. *SIAM J. Numer. Anal.*, 40(6):2195–2218, 2002.
- [87] J. Leray. Essai sur les mouvements d’un liquide visqueux emplissant l’espace. *Acta Math.*, 63:193–248, 1934.
- [88] T. Levy and E. Sánchez-Palencia. On boundary conditions for fluid flow in porous media. *Int. J. Engng. Sci.*, 13:923–940, 1975.
- [89] J.L. Lions. *Quelques Méthodes de Résolution des Problèmes aux Limites Non Linéaires*. Ed. Dunod, 1969.
- [90] D. Loghin and A.J. Wathen. Schur complement preconditioners for the Navier-Stokes equations. *Internat. J. Numer. Methods Fluids*, 40:403–412, 2002.
- [91] G. I. Marchuk. Splitting and alternating direction methods. In P. G. Ciarlet and J. L. Lions, editors, *Handbook of Numerical Analysis*, pages 197–462. Elsevier Science Publishers B. V., 1990.
- [92] A. Masud and T. J. R. Hughes. A stabilized mixed finite element method for Darcy flow. *Comput. Methods Appl. Mech. Engrg.*, 191:4341–4370, 2002.
- [93] H.G. Matthies and J. Steindorf. Partitioned strong coupled algorithms for fluid-structure interaction. *Comput. & Structures*, 81:805–812, 2003.
- [94] D. A. McDonald. *Blood Flow in Arteries*. Edward Arnold Ltd. - London, 1990.
- [95] G. McKay. The Beavers and Joseph condition for velocity slip at the surface of a porous medium. In B. Straugham, R. Greve, and H. Ehrentraut, editors, *Continuum mechanics and applications in geophysics and the environment*, pages 126–139. Springer, Berlin, 2001.

- [96] C. Michler, E. H. van Brummelen, and R. de Borst. An interface Newton-Krylov solver for fluid-structure interaction. *Internat. J. Numer. Methods Fluids*, 47(10-11):1189–1195, 2005.
- [97] D.P. Mok and W.A. Wall. Partitioned analysis schemes for transient interaction of incompressible flows and nonlinear flexible structures. In *Trends in computational structural mechanics (W.A. Wall, K.U. Bletzinger and K. Schweizerhof, Eds.)*, CIMNE, Barcelona, Spain, 2001.
- [98] M. A. Murad, J. N. Guerreiro, and A. F. D. Loula. Micromechanical computational modeling of reservoir compaction and surface subsidence. *Math. Contemp.*, 19:41–69, 2000.
- [99] M. A. Murad, J. N. Guerreiro, and A. F. D. Loula. Micromechanical computational modeling of secondary consolidation and hereditary creep in soils. *Comput. Methods Appl. Mech. Engrg.*, 190(15-17):1985–2016, 2001.
- [100] C. M. Murea. Computer modeling of cardiovascular fluid-structure interactions with the deforming-spatial-domain/stabilized space-time formulation. *ESAIM: Math. Model. Numer. Anal.*, 40:1101–1125, 2006.
- [101] J. C. Nédélec. Mixed finite elements in \mathbb{R}^3 . *Numer. Math.*, 35:119–136, 1980.
- [102] J. C. Nédélec. A new family of mixed finite elements in \mathbb{R}^3 . *Numer. Math.*, 50:57–81, 1986.
- [103] D. A. Nield and A. Bejan. *Convection in Porous Media*. Springer-Verlag, New York, 1999.
- [104] F. Nobile. *Numerical Approximation of Fluid-Structure Interaction Problems with Application to Haemodynamics*. PhD thesis, École Polytechnique Fédérale de Lausanne, 2001.
- [105] F. Nobile and C. Vergara. An effective fluid-structure interaction formulation for vascular dynamics by generalized Robin conditions. *SIAM J. Sci. Comp.*, 30(2):731–763, 2008.
- [106] A. A. Oberai and P. M. Pinsky. A multiscale finite element method for the Helmholtz equation. *Comput. Methods Appl. Mech. Engrg.*, 154:281–297, 1998.
- [107] J.T. Oden and L.Z. Demkowicz. *Applied Functional Analysis*. CRC Press, 1996.

BIBLIOGRAPHY

- [108] L. E. Payne and B. Straughan. Analysis of the boundary condition at the interface between a viscous fluid and a porous medium and related modelling questions. *J. Math. Pure Appl.*, 77(4):317–354, 1998.
- [109] K. Perktold, E. Thurner, and T. Kenner. Flow and stress characteristics in rigid wall and compliant carotid models. *Medic. and Biolog. Eng. and Comp.*, 32:19–26, 1994.
- [110] J.B. Perot. An analysis of the fractional step method. *J. Comp. Phys.*, 108:51–58, 1993.
- [111] S. Piperno and C. Farhat. Partitioned procedures for the transient solution of coupled aeroelastic problems-Part II: energy transfer analysis and three-dimensional applications. *Comput. Methods Appl. Mech. Engrg.*, 190:3147–3170, 2001.
- [112] M. Prosi, P. Zunino, K. Perktold, and A. Quarteroni. Mathematical and numerical models for transfer of low-density lipoproteins through the arterial wall: a new methodology for the model set up with applications to the study of disturbed luminal flow. *J. Biomechanics*, 38:903–917, 2005.
- [113] A. Quaini and A. Quarteroni. A semi-implicit approach for fluid-structure interaction based on an algebraic fractional step method. *Math. Models Methods Appl. Sci.*, 17(6):957–983, 2007.
- [114] A. Quarteroni and L. Formaggia. *Mathematical Modelling and Numerical Simulation of the Cardiovascular System*, volume Modelling of Living Systems, Handbook of Numerical Analysis. Elsevier Science, 2003.
- [115] A. Quarteroni, G. Sacchi Landriani, and A. Valli. Coupling viscous and inviscid Stokes equations via a domain decomposition method for finite elements. *Numer. Math.*, 59:831–859, 1991.
- [116] A. Quarteroni, F. Saleri, and A. Veneziani. Analysis of the Yosida method for the incompressible Navier-Stokes equations. *J. Math. Pures Appl.*, 78:473–503, 1999.
- [117] A. Quarteroni, F. Saleri, and A. Veneziani. Factorization methods for the numerical approximation of Navier-Stokes equations. *Comput. Methods Appl. Mech. Engrg.*, 188:505–526, 2000.
- [118] A. Quarteroni, M. Tuveri, and A. Veneziani. Computational vascular fluid dynamics: Problems, models and methods. *Comp. Vis. Science*, 2:163–197, 2000.
- [119] A. Quarteroni and A. Valli. *Numerical Approximation of Partial Differential Equations*. Springer-Verlag, 1994.

BIBLIOGRAPHY

- [120] A. Quarteroni and A. Valli. *Domain Decomposition Methods for Partial Differential Equations*. Oxford Science Publications, 1999.
- [121] R. Rannacher. *On Chorin's Projection Method for Incompressible Navier-Stokes Equations*, Lecture Notes in Mathematics, volume 1530, pages 167–183. Springer, Berlin, 1992.
- [122] P. A. Raviart and J. M. Thomas. *A Mixed-Finite Element Method for Second Order Elliptic Problems*, volume Mathematical aspects of the finite element method, Lecture Notes in Mathematics. Springer, New York, 1977.
- [123] P. A. Raviart and J. M. Thomas. *Introduction à l'Analyse Numérique des Équations aux Dérivées Partielles*. Masson, Paris, 1983.
- [124] V. C. Rideout and D. E. Dick. Analog studies of the human systemic arterial tree. *IEEE Transaction on Biomedical Eng.*, 14(3):171–177, 1967.
- [125] S. Rugonyi and K. J. Bathe. On finite elements analysis of fluid flows coupled with structural interaction. *CMES - Comput. Model. Engrg. Sci.*, 2:195–212, 2001.
- [126] Y. Saad. SPARSKIT: A basic tool for sparse matrix computation. Technical Report CSRD TR 1029, CSRD, University of Illinois, 1990.
- [127] Y. Saad. *Iterative Methods for Sparse Linear Systems*. PWS Publishing, Boston, MA, 1996.
- [128] A. G. Saffman. On the boundary condition at the surface of a porous medium. *Studies in Appl. Math.*, 1:93–101, 1971.
- [129] F. Saleri and A. Veneziani. Pressure correction algebraic splitting methods for the incompressible Navier-Stokes equations. *SIAM J. Numer. Anal.*, 43(1):174–194, 2005.
- [130] A. G. Salinger, R. Aris, and J. J. Derby. Finite element formulations for large-scale, coupled flows in adjacent porous and open fluid domains. *Internat. J. Numer. Methods Fluids*, 18:1185–1209, 1994.
- [131] R. Salvi. On the existence of weak solutions of a non-linear mixed problem for the Navier-Stokes equations in a time dependent domain. *J. Fac. Sci. Univ. Tokyo, sect. 1A*, 32:213–221, 1985.
- [132] R. Salvi. On the existence of periodic weak solutions of Navier-Stokes equations in regions with periodically moving boundaries. *Acta. Appl. Math.*, 37:169–179, 1994.

BIBLIOGRAPHY

- [133] E. Sánchez-Palencia. *Nonhomogeneous Media and Vibration Theory*. Lecture Notes in Physics. Springer-Verlag, Berlin, 1980.
- [134] R. E. Showalter. Poroelastic filtration coupled to Stokes flow. In O. Imanuvilov, G. Leugering, R. Triggiani, and B. Zhang, editors, *Lecture Notes in Pure and Applied Mathematics, vol. 242*, pages 229–241. Chapman & Hall, Boca Raton, 2005.
- [135] P.J. Silvester and N. Kechkar. Stabilised bilinear-constant velocity-pressure finite elements for the conjugate gradient solution of the Stokes problem. *Comput. Methods Appl. Mech. Engrg.*, 79:71–86, 1990.
- [136] S. Sy and C. M. Murea. A stable time advancing scheme for solving fluid-structure interaction problem at small structural displacements. *Comput. Methods Appl. Mech. Engrg.*, in press, 2008.
- [137] P. Le Tallec and J. Mouro. Fluid structure interaction with large structural displacements. *Comput. Methods Appl. Mech. Engrg.*, 190:3039–3067, 2001.
- [138] R. Temam. Sur la stabilité et la convergence de la méthode des pas fractionnaires. *Ann. Mat. Pura Appl.*, LXXIV:191–380, 1968.
- [139] R. Temam. Une méthode d’approximations de la solution des equations de Navier–Stokes. *Bull. Soc. Math. France*, 98:115–152, 1968.
- [140] R. Temam. Sur l’approximation de la solution des équations de Navier–Stokes par la méthode des pas fractionnaires (I). *Arch. Ration. Mech. Anal.*, 32:135–153, 1969.
- [141] R. Temam. Sur l’approximation de la solution des équations de Navier–Stokes par la méthode des pas fractionnaires (II). *Arch. Ration. Mech. Anal.*, 33:377–385, 1969.
- [142] R. Temam. *Navier-Stokes Equations*. North-Holland, 1984.
- [143] R. Temam. Remark on the pressure boundary condition for the projection method. *Theoretical Computational Fluid Dynamics*, 3:181–184, 1991.
- [144] T. E. Tezduyar. Finite element methods for fluid dynamics with moving boundaries and interfaces. *Arch. Comput. Meth. Engrg.*, 8:83–130, 2001.
- [145] J. M. Thomas. *Sur l’Analyse Numérique des Méthodes d’Éléments Finis Hybrides et Mixtes*. PhD thesis, Université Pierre et Marie Curie, 1977.

BIBLIOGRAPHY

- [146] R. Torii, M. Oshima, T. Kobayashi, K. Takagi, and T. E. Tezduyar. Computer modeling of cardiovascular fluid-structure interactions with the deforming-spatial-domain/stabilized space-time formulation. *Comput. Methods Appl. Mech. Engrg.*, 195:1885–1895, 2006.
- [147] S. Turek. *Efficient Solvers for Incompressible Flow Problems*. Lecture Notes in Computational Science and Engineering. Springer, 1999.
- [148] A. Veneziani. *A Mathematical and Numerical Modeling of Blood Flow Problems*. PhD thesis, University of Milan, 1998.
- [149] T. Washio, T. Hisada, H. Watanabe, and T.E. Tezduyar. A robust preconditioner for fluid–structure interaction problems. *Comput. Methods Appl. Mech. Engrg.*, 194(39–41):4027–4047, 2005.
- [150] N. Westerhof, F. Bosman, C. D. Vries, and A. Noordergraaf. Analog studies of the human systemic arterial tree. *J. of Biomech*, 2:121–143, 1969.
- [151] M. Whale, A. Grodzisky, and A. Johnson. The effect of aging and pressure on the patient hydraulic conductivity of the aortic wall. *Biorheology*, 33:17–44, 1996.
- [152] X. Y. Xu, M. W. Collins, and C. J. H. Jones. Flow studies in canine aortas. *ASME J. Biomech. Eng.*, 114(11):504–511, 1992.
- [153] N. N. Yanenko. *The Method of Fractional Steps*. Springer Verlag, New York, 1971.
- [154] P. Zunino. *Mathematical and Numerical Modeling of Mass Transfer in the Vascular System*. PhD thesis, École Polytechnique Fédérale de Lausanne, 2002.

BIBLIOGRAPHY

Curriculum Vitæ

Annalisa Quaini

Personal Information:

Date of birth: May 20th, 1980.

Place of birth: Sant'Angelo Lodigiano, Italy.

Education:

2005-2008: PhD student at CMCS (Chaire de modélisation et calcul scientifique) at EPFL.

2005: MS (cum laude) in aerospace engineering with a specialization in aerodynamics.

Training and master degree thesis at CMCS at EPFL.

1999-2005: Student in aerospace engineering at Politecnico di Milano.

Publications:

1. S. Badia, A. Quaini, and A. Quarteroni. Modular vs. non-modular preconditioners for fluid-structure systems with large added-mass effect. *Comput. Methods Appl. Mech. Engrg.*, 197(49-50):4216-4232, 2008.
2. S. Badia, A. Quaini, and A. Quarteroni. Splitting methods based on algebraic factorization for fluid-structure interaction. *SIAM J. Sci. Comput.*, 30(4):1778-1805, 2008.
3. A. Quaini and A. Quarteroni. A semi-implicit approach for fluid-structure interaction based on an algebraic fractional step method. *Math. Models Methods Appl. Sci.*, 17(6):957-983, 2007.
4. A. Quarteroni, G. Rozza, and A. Quaini. Reduced basis methods for optimal control of advection-diffusion problems. In *Advances in Numerical Mathematics*, W. Fitzgibbon, R. Hoppe, J. Periaux, O. Pironneau, and Y. Vassilevski, Editors, pages 193-216, Moscow, Russia and Houston, USA, 2007.
5. A. Quarteroni, G. Rozza, L. Dedè, and A. Quaini. Numerical approximation of a control problem for advection-diffusion processes. In *System modeling and optimization*, Ceragioli et al. (Eds.), volume 199, pages 261-273. Springer, Boston, 2006. Proceedings of 22nd IFIP TC7 Conference, Turin, 2005.